



Watching nanomaterials with X-ray eyes: Probing different length scales by combining scattering with spectroscopy

Cinzia Giannini^a, Vaclav Holy^{b,c}, Liberato De Caro^a, Lorenzo Mino^d, Carlo Lamberti^{e,f}

^a Institute of Crystallography, National Research Council, Amendola 122, Bari 7016, Italy

^b Department of Condensed Matter Physics, Faculty of Mathematics and Physics, Charles University in Prague, Ke Karlovu 5, 121 16 Praha, Czech Republic

^c CEITEC at Masaryk University, Kotlářská 2, 61137 Brno, Czech Republic

^d Department of Chemistry, Interdepartmental Centre NIS, University of Torino, via Giuria 7, 10125 Torino, Italy

^e Department of Physics, Interdepartmental Centre CrisDi and INSTM reference center, University of Torino, via Giuria 1, 10125 Torino, Italy

^f Smart Materials Research Institute, Southern Federal University, Sladkova 178/24, 344090 Rostov-on-Don, Russia

ABSTRACT

Everybody dreams to have X-ray eyes and discover the most invisible secrets of the world around us. X-rays can probe matter (depth resolved) down to atomic resolution, if relying on diffraction-based techniques. An X-ray diffraction pattern may contain information over many length scales (atomic structure, microstructure, mesostructure). This peculiarity justifies the well-recognized impact of several X-ray diffraction-based techniques to diverse fields of research. On the other hand, X-ray spectroscopies (both in absorption and in emission) provide insights on the electronic structure and, exploiting element selectivity and local environment, can complement or even replace scattering techniques for diluted systems and amorphous materials. Herein, we provide a theoretical foundation which spans from very basic concepts, through well-known techniques, with applications to nanomaterials research. An increasing level of material complexity is explored: *size and shape* analysis of nanoparticles dispersed in solution or single nanostructures localized onto surfaces; local *morphology/strain* analysis of nanostructured surfaces; average *defects* analysis of stacking faulted nanocrystals; *regular 2D and 3D lattices* of self-assembled nanocrystals; *clusters* of nanocrystals without any nanoscale lattice order, standing alone as isolated objects or embedded in tenths-of- μm -thick polymers (here coherent and focused X-rays are mandatory to explore the spatial inhomogeneity and lattice (in)coherence of the materials).

1. Premises

1.1. Tailoring physical properties of matter

Today, many novel nanomaterials (nanoparticles – NPs – and/or nanocrystals – NCs) can be synthesized by physical (e.g. Molecular Beam Epitaxy, Laser Ablation, Sputtering and Metal Organic Vapour Phase Epitaxy) [1] or by chemical (e.g. Chemical Vapour Deposition or colloidal synthesis) [2,3] approaches. Independent of the adopted synthesis route, the emerging properties of nanoscale materials are often distinct and tunable with respect to the corresponding bulk, allowing additional degree of freedom towards improvements for the desired applications. Nanomaterials are characterized by *i*) a confined electronic density of states, due to their reduced size and *ii*) an extraordinary high (> 50% for nanocrystals of the order of 1–2 nm) [4,5] surface-to-volume atoms' ratio. New physical and chemical emergent properties may appear in the nanometer size regime. We refer to them as mesoscopic state and mesoscopic phenomena. Novel electronic, magnetic, optoelectronic or catalytic properties, not found in either bulk or molecular systems, can be engineered by varying the nanostructure size and shape, under a tight control of the synthesis parameters. So far, NCs with different shapes (spheres, disks, cubes, rods, multipods) have been manufactured [6–11] and elaborated hybrid nanocrystals

E-mail address: cinzia.giannini@ic.cnr.it (C. Giannini).

<https://doi.org/10.1016/j.pmatsci.2020.100667>

Received 7 May 2018; Received in revised form 11 March 2020; Accepted 16 March 2020

Available online 27 March 2020

0079-6425/ © 2020 Elsevier Ltd. All rights reserved.

synthesized [12,13]. These hybrid nanostructures consist of multi-material domains attached each other through hetero-interfaces. In the last decade, innovative and creative concepts such as assembly and self-assembly [14–16] have become central to modern nanotechnology, with the design of assembled superstructures made by ordered or random aggregation of individual building blocks. This is the case of super-crystals made by NCs organized according to a two-dimensional/three-dimensional (2D/3D) periodic or non-periodic superlattices [17], which emerging properties are not explainable as the linear combination of their building blocks.

In summary, in the last twenty years, NC synthesis has evolved from single-material nanocrystals (NCs) to multi-domain NCs and complex NC architectures, assisted by different local and ensemble characterization methods [18–23], such as: high-resolution transmission electron microscopy (HRTEM), scanning transmission electron microscopy (STEM) [24–26], eventually equipped with electron energy loss facility [27,28], electron diffraction (ED) [29–34], X-ray diffraction (XRD) [35–37], small and wide angle X-ray scattering (SAXS [23,38–49] total scattering [50,51], and WAXS [23]), magnetic neutrons scattering and X-ray diffraction [52], Raman [34,53–64], Mössbauer [65–67], X-ray absorption (XAS) [68–76], X-ray-emission (XES) [77–87] and X-ray fluorescence (XRF) [88–91] spectroscopies.

1.2. Nanostructure generations

The manipulation of matter at atomic, molecular and supramolecular levels is realized by nanotechnology with the aim to create novel hybrid materials, devices, and systems (hybrid means a mixture of inorganic and organic components).

Independently if fabricated with bottom-up or top-down techniques [1], distinct generations of nanostructures, in terms of complexity, can be identified [92]:

- I. **passive nanostructures** where the scientist's ability was devoted to the control of the chemistry and of the morphology of nanoparticles, nanotubes, nanocomposites, nanocoatings and nanostructured materials in order to obtain monodispersed and single crystalline phase structures;
- II. **active nanostructures** with tailored material functions to apply as electronics, as sensors, targeted drugs or adaptive structures;
- III. **hierarchical nanosystems** which means μm -scaled 3D supramolecular assembly of nanostructures with material properties dependent on the building nanosystems and their relative positions;
- IV. **smart nanosystems** which are evolutionary bio-nano systems, merging molecules and nanostructures, with hierarchical functions which change in time following precise stimuli.

Similar to biological systems, which continuously modify themselves in response to the stimuli they receive from the surrounding, "smart materials", if triggered by an external stimulus, can modify their properties [93–96], often in a reversible manner. Various stimuli can be identified: temperature, light, electric or magnetic fields, stress, strain, changes of pH, or of analyte concentrations in air, water, biological fluids.

Fig. 1 shows different length scales from natural and engineered world, but selecting only carbon-based materials [97]. Indeed, carbon is the most versatile element of the periodic table, being present in all proteins, peptides, nucleic acids, carbohydrates, as well as forming many allotropes due to its valence and hybridization: diamond, graphite, lonsdaleite, C60 buckminsterfullerene, C540 fullerite, C70, amorphous carbon, carbon nanotubes and, although chemically not pure, active carbons.

To fully exploit the vast potential of active nanostructures, hierarchical nanosystems and smart materials, non-destructive structural and morphological characterization techniques are required, since most of their novel properties depend on both analytical and structural features of each inorganic and biological nano-components as well as on their interaction.

The engineering of a complex material, such as hierarchical or smart materials, should require structural and morphological studies across multiple length scales, from the building blocks (NPs/NCs) to the whole architecture. In this review, we will focus on a selection of X-ray techniques, both diffraction-based and spectroscopy-based ones, the former being the core of materials structural analysis and the latter having the peculiarity of providing element selectivity. An X-ray diffraction pattern indeed may contain information over many length scales: the atomic structure, the microstructure, as well as the mesostructure of the material. Examples of nanotechnology-beneficiary smart materials are theranostics systems [98,99], nanomaterials for environmental science [100–108], tissue engineered bio-inspired scaffolds [109–114] electronic [115–118], optoelectronic [115,119–124], spintronic [125,126], photovoltaic [115,127–130], catalysis [131–145], sensing [146–149] etc. In the fraction of mentioned systems, where "nano meets biology" [150], the interactions of the nanoparticles or nanocrystals with the biosystem [151] have to be described as a multi-dimensional and multiscale problem.

Laboratories aiming to fabricate a scaffold able to mimic a tissue/organ, need to reproduce the hierarchic structure and composition of the natural tissue [152,153] to replace or repair. Typical questions concern the structure and morphology of such bio-material: is it amorphous or crystalline? What is the actual phase composition of the crystalline component? Does it contain an organic component? What is the structural correlation between inorganic and organic component? Which are the structural changes with time? Is the change related to the organic or inorganic component? Is the scaffold laterally inhomogeneous? An efficient non-destructive characterization tool is required to find quantitative answers to these questions.

Focused X-ray beams are today available to locally sample heterogeneity by imaging and mapping the micro- and nano-scale spatial variations [154–160] of structural, morphological or electronic properties across the different length scales. This achievement has been enabled by the advent of high-brilliance, third-generation synchrotron sources of X-ray radiation and by the fabrication of high-resolution X-ray focusing optics [161]. Focused micro and nano X-rays beams allow to study single nanomaterial objects and nanostructures, either organized in hetero-structures or assembled in periodic or disordered architectures, or embedded in a

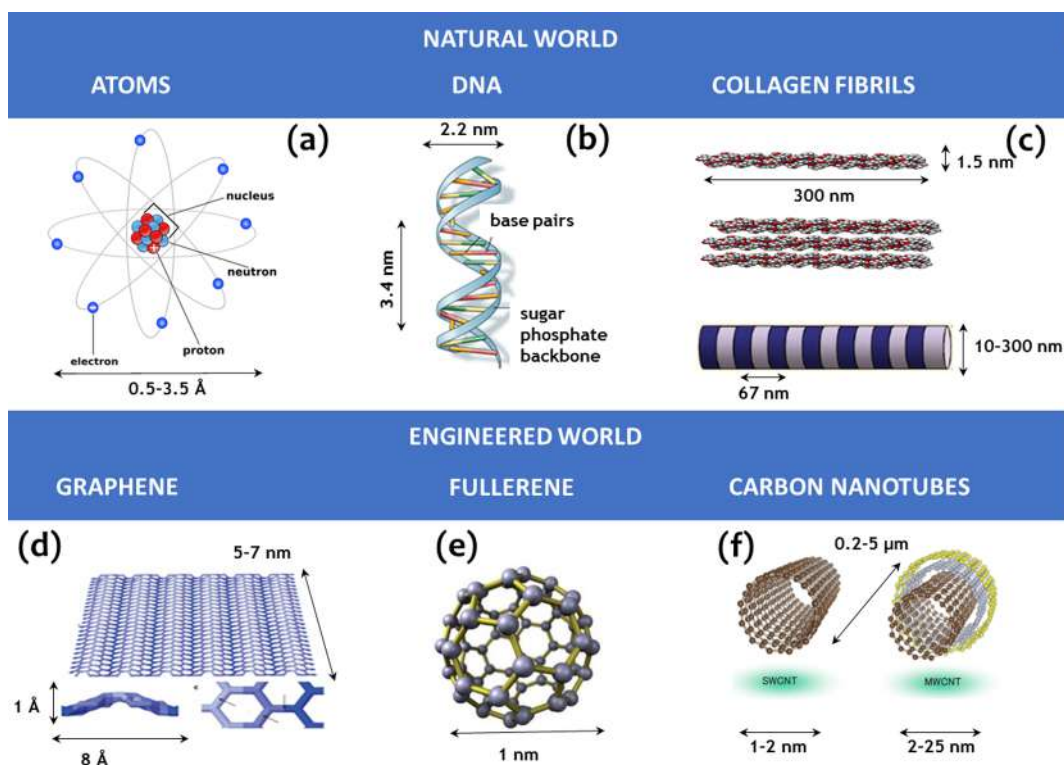


Fig. 1. Length scales from the natural and engineered world. Panel (d) reprinted with permission from Ref. [97]. Copyright 2012, Nature Publishing Group.

biological environment. Focused X-ray beams are used to: monitor the sample heterogeneity at different length scales [160], with a spatial resolution set by the focused beam size; induce functionalities to the NCs by X-ray micro and nano-patterning [162–168].

In what follows, we will describe the power of hard X-rays (in literature photons with energies above 5 keV are referred as hard X-rays) to probe matter. Key features, such as the large penetration depth (from several microns to tents of millimeters) and the short wavelength (Ångstroms and sub-Ångstrom), will be related to the unique possibility offered by hard X-rays to achieve (depth resolved) atomic resolution, at least in principle. It is well known that atomic resolution can be reached by electron microscopies, but with severe limitations on sample thickness and sample environment, restrictions which are overcome by hard X-rays. Indeed, hard X-rays can probe matter at mm depths. In addition, *in vivo* [169–174], *in situ* [71,73,82,134,139,175–179] and *operando* [73,139,180–188] experiments can be realized to monitor in real time a specific process.

The review will introduce basic principles behind scattering-based techniques, choosing the most widely used to study structure and morphology of nanomaterials (SAXS, WAXS, total scattering). In addition, some hints will be given on the novel opportunities offered by recent microscopies (X-ray scanning microscopy and coherent diffractive imaging) which adopt (incoherent/coherent) X-rays micro and nano beams. The latter are particularly suitable for the structural characterization of NCs as such materials fulfilling the translational symmetry at the local scale only; consequently, the standard diffraction approaches are of non-straightforward application. In parallel, we will consider also X-ray spectroscopies, such as extended X-ray absorption fine structure (EXAFS), X-ray absorption near edge structure (XANES) and X-ray emission spectroscopy (XES) allowing both electronic investigation and structural determination at the local scale to be achieved.

The review aims to introduce scientists working in the field of nanotechnology to specific X-ray diffraction techniques suitable for the structural/morphological characterization of nanocrystals. However, basic notions of crystallography (direct and reciprocal space, lattice symmetry, Miller indexes, Bragg law [189,190]) are mandatory to fully profit of the reading. Case studies will be discussed, specifying if a focused but partially coherent nano/micro X-ray beam was utilized. Considering the number of experiments using X-ray diffraction-based techniques for the analysis of modern nanomaterials which recently appeared in literature, it is impossible to give a comprehensive collection of experiments in this overview. We have picked up few selected applications from literature related to standard as well as more exotic nanomaterial studies.

2. Imaging regimes

When light approaches matter, each point of the illuminated object scatters the incident illumination into spherical waves according to the Huygens principle [191]. A few microns away from the object surface, the waves emanating from all object points become entangled, delocalizing the object's details. Therefore, a method must be found to reassign (“focus”) all the waves that are

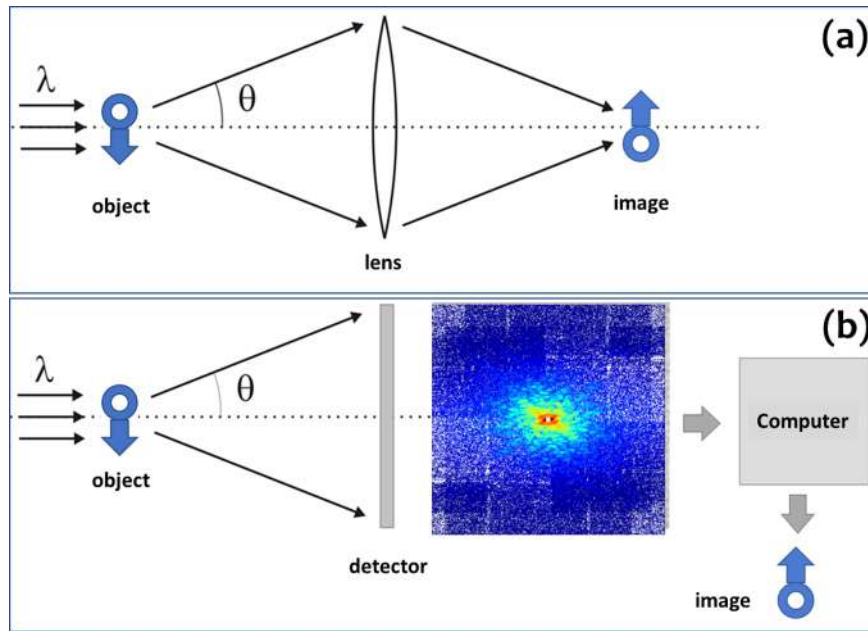


Fig. 2. (a): sketch of a conventional full-field imaging setup with a lens. (b): schematic lens-less imaging set-up. Previously unpublished figure.

emanated from a single point object into another point in space (the “image”), as done by microscopes. A microscope adopts an objective lens to create the object image by recombining the scattered waves with correct phases (see Fig. 2a). Microscopes exist for visible light, X-rays or electrons. In all of them, the image reconstruction has a resolution which is always affected by the lenses. For comparison, a lens-less set-up is schematically shown in Fig. 2b. Here, the X-ray beam scattered by the object freely propagates until it reaches the 2D detector. Since the detector can only register intensities, the phases of the propagated complex-valued wavefront are lost in the measurement process. Therefore, a phase retrieval algorithm substitutes the lens in order to recover the image of the object. The algorithm engine works as virtual optics. The resolution in both imaging methods is given by $\frac{\lambda}{\sin(\theta)}$, with λ being the X-ray wavelength and θ the maximum scattering angle accepted by the lens or by the detector (numerical aperture). Wavelength, numerical aperture, noise, mechanical precision and stability and sample radiation damage are all factors affecting and limiting the final phase retrieved image resolution.

A certain degree of coherence of the incoming radiation is required. The spatial and temporal coherence of light is the property which correlates regions of the wavefield separated laterally (spatial coherence) or longitudinally (temporal coherence). Temporal coherence can be introduced, for example, by a bandpass frequency filter, whereas spatial coherence is imparted by any spatial filter, such as a pinhole. The price for obtaining this partially coherent wave is, of course, the loss of optical energy (i.e. intensity) introduced by the temporal and spatial filtering processes. In chaotic sources, the spatial coherence length (ξ_c) is related to the size w of the source and to the distance R relative to the source by $\xi_c = \frac{\lambda}{w}R$. The temporal coherence length (L_c) is related to the beam monochromaticity $\Delta\lambda$ and is $L_c = \frac{\lambda^2}{2\Delta\lambda}$.

High-brilliance X-ray sources normally used in most of the imaging experimental setups (synchrotron sources [192–197] or free electron lasers [198–203]) may allow to produce coherent or partially coherent beams with low divergence characteristics. The extremely small divergence of this kind of sources allows most theoretical treatments to adopt the paraxial approximation, and to describe the diffraction theory within the scalar formulation.

If the source-specimen distance is z_1 and the specimen-detector is z_2 , the defocusing distance $z_d = \frac{z_1 z_2}{z_1 + z_2}$ and the magnification factor $M = \frac{z_1 + z_2}{z_1}$ can be defined (projection geometry), where the registered image is M times the real size of the object.

Three different imaging regimes can be exploited as a function of the Fresnel distance $d_f = \frac{a^2}{\lambda}$ where a is the typical object size and λ is the wavelength (Fig. 3).

Near-Field regime ($z_d \ll d_f$) In this case the contrast arises as an edge-enhanced image and the sharp edges of the object appear as characteristic fringes of oscillating intensity.

Fresnel regime ($z_d \sim d_f$) This situation is called also “holographic regime” and an interference pattern is formed by a great number of alternating fringes more and more closely spaced. In the Fresnel regime, the scattered intensity has a curved wavefront.

Fraunhofer regime ($z_d \gg d_f$) Finally we mention the far-field or Fraunhofer regime. This condition means that the typical size of the object is negligible compared with the distance involved. Any resemblance between recorded image and object is lost. The far-field is usually described as the region where the detected wavefield can be well defined by the Fourier transform of the exit surface wave of the object. The scattered intensity has a plane wavefront, i.e. the phases of the secondary waves scattered from the object in the detector plane depend linearly on the coordinates of the scattering centers.

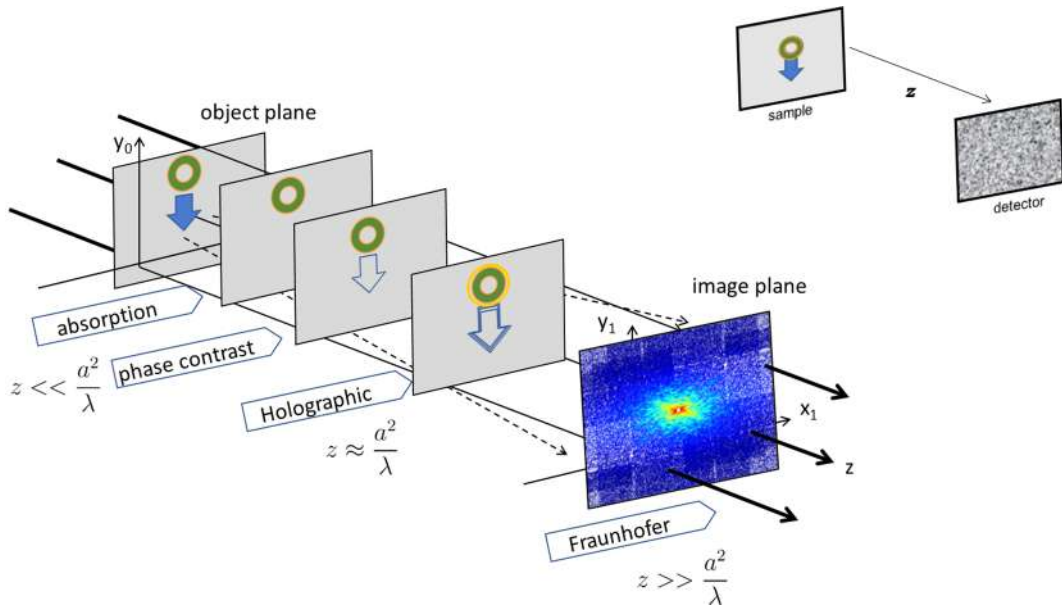


Fig. 3. Different lens-less imaging regimes: absorption contrast i.e. contact mode where only absorbing part is imaged; phase contrast and Fresnel regime where the borders of the less absorbing part of the object is imaged; far field regime where any resemblance with the object is lost. Previously unpublished figure.

2.1. Phase importance

Whenever X-rays interact with a coherent medium (crystal) or for coherent X-rays interacting with a disordered specimen we will have to take into account the relative positions of the scattering centers, mathematically described by phase factors.

Let's see how important is the phase contribution for whatever scattering process.

Parts (a) and (b) of Fig. 4 show a schematic representation of the fullerene and XY chromosomes electron density, respectively.

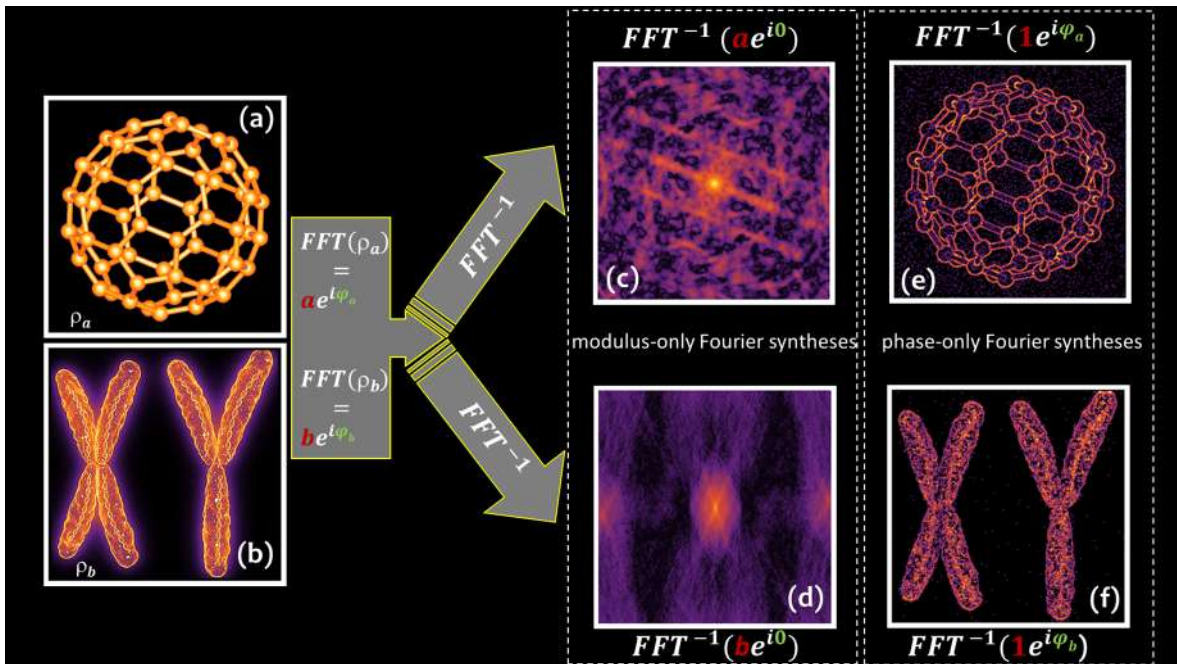


Fig. 4. (a) and (b) show a schematic representation of the fullerene and XY chromosomes electron density; (c) and (d) modulus-only Fourier syntheses obtained from FFT^{-1} of $a e^{i\varphi_a}$ and $b e^{i\varphi_b}$, using zero phase and the correct modulus of each pashor; (e) and (f) phase-only Fourier syntheses obtained from FFT^{-1} of $a e^{i\varphi_a}$ and $b e^{i\varphi_b}$, using the correct phase of each pashor but modulus equal to one. Previously unpublished figure.

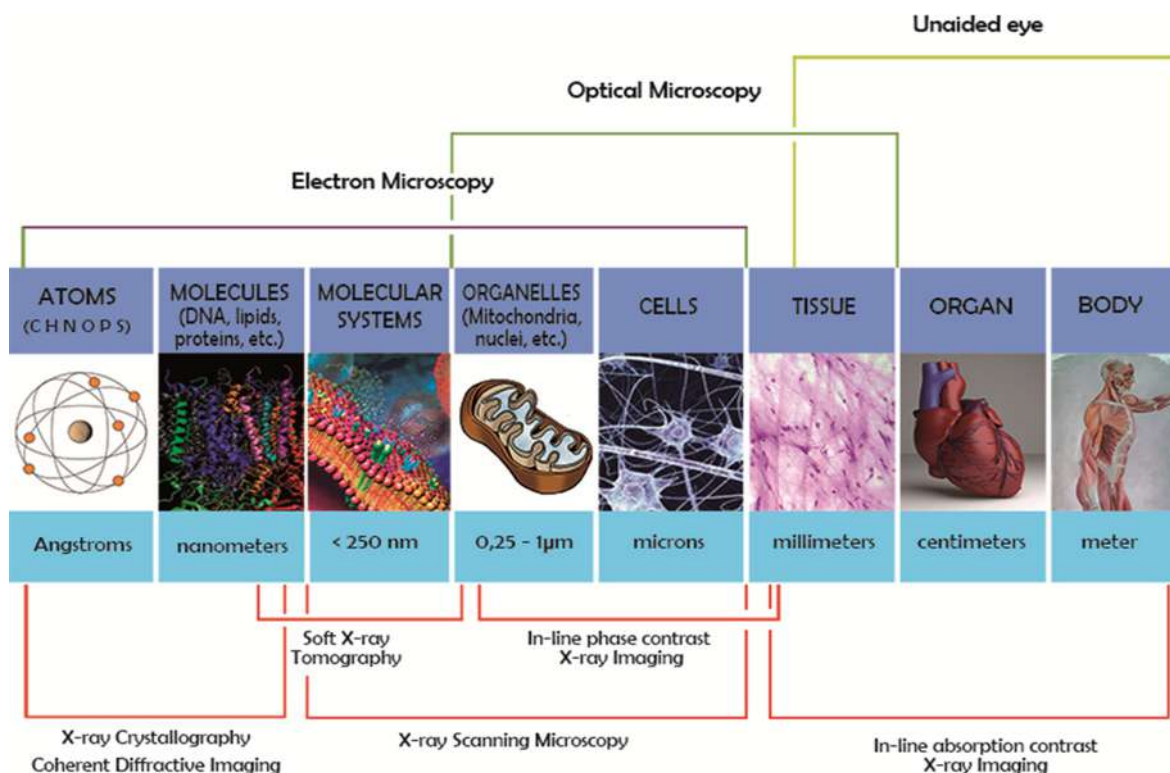


Fig. 5. Pictorial view of some X-ray Imaging techniques, in comparison with optical and electron microscopies. Reprinted with permission from Ref. [222].

The Fast Fourier Transform (FFT) of each image are the phasors $ae^{i\varphi_a}$ and $be^{i\varphi_b}$, complex functions to be inverted (by computing the inverse FFT, FFT^{-1}) in order to find back the original images. We can make this inversion in two different ways: *i*) using the correct modulus of each phasor but zero phase (modulus-only Fourier syntheses), obtaining the results in Fig. 4c,d, or *ii*) using a dummy modulus (assumed here equal to one) but the correct phases (phase-only Fourier syntheses), computing the images in Fig. 4e,f. This comparison clearly shows that spectral amplitude and phase play significantly different roles: the image information is preserved if the phase is retained. Indeed, only the images reconstructed through the phase-only Fourier syntheses (Fig. 4e,f) have many important features in common with the originals. This simple calculation is a strong evidence that phase shifts should be measured as carefully as possible (not feasible in a real experiment) or at least recovered *a posteriori* from the diffraction data by means of dedicated algorithms. We will deepen this argument in § 6.6. and § 6.7 In summary, phase contains the essential information of a wave signal describing an elastic scattering with respect to the amplitude which does not change as dramatically.

Fig. 5 provides a pictorial view of some X-ray imaging techniques available today, where X-ray crystallography and X-ray coherent diffraction imaging can be considered as different ways to access matter, respectively crystalline and not, at atomic/nanometric resolution. Crystallography, in the realm of imaging techniques, is the right tool to discover the most invisible secrets of the world around us, which can be explored down to atomic resolution [204]. For many years, in the X-ray field, it has been the only technique available at this resolution, with the ultimate limitation of using a crystal of sufficient quality and size to produce a significant diffraction signal. Since the beginning and up to a few years ago, this stringent condition has prevented several materials not readily makeable in form of crystals, such as membrane proteins and all intrinsically disordered proteins, or - to better say - in crystals of insufficient size and quality, from being studied. In the last decade a novel technique, called X-ray coherent diffractive imaging (CDI), appeared [154,205–211]. This technique uses coherent hard X-ray beams and has been conceived to image non crystalline matter (such as most of the biologic world), at least at nanometric resolution. In the interaction with matter the beam coherence is perturbed encoding structural fingerprints of the irradiated matter (sample). The fundamental ingredient is therefore the coherence of the X-rays source, only available at third generation synchrotron facilities [192–197], and fourth generation synchrotron facilities [212–214] or from free electron lasers (FEL) [198–203,215,216]. In cases when dose related problems can be overcome [217], interesting crystallographic results have been achieved so far with X-ray coherent beam to solve the structure solution of protein nanocrystals [218–220].

Before exploring the interesting world of X-ray scattering techniques, at the base of modern microscopies [221,222], we will resume basic concepts in common to all X-ray scattering-based techniques.

2.2. Scattering from atoms –Thomson and Rayleigh scattering

Scattering of an x-ray photon by free or bound electron is a quantum mechanical process. In the case of free electron, the scattering process (the Compton scattering) is incoherent, i.e., the phase of the scattered wave is random and the scattered wave only increases the background. The scattering from the bound electron can be described within quantum theory as well [223–228] (some citation). However if we restrict ourselves to elastic scattering and if the energy of the scattered photon is far from the energies of the electron transitions in the scattered material (in particular, ionization energies of various electron states in the atoms), the classical approximation (the Thomson scattering) can be used. In this approximation, the differential cross-section of the scattering is:

$$\frac{d\sigma}{d\Omega} = r_e^2 C^2, \quad (1)$$

where

$$r_e = \frac{e^2}{4\pi\epsilon_0 mc^2} \approx 2.818 \times 10^{-15} \text{ m} \quad (2)$$

is the classical electron radius (electron scattering length) and

$$C = \sin\varphi = \begin{cases} 1 & \text{for S polarization} \\ \cos(2\Theta) & \text{for P polarization} \end{cases} \quad (3)$$

is the linear polarization factor (2Θ is the scattering angle). This factor depends on the polarization of the incoming radiation; φ is the angle between the polarization vector of the incoming radiation and the vector $\mathbf{r} - \mathbf{r}'$. In the S polarization, the polarization vector \mathbf{E}_i is perpendicular to the common plane of \mathbf{k}_i and $\mathbf{r} - \mathbf{r}'$ (scattering plane), and $\sin\varphi = 1$. In the P polarization \mathbf{E}_i lies in the scattering plane and $\sin\varphi = \cos(2\Theta)$. The polarization direction of the scattered wave is parallel to the projection of \mathbf{E}_i into the plane perpendicular to the propagation direction i.e. to $\mathbf{r} - \mathbf{r}'$. In many x-ray scattering experiments the primary x-ray beam can be assumed fully non-polarized; in this case the scattered radiation is an incoherent superposition of S and P components. Therefore, the scattered intensity contains the average of the squares of the C values for these two linear polarizations

$$\frac{1}{2}[1 + \cos^2(2\Theta)] \quad (4)$$

which is usually called polarization factor. The fact that the scattering electrons are bound in electron shells around an atom core plays a role if the photon energy is close to the ionization energy. In this case, the scattering cross-section is corrected by dispersion (Hoehn) corrections – see below.

The wave scattered by an atom can be described as a coherent superposition of waves scattered by individual electrons.

Let us introduce the scattering vector or wave vector transfer \mathbf{q} as the difference between incident (\mathbf{k}_i) and scattered (\mathbf{k}_s) wave vectors: $\mathbf{q} = \mathbf{k}_s - \mathbf{k}_i$. Since the scattering process is assumed elastic, its modulus q is the following function of the wavelength λ and of the scattering angle θ :

$$q = |\mathbf{q}| = 2k\sin\theta = \frac{4\pi}{\lambda}\sin\theta \quad (5)$$

Let us consider now scattering from a single atom. The amplitude of the wave scattered from an atom equals the amplitude of a wave scattered from a free electron lying in the center times the **atomic scattering factor**

$$f^0(\mathbf{q}) = \int d^3\mathbf{r}\rho(\mathbf{r})e^{-i\mathbf{q}\cdot\mathbf{r}} \quad (6)$$

Obviously, we completely neglect scattering from the atomic nucleus, which is (except for special “resonant” cases) indeed negligible.

The atomic scattering factor, or atomic form factor, is maximum at $\theta = 0$ ($f^0(q = 0) = Z|e|$), i.e. in the forward direction, where the scattered waves add all in phase, and coincides with the atomic number (see Fig. 6 for a comparison between silicon and carbon). In the whole q range, $f^0(q)$ decreases monotonically as a function of q and thus of the scattering angle. At $q \rightarrow \infty$, $f^0(q \rightarrow \infty) = 0$ because of the destructive interference to the integral (6) of the electron density $\rho(\mathbf{r})$, coming from different positions \mathbf{r} in space. It is worth noting that, for an isolated atom, the electron density $\rho(\mathbf{r})$ can be assumed isotropic in an atom in a ground state so that its atomic scattering factor is a real function of the length $q = |\mathbf{q}|$ of the scattering vector.

In summary:

The scattering factor depends on both q and λ :

- For a fixed λ : f^0 decreases monotonically with q i.e. with the scattering angle; consequently, the scattering factor in the small angle X-ray scattering (SAXS) range (few degrees), due to the loosely bound valence electrons, is higher than in the wide angle X-ray scattering (WAXS), due to the tightly bound core electrons.
- For a fixed q : the smaller λ the smaller f^0 , meaning the smaller the wavelength the lower the contribution to the coherent scattering.

If the photon energy is close to the ionization energy of any electron state in the atom, i.e. if the energy is close to an absorption

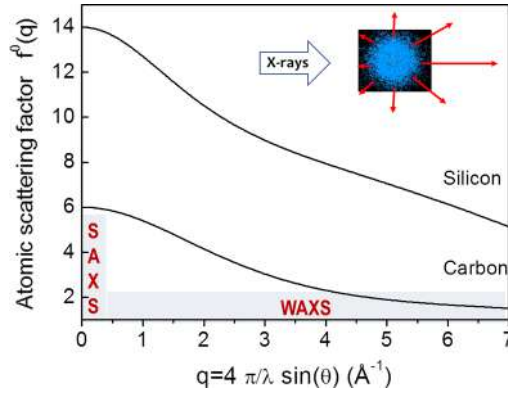


Fig. 6. Atomic scattering factor for silicon and carbon. Previously unpublished figure.

edge [229,230], the correction of the Thomson atomic scattering factor (the dispersion correction the Hoehnl correction) becomes important. In the first approximation, the Hoehnl correction can be expressed as a complex function of the photon energy $E = \hbar\omega$ so that the complete expression for the atomic scattering factor is:

$$f^0(q, E) = f^0(q) + f'(E) + if''(E) \tag{7}$$

The values of the real and imaginary dispersion corrections $f'(E)$, $f''(E)$ can be found in the literature or on various web databases [231–234]. It is worth mentioning that these functions are not independent and they are mutually connected by Kramers-Kronig integral transformation [235,236]. In Fig. 7 we present these functions for Mn for energies around the Mn K-absorption edge. At the absorption edge, the real part of the dispersion corrections exhibits a steep dip, while the imaginary part steeply increases. This increase is manifested by a step-like increase of x-ray absorption, due to the opening of the photoelectric channel; this effect is called absorption edge.

The neighborhood of an atom affects its scattering factor especially in the energy range just above an absorption edge. If the photon energy is larger than the ionization energy of an electron, the photon absorption results in the emission of a photoelectron. The interaction of the photoelectron with the neighboring atom affects the absorption cross-section and consequently modifies the functions $f'(E)$, $f''(E)$, see Fig. 8 for the GaAs case. This effect is used in various x-ray absorption spectroscopy methods (EXAFS [68,237–240], XANES [69,241–244], DAFS [245,246]), the description of which will be briefly provided in section 3.2.) for the electric susceptibility determines also the index of refraction n of x-rays, using the well-known formula

$$n = 1 + \chi = 1 - \frac{\lambda^2 r_e}{\pi} \langle \rho(\mathbf{r}) \rangle \tag{8}$$

which contains the electron density averaged over a volume much larger than the crystal unit cell (or larger than the inter-atomic distances in case of amorphous materials). Taking into account the dispersion corrections in Eq. (8), the refraction index is [73,247–249]:

$$n = 1 - \frac{\lambda^2 r_e}{2\pi} \sum_j n_j [Z_j + f'_j(E) + if''_j(E)] \equiv 1 - \delta + i\beta \tag{9}$$

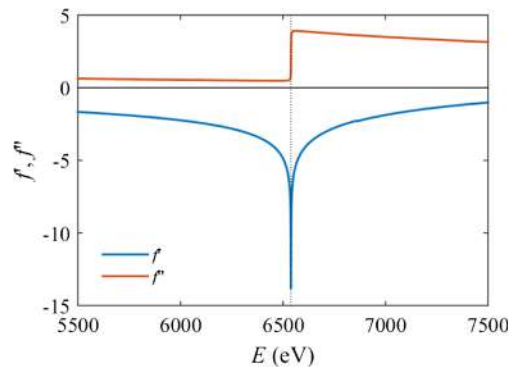


Fig. 7. Real (blue) and imaginary (yellow) Hoehnl dispersion correction of Mn calculated in the neighborhood of the Mn K-absorption edge (6539 eV – vertical dotted line). (For interpretation of the references to color in this figure legend, the reader is referred to the web version of this article.)

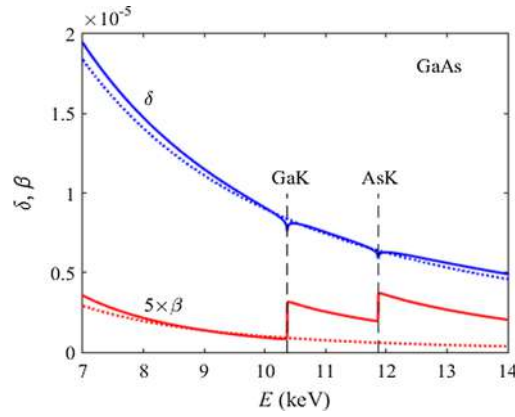


Fig. 8. Real (δ , blue) and imaginary (β , red) parts of $1 - n$ calculated for GaAs in the vicinity of the absorption edges GaK and AsK (vertical dashed lines). The dotted lines show the power laws E^{-2} (blue) and E^{-3} (red), respectively. Previously unpublished figure. (For interpretation of the references to color in this figure legend, the reader is referred to the web version of this article.)

where n_j is the density of atoms of type j (number of atoms per unit volume), Z_j is its atomic number, and f_j', f_j'' are its dispersion corrections. It is worthy to note that $\text{Re}(n) = 1 - \delta < 1$ and $\beta > 0$.

As an example, we present here the energy dependences of β and δ for GaAs in the vicinity of the absorption edges GaK and AsK (Fig. 8). An absorption edge, i.e. a steep increase of β corresponds to a narrow dip in δ ; the functions $\beta(E)$ and $\gamma(E)$ are connected by the Kramers-Kronig transformation [235,236]. Between the edges the functions $\beta(E)$ and $\gamma(E)$ can be approximated by E^{-2} and E^{-3} , respectively [250].

3. Scattering from molecules and crystals

3.1. Scattering from molecules – molecular morphology

The scattering factor of a molecule, also called **molecule form factor** [250], is computed by taking into account the scattering of all the electrons in all the atoms of the molecule, and considering that the atoms sit at precise relative positions:

$$F^{\text{mol}}(\mathbf{q}) = \int d^3r \rho^{\text{mol}}(\mathbf{r}) e^{-i\mathbf{q}\cdot\mathbf{r}} = \sum_n f_n(q) e^{-i\mathbf{q}\cdot\mathbf{r}_n} \quad (10)$$

Here we denoted $\rho^{\text{mol}}(\mathbf{r})$ the electron density belonging to all atoms constituting the molecule, the sum is running over the atoms in the molecule, and $f_n(q)$ is the atomic form factor of the n -th atom, see Eq. (6).

Let's consider the C60 fullerene molecule in Fig. 9. The molecule form factor, here shown, is computed two-dimensionally (2D) for specific conditions: $\lambda = 1 \text{ \AA}$, detector pixel size = 200 μ , linear detector size = 20 cm; sample-to-detector distance = 5 cm (WAXS) or 100 cm (SAXS). The 2D molecular form factors has a complex electronic distribution: if computed at few cm distance from the sample (Fig. 9b) disclose atomic information (WAXS range), if computed at 100 cm distance or more (Fig. 9c) contains only nanoscale information (SAXS range), as marked by the dotted white circles.

Scattering from an ensemble of N molecules can be described within the kinematical approximation if we assume that multiple scattering (i.e. successive scattering of a photon from two or more molecules) can be neglected (this represents an important advantage in the analysis of the scattering from X-rays with respect to that from electrons) [251–253]. The scattered wave is then created by a superposition of spherical waves originating from different molecules. If, for simplicity the far-field limit is assumed not only for a single molecule, but also for the whole molecule ensemble (i.e. the entire “sample” is smaller than the first Fresnel zone) we obtain the following simple formula for the scattered wave

$$E_s(\mathbf{q}) = KE_i \sum_{j=1}^N F_j^{\text{mol}}(\mathbf{q}) e^{-i\mathbf{q}\cdot\mathbf{R}_j} \quad (11)$$

where F_j^{mol} and \mathbf{R}_j are the scattering factor and position vector of the j -th molecule. K is the multiplicative factor

$$K = -r_c \frac{e^{ikR}}{R} C \quad (12)$$

Usually, our irradiated sample volume contains a very large number N of randomly placed molecules. Therefore, the scattered intensity is expressed as a huge double sum of all molecules. In the following we assume that the sample volume is so large that all possible local configurations of molecules are present in it. In other words, any change of local positions of the molecule would result in a negligible change of the scattered intensity. Therefore, the scattered intensity can be considered averaged over an infinite number of local configurations of N molecules:

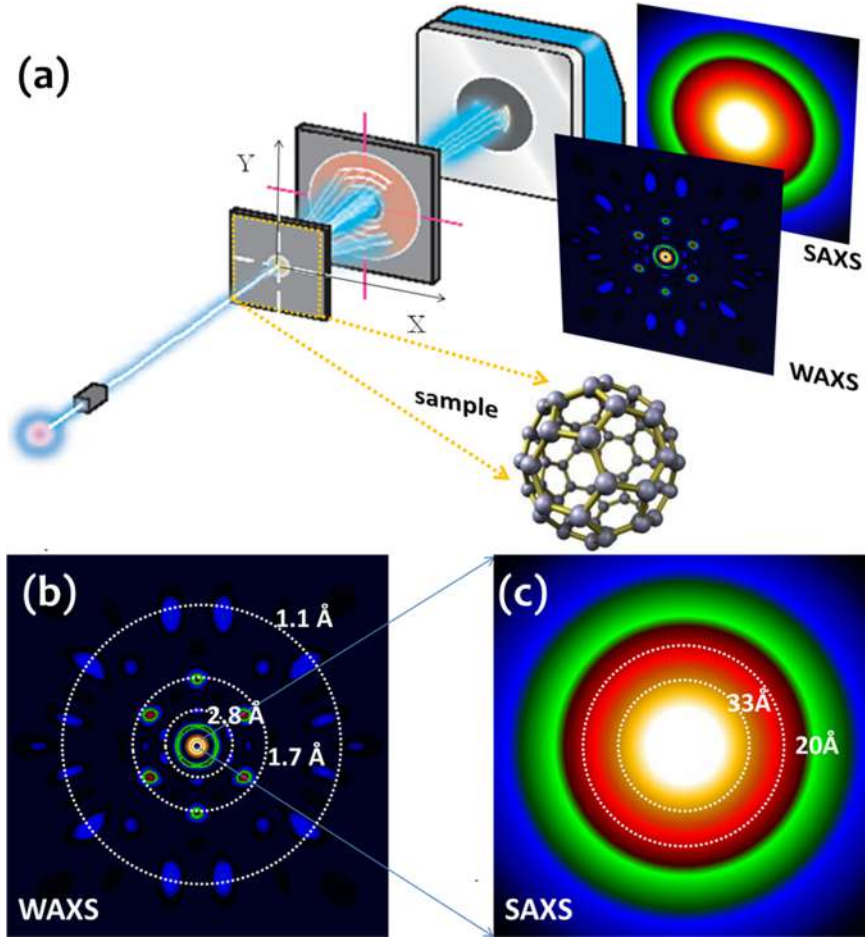


Fig. 9. (a): experimental set-up allowing to collect simultaneously WAXS and SAXS. (b): form factor at 5 cm sample-detector distance (WAXS range). (c): form factor at 100 cm sample-detector distance (SAXS range). The form factor has been computed with the program nearBragg by James Holton, available for the scientific community at the web page <http://bl831.als.lbl.gov/~jamesh/nearBragg/>.

$$I_s(\mathbf{q}) = |K|^2 I_i \left\langle \sum_{j=1}^N \sum_{j=1}^N F_j^{\text{mol}}(\mathbf{q}) [F_j^{\text{mol}}(\mathbf{q})]^* e^{-i\mathbf{q}\cdot\mathbf{A}\cdot(\mathbf{R}_j - \mathbf{R}_j)} \right\rangle_{\text{pos,mol}} \quad (13)$$

where the averaging runs over the positions of the molecules and over all other molecular degrees of freedom (orientation, conformation, etc). In most cases we can assume that the random molecule positions are not statistically correlated to the molecular degrees of freedom, so that the averaging can be factorized. After some algebra we obtain the following expression for the ensemble-averaged scattered intensity:

$$I_s(\mathbf{q}) = |K|^2 I_i \{ N [\langle |F^{\text{mol}}(\mathbf{q})|^2 \rangle - |\langle F^{\text{mol}}(\mathbf{q}) \rangle|^2] + |\langle F^{\text{mol}}(\mathbf{q}) \rangle|^2 G(\mathbf{q}) \} \quad (14)$$

where

$$G(\mathbf{q}) = \left\langle \sum_{j=1}^N \sum_{j=1}^N e^{-i\mathbf{q}\cdot\mathbf{A}\cdot(\mathbf{R}_j - \mathbf{R}_j)} \right\rangle_{\text{pos}} \quad (15)$$

is the correlation function of the molecule positions.

In a real experiment the primary X-ray wave is only partially coherent so that it cannot be described by an ideal plane wave. In this case, the equations must be reformulated taking into account the mutual coherence function (MCF) of the primary wave. For simplicity, let us restrict now to an ideally monochromatic partially coherent wave. The MCF is then defined as

$$\Gamma_i(\mathbf{r}, \mathbf{r}') = \langle E_i(\mathbf{r}) [E_i(\mathbf{r}')]^* \rangle_{\text{field}} \quad (16)$$

where the averaging is performed over all microstates of the incident x-ray field. Let us assume that the incoming field is statistically

homogeneous, i.e. $\Gamma_i(\mathbf{r}, \mathbf{r}') = \Gamma_i(\mathbf{r} - \mathbf{r}')$, then the ensemble-averaged scattered intensity can be expressed as:

$$I_s(\mathbf{q}) = |K|^2 \int \frac{d^2\mathbf{k}^0}{k^2} \Gamma_i(\mathbf{k}) \left\langle \sum_{j=1}^N \sum_{j=1}^N F_j^{\text{mol}}(\mathbf{k} - \mathbf{k}_i) [F_j^{\text{mol}}(\mathbf{k} - \mathbf{k}_i)]^* e^{-i(\mathbf{k} - \mathbf{k}_i)\hat{A} \cdot (\mathbf{R}_j - \mathbf{R}_j')} \right\rangle_{\text{pos,mol}} \quad (17)$$

where we have expressed the primary beam as a random superposition of many plane wave components with various wave vectors \mathbf{k}

$$\Gamma_i(\mathbf{r} - \mathbf{r}') = \int \frac{d^2\mathbf{k}^0}{k^2} \Gamma_i(\mathbf{k}) e^{i\mathbf{k}\hat{A} \cdot (\mathbf{r} - \mathbf{r}')} \quad (18)$$

Deriving Eq. (17) we made a natural assumption that the averaging $\langle \rangle_{\text{field}}$ over all microstates of the incident field is independent from the averaging $\langle \rangle_{\text{pos,mol}}$ over the microstates of the sample. From Eqs. (17) and (18) it follows that in the case of a partially coherent primary wave the scattered wave is expressed as a convolution of the Fourier transformation of the MCF of the primary beam with the reciprocal-space distribution of the scattered wave for an ideally coherent primary field.

In an usual experimental arrangement the irradiated sample volume is much larger than the coherence width and/or length of the primary radiation so that the irradiated volume can be described as many coherently irradiated volumes (CIVs). The waves scattered from the particles (molecules) within one CIV interfere, while the waves stemming from different CIVs have random phases and therefore their interference disappears due to averaging $\langle \rangle_{\text{field}}$ over all microstates of the primary wave. Therefore, the measured radiation can be expressed as incoherent (intensity) superposition of the waves stemming from various CIVs. Since different CIVs contain different microstates of the sample, the measured signal is averaged $\langle \rangle_{\text{pos,mol}}$ over the sample microstates as well.

In order to investigate one microstate of the sample, the irradiated sample volume must contain one CIV, i.e. the cross-section of the primary beam must be comparable to its coherence width and the primary beam must be (almost) fully coherent. This so called coherent diffraction or coherent diffraction imaging (CDI) can be realized on synchrotron sources using a very narrow primary beam (see §6.3).

Monodisperse systems consisting of identical molecules dispersed in a buffer (such as water) can form a very diluted (gas-like) or a more correlated system (liquid-like), as depicted in Fig. 10a and b, respectively. This difference offers a practical way to determine the form factor (F_j^{mol}) of a specific molecule.

In a gas-like system the correlation of the molecule positions can be completely neglected, i.e.

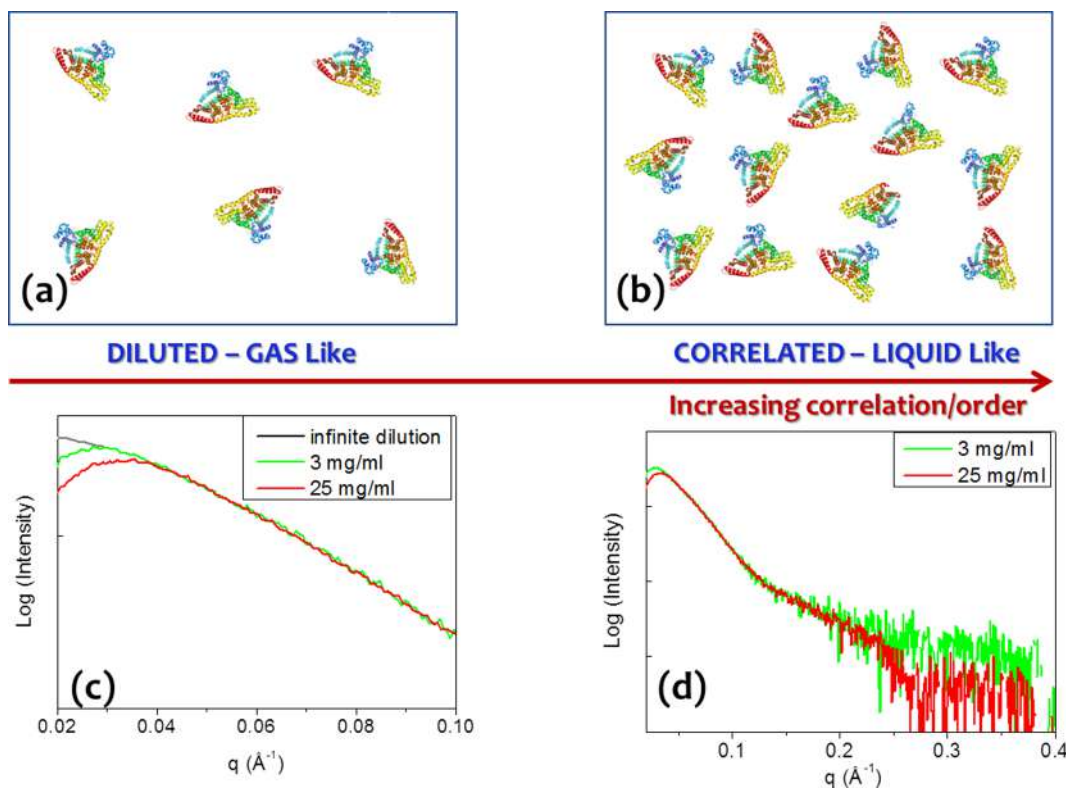


Fig. 10. (a): system of diluted (gas-like) BSA molecules. (b): system of correlated (liquid-like) BSA molecules. (c) SAXS profiles for 3 mg/ml system (green line), 25 mg/ml system (red line), infinite dilution (black curve). (d) as part (c) in an extended q region. Previously unpublished figure. (For interpretation of the references to color in this figure legend, the reader is referred to the web version of this article.)

$$\left\langle e^{-iq\hat{A}\cdot(\mathbf{R}_j-\mathbf{R}_j)} \right\rangle_{\text{pos}} \approx \delta_{j,j'} \quad (19)$$

and $G(\mathbf{q}) = N$. Then, the scattered intensity is

$$I_s(\mathbf{q}) = |K|^2 f_i N \langle |F^{\text{mol}}(\mathbf{q})|^2 \rangle \quad (20)$$

i.e. proportional to the average of the square of the scattering factor of a single molecule.

When a gas-like system is needed, concentration must be decreased until the inter-molecular scattering can be neglected. The way to control this contribution is by monitoring the SAXS pattern at extremely low scattering vectors: infinite dilution is identified as the black curve in Fig. 10c. At higher concentration the mean correlation distance between molecules is higher and affects the low angle scattering and the curve deviates from the back profile in Fig. 10c.

For liquid-like systems (Fig. 10b) Eq. (14) has to be used, i.e. the scattered intensity depends both on the molecule structure factor and on the correlation function of the molecule positions.

Fig. 10d shows the difference in a wider scattering range between the scattering curves of a more (green line) and a less diluted (red line) system containing the same Bovine Serum Albumine (BSA) molecule at increasing concentrations. In very diluted solutions, the interaction among molecules is negligible and the information which is encoded in the scattering curve is only morphological (size and shape of the molecule, alias form factor, and molecular weight).

3.2. Scattering from crystals – Bragg law

Whenever the correlation among atoms/molecules increases and the relative distance between them remains constant (i.e. periodic) along nanometric or micrometric distances we are dealing with a crystal. Hard X-rays have wavelengths $\lambda = 0.1\text{--}2 \text{ \AA}$, representing a range of distances comparable to the typical crystalline interatomic distances (2 \AA) or one order of magnitude smaller (0.1 \AA); they are consequently an appropriate radiation to investigate the atomic structure of matter. X-rays are first scattered by the electronic cloud of each atom/molecule. The diffused secondary waves, due to the periodic atom/molecule positions, interfere constructively or destructively along specific directions, as depicted in Fig. 11. Indeed, the word “diffraction”, which is the combination of scattering and interference, originates from the Latin word “diffrangere” which means “to break in more parts”. The wavefront breaks in the intensity maxima as a consequence of the interference of the scattered secondary waves, as shown in Fig. 11. As explained in §2, different diffraction regimes can be defined comparing the propagation distance L of the diffracted wavefront to the Fresnel distance $d_F = d^2/\lambda$ where d is the size of the scattering object. For $L \sim d_F$ (near field, Fresnel regime) only a small portion of the scattered secondary waves (in the proximity of the scattering sample) has the possibility to interfere. For $L \gg d_F$ (far field, Fraunhofer regime) all secondary waves, have the possibility to interfere.

X-ray Bragg diffraction [189,190,254] is the result of the interference among the secondary waves produced by the scattering between X-rays and atoms/molecules in a crystal, and holds in a Fraunhofer diffraction regime, as the sample to detector distance is macroscopic. The total scattered radiation, arising both from the elastic (Rayleigh) and inelastic (Compton [255] and photoelectric effect [256]) scattering events, which occur at different atoms in a material, produces the observed pattern. The effect of the elastic Rayleigh scattering gives rise to the prominent Bragg reflections: intensity maxima along specific angular directions which depend on the crystal unit cell dimension and atomic content.

The theoretical description of X-ray scattering starts from Eq. (13) or Eq. (17) (for ideally coherent or incoherent primary wave, respectively). We assume an ideal crystal, therefore the structure factors $F_j(\mathbf{q})$ of the molecules or other structure units (primitive unit cells) are identical and the position vectors of these units are integer linear combination of three basis vectors $\mathbf{a}_{1,2,3}$ of the primitive lattice:

$$\mathbf{R}_j = j_1 \mathbf{a}_1 + j_2 \mathbf{a}_2 + j_3 \mathbf{a}_3, j_{1,2,3} \in \mathbb{N} \quad (21)$$

The scattered intensity then reads

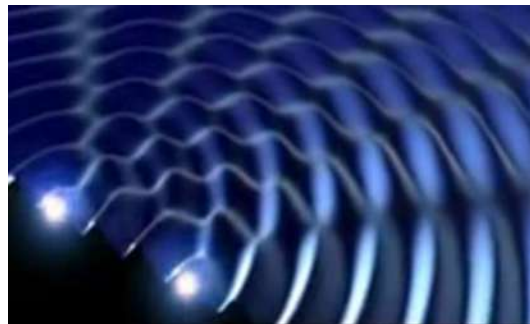


Fig. 11. X-rays are scattered by the two atoms (bright spots in the left bottom corner). Interference occurs forming destructive (black) and constructive (bright) zones.

$$I_s(\mathbf{q}) = |K|^2 I_1 |F(\mathbf{q})|^2 \left| \sum_{j_{1,2,3} \in \Omega} e^{-i\mathbf{q} \cdot (\mathbf{a}_1 j_1 + \mathbf{a}_2 j_2 + \mathbf{a}_3 j_3)} \right|^2 \quad (22)$$

Here the symbol Ω denotes the crystal volume. Thus, the scattered intensity is a product of two terms:

1. Square of the structure factor of the primitive unit cell $F(\mathbf{q})$; this factor depends on the positions of the atoms in the unit cell and does not depend on the arrangement of the cells.
2. Square of the geometrical factor (lattice sum) $G(\mathbf{q}) = \sum_{j \in \Omega} \dots$ containing the positions of the cells and not depending on the atom positions within the cell.

We define the reciprocal lattice with the basis vectors $\mathbf{b}_{1,2,3}$ obeying the orthogonality relation to the basis vector of the primitive lattice \mathbf{a}_j . $\mathbf{b}_k = 2\pi\delta_{j,k}$. Then the geometrical factor can be obtained in the form

$$G(\mathbf{q}) = \sum_{\mathbf{g}} \Omega^{\text{FT}}(\mathbf{q} - \mathbf{g}) \quad (23)$$

where $\mathbf{g} = g_1 \mathbf{b}_1 + g_2 \mathbf{b}_2 + g_3 \mathbf{b}_3$, $g_{1,2,3} \in \mathbb{N}$ are the vectors of the reciprocal lattice and

$$\Omega^{\text{FT}}(\mathbf{q}) = \int d^3\mathbf{r} \Omega(\mathbf{r}) e^{-i\mathbf{q} \cdot \mathbf{r}} \quad (24)$$

is the Fourier transformation of the shape function of the crystal $\Omega(\mathbf{r})$ (which is unity in the crystal volume and zero outside it). Thus, the geometrical factor equals the sum of the Fourier transformations of the crystal shape functions centered in all points of the reciprocal lattice. Explicit expression of the geometrical factor exists only for the simplest crystal shapes.

In Fig. 12 we present a simple sketch demonstrating the geometrical factor as a superposition of individual “clouds”, which illustrate the Fourier transformation of the shape function (Fig. 12a). The Ewald sphere [257] is represented by the red dashed circle, the intersections of this circles with the “clouds” determine the ending points of possible wave vectors \mathbf{k}_s of the scattered wave.

If the scattering vector \mathbf{q} is close to a chosen reciprocal lattice vector $\mathbf{g} = \mathbf{h}$, then in the sum in Eq. (23) all terms with $\mathbf{g} \neq \mathbf{h}$ can be neglected (so called two-beam case) and the geometrical factor equals the Fourier transformation of the crystal shape. Unfortunately, this approximation cannot be used in the case of small crystals, since the overlap of the functions Ω^{FT} centered in neighboring reciprocal lattice points cannot be neglected. The geometrical factor is a very rapidly varying function of \mathbf{q} . A maximum of the geometrical factor appears if the scattering vector equals any of the reciprocal lattice vectors: $\mathbf{k}_s - \mathbf{k}_i \equiv \mathbf{q} = \mathbf{g}$.

From the theory of reciprocal lattice it follows that the length $|\mathbf{g}| = |h\mathbf{b}_1 + k\mathbf{b}_2 + l\mathbf{b}_3|$ of a reciprocal lattice vector is $|\mathbf{g}| = 2\pi/d_{hkl}$, where d_{hkl} is the interplanar distance, i.e. the distance of the crystallographic planes with the h, k, l Miller indexes [258]. Then using Eq. (5) we obtain the famous **Bragg's law** [189,190,254] connecting the interplanar distance with the scattering angle, called the Bragg angle θ_B in this case:

$$2d_{hkl} \sin\theta = \lambda \quad (25)$$

The interplanar distances of the crystal are related to the unit cell by simple formulae for each crystal system (see International Tables of Crystallography).

For interplanar distances at the atomic scale (i.e. $d_{hkl} = 5 \text{ \AA}$) and at the nanoscale (i.e. $d_{hkl} = 50 \text{ \AA}$), and for a wavelength $\lambda = 1 \text{ \AA}$, the Bragg peaks are typically registered at $2\theta \sim 11.48^\circ$ (wide angle x-ray diffraction, WAXD) and at very low angles $2\theta \sim 1.15^\circ$ (small angle x-ray diffraction, SAXD), respectively. This explains why X-ray diffraction is a multiple length scale characterization tool which is efficiently used to study both atomic and nanometric order in crystals. At the same length scales, if matter is not crystalline or alternatively if atoms/molecules do not occupy periodic positions in space, we should not talk of diffraction anymore but simply of

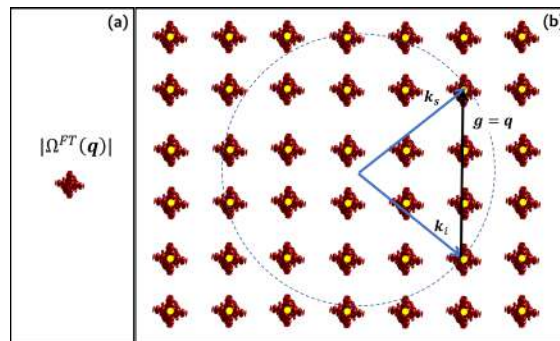


Fig. 12. (a) Modulus of the FT of the shape function, $\Omega^{\text{FT}}(\mathbf{q})$. (b): Illustration of the geometrical factor, as a superposition of individual “clouds” (red colored) positioned at the reciprocal lattice points (yellow spots), which illustrates the Fourier transformation of the shape function, and the Ewald sphere (dashed line). Previously unpublished figure. (For interpretation of the references to color in this figure legend, the reader is referred to the web version of this article.)

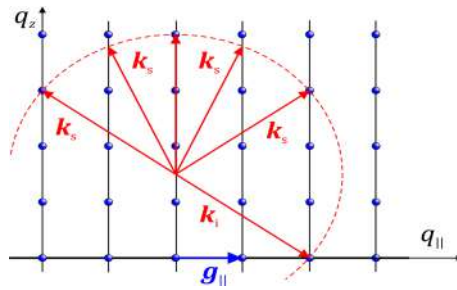


Fig. 13. Lateral diffraction condition; the blue spheres represent the reciprocal-lattice points, the Ewald sphere is indicated by red dashed circle. Previously unpublished figure. (For interpretation of the references to color in this figure legend, the reader is referred to the web version of this article.)

scattering or diffuse scattering. In these cases, it is correct to define them wide angle x-ray scattering (WAXS) and small angle x-ray scattering (SAXS). For further details see §3.4.

The Bragg law cannot predict the relative intensity of the diffraction maxima, but only the peak position for a specific crystal (when d_{hkl} are known).

If the diffracting crystal is laterally very large, the Fourier transformation of the crystal shape function $\Omega^{FT}(\mathbf{q})$ is represented by a vertical, laterally very narrow pencil (crystal truncation rod – CTR). Then, the lateral diffraction condition is valid:

$$\mathbf{q}_{\parallel} \equiv \mathbf{k}_{s\parallel} - \mathbf{k}_{i\parallel} = \mathbf{g}_{\parallel} \tag{26}$$

i.e. the difference of the lateral components of the scattered and primary wave vectors equals the lateral component of a reciprocal lattice vector. The lateral diffraction condition is illustrated in Fig. 13.

Similar image of the geometrical factor is obtained if we consider absorption of the primary and scattered wave. If the absorption is strong enough, only a thin surface layer of the scattering crystal is irradiated, and the Fourier transformation of the shape function of the irradiated part of the sample gives rise to the CTR as well.

The structure factor $F(\mathbf{q})$ is the Fourier transform of the electron density of atoms belonging to one primitive unit cell (or to one mole). It is a complex function which depends on the atomic scattering factor of the atoms in the unit cell (contributing to the modulus) and on the actual relative position of the atoms (encoded in the phase term $\exp(-i\mathbf{q}\hat{A}\cdot\mathbf{r}_j)$). Every crystal works as a signal amplifier: more unit cells form the crystal (more extended crystalline domains) more intense and more concentrated the diffracted beams will be (therefore easily measurable). The coherent length of the crystal (ξ), namely the crystalline domain size, is derived by the analysis of the peak widths: the larger the peak width the smaller the crystalline domains. At the limit of complete loss of long-range order (amorphous) a featureless diffraction curve, with few broad bumps, is registered.

Fig. 14 displays the Bragg law defining only the peak positions (Fig. 14a), the atomic (Fig. 14b) and structure factors (Fig. 14c) needed to compute the intensity diffracted by a silicon crystal.

It is worth highlighting that the accuracy in the determination of the lattice parameter, precious information encoded in the Bragg law (25), depends on the number of terms in the lattice sum, see Eq. (47). Indeed, if the crystal coherency is $\xi = N a$, where N is the number of unit cells and a the unit cell size, the accuracy in the lattice parameters is λ/N . The smaller the crystal coherence (the lower the crystallinity) the less reliable the crystal periodicity derived by the Bragg law [259].

The Bragg law [189,190,254] is equivalent to the Laue equation [260] which states that constructive interference will occur provided that scattering vector or wave transfer vector \mathbf{q} is a vector of the reciprocal lattice ($\mathbf{g} = \mathbf{q} = \mathbf{k}_s - \mathbf{k}_i$) [261]. In other words, interference is constructive at the perpendicular bisecting plane (Bragg plane) between two reciprocal lattice points. Note that in the

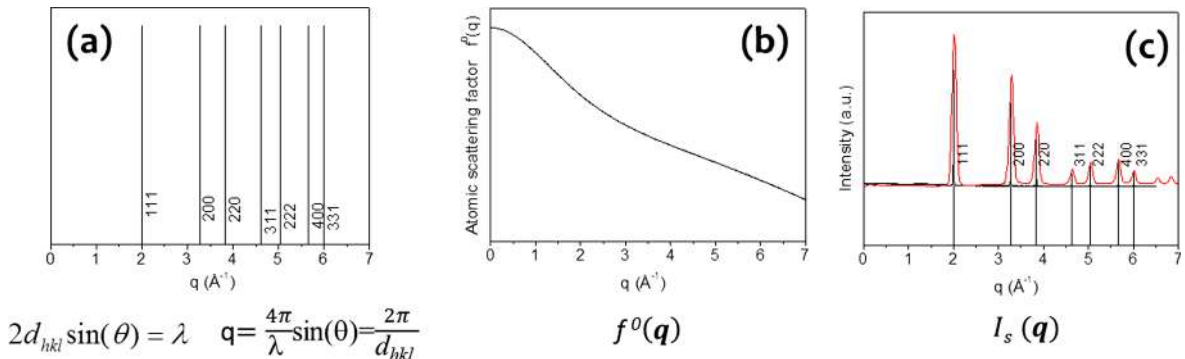


Fig. 14. (a): peak positions computed for $\lambda = 1.5405 \text{ \AA}$ from the Bragg law for a silicon crystal. (b): atomic scattering factor (atomic form factor) of silicon. (c): intensity diffracted by a silicon crystal. Previously unpublished figure.

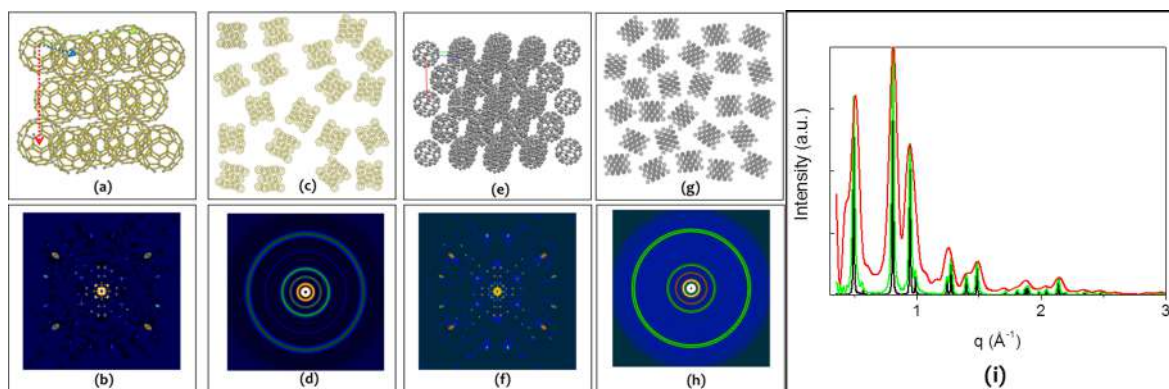


Fig. 15. (a): unit cell made of C60 molecules placed at the corners of a cube and at the center of each face of the cube (ICSD number 74523). (b): 2D diffraction pattern along the [111] projection of the f.c.c. unit cell shown in (a). (c): assembly of unit cells, randomly oriented. (d) 2D diffraction pattern of the unit cells assembly shown in (c). (e) crystal lattice made of $2 \times 2 \times 2$ unit cells, each unit cell identical to (a). (f) 2D diffraction pattern along the [111] projection of the crystal lattice made of $2 \times 2 \times 2$ unit cells shown in (e). (g): random assembly of unit cells, with each unit cell identical to (e). (h) 2D diffraction pattern of the crystal lattice made of $2 \times 2 \times 2$ unit cells shown in (g). (i): 1D diffraction profiles of the unit cells assembly shown in (h): red for $2 \times 2 \times 2$ unit cells, green for $10 \times 10 \times 10$ unit cells, black for $30 \times 30 \times 30$ unit cells. Intensities have been rescaled to the same maximum to better appreciate the differences. Previously unpublished figure. (For interpretation of the references to color in this figure legend, the reader is referred to the web version of this article.)

original real lattice, these perpendicular bisecting planes are the planes we use to construct the Wigner-Seitz cell. For the neighbors nearest to the origin, the Wigner-Seitz cell of the reciprocal lattice is called the first Brillouin zone [261–264].

The concept of the Brillouin zones, which is used mainly in the theory of electron gas in solids, is suitable also for the description of X-ray diffraction. In the diffraction maximum the diffraction condition $\mathbf{g} = \mathbf{k}_s - \mathbf{k}_i$ is fulfilled and the total wavefield in the diffracting lattice can be written in the form of the Bloch waves

$$\mathbf{E}(\mathbf{r}) = e^{i\mathbf{k}_i \cdot \mathbf{r}} (\mathbf{E}_i + \mathbf{E}_s e^{i\mathbf{g} \cdot \mathbf{r}}) \quad (27)$$

where the wave vector \mathbf{k}_i is chosen from the first Brillouin zone and $|\mathbf{k}_i| = |\mathbf{k}_s| = k$.

Let's compute a simple crystal lattice made of one unit cubic cell, with C60 molecules placed at the corners of a cube and at the center of each face of the cube (ICSD number 74523), as described in Fig. 15a. The structure factor modulus of this single face-centered cubic (f.c.c.) cell lattice, computed along the [111] projection for a $\lambda = 1 \text{ \AA}$, detector pixel size = 200μ , linear detector size = 20 cm and sample-to-detector distance = 5 cm is shown in Fig. 15b. If we add other cells, without any lattice coherence but randomly assembled in direct space (Fig. 15c), the corresponding diffraction pattern (Fig. 15d) is obtained by the incoherent sum of all contributions. The random relative rotation of the unit cells in direct space explains the collapse, in reciprocal space, of the diffraction spots of Fig. 15b into the 2D rings of Fig. 15d. We can compute a more complex crystal lattice made of 2 f.c.c. unit cells along each crystal axis, for a total of $2 \times 2 \times 2$ unit cells (Fig. 15e). The corresponding structure factor modulus, computed along the [111] projection for a $\lambda = 1 \text{ \AA}$, detector pixel size = 200μ , linear detector size = 20 cm and sample-to-detector distance = 5 cm , is reported in Fig. 15f, which looks almost identical to Fig. 15b apart for the sharper diffraction spots. The assembly of $2 \times 2 \times 2$ unit cells crystals, randomly oriented in direct space is shown in Fig. 15g; the corresponding diffraction pattern obtained by the incoherent sum of all contributions is displayed in Fig. 15h. These 2D rings can be reduced to 1D profiles by integration along the azimuthal angle, which are reported in Fig. 15i for different crystal coherency ($\xi = N a$, here N is the number of cells): red for $N = 2$, green for $N = 10$ and black for $N = 30$. The crystal coherency reflects itself in the full-width of the diffraction peaks: the smaller the crystal coherence the broader the peaks. The two extreme cases identify here: a small nanocrystal (domain size $\sim 4 \text{ nm}$) made of $2 \times 2 \times 2$ unit cells and a larger nanocrystal (domain size $\sim 60 \text{ nm}$) made of $30 \times 30 \times 30$ unit cells.

3.3. Scattering from nanocrystals, polymers or amorphous materials

As stated in the introduction a complex material can be today an assembly of a polymer with inorganic nanocrystals, or a molecule coating a gold core, etc. Verbatim from Egami & Billinge's book [259] "... polymers are structurally highly complex, with millions of atoms constituting chain molecules, which are assembled in a complex morphology, partly crystalline and partly amorphous... complex materials have a structure that locally deviates from the perfect crystal structure, even when they may appear superficially crystalline. In real life as well a complex person is always more interesting than a simple one, since such a person is unpredictable. A perfectly periodic crystal may be beautiful in some sense, but is totally predictable and can be extremely boring; even the most beautiful theme of Mozart would become boring if it were repeated a million times! Modern complex materials, on the other hand, are far from boring... the more directed the functionality of a material, the greater its structural complexity".

When we cannot rely on a distinct periodicity, we cannot compute the crystal diffracted intensity as previously defined in Eq. (47). In these cases (amorphous, magic clusters or noble metal nanoclusters, polymers with partly crystalline and partly amorphous sections) we have to define a continuous structure factor which computes the total scattering across the entire sample extension,

without relying on any periodicity rules. It takes into account both Bragg and diffuse intensity. The continuous structure factor is:

$$\Psi(\mathbf{q}) = \frac{1}{\rho_0 V} \int d^3\mathbf{r} \rho(\mathbf{r}) e^{-i\mathbf{q}\cdot\mathbf{r}} \quad (28)$$

whose squared amplitude, $S(q)$, is proportional to the measured intensity averaged over all orientations of the local atom arrangements:

$$S(q) = \langle |\Psi(\mathbf{q})|^2 \rangle_{\text{orient}} \quad (29)$$

The Fourier transform of $S(q)$ gives [50,265]:

– Reduced pair distribution function

$$G(r) = 4\pi r \rho_0 (P(r) - 1) = \frac{2}{\pi} \int_0^\infty dq q [S(q) - 1] \sin(qr) \quad (30)$$

– Pair distribution function - PDF

$$P(r) = \rho_0 g(r) = \frac{1}{4\pi N r^2} \left\langle \sum_k \sum_j \delta(r - r_{jk}) \right\rangle_{\text{orient}} \quad (31)$$

– Pair density function

$$\rho(r) = \rho_0 P(r) \quad (32)$$

– Radial distribution function

$$R(r) = 4\pi r^2 \rho_0 P(r) \quad (33)$$

Here, ρ_0 is the number density of atoms in the system of N atoms; δ is a Dirac delta function; $r_{jk} = |\mathbf{r}_k - \mathbf{r}_j|$ is the distance separating

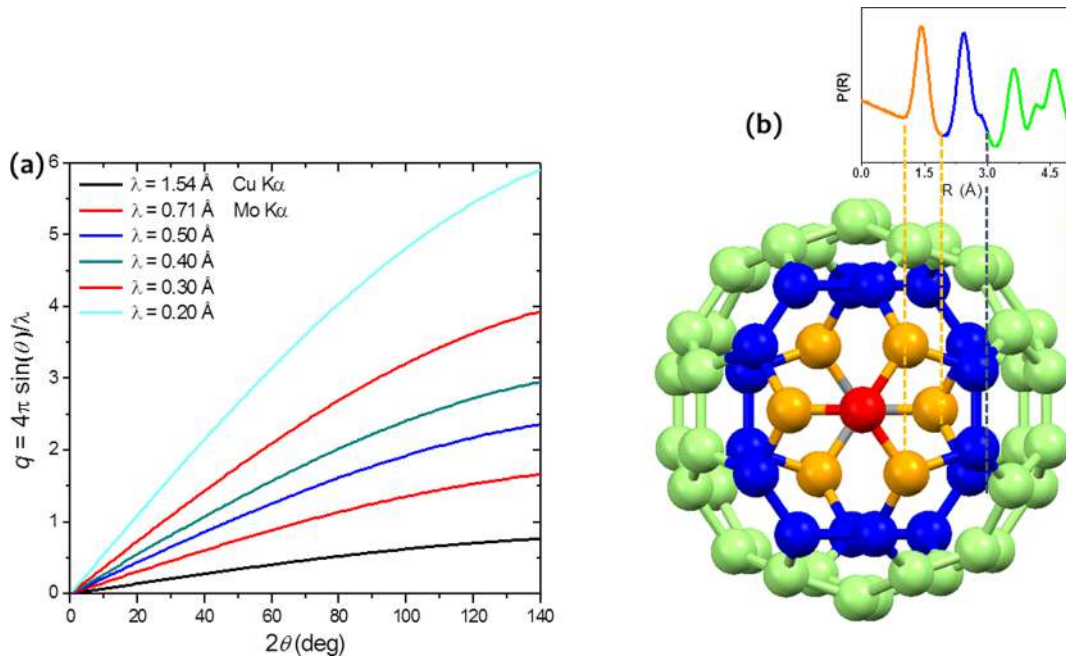


Fig. 16. Part (a): graphical representation of the q vs. 2θ relationship for different λ values including the most used laboratory tubes and some typical hard-X-rays values used at the synchrotrons. High q values can be obtained at synchrotron sources using low λ . Part (b): Scheme of the radial PDF $R(r)$. The radial PDF quantifies the correlation between the particles within a given system. In particular, $R(r)$ measures the average probability of finding a particle at a distance r away from a given reference particle. The general algorithm to evaluate $R(r)$ involves the determination of the number of particles within r and $r + dr$ (circular gray shell in the figure) from the reference particle (depicted in red). In a sample showing short-range order, the $R(r)$ function shows a few oscillations before stabilizing at $R(r) = 1$ which correspond to local deviations from the isotropic condition, and are associated to the first coordination shells occurring at well-defined interatomic distances. (For interpretation of the references to color in this figure legend, the reader is referred to the web version of this article.)

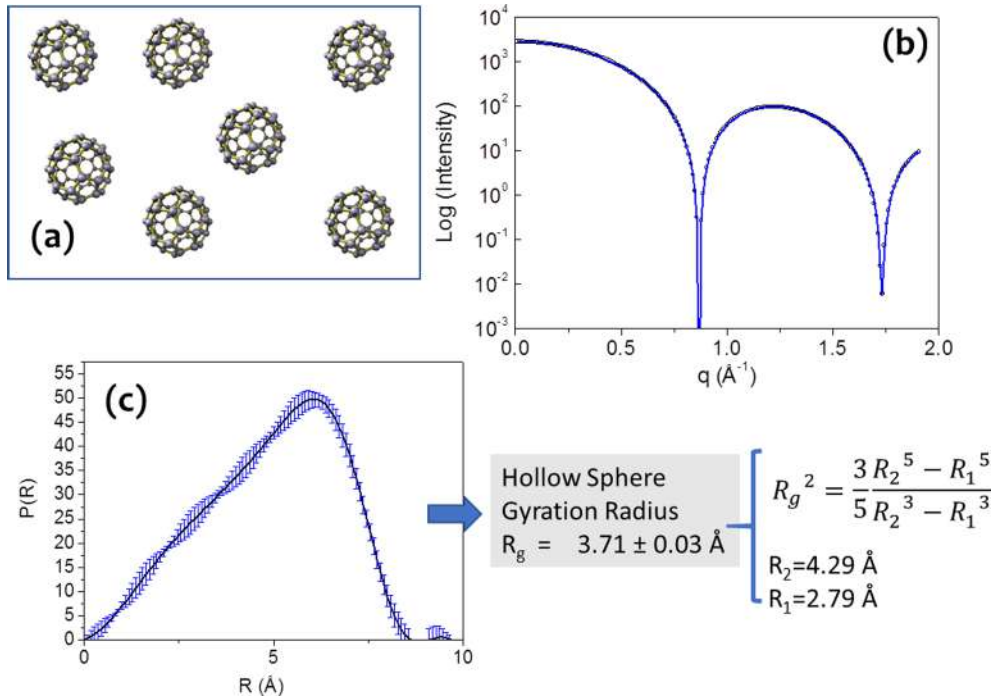


Fig. 17. (a) Diluted gas-like suspension of C60 molecules dispersed in a buffer; (b) SAXS data; (c) the pair distribution function (PDF) – $P(r)$. Previously unpublished figure.

the k^{th} from the j^{th} atoms. These functions allow reconstructing the structure of the investigated sample from the spatial correlations between pair of atoms (see Fig. 16).

When the scattering atoms/molecules adopt all orientations to the X-ray beam, only spherical average of the scattered intensity is experimentally accessible. Discretizing the sum, the diffracted intensity is:

$$I(q) \propto \sum_{k=1}^N \sum_{j=1}^N f_k(q) f_j(q) \langle e^{-i \cdot (\mathbf{r}_k - \mathbf{r}_j)} \rangle_{\text{orient}} = \sum_{k=1}^N \sum_{j=1}^N f_k(q) f_j(q) \frac{\sin(qr_{jk})}{qr_{jk}} \quad (34)$$

This is the well-known Debye formula [266,267] and holds for Small (SAXS) and Wide (WAXS) Angle X-ray Scattering data. Note that this approach to analyze the scattering data is not restricted to amorphous samples but may be also applied to crystalline (nano)materials, as shown in the following example, reported in Figs. 17 and 18. The data resolution (d_{min}), for whatever scattering/diffraction curve, depends on the maximum scattering vector (q_{max}) with a significant signal to noise ratio, i.e. on the maximum angle (θ_{max} , at given λ):

$$d_{\text{min}} = 2p/q_{\text{max}} = l/(2 \sin(q_{\text{max}})) \quad (35)$$

where the last equality derives from Eq. (25). SAXS data have a nanometric resolution and are therefore used to access information at the nanoscale, whereas WAXS data can reach atomic resolution (interatomic distances). SAXS data, when spatial correlations are negligible (gas-like dispersion), do not contain any structure information but only morphological ones (shape and size of the molecule or nanosized scattering object), as previously discussed, see Fig. 10.

The power of the PDF analysis is to extract structural information, independently of the crystallinity of the sample, especially important for so many hybrid or amorphous materials. The final resolution of the reconstructed structure will depend on the maximum q value of the scattering data, which is a function of the wavelength of the X-ray beam and of the maximum scattering angle in the recorded data. Typically, high quality data collections up to $q = 20\text{--}30 \text{ \AA}^{-1}$ are needed, requiring mandatory the use of very short λ , see Eq. (35). For standard Cu K α ($\lambda = 1.54 \text{ \AA}$) and Mo K α ($\lambda = 0.71 \text{ \AA}$) tubes a collection up to $2\theta = 140^\circ$ results in $q = 7.7$ and 16.6 \AA^{-1} , respectively. Usually PDF studies are performed using synchrotron sources (see §6.1.2.) that provide high X-ray fluxes even at short λ . As an example, at $\lambda = 0.5, 0.4, 0.3$ and 0.2 \AA , q values as high as $q_{\text{max}} = 23.6, 29.5$ and 39.4 and 59.0 \AA^{-1} , respectively, can be reached for a data collection up to $2\theta = 140^\circ$. This means to give access to $d_{\text{min}} = 0.27, 0.21, 0.16$ and 0.11 \AA length scales in direct space, respectively [268]. This is the resolution needed specially to study amorphous materials.

Let's suppose to analyze the same C60 molecules both dispersed in a buffer to form a diluted gas-like suspension (Fig. 17a) or organized in the molecular crystal according to a regular face centered cubic (f.c.c.) lattice, as shown in Fig. 18A. Let's suppose to have collected both the SAXS data from the solution (Fig. 17b) and the wide angle diffraction pattern (WAXS data) from the crystalline sample (Fig. 18b), for different crystal coherence (red for $2 \times 2 \times 2$ unit cells, green for $10 \times 10 \times 10$ unit cells, black for $30 \times 30 \times 30$ unit cells, as already described in Fig. 15h). The analysis of the SAXS profile (Fig. 17B), realized for example with the

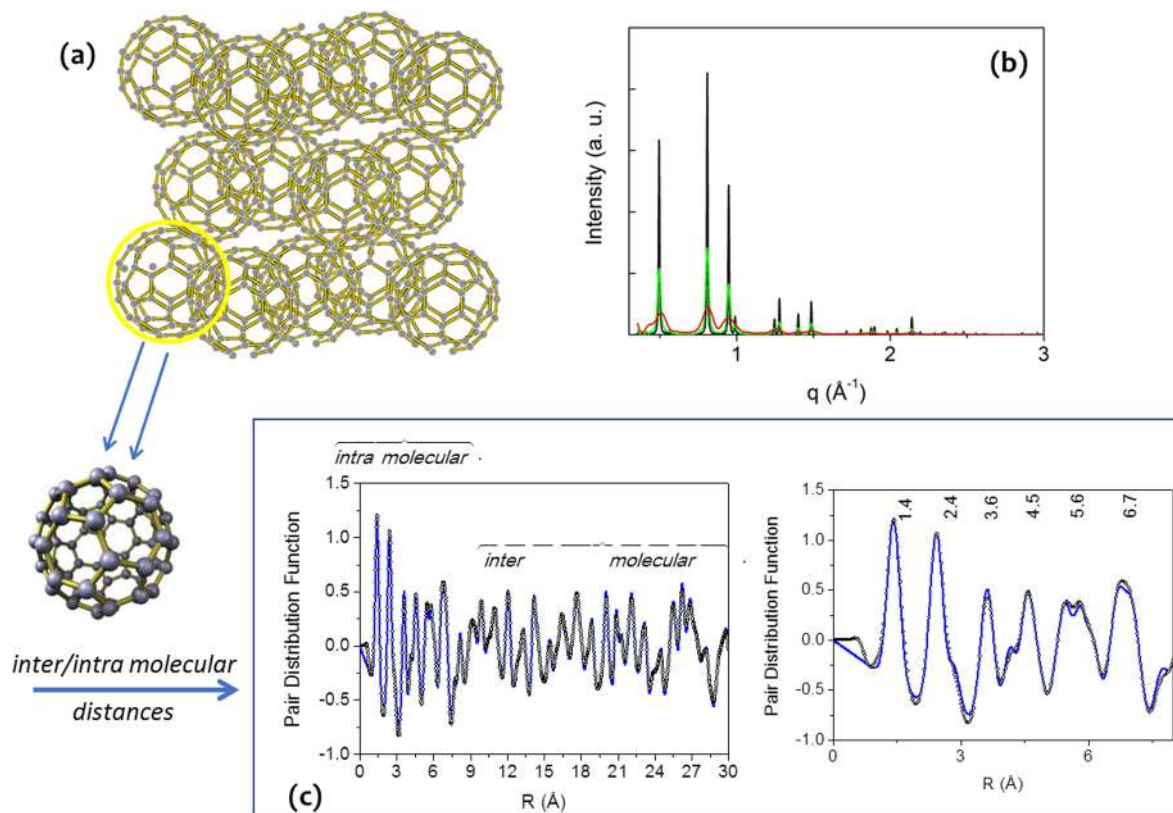


Fig. 18. (a) C60 molecules organized in a crystal according to a regular face centered cubic (f.c.c.) lattice; (b) WAXS data (red profile for $2 \times 2 \times 2$ unit cells, green for $10 \times 10 \times 10$ unit cells, black for $30 \times 30 \times 30$ unit cells); (c) pair distribution function (experimental is the black dotted curve and the simulated profile is the blue line) extracted from the WAXS data where it is possible to distinguish the intermolecular and the intramolecular lattice distances of the C60 f.c.c. crystal. Previously unpublished figure. (For interpretation of the references to color in this figure legend, the reader is referred to the web version of this article.)

GNOM program [269], allows us to extract the pair distribution function (PDF – $P(r)$ - Fig. 17C). Table 1 provides a list of $P(r)$ and corresponding SAXS profiles for relevant shapes (full sphere, hollow sphere, cylinder, flat disk and dumbell), along with the formulas linking the gyration radius (R_g) to the main lengths of the object. The radius of gyration represents the effective size of the scattering “particle” whether it is a molecule, a nanocrystal or nanoparticle, a polymer chain, part of a protein, a micelle, or a domain in a multiphase system. The $P(r)$ extracted from Fig. 17c clearly allows us to identify the hollow shape of the C60 molecules, and the gyration radius $R_g = 3.71 \pm 0.03 \text{ \AA}$, derived from analyzing the data, correlates very well with what expected for an external and internal radii $R_2 = 4.29 \text{ \AA}$ and $R_1 = 2.79 \text{ \AA}$ of the fullerene molecule [270]. This example shows the typical outcome of a morphological analysis performed by SAXS.


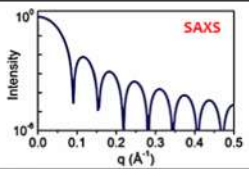
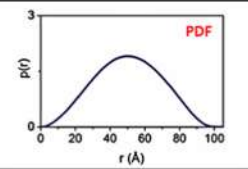

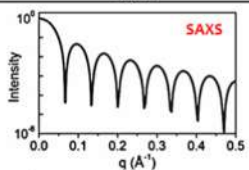
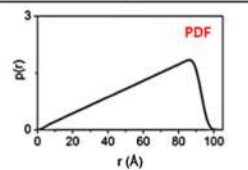

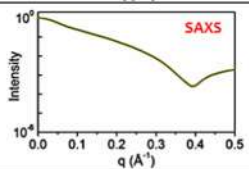
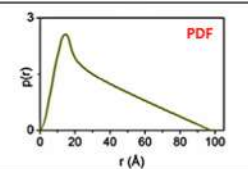
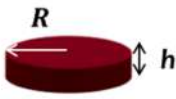
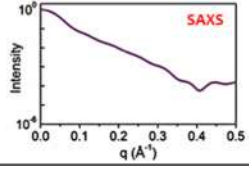
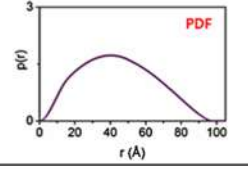

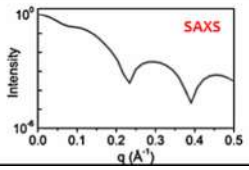
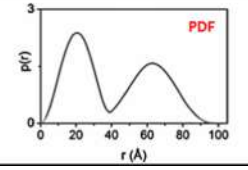
Let's proceed with the analysis of the wide angle diffraction pattern (WAXS data) from the molecular crystal (Fig. 18B). The analysis is realized in two steps: (1) extraction by the PDFGETX3 program [271] of the pair distribution function – $P(r)$ – (black dotted curves in Fig. 18C,D) from the black WAXS data in Fig. 18B); (2) fit of the $P(r)$ data with the PDFGUI program (blue lines in Fig. 18C and D) [272]. In the $P(r)$ it is possible to distinguish the intermolecular and the intramolecular lattice distances of the C60 f.c.c. crystal [273]. It is worth noting that, in this system, the border between inter and intramolecular distances occurs at about $8 \text{ \AA} \sim 2R_2$, which corresponds to the external diameter of the fullerene molecule. The analysis is reported for the WAXS data computed for $30 \times 30 \times 30$ unit cells (black profile in Fig. 18B). Similar results are found for $2 \times 2 \times 2$ and $10 \times 10 \times 10$ unit cells. Interestingly, (200) diffraction from the fcc crystal of C60 molecules, at 0.57 \AA^{-1} , is missing even if the structure factor of a f.c.c. lattice is not zero for (200). The reason of this extinction is the structure factor of a single molecule C60, which is zero for $\mathbf{q} = \mathbf{g}_{200}$. This fact can be shown by a simple calculation in which we assume that all the electrons in the molecule lie on a spherical surface with the radius R . In this assumption, the structure factor of the molecule is:

$$F(\mathbf{q}) = Z \frac{\sin(qR)}{qR} \quad (36)$$

where Z is the total number of electrons in the fullerene molecule. The lattice parameter of the fcc fullerene crystal is $a = 1.411 \text{ nm}$, and the C60 radius is $R = 0.35 \text{ nm}$. In the (200) diffraction maximum $q = |\mathbf{g}_{200}| = 4\pi/a$ holds and the structure factor is therefore very small ($F/Z \approx 0.007$).

Table 1

List of SAXS profile and corresponding pair distribution function $P(r)$ computed for relevant shapes (full sphere, hollow sphere, cylinder, flat disk and dumbbell), along with the formulas linking the gyration radius (R_g) to the main lengths of the object. Previously unpublished table.

SPHERE 			$R_g^2 = \frac{3}{5} R^2$
HOLLOW SPHERE 			$R_g^2 = \frac{3 R_2^5 - R_1^5}{5 R_2^3 - R_1^3}$
CYLINDER 			$R_g^2 = \frac{a^2 + b^2}{4} + \frac{h^2}{12}$
FLAT DISK 			$R_g^2 = \frac{R^2}{2} + \frac{h^2}{12}$
DUMBBELLS 			$R_g^2 = \frac{\int_0^{d_{max}} P(r) r^2 dr}{\int_0^{d_{max}} P(r) dr}$

3.4. Submolecular and supramolecular study of fibers

SAXS and WAXS techniques are ideal to explore materials with hierarchical order such as, for example, polymer based fibers [274–276], nanostructured carbons [277], and catalysts with hierarchical pore structure [278–280]. Self-assembly is an increasingly attractive tool for the fabrication of novel nanomaterials. In this field, self-assembled peptides have received considerable interest because of their intrinsic biocompatibility, relative simple synthesis and preparation, versatility and functional diversity [281,282]. For example, Diphenylalanine (FF) can self-assemble into well-ordered tubular structures with a long persistence length (~100 μm) by the combination of hydrogen bonding and π - π stacking of aromatic residues. Diphenylalanine homodimers show a very high morphological variability depending on the experimental preparation conditions such as solvent, pH or temperature. Moreover, chemical modifications of the aromatic dipeptide (e.g. the introduction of a thiol group or of a fluorenylmethoxycarbonyl group) can alter the self-assembly. Nanotubes, nanowires, nanofibrils, spherical vesicles and organogels are just a few examples of the new peptide materials based on FF self-assembly [283]. Several applications in biology, nanomedicine and nanofabrication fields (for tissue engineering, drug delivery, bioimaging and fabrication of biosensors) have been proposed for these nanostructures [283–286]. According to their morphological features, these materials exhibit also mechanical, electrochemical, magnetic or optical (photoluminescence and optical waveguide) properties. Moreover, their high thermal, chemical and proteolytic stability provides them the features for potential applications in industrial fields. Despite the growing literature about FF, only few examples of nanomaterials obtained by the self-assembling of others aromatic analogues (naphthylalanine, tyrosine, tryptophan) or of long poly-phenylalanines have been reported until now. Fiber diffraction, registered in SAXS and WAXS regimes, is the perfect tool to explore the nano and atomic packing of these novel nanomaterials with hierarchical order [275,276]. Fig. 19 refers to the case of a novel peptide building block composed of six phenylalanine residues and eight PEG units (PEG8-F6), which showed blue photoluminescence both in solution and at the solid state. The photoluminescence (PL) properties were correlated with the structural organization of the peptide building block at the micro-, nano- and atomic scale by means of the combination of a micro-probe with SAXS and WAXS techniques. WAXS and SAXS data were collected at the X-ray MicroImaging Laboratory (XMI-L@b) [287,288] with a beam spot of ~100 μm . Three length scales were explored in this experiment:

- **Micro scale:** The PEG8-F6 fiber in Fig. 19a was placed under a micro-focused X-ray beam which allowed to explore different

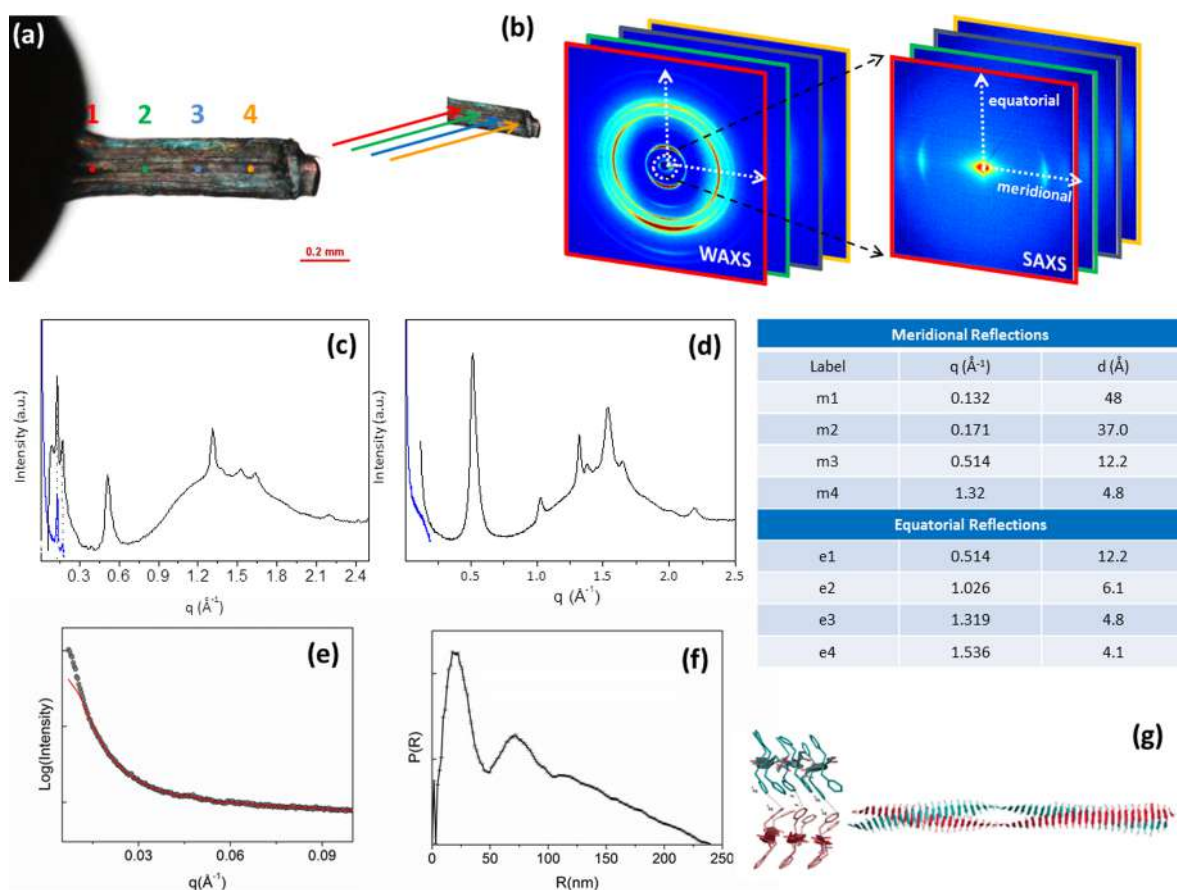


Fig. 19. (a) PEG8-F6 fiber as placed under a micro-focused X-ray beam and explored across different micrometric regions; (b) WAXS and SAXS data, collected along the fiber; (c) 1D WAXS (dark) and SAXS (blue) meridional profiles; (d) 1D WAXS (dark) and SAXS (blue) equatorial profiles; (e) experimental (dots) and computed (red line) equatorial SAXS profiles; (f) nPDF derived from the analysis of the equatorial SAXS profile in (e); model the PEG8-F6 fiber resulting from molecular dynamics simulations. Adapted with permission from Ref. [276], copyright Wiley-VCH 2016. (For interpretation of the references to color in this figure legend, the reader is referred to the web version of this article.)

micrometric regions marked in red (1), green (2), blue, (3), and orange (4), placed at a relative distance of 200 μm . The WAXS and SAXS data, collected along the fiber, grouped in Fig. 19b, did not report relevant differences proving the lateral homogeneity of the fiber.

- **Nano scale:** SAXS data were acquired placing a 2D detector at about 2 m from the sample.
- **Atomic scale:** WAXS data were acquired placing a 2D detector at about 10 cm from the sample.

Both WAXS and SAXS 2D data present a high anisotropy in the diffracted intensity, with the typical cross- β diffraction pattern in the WAXS regime with meridional and equatorial peaks along the fiber axis and perpendicular to it, respectively. The 2D data were centered, calibrated and folded into 1D profiles and showed in Fig. 19c and d along the meridional and equatorial directions, respectively. The blue and black lines refer to the SAXS and WAXS data, respectively. The peak positions were identified and summarized in the table. Remarkable peaks are the meridional and equatorial reflections at $4.8 \pm 0.3 \text{ \AA}$ (m4 in the table of Fig. 19) and $12.2 \pm 0.3 \text{ \AA}$ (e1 in the table) which correspond to the typical hydrogen bonding distance between β -strands and to the inter-sheet distance [289]. In the SAXS regime, diffraction was measured only in the meridional direction (m1 in the table). In order to extract only morphological information (size and shape of the fiber), the equatorial profile was fitted with the GNOM program [290] (Fig. 19c) to evaluate the nPDF (Fig. 19d), i.e. the PDF at the nano scale. The evaluated nPDF is the typical distribution of elongated scattering object with gyration radius of $R_g = 69 \pm 1 \text{ nm}$. Molecular dynamics simulations allowed to model the hexaphenylalanine formation in aqueous solution and its evolution and stabilization in time, finding the twisted model in Fig. 19g. Simulations were perfectly in line with the WAXS data (equatorial reflection at $\sim 12.5 \text{ \AA}$) and to the SAXS gyration radius.

This is a very didactic example of application of SAXS, WAXS and nPDF analysis to inspect atomic and nanometric structure of these peptide-based nanomaterials, which profits of the micro-sized X-ray source to explore the lateral heterogeneity of the fiber and to complete the structural investigation up to the micrometric scale.

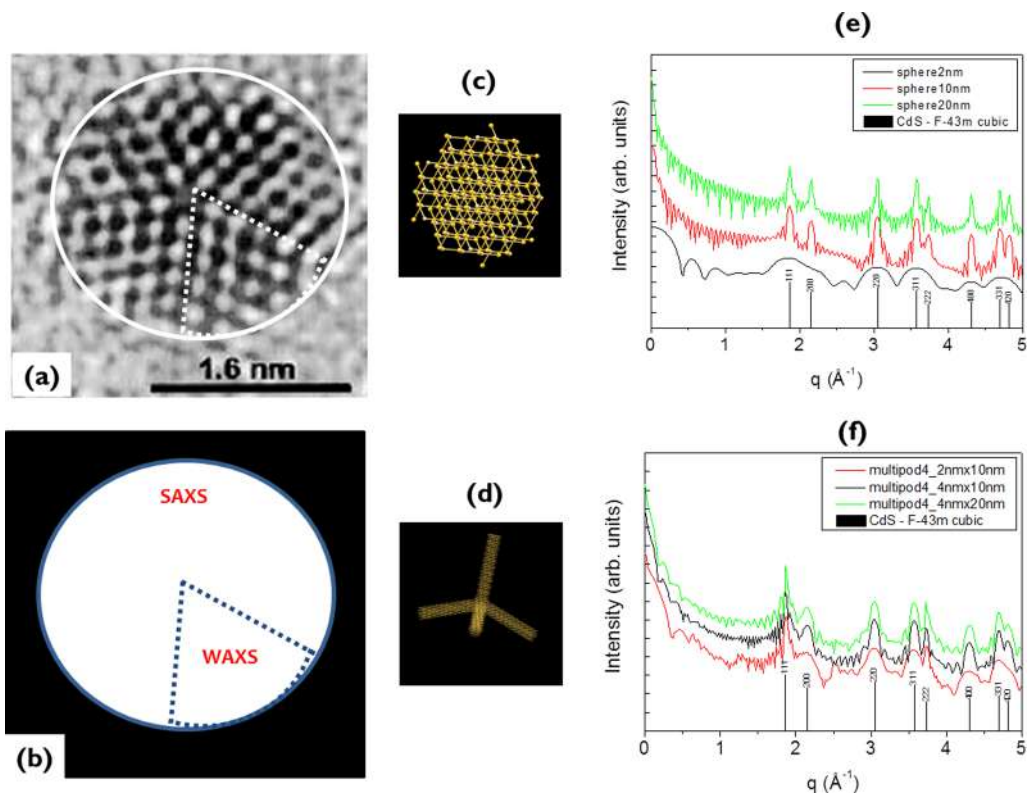


Fig. 20. (a) HRTEM image of a gold multiple twinned nanocrystal, reprinted with permission from [292]; (b) spherical shape, marked by the full line circle, with several smaller crystalline domains, marked by the dotted line sector; (c) atomic model of nanocrystals with spherical shape and zincblende crystal structure (left) and corresponding SAXS and WAXS profiles (right) computed for spheres of increasing size (a sphere of diameter $d = 2$ nm – black; $d = 10$ nm – red; $d = 20$ nm – green); (d) atomic model of nanocrystals with octapod shape and zincblende crystal structure (left) along with the SAXS/WAXS simulations (right, e–f) computed for increasing size (octapod with arms of diameter d and length l : $d = 2$ nm and $l = 10$ nm – red; $d = 4$ nm and $l = 10$ nm – black; $d = 4$ nm and $l = 20$ nm – green). (For interpretation of the references to color in this figure legend, the reader is referred to the web version of this article.)

3.5. Size, shape, defects analysis

A WAXS profile, registered on randomly oriented nanocrystals, may encode several structural and morphological information: size, strain, shape, structures, defects [291]. It is worth reminding that the domain size encoded in the WAXS data can differ from the nanocrystal overall size. Fig. 20A is the HRTEM image of a gold multiple twinned nanocrystal [292]. Clearly the overall shape is a sphere, but it contains smaller crystalline domains (Fig. 20B). Consequently, both SAXS and WAXS scattering patterns should be registered to determine nanocrystalline domain size from WAXS and overall nanoparticle shape from SAXS. Their compared analysis could disclose this relevant difference, if present. Fig. 20C shows the atomic model of nanocrystals with spherical shape and zincblende crystal structure. The corresponding SAXS and WAXS profiles are computed with the Debye function for spheres of increasing size (a sphere of diameter $d = 2$ nm – black; $d = 10$ nm – red; $d = 20$ nm – green). Fig. 20D shows the atomic model of nanocrystals with octapod shape and zincblende crystal structure along with the SAXS/WAXS simulations computed for increasing size (octapod with arms of diameter d and length l : $d = 2$ nm and $l = 10$ nm – red; $d = 4$ nm and $l = 10$ nm – black; $d = 4$ nm and $l = 20$ nm – green). This comparison clearly shows that for a symmetric shape, as the size increases, all WAXS peaks reduce in width and the frequency of the SAXS diffraction fringes increases. For a very anisotropic shape, as the octapod, the WAXS peak width is largely anisotropic and the domain size and shape can be retrieved only by a proper data analysis of the whole spectra. The same information is also encoded in the SAXS range, when domain size and particle size coincide, but in a less direct and clear way.

In Fig. 21 SAXS and WAXS patterns [293], in conjunction with Debye formula simulations from atomistic models, were used to complement and extend microscopic studies of anisotropic nanocrystals with monodispersed size. With respect to electron microscopy characterization, SAXS and WAXS data have the intrinsic advantage to contain information which are statistically relevant, as often needed for many material applications, which can be directly collected also for nanocrystals dispersed in solutions. This information is averaged on the ensemble of nanocrystals illuminated by the X-ray beam. Conversely, the drawback of the SAXS/WAXS approach is that once information is obtained in the reciprocal space, structural models in real space are needed to interpret the data. For these reasons the two approaches, SAXS/WAXS and TEM, support and complement each other.

The importance to extract size and shape information from SAXS and WAXS data of nanoparticles directly in solutions is pretty

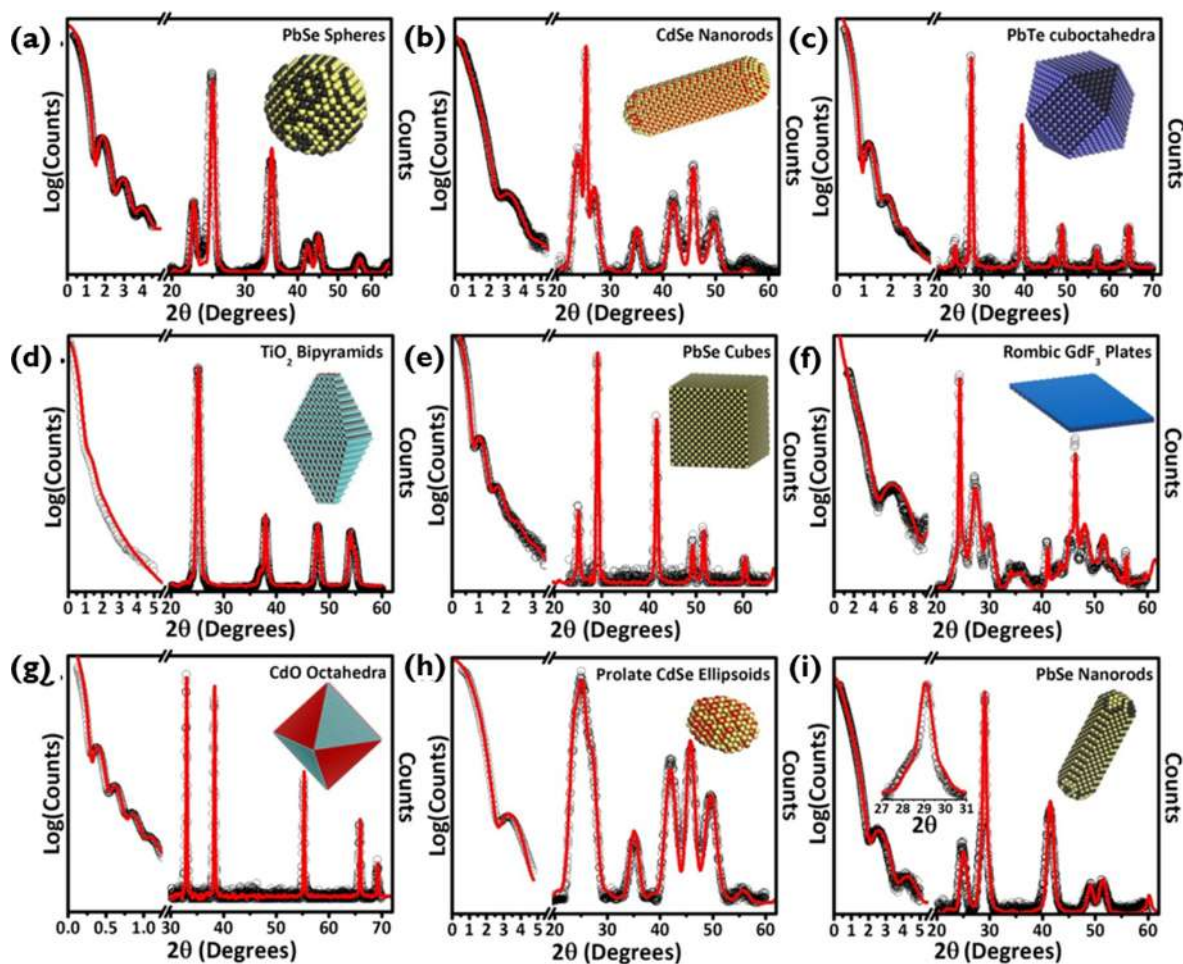


Fig. 21. Main parts: SAXS and WAXS patterns from different atomistic models of anisotropic nanocrystals (insets) with monodispersed size. In all parts the experimental data (scattered circles) are compared with the Debye formula simulations (full red line). Reprinted with permission from ref. [293] copyright American Chemical Society, 1997. (For interpretation of the references to color in this figure legend, the reader is referred to the web version of this article.)

clear for nanomedicine applications. Indeed, scientists dream to have a full control on the size, shape, surface properties and mechanical stiffness of their nano-constructs, before deliver them to human body, diluted for example in water, and navigate them through the circulatory system for therapy or theranostics [294,295]. For samples containing nanoparticles with a unique shape and with homogeneous size, size and shape can be directly extracted from SAXS and WAXS data. In more complex cases, like bi- or multi-modal shape distribution and heterogeneous size distribution, shape and size distributions may be reconstructed from an accurate analysis of the SAXS and WAXS data according to supplementary information coming from independent techniques, such as e.g. TEM.

In the next case [296] the authors studied a random assembly (powder) of nanocrystals with tetrapod shape, realized by the synthesis of a sphalerite core and four wurtzite arms (Fig. 22A). The aim of the study was not to identify a specific nanocrystal in the assembly but to study their average structural and morphological properties. Therefore, X-ray diffraction data were collected with a laboratory diffractometer, exploring millimetric areas. Fig. 22B shows as red dotted lines the experimental X-ray diffraction patterns collected on three representative nanocrystal samples, CdSe/CdTe, ZnTe/CdTe, and ZnTe/CdS tetrapods, as well as the corresponding simulated patterns as black solid lines. Depending on the material chosen for core and arms, the X-ray diffraction pattern changes in a quite significant way. Indeed, when using ZnTe core and CdS arms, the experimental pattern can be correctly described by the expected wurtzite crystalline CdS phase (the contribution to the diffraction from the central core is practically negligible). On the contrary, in the combination between ZnTe or CdSe core and CdTe arms, the experimental profile (red dotted curves) cannot be described by the corresponding CdTe wurtzite crystalline phase. A dampening in the intensities of the $10l$ ($l = 1, 2, 3, \dots$) reflections was clearly observed and was interpreted as the fingerprint of a disordered wurtzite CdTe phase. A similar dampening of the $10l$ reflections was found, for instance, by Frey and Boysen [297] for cobalt crystals grown in mixed hexagonal “hcp” and cubic “fcc” phases; an entire family of reflections, in correspondence of the $(10l)$ planes was missing. Fig. 22C indeed shows electron microscopy investigation of a single tetrapod. It is remarkable to note the changes of the lattice fringes contrast along the arms of the tetrapod, which indicates the presence of regions with either different orientations, or structure, or composition. Atomistic model with Debye

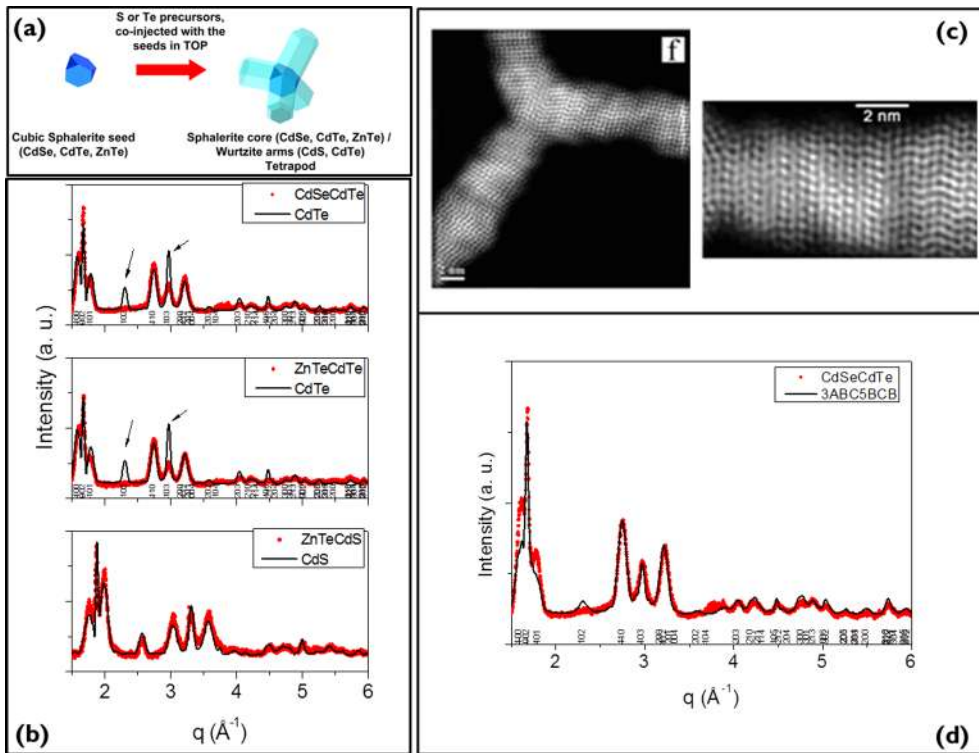


Fig. 22. (a) Random assembly of nanocrystals with tetrapod shape realized by the synthesis of a sphalerite core and four wurtzite arms; (b) experimental x-ray diffraction profiles (dotted red curve) and fitted profile (black full line); (c) electron microscopy investigation of a single tetrapod; (d) Debye function simulations of the 3ABA5BCB atomistic stacking sequence, which best fitted the X-ray diffraction pattern of the defected structures. Reprinted with permission from ref. [296], copyright American Chemical Society, 2009. (For interpretation of the references to color in this figure legend, the reader is referred to the web version of this article.)

function simulations of the X-ray diffraction pattern were therefore computed and screened against the experimental pattern. Accordingly, the CdTe arms could be better modeled as composed of mixed regions of wurtzite and sphalerite phases in a 3ABA5BCB stacking sequence (Fig. 22D). (Note that the ABC type of sequences corresponds to a sphalerite region, and the CB sequences correspond to a wurtzite region).

3.6. Correlated scattering clusters

In the previous description, we assumed that the measured signal is averaged over all orientations of the scattering clusters (molecules, nanoparticles etc). The consequence of this averaging is the fact that the reciprocal-space distribution of the measured intensity $I(\mathbf{q})$ depends only on the modulus q of the scattering vector. Eq. (13) assumes that the positions of individual clusters are not correlated so that the scattered intensity is proportional to the intensity scattered from a single cluster averaged over all orientations. This approximation is valid only for much diluted systems, in other cases an interaction between the clusters must be considered, which results in a correlation in the cluster positions. In this case, Eqs. (14), (15) can be used, where $F(\mathbf{q})$ is the (random) scattering factor of a single cluster and $G(\mathbf{q})$ is the correlation function of the cluster positions.

Several models can be used for calculation of $G(\mathbf{q})$. Here we mention the Ornstein-Zernicke theory [298,299]. Let us define the pair distribution function $g(\mathbf{r})$ of the clusters as

$$g(\mathbf{r}) = \frac{\rho(\mathbf{r})}{\rho_0} = 1 + \frac{1}{N\rho_0} \left\langle \sum_{j \neq k} \delta^{(3)}(\mathbf{r} - (\mathbf{r}_j - \mathbf{r}_k)) \right\rangle \quad (37)$$

and the total correlation function $h(\mathbf{r}) = g(\mathbf{r}) - 1$. Ornstein and Zernike divided the total correlation function in two parts, the first describing “direct” interaction between the clusters in points 0 and \mathbf{r} and the second covering all indirect interactions mediated by all other clusters in the sample:

$$h(\mathbf{r}) = c(\mathbf{r}) + \rho_0 \int d^3\mathbf{r}' c(\mathbf{r}') h(\mathbf{r} - \mathbf{r}') \quad (38)$$

The Fourier transformation of $h(\mathbf{r})$ which occurs in the formula for the scattered intensity can be directly obtained as

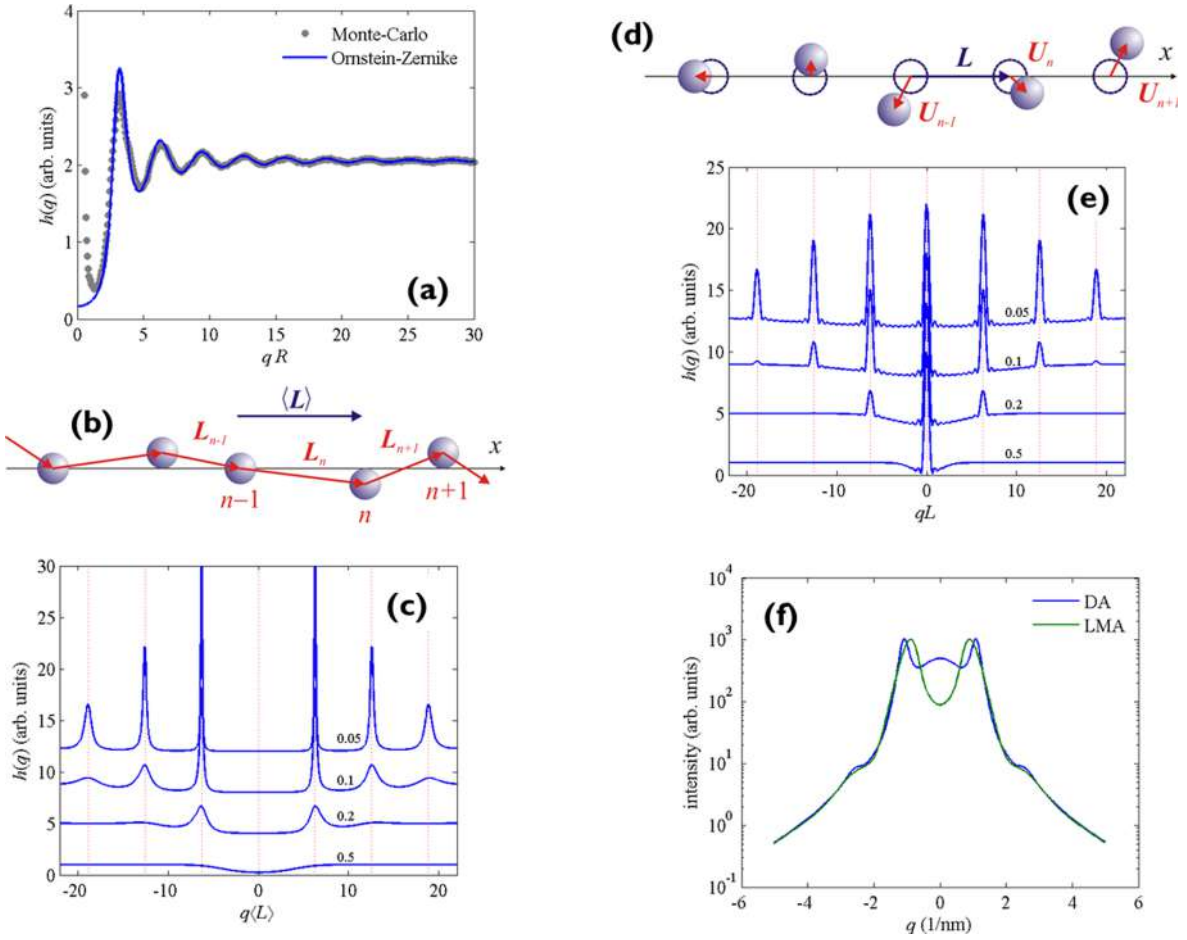


Fig. 23. (a) $h(q)$ of a random ensemble of uniform hard spheres simulated by the Percus-Yevick approach of the Ornstein Zernicke theory (line) and using a Monte-Carlo simulation (dots); (b) one-dimensional short-range order model of particle ordering; (c) functions $h(q)$ simulated within the one-dimensional SRO model for various root-mean square deviations σ_L of the particle distances. The parameters of the curves are the values of $\sigma_L/\langle L \rangle$. The curves are shifted vertically for clarity. The vertical dotted lines denote the positions of the averaged one-dimensional reciprocal lattice points $q_n = 2\pi n/\langle L \rangle$; (d) Sketch of the one-dimensional long-range order model; (e) The functions $h(q)$ simulated within the one-dimensional LRO model for various rms deviations σ_U of the particle displacements and for $N = 10$. The parameters of the curves are the values of $\sigma_U/\langle L \rangle$. The curves are shifted vertically for clarity. The vertical dotted lines denote the positions of the averaged one-dimensional reciprocal lattice points $q_n = 2\pi n/\langle L \rangle$; (f) scattering curves calculated for a one-dimensional chain of spheres, the spheres are arranged according to the SRO model (see the main text for all details). The difference between the DA and LMA models are obvious. Previously unpublished figure.

$$h(\mathbf{q}) = \frac{1}{\rho_0} \left[\frac{1}{N} G(\mathbf{q}) - 1 \right] = \frac{c(\mathbf{q})}{1 - \rho_0 c(\mathbf{q})} \tag{39}$$

The Percus-Yevick approximation [300] uses the following closure relation in order to solve the Ornstein-Zernike integral equation

$$c(\mathbf{r}) = [h(\mathbf{r}) + 1] \left[1 - \exp\left(-\frac{w(\mathbf{r})}{k_B T}\right) \right] \tag{40}$$

where $w(\mathbf{r})$ is the potential energy of a pair of clusters. If, for instance, the clusters are approximated by uniform hard spheres, then

$$w(\mathbf{r}) = \begin{cases} 0 & \text{for } r > D \\ \infty & \text{for } r \leq D \end{cases} \tag{41}$$

where D is the cluster diameter. Inserting Eq. (40) into Eq. (38) and using Eq. (41), the resulting equation for $c(r)$ can be solved analytically. The final formula is quite cumbersome and it can be found in [301,302].

In Fig. 23A we present the function $h(q)$ simulated by the Percus-Yevick approach and using a Monte-Carlo simulation. In the simulation we used the radius of 3 units of the non-penetrating hard spheres, $N = 2000$ spheres were randomly placed in the simulation cube with the edge $L = 1000$ units. From figure it is obvious that both approaches yield almost same results. The function

$h(q)$ exhibits side maxima; however these maxima are not connected with any mean distance between the spheres and they cannot be interpreted as a sign of an ordering of the positions of the spheres.

In many experimental cases the ordering of the positions of the clusters (nanoparticles) is stronger than that following from the fact that the particles do not penetrate. Let us assume for simplicity that the particles create a random one-dimensional chain according to Fig. 23B.

The random vector connecting the centers of particles $n-1$ and n is denoted L_n and we assume that the vectors L_n have the mean value $\langle L \rangle$, and L_n, L_m are statistically independent if $n \neq m$. This model is called one-dimensional short-range order model (SRO). In this model, the function $h(q)$ can be obtained directly

$$h(\mathbf{q}) = \langle L \rangle \left\{ 1 + 2\text{Re} \left[\frac{\xi}{1 - \xi} \left(1 - \frac{1}{N} \frac{1 - \xi^N}{1 - \xi} \right) \right] \right\}, \xi = \langle e^{-i\mathbf{q} \cdot L} \rangle \tag{42}$$

In the limiting case of very large number of particles ($N \rightarrow \infty$) we obtain the paracrystal model [303–305]. Fig. 23C shows the functions $h(q)$ simulated within the one-dimensional SRO model for various root-mean square deviations (rms) σ_L of the particle distances L .

The function $h(q)$ exhibits side maxima approximately in the points of the averaged reciprocal lattice of the particles, however with increasing σ_L the maxima move towards smaller $|q|$. The widths of the maxima increase with increasing σ_L and they are approximately proportional to n^2 , i.e. with increasing order n of the maximum the maximum becomes broader.

In the SRO model the particle “feels” only the neighboring particles so that there are no a-priori defined ideal particle positions. On the other hand, the long-range order model (LRO) assumes that the particles are displaced by a random vector U from a-priori defined periodic particle positions (Fig. 23D).

Again, the direct calculation of $h(q)$ is easy within this model:

$$h(\mathbf{q}) = L \left(1 - \zeta^2 + \frac{\zeta^2}{N} \left| \sum_{n=1}^N e^{-i\mathbf{q} \cdot L} \right|^2 \right), \zeta = \langle e^{-i\mathbf{q} \cdot U} \rangle \tag{43}$$

Simulated $h(q)$ curves are shown in (Fig. 23E).

In contrast to the SRO model, in the LRO model the width of the satellite maxima are not affected by the random displacements are inversely proportional to the size NL of the particle chain. The disorder gives rise to a homogeneous background which increases with increasing σ_U .

It is not easy to generalize the one-dimensional SRO model to more dimensions. A discussion of this problem can be found in [306]. A combined three-dimensional SRO-LRO model which can be used for the description of the positions of self-organized nanoparticles in multilayers can be found in [307].

Up to now we considered random positions of the clusters (nanoparticles) and random sizes/shapes of the particles but we ignored the possibility of statistical correlation of the particles’ sizes and positions. In particular, Eq. (14) was derived assuming that the sizes and positions of the particles are completely statistically independent. This is so called decoupling approximation (DA) [43], where the sizes and distance are completely decoupled. In reality, this is the case only for much diluted systems, where the particle interaction can be completely neglected. For instance, in most random ensembles of particles one can expect that the mean distance between the particles increases with increasing mean particle size. In local monodisperse approximation (LMA) one assumes that the sample consists of many small regions with identical particle sizes. Then, the scattered intensity can be calculated as follows:

$$I_s(\mathbf{q}) = |K|^2 I_i \left\langle \sum_{n=1}^N \sum_{m=1}^N F_n(\mathbf{q}) F_m^*(\mathbf{q}) e^{-i\mathbf{q} \cdot (R_n - R_m)} \right\rangle_{\text{size, pos}} \approx |K|^2 I_i \langle |F^{(\text{size})}(\mathbf{q})|^2 G^{(\text{size})}(\mathbf{q}) \rangle_{\text{size}} \tag{44}$$

where $F^{(\text{size})}(\mathbf{q})$ is the structure factor of a particle with given size (and shape) and

$$G^{(\text{size})}(\mathbf{q}) = \left\langle \sum_{n=1}^N \sum_{m=1}^N e^{-i\mathbf{q} \cdot (R_n - R_m)} \right\rangle_{\text{pos}} \Bigg|_{\text{size=const}} \tag{45}$$

is the correlation function of the positions of particles with the given size. This correlation function can be constructed assuming a suitable ordering model (SRO, for instance), the parameters of this model (mean particle distance and its rms deviation) scale with the actual particle size. Then, the final averaging over the sizes in Eq. (44) must be performed numerically.

Fig. 23F demonstrates the difference between the DA and LMA models. In this figure, we present the scattered intensities simulated using Eqs. (14) and (44) of a one-dimensional SRO distribution of spheres, the mean sphere radius $\langle R \rangle = 2$ nm, mean distance $\langle L \rangle = 6$ nm. We used the rms deviations $\sigma_R = 0.35$ nm and $\sigma_L = 4$ nm; in the LMA model we assumed that both the mean distance $\langle L \rangle$ and is rms deviation σ_L are proportional to the local (random) sphere radius R . From the figure, it follows that both models yield almost identical tails of the scattering curve, however the central parts of the curves including the first-order satellite maxima differ substantially. The DA model overestimates the diffuse background between the maxima. In many experimental cases, a weighted average of the DA and LMA curves is a good choice for fitting the experimental data.

4. Chemical specificity: The role of X-Ray spectroscopies

4.1. X-ray absorption spectroscopies: EXAFS and XANES

X-ray absorption spectroscopy (XAS), including both X-ray absorption near edge (XANES) and extended X-ray absorption Fine structure (EXAFS), is a powerful tool to investigate the local atomic environment in condensed matter since it couples chemical selectivity and high resolution at the short distance scale [68,73,237,308–311]. These peculiar features of the technique are extremely useful in the characterization of nanomaterials which may be made up of a very low number of atoms, often embedded in a hosting matrix, which can dominate the response of any non-atomic selective characterization technique [21,312,313]. Moreover, as already discussed, the intrinsic nanometric dimension of the nanomaterials hinders the straightforward application of standard Bragg approach diffraction techniques which require a long-range order. Finally, the XAS spectrum can provide information on the electronic structure and local coordination geometry of the absorber atom. Therefore, XAS has been widely applied in the study of nanostructures, significantly contributing to their characterization at the sub-nm level and to the understanding of the relation between atomic structure and physical properties [75,314–320].

XAS is based on the acquisition and the analysis of the X-ray absorption coefficient $\mu(E)$ as a function of the incident photon energy E in the region around the absorption edge of an element present in the sample. The region including few eV before and several eV after the edge is usually called X-ray Absorption Near Edge Structure (XANES [69,241,243,244,321]) for hard X-rays or (Near Edge X-ray Absorption Fine Structure (NEXAFS [322–325]) for soft X-rays, while the following energy range (up to more than 1 keV after the edge) is the Extended X-ray Absorption Fine Structure (EXAFS) region [68,238–240].

The photoelectric absorption process can be described as a transition between an initial state $|\psi_i\rangle$ (incident photon of energy $E = \hbar\omega$ and electron in a core orbital with binding energy E_0) and a final state $|\psi_f\rangle$ (core hole and excited electron). If the energy is lower than E_0 , the electron is promoted to empty bound atomic states and the unoccupied density of states (DOS) is probed. Conversely, when the photon energy is higher than E_0 , the electron is excited to the continuum and it can be described as an outgoing wave with wavenumber k [68,73,75,119]:

$$k = \frac{\sqrt{2m(E - E_0)}}{\hbar} \quad (46)$$

where m is the free electron mass. The photoelectron extracted from the absorber interacts with the surrounding atomic environment and the final state is composed not only by the outgoing wave, but also by the backscattered waves which perturb the process.

This phenomenon can be described in a quantitative way applying the Fermi's golden rule [326–328], using as Hamiltonian the excitation by electromagnetic waves:

$$\mu(k) \propto |\langle \psi_f | \hat{\mathbf{e}} \cdot \vec{r} e^{i\vec{k} \cdot \vec{r}} | \psi_i \rangle|^2 \rho_{unocc}(E_f) \delta(E_f - E_i - \hbar\omega) \quad (47)$$

where μ , $\hat{\mathbf{e}}$ and $\hbar\vec{k}$ are the X-ray absorption coefficient of the material, polarization versor of the X-ray beam and photoelectron momentum, respectively, and where $\rho_{unocc}(E_f)$ represents the unoccupied DOS at energy E_f and where the Dirac δ function guarantees the energy conservation in the process. The occupied DOS of the initial state $|\psi_i\rangle$, $\rho_{occ}(E_i)$ is always one in XAS experiments.

4.1.1. EXAFS region

In the EXAFS region, in order to simplify Eq. (47), it is possible to expand the exponential term as a series $\left(1 + i\vec{k} \cdot \vec{r} + \dots\right)$ where the first and dominant term is representing the dipole interaction, and the following terms are associated with quadrupole and higher order multipoles. Moreover, the absorption coefficient $\mu(k)$ is usually represented as the sum of two contributions: the atomic absorption $\mu_0(k)$, describing the contribution of the absorbing atom as if it was isolated (i.e. without neighbors), and the EXAFS function $\chi(k)$, accounting for the scattering effects [314]:

$$\mu(k) = \mu_0(k)[1 + \chi(k)] \quad \text{i. e.} \quad \chi(k) = \frac{\mu(k) - \mu_0(k)}{\mu_0(k)} \quad (48)$$

Experimentally, the absorption coefficient is obtained by measuring, in transmission mode, the X-ray beam intensity before $I_0(E)$ and after $I_1(E)$ the sample [21,22,73,75,314] and applying the Lambert-Beer law [329,330]:

$$I_1(E) = I_0(E)e^{-\mu(E)x} \Rightarrow \mu(E)x = \ln \left[\frac{I_0(E)}{I_1(E)} \right] \quad (49)$$

where x is the sample thickness. In case the selected element for XAS experiment is too diluted or the sample thickness is too large (and cannot be reduced), then transmission experiments become unfeasible and experimentalists are forced to measure one of the decay channels of the photon absorption process that are either the Auger or the X-ray fluorescence phenomena [331–333]. In such cases $\mu(E)$ is obtained as [21,22,73,75,314]:

$$\mu(E) = \frac{I_{Fluo}(E)}{I_0(E)} \quad \text{or} \quad \mu(E) = \frac{I_{Auger}(E)}{I_0(E)} \quad (50)$$

being $I_{Fluo}(E)$ and $I_{Auger}(E)$ the measured fluorescence and Auger yields, respectively. The dependence of the absorption coefficient

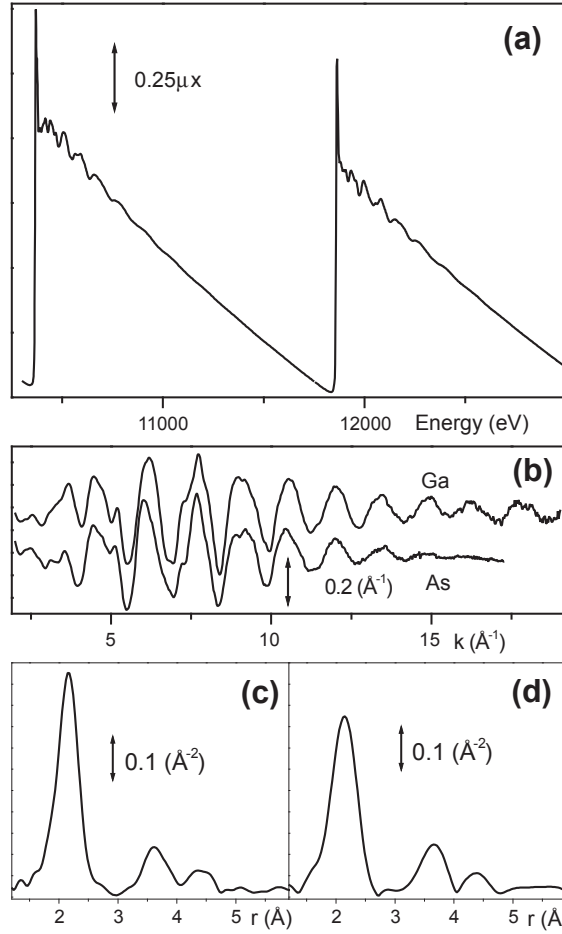


Fig. 24. (a): Absorption coefficient μx vs. the photon energy, measured in transmission mode, in the 10250–13000 eV range of a GaAs bulk polycrystalline sample (being \times the sample thickness). The first discontinuity across 10.367 keV corresponds to the Ga K-edge, while the second one, around 11.867 keV, corresponds to the As K-edge. (b): Ga (top) and As (bottom) K-edge EXAFS oscillations, $k\chi(k)$, as a function of k , obtained from the raw datum reported in part (a) after removal of the background absorption and normalization to the jump edge, see Eq. (48). (c): Fourier transform of the Ga K-edge $k\chi(k)$ into r -space, where the contributions of the first (Ga-As), second (Ga-Ga) and third (Ga-As) coordination shells around Ga can be distinctly observed around 2.2, 3.7 and 4.4 \AA respectively. Note that these distances are slightly shorter with respect to the actual ones since the Fourier transform has not considered the phase function $[2\delta(k) + \Phi(k, \Gamma_N)]$, see equation (52). (d): as part (c) for the As K-edge $k\chi(k)$ function. Reproduced with permission from Ref. [119] (copyright Elsevier, 2004).

with respect to the photoelectron wavevector k is than obtained applying Eq. (46) to Eqs. (49) or (50) for all energy values $E > E_0$.

Fig. 24a reports the experimental $\mu x(E)$ of a GaAs bulk polycrystalline sample in the region covering both Ga and As K-edges. The two k -weighted $\chi(k)$ functions, extracted using Eq. (48), are shown in Fig. 24b top and bottom curves for the Ga and As K-edges, respectively; Parts (c) and (d) report the corresponding phase-uncorrected FT.

The $\chi(k)$ function can be expressed as a sum of contributions due to all possible N -bodies scattering $\chi_N(k)$ from $N = 2$, two bodies interaction or single scattering (SS) paths, to $N > 2$ interactions or multiple scattering (MS) paths [68,75,312,334,335]:

$$\chi(k) = \sum_{N=2}^{\infty} \chi_N(k) \quad (51)$$

Each $\chi_N(k)$ term is given by the sum over all Γ_N paths where the photoelectron, once leaving the excited atom (located in \mathbf{r}_0), interacts with $(N - 1)$ neighbors (located in \mathbf{r}_i ; $i = 1, 2, \dots, N - 1$) before recombining in \mathbf{r}_0 :

$$\chi_N(k) = \sum_{\Gamma_N} A(k, \Gamma_N) \sin[kR_{\Gamma} + 2\delta(k) + \Phi(k, \Gamma_N)] \quad (52)$$

where $\delta(k)$ is the phase shift undergone by the photoelectron interacting with the other electron clouds of the excited atom and where $A_{\Gamma}(k, \Gamma_N)$ and $\Phi(k, \Gamma_N)$ are the k -dependent amplitude and phase functions that takes into account all $(N - 1)$ interactions of the Γ_N path and where R_{Γ} is the path length:

$$R_{\Gamma} = \left(\sum_{i=1}^{N-1} |r_i - r_{i-1}| \right) + |r_0 - r_{N-1}| \quad N \geq 2 \quad (53)$$

While the series (51) and (52) are formally infinite, in all real cases, due to the finite lifetime of the excitation (related to the core-hole life time [336]) and to the exponential dumping of the path Γ contribution as a function of the path length R_{Γ} , only the first few terms contribute significantly to the measured $\chi(k)$ function. In amorphous or nano-crystalline materials the number of relevant paths is smaller than in ordered crystalline materials.

When recombining in r_0 , after having travelled the whole Γ_N path, the photoelectron wavefunction is out of phase with respect to the wavefunction of the emitted photoelectron since it travelled a path length of R_{Γ} and as a consequence of the $(N - 1)$ interactions with neighbors and of the double interactions with the external electron clouds of the excited atom itself, see the argument of the sinus function in Eq. (52). The kR_{Γ} term can be modulated changing the photoelectron wavenumber k , i.e. changing the photon energy according to Eq. (46). The outgoing and the incoming wavefunctions interfere and the interference can assume any configuration between full constructive [$\Delta\varphi = 2n\pi$] and full destructive [$\Delta\varphi = 2(n + 1)\pi$] depending on the difference of phase between the two waves. The energy scan performed in the data collection, reported in Fig. 24a, measured along several periods this interference phenomenon, which causes oscillations in the absorption coefficient $\mu(E)x$ after both edges, better visible in the $k\chi(k)$ functions reported in Fig. 24b.

A decomposition of the cross-section in the EXAFS region, alternative to the MS approach described above, has been reported by Filipponi, Di Cicco and Natoli into irreducible N-body signals [238,239,337,338].

The historical expression highlighted by Stern, Sayers and Lytle in the early 1970s for the $\chi(k)$ function [237,339,340], represents the single scattering approximation of Eqs. (51) and (52):

$$\chi(k) = S_0^2 \sum_j \frac{N_j}{kr_j^2} |f_j(k, r_j)| e^{-\frac{2r_j}{\lambda_e(k)}} e^{-2k^2\sigma_j^2} \sin\{2kr_j + 2\delta_0(k) + \varphi_j(k)\} \quad (54)$$

Where S_0^2 is the passive electron amplitude reduction factor [341,342], estimated as squared projection of the many-body wave functions of the $(Z - 1)$ “passive” electrons before and after excitation of the photoelectron: $S_0^2 = |\langle \Psi_{Z-1}^i | \Psi_{Z-1}^f \rangle|^2$ [75], being Z the number of electrons of the excited atom, before excitation. Usually S_0^2 is close to unit and can be either computed from theory or determined experimentally using model compounds. The sum in Eq. (54) is performed over “coordination shells”, which are defined as groups of atoms of the same element at similar distances from the absorber; N_j is the number of atoms in the shell, R_j is the average j -th shell bond distance (for single scattering paths $R_{\Gamma} = 2r_j$), σ_j^2 is the Debye-Waller factor depending on the mean square variation of distances about the average and on the thermal motion of the single atoms, $|f_j(k, r_j)|$ and $\varphi_j(k)$ are the modulus and the phase of the complex electron scattering amplitude of the scattering atom j , $\delta_0(k)$ is a phase depending on the absorbing atom, $\lambda_e(k)$ is the photoelectron mean free path (typically few Å, depending on k and on the surrounding atoms [343]). Therefore, the analysis of the EXAFS signal allows determining the interatomic distances r_j , the coordination numbers N_j and to estimate the thermal and static disorder, estimated having a Gaussian distribution around the equilibrium distance R_j of standard deviation σ_j , typical of harmonic interatomic potential [344]. This term will be further discussed in the following.

Summarizing, the total EXAFS function $\chi(k)$ will be the sum of all the SS and MS paths, as indicated by Eq. (51). In principle, there is an infinite number of such paths, but, in practice, their number is limited by the fast damping of the signal for long R_{Γ} (usually paths with $R_{\Gamma} > 10$ Å have negligible amplitude) and by the fact that the amplitude of MS signal quickly decreases with the order N (usually paths with $N > 4$ can be neglected). Usually SS path have a much stronger intensity of the MS ones, because of both shorter path lengths R_{Γ} and of larger $A_{\Gamma}(k, \Gamma_N)$ scattering amplitudes. However, exceptions occur in case of an alignment of three (or more) atoms in an almost collinear geometry resulting in MS path with scattering angles close to 0 or to 180°, which amplitude is enhanced by focusing effects [345]. This is the case e.g. of linear triatomic molecules (such as HgBr_2 , HgCl_2 , AuBr_2^- , and CuBr_2^- [346]); of several metal carbonyl complexes [347–351]; of some other organometallic complexes [352–354]; of crystalline solids with specific space groups (e.g. $Pm-3m$ for ReO_3 [355] $Fm-3m$ for NiO [356,357] or MgO [358]); of metals [359,360] and metal NPs that crystallize in the fcc or bcc phases [131,361–366] etc ...

As an example of a case where MS contributions are relevant, Fig. 25a reports for a bulk polycrystalline NiO measured at RT the $k^3\chi(k)$ -weighted, phase uncorrected, modulus of the FT together with the corresponding best fit scattered gray circles and solid black line, respectively [356]. The contributions of the independent scattering paths, as obtained from the fit, are also shown: SS paths are reported in red for oxygen scatterers and in blue for nickel scatterers, while the most relevant MS paths are reported in green. For the assignment of the different paths refer to the figure caption and to part (b) of Fig. 25, where the absorbing atom is labelled as (0) and the scattering neighbors are numbered as a function of the progressive shells.

According to Eq. (54), each path included in the fit requires the optimization of three parameters: (N_j , r_j and σ_j^2), together with the two parameters S_0^2 and E_0 that are common for all paths, the latter defining the relationship between the photon energy E and the photoelectron wavenumber k , see Eq. (46). The analysis of an EXAFS spectrum which exhibits a good signal up to high R values, such as that reported in Fig. 25a, has to face the problem that the number of scattering paths Γ_N increases rapidly with the distance R from the absorber and so do the number of parameters to be optimized, see black circles in Fig. 25c. The Nyquist-Shannon theorem (or sampling theorem) [367–369], defines the maximum number (n_{ind}) of optimized parameter as the product of the sampled interval in k -space (Δk) and the interval in R -space (ΔR) where the fit is performed [73,312]:

$$n_{ind} = 2\Delta k \Delta R / \pi. \quad (55)$$

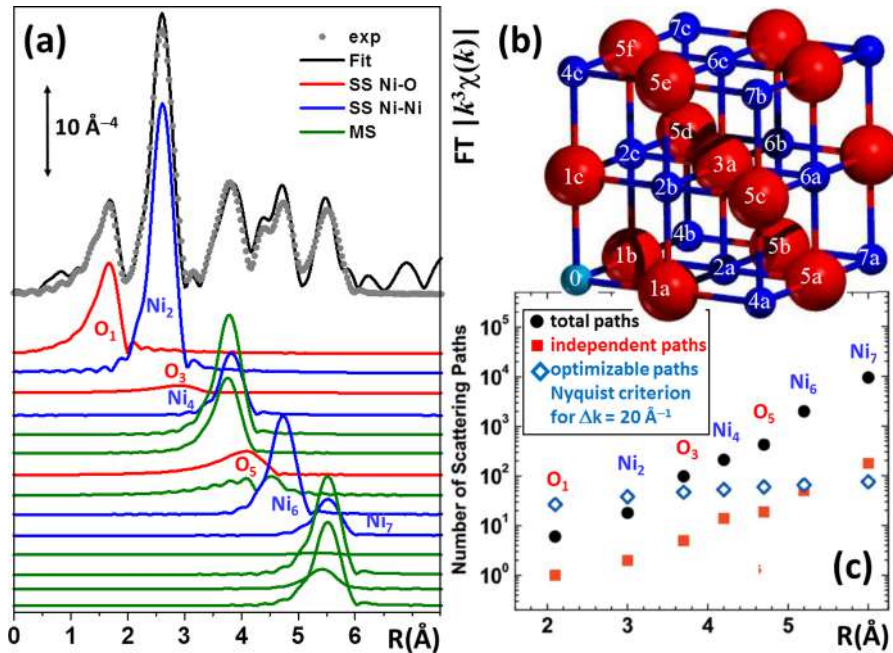


Fig. 25. (a) k^3 -weighted, phase uncorrected, FT of the experimental Ni K-edge $\chi(k)$ of polycrystalline NiO collected at room temperature (gray scattered points) superimposed with the best fit up to the 7th coordination shell (solid line) together with the SS Ni-O (red lines), the SS Ni-Ni (blue lines) and the most relevant MS paths. In particular, vertically shifted, from top to bottom: 1st shell SS Ni₀-O_{1a}-Ni₀; 2nd shell SS Ni₀-Ni_{2a}-Ni₀; 3rd shell SS Ni₀-O_{3a}-Ni₀; 4th shell SS Ni₀-Ni_{4a}-Ni₀; Ni₀-O_{1a}-Ni_{4a}-Ni₀ 3-body MS path; Ni₀-O_{1a}-Ni_{4a}-O_{1a}-Ni₀ 4-body MS path; 5th shell SS Ni₀-O_{5a}-Ni₀; Ni₀-O_{1a}-O_{5a}-Ni₀ 3-body MS path; 6th shell SS Ni₀-Ni_{6a}-Ni₀; 7th shell SS Ni₀-Ni_{7a}-Ni₀; Ni₀-Ni_{2a}-Ni_{2a}-Ni₀ 3-body MS path; Ni₀-Ni_{2a}-Ni_{7a}-Ni₀ 3-body MS path; Ni₀-Ni_{2a}-Ni₀-Ni_{2a}-Ni₀ 4-body MS path; Ni₀-Ni_{2a}-Ni_{7a}-Ni_{2a}-Ni₀ 4-body MS path. The atoms labeling is reported in (b); negative atom labeling refers to atoms located in symmetric opposite positions with respect to Ni₀; according to Eq. (53) all paths start and end in Ni₀. (b) Cubic NiO cluster with Ni and O atoms represented as small blue and big red numbered spheres, respectively. Number 0 identifies the absorbing Ni atom, while the progressive 1–7 numbers refer to the 1st – 7th coordination shell around Ni(0). All atoms belonging to the same shell are degenerate in the cubic symmetry of the bulk case, resulting in equivalent scattering paths. The letters following the numbers are used to distinguish atoms of the same shell once the degeneration is removed by tetragonal distortion (vide infra). (c) Total number of scattering paths (black dots), number of independent scattering paths (red squares) and maximum number of optimizable shells for a Δk interval of 20 \AA^{-1} (blue open diamonds) present considering a sphere of radius R centered in the absorbing atom Ni₀. A logarithmic scale has been adopted for ordinate axis. Previously unpublished figure obtained adapting graphical material from Ref. [356] (a,b), and from Ref. [312] (c). (For interpretation of the references to color in this figure legend, the reader is referred to the web version of this article.)

The open diamonds in Fig. 25c represents the number of optimizable paths according to the Nyquist-Shannon theorem for a Δk interval as large as 20 \AA^{-1} . The black dots and the open diamond curves cross before $R = 4 \text{ \AA}$, making apparently impossible the analysis of higher shells. This apparent contradiction is overcome by considering the high symmetry of the NiO crystals, that makes several Γ_N paths equivalent, so that the same N_j , r_j and σ_j^2 parameters can be used for them. This is e.g. the case for the 6-equivalent first shell Γ_2 paths connecting Ni₀ to O_{1a}, O_{1b}, O_{1c}, O_{-1a}, O_{-1b} and O_{-1c} (the last three not explicitly represented in Fig. 25b). In such a case the situation improves (see red squares in Fig. 25c), but the constrain of the Nyquist-Shannon theorem appears again for $R > 5.5 \text{ \AA}$. [312] In case of ordered materials for which a hypothesized structural model (obtained either from XRPD Rietveld refinement or from DFT optimization) needs to be verified by EXAFS, then the number of optimizable parameters can be significantly reduced as all coordination numbers N_j are fixed by the model and as a single isotropic enlargement factor α can be used to define all path distances R_j :

$$R_j = (1 + \alpha) R_j^0 \quad (56)$$

where R_j^0 is the path distance defined in the tested structural model. This approach, has been successfully applied to understand the local structure of metal-organic frameworks (MOFs) [370–378], of organometallic complexes [379–383] and of metal atoms in zeolites [178], and has been named XRD- assisted (or DFT-assisted EXAFS) analysis. Using this method, when different structural models are considered, the selection of the most reliable structural model is based on (a) the agreement between experimental and theoretical EXAFS curves (R-factor); (b) the agreement between DFT- and EXAFS-optimized interatomic distances (α value in the $-0.01 < \alpha < 0.01$ range); (c) error bars associated with the optimized parameters, and (d) physical meaningfulness of the non-structural parameters (ΔE and σ^2) [178,383,384].

The problem becomes much more complex for nanomaterials because the relaxation of the structure at the surface leads to the appearance of non-equivalent atoms as photon absorbers and removes the degeneration of the scattering path implying a reduction of the coordination numbers and a variation of the paths length [312,356,358]. In this regard, a decrease in N_j and a shortening of the

average R_T , accompanied by an increase in static disorder, has been observed in Rh NPs supported on carbons upon decreasing the average particle size distribution [385].

In order to perform a more advanced analysis of the EXAFS signal, it is necessary to go into a deeper detail on the term $\exp(-2k^2\sigma_j^2)$ in Eq. (54). The origin of this term is related to the different time scales of the photoabsorption and consequent scattering processes ($\sim 10^{-16}$ – 10^{-15} s) and of the atomic vibrations in molecules and condensed phases (10^{-13} s). Consequently, each single photon absorption in the XAFS phenomenon captures a snapshot of instantaneous atomic positions. The actual experiment implies the sum of a huge number of elementary processes, implying that XAFS actually probes the configurational average of the atomic positions [75,312]. In this context, it is relevant to underline that the EXAFS σ_j^2 factor depends on the degree of correlation of the vibration of the absorbing atom in r_0 and of the scattering atom in r_j , while the analogous Debye-Waller factor which affects the intensity of the Bragg peaks in X-ray diffraction experiments depends only on the mean square deviation of each atom's position with respect to its equilibrium value, projected in the direction of the scattering vector [75]. As already suggested in the seminal work of Sayers, Stern Lytle [237], the effect of a small static structural disorder can be taken into account by a supplementary Debye-Waller factor ($\sigma_{j,stat}^2$) which is added in quadrature to the thermal one ($\sigma_{j,ther}^2$) [73,75]:

$$\sigma_j^2 = \sqrt{\sigma_{j,ther}^2 + \sigma_{j,stat}^2} \quad (57)$$

Moreover, the term $\exp(-2k^2\sigma_j^2)$ accounts for the radial disorder only, whereas both the scattering amplitude $f_j(k, r_j)$ and phase shift $\varphi_j(k)$ functions exhibit a nonlinear angular dependence that is particularly relevant for an almost collinear configuration of atoms [312,345,386]. In case of systems with a relative small disorder, a low-order Taylor expansion of $f_j(k, r_j)$ and $\varphi_j(k)$ functions represents a good approximation [238,239].

To treat in a more accurate the thermal and the static disorder, some advanced approaches, based on calculation of the configuration averaged EXAFS signal using a set of atomic configurations, have been developed. They are based on: (i) classical molecular dynamics [387–408]; (ii) *ab initio* molecular dynamics [397,409–418]; (iii) Monte Carlo (MC) simulations [419–429]; (iv) or reverse Monte Carlo (RMC) simulations [403,430–447]; and (v) evolutionary algorithm [403,448–457]. Method (v) represents a computationally more efficient extension of method (iv), that to analyze SS and MS contributions to the EXAFS data up to high R values considering the disorder of both thermal and static origin. It is worth mentioning that molecular dynamics (both classical and *ab initio*) and Monte-Carlo methods need a reliable force-field model to describe the interactions between atoms [458], while reverse Monte Carlo approaches does not [312,437,459].

In this context we will briefly describe the general scheme (Fig. 26a) used to analyze the EXAFS data using a configuration averaging coming from molecular dynamics [312]. The first step is the definition of both the force-field model that describe all relevant interactions among atoms and the starting the structural model representative of the sample (Fig. 26a, top part). The former must be *a priori* tested to verify its ability to reproduce the material properties [458]. For NiO NPs, the latter point consists in defining the Ni_xO_y chemical composition, the size and the shape of the NPs as well as the density of atomic vacancies [312,460]. Then molecular dynamic simulations are performed at the experimental temperature/pressure used in the EXAFS data collection (Fig. 26a, middle part). Note that in case the temperature of the experiment is lower than the Debye temperature of the material, *ab initio* molecular dynamic must be used, otherwise classical molecular dynamic calculations are reliable [312,461]. The molecular dynamic calculations provide the partial radial distribution functions that, in turn, give the interatomic distances (r_j) and the coordination numbers (N_j), of the different coordination shells. The so determined r_j and N_j values are then compared with those obtained from a

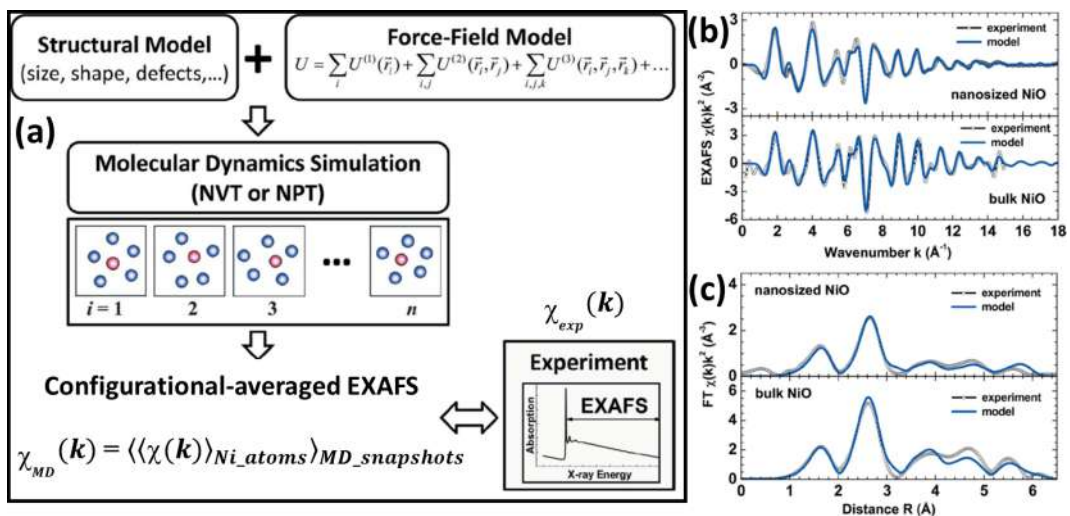


Fig. 26. (a) Scheme of the MD-EXAFS calculations. (b) Comparison of experimental (open circles) and configuration-averaged (solid lines) Ni K-edge, $k^2\chi(k)$ EXAFS curves collected at 300 K for bulk [462] and nanosized [460] NiO: bottom and top panels, respectively. (c) as (b) for the corresponding Fourier transformed data. Adapted with permission from [312], copyright IUCr 2014.

conventional analysis of EXAFS spectrum: at this stage, the quality of the agreement between the two sets of structural parameters is used as a criterion for tuning the force-field model in order to avoid an unreliable evolution of the NP structure during the molecular dynamic run and to minimize the number of EXAFS calculations in the successive step. The configuration-averaged EXAFS spectrum $\chi_{MD}(k)$ is obtained by averaging the EXAFS spectra of the simulated NP over all accepted Monte Carlo snapshots ($\langle \dots \rangle_{MD_snapshots}$ average), that, in turn, are obtained by averaging the EXAFS spectra computed, for a given NP configuration, over all the Ni atoms of the NP ($\langle \dots \rangle_{Ni_atoms}$ average):

$$\chi_{MD}(k) = \langle \langle \chi(k) \rangle_{Ni_atoms} \rangle_{MD_snapshots} \quad (58)$$

The agreement between the calculated EXAFS spectrum $\chi_{MD}(k)$ and the experimental one $\chi_{exp}(k)$ is adopted as a criterion to select the best structural model of the NiO NP [312,460] (Fig. 26a, bottom part). The advantage of this methodology is that it requires only few independent free parameters to model the NP structure, which are optimized to find the best agreement between $\chi_{MD}(k)$ and $\chi_{exp}(k)$ considering all SS and MS paths (which amplitude is larger than a fixed value) and by taking into account the NP disorder (both thermal and static) effects within a large real-space range [312,460].

The agreement between experiment and theory obtained by Kuzmin and coworkers adopting the described methodology on NiO NPs (particle size in the 3.6–4.2 nm range and Ni vacancies in the 0.4–1.2%) and measured at 300 K is reported in the top parts of Fig. 26b and c in the k - and R -spaces, respectively [312,460]. For the validation of the approach, the authors reproduced successfully also the EXAFS spectrum of NiO bulk (bottom top parts in Fig. 26b,c) [312,462].

4.1.2. XANES region

The experimental XANES spectra are collected simultaneously to the EXAFS part in transmission, fluorescence yield or electron yield modes, see Eq. (49) and (50), depending on the sample characteristics.

Eq. (54) cannot be used to describe the XANES region since it can be correctly applied only when the energy is sufficiently higher than the absorption edge. However, already a decade before the seminal papers which made EXAFS a powerful structural characterization technique [237,339,340], Van Nordsthand [463] investigated by XANES several transition metal compounds and discussed their XANES spectra according to the local structure and valence of the metal element, highlighting also the chemical shift with valence. This was a first demonstration that the XANES spectral region can provide interesting structural and electronic information, being very sensitive not only to the interatomic distances, but also to the symmetry of the coordinated atoms, distribution of charges and potential around the absorbing atom [74,464].

A significant example of the versatility and usefulness of XAS spectroscopy in the study of nanomaterials is the use of C K-edge XANES/NEXAFS spectroscopy to simultaneously characterize the electronic, orientational, and structural properties of carbon-based materials and nanomaterials. Starting from the seminal studies on graphite [465], several groups have experimentally investigated the XAS spectra of a 2D monolayer and few layer graphene [466–468]. They highlighted the presence of two main spectral features at about 285 and 292 eV, assigned to π^* and σ^* final states, respectively. They also observed a polarization dependence of the peak

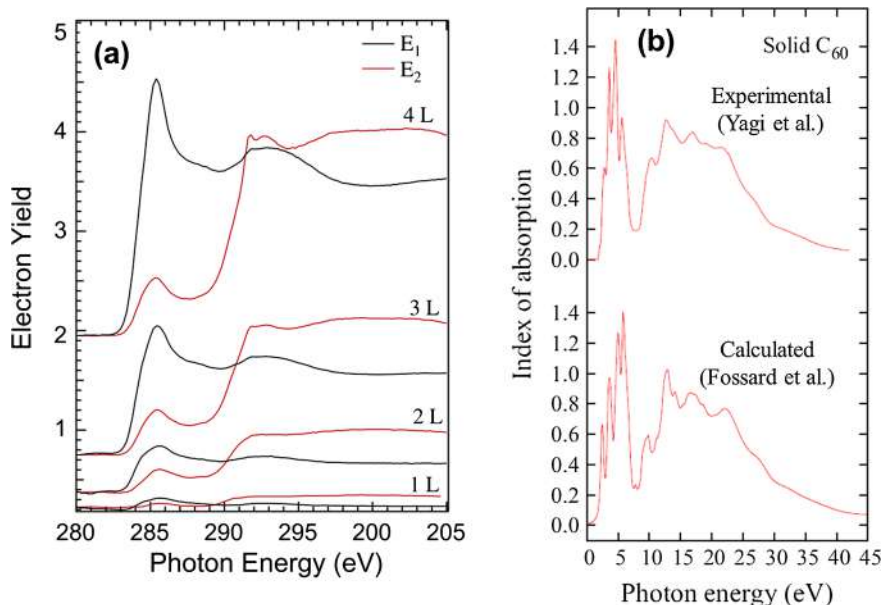


Fig. 27. (a) C K-edge NEXAFS spectra from single- to four-layers graphene flakes measured with the linear polarization vector nearly-parallel (E_1 , black curves) or perpendicular (E_2 , red curves) to the graphene basal plane. (b) Calculated and experimental (taken from Ref. [476]) index of absorption for C_{60} . Part (a) adapted with permission from Ref. [468], Copyright Elsevier (2009); part (b) adapted with permission from Ref. [475], Copyright American Physical Society 2017. (For interpretation of the references to color in this figure legend, the reader is referred to the web version of this article.)

intensity [468], which was in agreement with the previous results obtained on graphite (see Fig. 27a) [465]. As suggested by Hua et al. [469], also two other peaks, which are observed at 283.7 and 288 eV, are very interesting since they can be used as fingerprints to estimate the defect concentration or the sample size.

C K-edge NEXAFS spectroscopy has been also widely applied in the study of carbon nanotubes (CNTs). The energy position of the σ^* resonances in functionalized CNTs is particularly sensitive to the bond distances between the C absorber and the surface functional groups, while monitoring the π^* band it is possible to study the bond hybridization, thus measuring the percentage of sp^2 and sp^3 in mixed sp^2/sp^3 -bonded systems [470]. Moreover, from a detailed analysis of the already mentioned π^* and σ^* resonances, it is possible to evaluate the oxidation level of the sample and presence of oxygenated functionalities [471–473].

It is worth noting that for several years XANES spectra have been basically discussed in a qualitative way: considering the absorption edge shift, observing the presence or absence of specific spectral fingerprints and comparing the results with data acquired on model compounds. A significant improvement is represented by the CONTINUUM code released in the early '90s by Natoli and co-workers [474], which was the first code able to compute a theoretical spectrum starting from a hypothesized local structure. Thanks to the following impressive developments in computational power and to the appearance of more sophisticated modeling approaches, as discussed also for EXAFS in the previous section, nowadays XANES spectroscopy is becoming a mature technique for the quantitative structural determination of the local environment of nanomaterials. The effectiveness of modern modeling approaches in reproducing fine spectral features can be appreciated for carbon based nanomaterials in the study of Fossard et al. [475]. They calculated for fullerene both the valence excitation spectrum of solid C_{60} below 70 eV and the C1s near-edge spectra over a comparable energy range. The simulations captured most of the valence oscillator strength, in good agreement with experimental data (Fig. 27b).

The chemical selectivity of XAS is also extremely useful in the investigation of functionalized carbon materials. Xing et al. [477], for instance, combined XPS and Pt L_{III} -edge XAS to study the anchoring of Pt nanoparticles on graphene. They showed that the electron density shifts from Pt to graphene depending on the strength of the Pt-graphene interaction. Another interesting example concerns the formation mechanism of Pt nanoparticles confined within the channel of carbon nanotubes [478]. The authors coupled C K-edge and Pt L_{III} -edge XAS spectra to show that charge transfer from multi-walled carbon nanotubes (MWCNTs) to the encapsulated H_2PtCl_6 precursor caused the spontaneous reduction of Pt^{4+} to metallic Pt, as highlighted by the decrease in intensity of the white line peak in the XANES region (Fig. 28a). Moreover, the analysis of the EXAFS spectral region showed that, varying the inner diameter of MWCNTs from 15 nm to 10 nm and 5 nm, the Pt–Pt bond length of the confined Pt nanoparticles decreased gradually (Fig. 27b).

4.2. X-ray emission spectroscopies

As described in the previous sections, the excitation of a core electron by X-rays implies the formation of a core hole with a specific lifetime. Such excited state can undergo a radiative decay yielding X-rays emission of energy $h\omega$. In X-ray emission spectroscopy (XES) the emitted fluorescence radiation is recorded with a high energy resolution. Usually, this excited state is induced by the absorption of photons in the X-ray region of the electromagnetic spectrum, but also other particles (i.e. protons induced X-ray emission - PIXE) can be employed [479].

The acquisition of XES requires, besides the standard monochromator employed to select the energy $h\Omega$ of the incoming X-ray photons (present in every XAS beamline), an additional X-ray spectrometer able to analyze the energy $h\omega$ of the fluorescence X-rays emitted by the sample in the radiative decay process. Indeed, the energy resolution of standard solid-state fluorescence detectors,

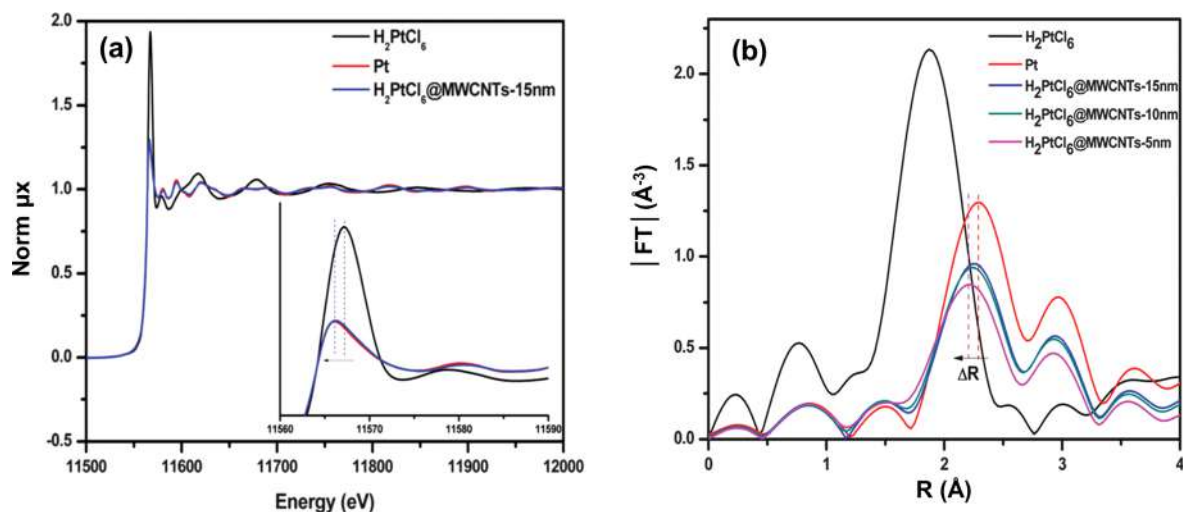


Fig. 28. Pt L_{III} -edge XAS spectra (a) and corresponding modulus of the FT of the EXAFS signal (b) for the H_2PtCl_6 precursor encapsulated in MWCNTs with different diameters (5, 10 and 15 nm). Adapted with permission from Ref. [478], Copyright Owner Societies (2016).

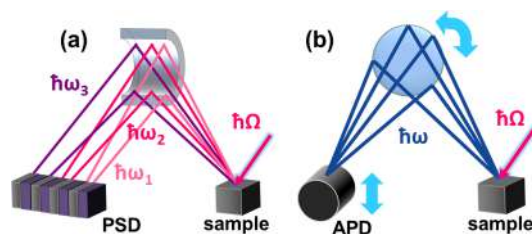


Fig. 29. (a) Scheme of a XES spectrometer in von Hamos geometry based on a polychromator employing a cylindrical Bragg crystal. This configuration has no moving parts and the XES spectrum (at fixed $\hbar\Omega$) is recorded in a single shot for a large range of emitted $\hbar\omega$ on a position sensitive detector (PSD). (b) Scheme of a XES spectrometer in 1:1 focusing Rowland geometry based on a spherical Bragg crystal. The XES spectrum is collected as a function of $\hbar\omega$, at fixed $\hbar\Omega$, by changing the angle of the analyzer (see curved arrow) and the position of the avalanche photodiode detector (APD) (see straight arrow). Unpublished figure.

conventionally employed to acquire XAS spectra in fluorescence mode (see Section 4.1), is 100–300 eV, which is, by far, insufficient for XES spectra. Therefore, XES spectrometers exploit the Bragg law to reach a resolution in $\hbar\omega$ in the order of 1 eV or better. Since fluorescence emission is isotropic, an ideal XES spectrometer has to combine the apparently contradictory requirements of a large angular acceptance with good energy resolution. The analyzer X-ray optics can be divided in two main categories as shown in Fig. 29. The first kind of analyzers are based on polychromators that disperse the emitted X-rays with different energies onto a position sensitive detector [480–482] (see Von Hamos spectrometer in Fig. 29a), while the second category employs a monochromator which is scanned across the $\hbar\omega$ spectral range of interest [483–485] (see spherically curved 1:1 focusing monochromator in Rowland geometry in Fig. 29b). The advantages of a polychromator with respect to a scanning monochromator are basically three: (i) there are no moving parts; (ii) it can achieve a better energy resolution; (iii) it can acquire all the $\hbar\omega$ spectrum simultaneously. Conversely, its main drawback is the smaller solid angle available for each analyzed energy resulting in a worse signal-to noise ratio owing to a more intense background arising from unwanted scattering.

All the complex spectral features of XES spectra can be described by *ab initio* calculations [77,486–491], however a comprehensive theoretical discussion is beyond the scope of this review, therefore we will introduce a simplified description relying on a one electron picture. To introduce the specific nomenclature of XES spectroscopy, we will discuss the case of a 3d-transition metal system with a 1s hole created by the excitation of the 1s electron to the continuum by incoming X-rays of energy $\hbar\Omega$ (see Fig. 30). This core

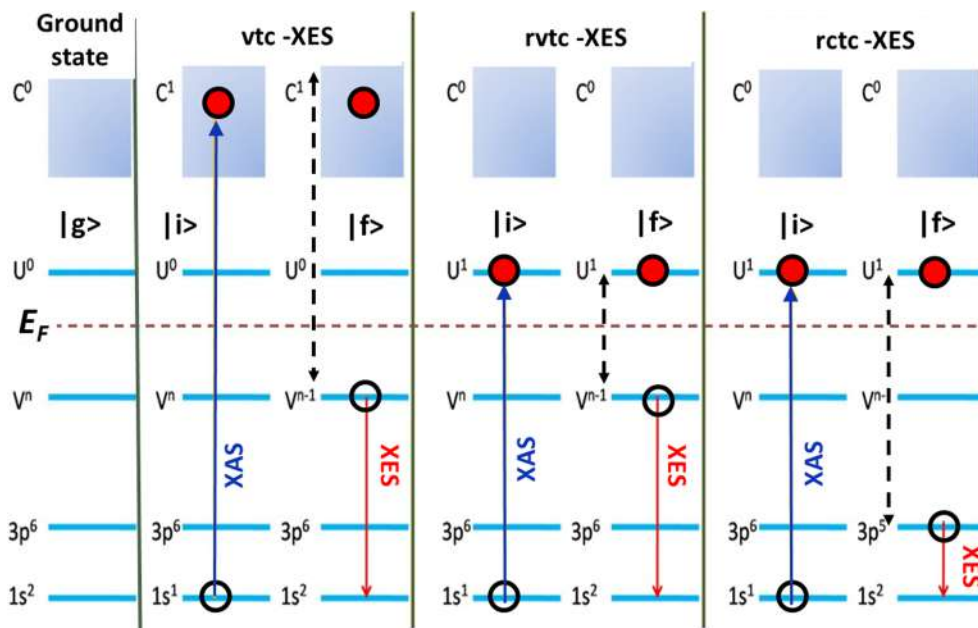


Fig. 30. (a) One electron representation of different XES processes including valence-to-core-XES, resonant-valence-to-core-XES and resonant-core-to-core-XES. V^n indicates the number (n) of electrons in the valence molecular orbitals (V) just below the E_F . U indicates the unoccupied molecular orbitals just above the Fermi energy (E_F) and C the continuum excitations. The blue arrows highlight the transition of an electron, which is in the $1s$ orbital in the ground state $|g\rangle$, after the absorption of the incoming X-rays of energy $\hbar\Omega$ to reach the intermediate state $|i\rangle$. The red arrows highlight the decay of an electron from a higher orbital to the core hole with final state $|f\rangle$, resulting in the emission of a photon of energy $\hbar\omega$. The energy transfer $\hbar(\Omega - \omega)$ is shown with a dashed black arrow. Unpublished Figure. (For interpretation of the references to color in this figure legend, the reader is referred to the web version of this article.)

hole can be filled by electrons belonging to different atomic orbitals with the consequent emission of photons with a specific energy $\hbar\omega$. The transition of a 3p electron to a 1s hole, known as core-to-core XES (ctc-XES), gives rise to the $K\beta$ main lines which are sensitive to the atom oxidation and spin state [492]. Conversely, the transition of a valence electron to fill the 1s hole gives rise to the valence-to-core XES (vtc-XES) which provides information on the type, distance and number of ligands as well as on the atom oxidation and spin state [21,22,493].

If the core electron is excited by the incoming $\hbar\Omega$ photons into an unoccupied level just above the Fermi level E_F , the process is defined as resonant (r). As in the non-resonant case, we distinguish between decays of the intermediate state where the 1s hole is filled by a valence electron (rvtc-XES) or by a core electron (rctc-XES), see Fig. 30. For resonant processes, we define the energy transfer $\hbar(\Omega - \omega)$, which represents the energy that remains in the atom [21,81]. Another way to refer to resonant-XES is resonant inelastic X-ray scattering (RIXS). For rvtc-XES the energy transfer can be only few eV, probing the energy range typical of optical spectroscopy (charge transfer and d-d transitions), but with the advantage of being element selective [83].

As described in Section 4.1, in a standard XAS experiment the transmitted photons, the total fluorescence yield (TFY) or the electron yield are monitored as a function of incident X-rays energy $\hbar\Omega$ across a selected absorption edge. In such experimental conditions, besides the limits of the X-ray optics, there is a lower limit in the FWHM of the observed features (ΔE_{TFY}), which arises from the lifetime broadening of the core hole of the investigated edge [22]:

$$\Delta E_{TFY} \approx \Gamma_{core} \equiv \hbar/\tau_{core} \quad (59)$$

where τ_{core} is the lifetime of the core hole created by the absorbed incoming photons. This limit can be overcome using the setups shown in Fig. 29 which allow measuring the fluorescence emission at a specific $\hbar\omega$ (corresponding to a particular fluorescence decay channel) while changing incident photon energy $\hbar\Omega$. This approach takes advantage of the longer core hole lifetime for decay transitions involving electrons coming from higher atomic orbitals (HL). In this way, since $\tau_{HL} \gg \tau_{core}$, the resulting XANES spectral features are characterized by an intrinsically smaller broadening [22]:

$$\Delta E_{HERFD} \approx [(\Gamma_{core})^{-2} + (\Gamma_{HL})^{-2}]^{-1/2} \quad (60)$$

This technique, known as high-energy resolution fluorescence detected (HERFD) XANES provides spectra with a higher energy resolution and sharper features [493]. Moreover, the HERFD approach allows obtaining oxidation state-specific EXAFS spectra since different oxidation states are characterized by slightly different fluorescence lines $\hbar\omega$, which can be selected using the XES spectrometer [77,487].

XES, being able to probe the occupied density of states, is highly complementary to XAS, which investigates the unoccupied density of states. An interesting example of combination of XAS and XES measurements is provided by the investigation by Eliseev *et al.* of $\text{CuX}@\text{SWCNT}$ ($X = \text{Cl}, \text{Br}, \text{I}$) nanostructures prepared by capillary filling of 1.4–1.6 nm single-walled carbon nanotubes (SWCNT) with copper halides [494]. By combining HRTEM (Fig. 31a) and Cu K-edge EXAFS data the authors highlighted that the material show a distorted two-layer hcp of halogen atoms arranged along the SWCNT and that Cu is partially coordinated to C atoms.

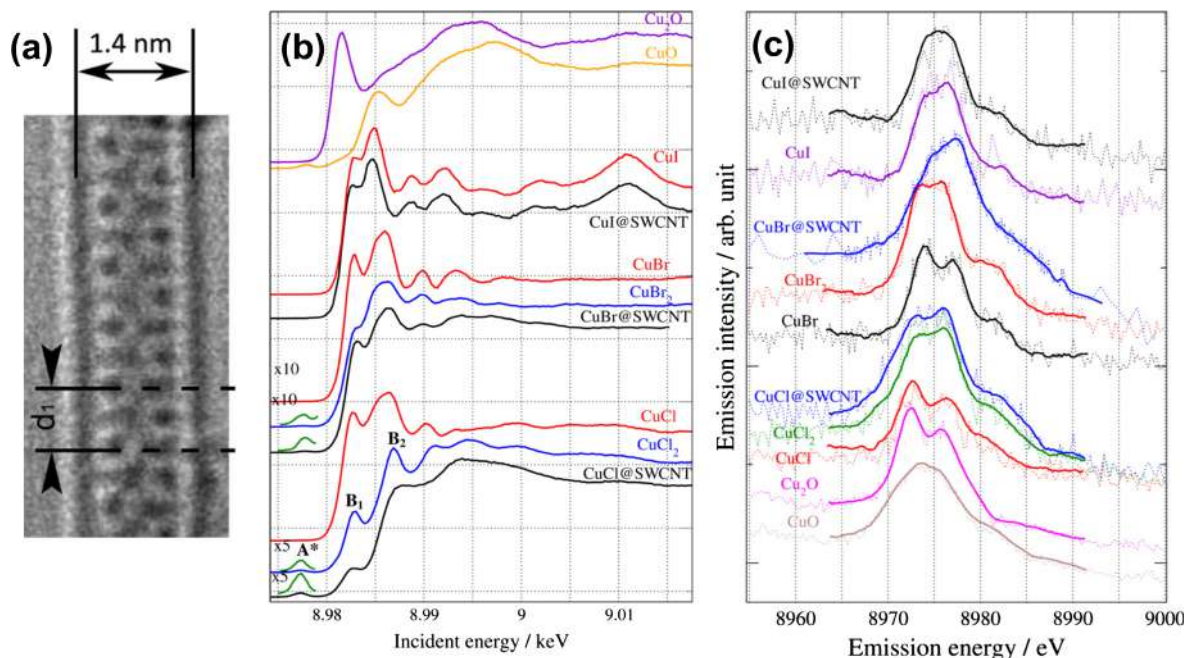


Fig. 31. (a) HRTEM image of a CuBr nanocrystal within a 1.4 nm SWCNT. (b) HERFD XANES of $\text{CuX}@\text{SWCNT}$ and reference compounds. The fluorescence emission was recorded at the maximum of the $\text{Cu } K\alpha_1$ line. (c) XES spectrum of the $\text{Cu } K\beta_5$ X-ray emission line of the $\text{CuX}@\text{SWCNT}$ and the reference compounds acquired at an incident photon energy $\hbar\Omega = 9.1$ keV. Adapted with permission from Ref. [494], Copyright Elsevier (2012).

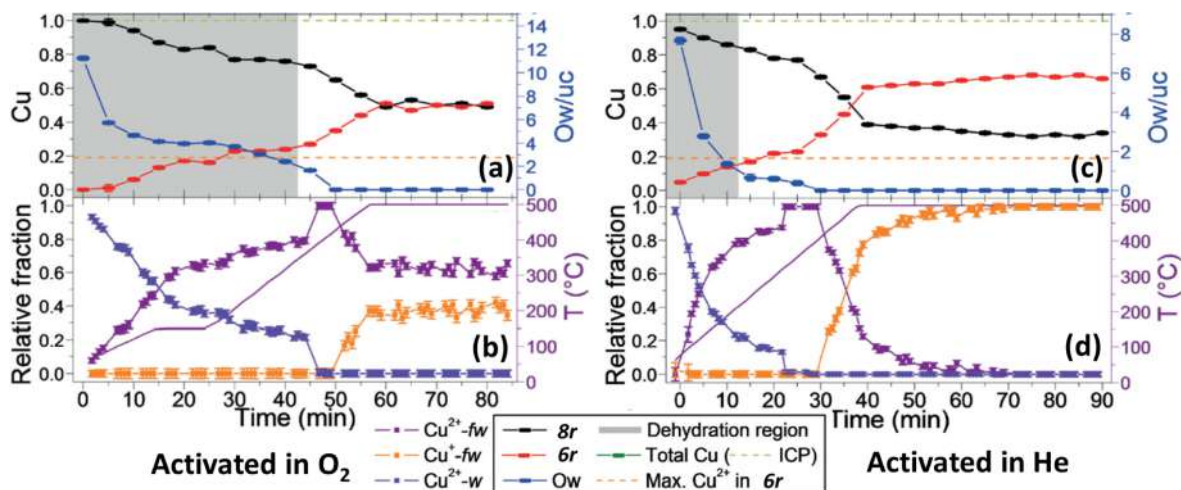


Fig. 32. (a) Evolution of the Cu occupancies in the 8r (black curve) and 6r (red curve) sites during activation in a 1:10 mixture of O₂ and He of Cu-CHA (Si/Al = 15.1; Cu/Al = 0.48) obtained from the Rietveld refinement of time-resolved XRD data. The blue curve shows the number of water molecules per unit cell optimized in the refinements (blue data). (b) Fraction of hydrated Cu(II) species (blue curve) of Cu(II) species interacting with the CHA framework (violet curve) and of Cu(I) species interacting with the CHA framework (orange data) calculated using a linear combination analysis of the XANES spectra acquired sequentially immediately after the XRD patterns. (c) As part (a) for activation in pure He. (d) As part (b) for activation in pure He. Unpublished Figure reproducing data published in ref. [501]. (For interpretation of the references to color in this figure legend, the reader is referred to the web version of this article.)

They also acquired HERFD XANES spectra (Fig. 31b) at the Cu K-edge by selecting the Cu K α_1 line emission with the XES spectrometer. These spectra show a pre-edge peak A* due to a quadrupole 1s–3d transition, ascribed to a Cu state with a partially vacant 3d orbital, and a main edge 1s–4p transition which is split into two components, B₁ and B₂. The pre-edge peak A*, whose intensity varies for different CuX@SWCNT, suggests that the bonding of one-dimensional intercalated crystals to the nanotube wall occurs via a hybridization of C 2p_z π orbitals and Cu 3d orbitals, which leads to new localized states formation. The combination of the HERFD XANES spectra with Cu K β_5 XES spectra (Fig. 31c) allowed the authors to conclude that the energy positions of these states are similar in all CuX@SWCNTs, irrespective of the halogen atom, but the density of states raises by increasing the electron affinity of the halogen atom.

4.3. Combining scattering and spectroscopy

The combination of spectroscopic and scattering techniques is a powerful tool to disclose both the short-range and long-range order in materials, able also to investigate, for instance, the evolution of the structural and electronic properties of the systems under operating conditions [495]. The simplest way to combine these techniques is to employ a sequential data acquisition procedure. An experimental setup optimized for this kind of experiments is available, for instance, at the Swiss-Norwegian beamline of the European Synchrotron Radiation Facility which is equipped with two independent monochromators, allowing a rapid (about 30 s) switch between X-ray absorption and X-ray diffraction acquisition [366,496–499]. Thus, both XAS spectra and XRD patterns (with a 2D detector) can be collected on exactly the same sample in almost the same conditions.

An emblematic example of this approach is provided by the combined XANES/XRD study of the correlation between Cu(II) self-reduction [178,500] and cation migration [501] in copper-exchanged zeolites with chabazite (CHA) topology. In particular, Andersen et al. [501] found that, after activation in oxygen, there is a migration of Cu species from the eight-membered rings (8r) into the six-membered rings (6r) site (black and red curves, respectively in Fig. 32a). This phenomenon is accompanied by a partial reduction of Cu(II) into Cu(I) (violet and orange curves in Fig. 32b). As highlighted by the independent XRD and XAS results, acquired almost simultaneously, this reduction phenomenon occurs when almost all water molecules have left the zeolite framework (see blue curves in Fig. 32a and b). The reduction of a fraction of Cu(II) into Cu(I), determined by linear combination analysis of the XANES data, is crucial to explain how, at the end of the thermal activation, copper species can occupy the 6r site with an occupancy almost twice than the maximum allowed for Cu(II) species considering the Si/Al ratio of the investigated zeolite (15.5, see gray dashed line in Fig. 32a). The same experiment activation process performed in He resulted in a more pronounced migration of copper species from the 8r to the 6r site and in a complete reduction of Cu(II) into Cu(I), which is independent from the occupied site (see Fig. 32c and d).

Another interesting example of the combination of scattering and spectroscopic techniques is provided by the study by Rønning et al. [502] of catalysts for Fischer Tropsch synthesis (FTS). They combined XRD and XAS to determine the crystallite size and the oxidation states of the active phase in a cobalt-based catalyst for FTS while monitoring methane formation by mass spectrometry. In particular, they showed that, during thermal reduction, the Co₃O₄ spinel structure of the freshly produced catalyst transforms to metastable CoO and then to metallic Co with reduced crystallite size. However, XANES data revealed that about 10% of the cobalt

remains in non-metallic phase after reduction.

More advanced approaches to combine scattering and spectroscopy include diffraction anomalous fine structure (DAFS) [119,503,504] and X-ray standing waves (XSW) [505–507].

DAFS measures the elastic Bragg reflection intensities versus photon energy. During a DAFS experiment, the X-ray energy is varied across an absorption edge to monitor the energy dependent modulation in Bragg peak intensities. The observed fine structure is similar to a conventional XAS spectrum and can be employed to obtain the same kind of information about the local environment of the absorber (i.e. bond lengths, coordination numbers, neighbor types, oxidation state), as described in Section 4.1. However, the technique combines this short-range order sensitivity, typical of XAS, with the long-range order and crystallographic sensitivity of XRD. Indeed, the obtained XAS-like spectra are site-specific and provide information on inequivalent sites of a single atomic species within the unit cell, depending on the selected Bragg reflection. One of the reasons of the limited application of this method is related to its tight experimental requirements. Indeed, a very high signal-to-noise ratio as a function of the energy is needed, as for XAS, to perform a quantitative analysis of fine structure oscillations, but this is difficult to achieve since the diffraction yield is only a very small fraction of the total one (usually few %) [503].

Also the XSW technique combines a diffraction based approach with spectroscopic measurements, providing element specific information on surface structures and molecules adsorbed on single crystal surfaces [508]. In a XSW experiment a standing wave with the periodicity of the substrate lattice is created by reflection from a single crystal. The resulting “two-beam” interference field (i.e. the interference of incident and Bragg-diffracted X-ray plane waves) induces a spatial dependence to the X-ray spectroscopic yields from atoms within the field. By monitoring the X-ray absorption of specific atomic species as a function of scattering condition within the total reflectivity range, it is possible to locate selected atoms, relative to the bulk scattering planes, not only within a crystal, but also at the surface of a crystal. XSW requires very high quality single crystals and therefore its application to nanomaterials is limited, however interesting investigations of surface processes involving nanostructures have been reported [509].

5. Scattering and spectroscopies from surfaces

5.1. Scattering from surfaces

Whenever nanomaterials are embedded in coatings or are active layers of planar devices, specific X-ray scattering techniques to study surfaces are needed.

X-rays follow the typical laws of the geometrical Optics [510]. Consider an X-ray beam (linearly polarized plane wave) travelling in vacuum or in air ($n_0 \approx 1$) and impinging on a material flat surface (described by a refractive index $n \neq 1$) with an incidence angle α_i . Incoming and reflected beams fulfill the Snell-Descartes laws:

$$\alpha_i = \alpha_f \quad (61)$$

$$\cos(\alpha_i) = n \cos(\alpha_f) \quad (62)$$

where α_i , α_f are the angles formed by the incident and reflected beams with the surface. It is worth defining the critical incident angle (α_c) which depends upon the electron density of the material layers close to the surface:

$$\alpha_c = \sqrt{2\delta} = \sqrt{\frac{r_e n_e}{\pi}} \lambda \quad (63)$$

For $\alpha_i < \alpha_c$ total reflection of the X-ray beam occurs [37,43,73,230]. The critical angle is typically a quite low value, i.e. few tenths of degrees.

5.2. Specular reflectivity

Let us consider a flat interface between vacuum (at $z > 0$) and a material with the refraction index n . The ratio of the amplitudes of the reflected and incident E -fields is the well-known Fresnel reflection coefficient. For the S and P polarizations of the primary field the coefficients read

$$r_s = \frac{\sin(\alpha_i) - n \sin(\alpha_f)}{\sin(\alpha_i) + n \sin(\alpha_f)}, \quad r_p = \frac{\sin(\alpha_f) - n \sin(\alpha_i)}{\sin(\alpha_f) + n \sin(\alpha_i)} \quad (64)$$

since, in the x-ray region $n \approx 1$ the reflection coefficients for both polarizations differ only very little and usually we can use the reflection coefficient r_s for both S and P polarizations. The reflectivity $R = |r|^2$ of a surface is therefore different from zero mainly at very small incident angles; for increasing α_i the reflectivity decreases as $(1 - n)^2/\alpha_i^4$.

This technique, called X-ray Specular Reflectivity, is used to inspect the electronic density at and just below the material surface. It allows surface investigations of thin films and coatings (layer deposition, molecular adsorption/desorption, surface oxidation, etc.).

Depending on the incident angle part of the incoming wave is reflected and part is refracted (transmitted). Precisely, when $\alpha_i < \alpha_c$, the component of the transmitted wave-vector normal to the surface becomes imaginary. The refracted wave is exponentially damped as a function of the distance below the surface, resulting in an evanescent wave travelling parallel to the surface. The penetration depth $\Lambda(\lambda, \alpha_i)$ of the X-rays can be calculated as a function of the photon wavelength (λ) and of the incident angle as [43]:

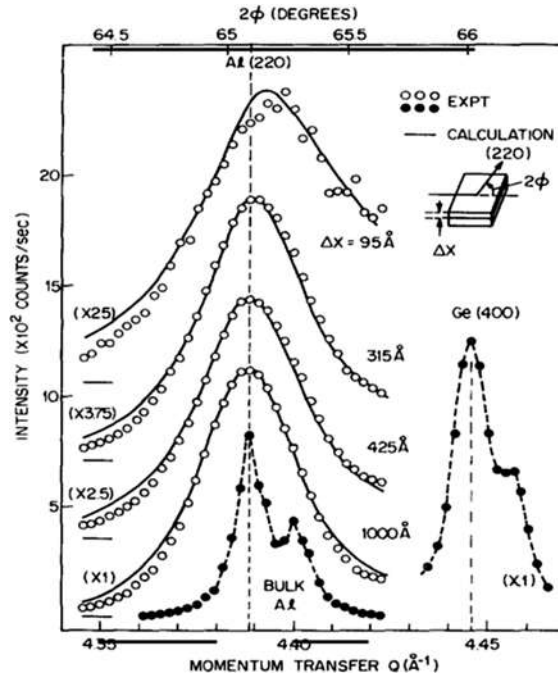


Fig. 33. Total-reflection X-ray diffraction patterns of the Al/Ge(0 0 1) interface as a function of the thickness of the Al epilayer, showing the Al (2 2 0) and Ge(4 0 0) reflections ($\alpha_i = 0.1^\circ$; both CuK α_1 and CuK α_2 lines are present in the X-ray beam). Scattered dots and full lines report the experimental data and the calculated patterns, respectively. The inset reports a scheme of the experimental scattering geometry. Reproduced with permission from Ref. [512], copyright Elsevier 1980.

$$\Lambda(\lambda, \alpha_i) = \frac{\lambda}{4\pi \text{Im}[\sqrt{\alpha_i^2 - \alpha_c^2 - 2i\beta}]} \tag{65}$$

where “Im[]” stands for imaginary part. Therefore, by varying the incident angle across the critical edge it is possible to finely tune the penetration depth of the transmitted beam below the sample surface and to probe electron density variation of objects laying at the surface or below it. This property was first exploited by Marra et al. [511] to investigate the structural details of the interface region of an epitaxial Al film grown on GaAs substrate. Successively, the same group [512] investigated the Al/Ge(0 0 1) interface finding that the lattice parameter perpendicular to the growth plane increases progressively from to accommodate the lattice mismatch of the germanium and aluminum, see Fig. 33. Authors found that the epitaxial Al layers are more disordered in proximity of the germanium substrate and found ordered domains with an average size of 32 nm, that is compatible with the average distance among misfit dislocations.

After those pioneering experiments surface scattering became a widely used technique. As a simple example, we plot in Fig. 34 the dependence of the penetration depth on the incidence angle and energy for GaAs, choosing the photon energy around the GaK and AsK

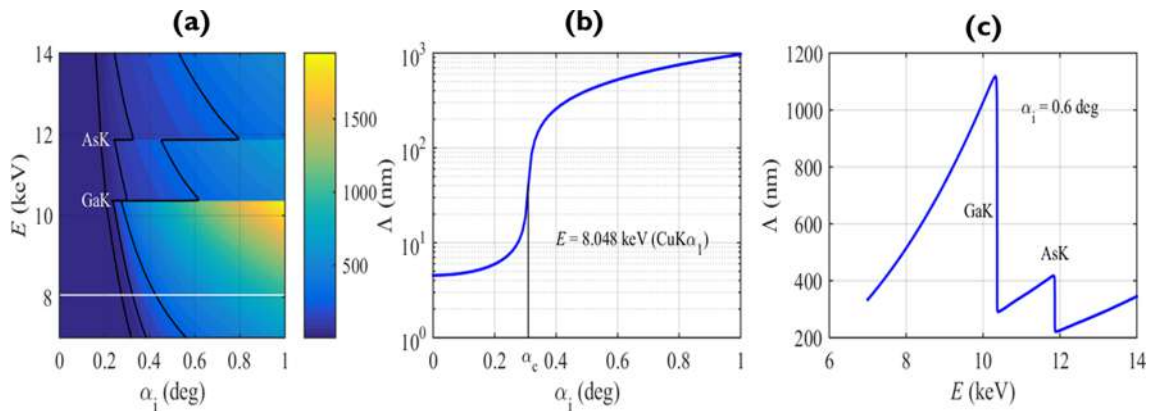


Fig. 34. The dependence of the penetration depth of x-rays on the energy and the incidence angle calculated for GaAs in the vicinity of the GaK and AsK absorption edges; see also Fig. 8 showing the energy dependence of the refraction index of GaAs.

AsK absorption edges. Outside an edge, the penetration depth exhibits a steep increase at α_c ; below the critical angle the penetration depth is only a few nm. Increasing the photon energy, the penetration depth generally increases, at an absorption edge it decreases by almost one decade. The dependence of the penetration depth on the energy follows the energy dependence of the imaginary part β of the refraction index (see Fig. 8).

X-ray Specular Reflectivity is one of the most widely used X-ray techniques to inspect electron density profile, thickness and surface/interface roughness of thin films and coatings, layers of planar devices.

This technique is also a valid choice if thin films and coatings are completely amorphous. No constraints are needed on the atomic nature of the investigated samples. When films are also nanostructured it can be combined with grazing incidence small angle X-ray scattering (GISAXS) suitable to study the morphology of objects and structures with nanometric size, laying at the surface and underneath it [37,43,513].

A typical X-ray Specular Reflectivity or GISAXS experiment is realized with an X-ray beam impinging onto the sample surface at quite small incident angle, near the critical one. The scattered wave field is registered with a 2D detector which allows collecting at the same time the components of the scattering parallel and perpendicular to the surface.

Fig. 35 describes three cases: a 10 nm C thin film coating an unstructured GaAs substrate (Fig. 35A), a multilayer made 6 repeated periods of Pt(3 nm)/Py(6 nm) onto a silicon substrate (Fig. 35B) and a surface with few nanostructures on top of it (Fig. 35C). In Fig. 35A and B X-ray Specular Reflectivity probes the electron density along the surface normal (q_z axis), which shows here only thickness fringes (Fig. 35A), due to the thin C film, or the typical structure factor of the Pt(3 nm)/Py(6 nm) unidimensional lattice (Fig. 35B). In Fig. 35C a different situation is described where the surface itself is not in the focus of the study but it is important to investigate the nanostructures on top of it. Therefore, a linear beam stopper is here inserted to obscure any direct contribution of the surface reflectivity itself ($q_y = 0$ line in the scattering q_y - q_z plane) which is by far too intense with respect to the lower scattering from the nanostructures. In this way, GISAXS data can be collected (here simply represented as two red lobes symmetrically positioned with respect to the Q_z axis) and from them morphological or structural nanoscale information of the nanostructures can be extracted (here the nanostructures are randomly organized disks, therefore the information is just morphological) [37,43,513].

A typical task of a X-ray reflection measurement is to characterize surface and interface roughness. A full description of this problem lies beyond the scope of this review; here we present only basics of the theoretical description and some characteristic results. Details can be found in specialized monographs [514,515].

The shape of a random interface is fully described by a random displacement function $u(x, y)$. We define the root-mean square (rms) roughness as $\sigma = \langle u^2 \rangle$, assuming $\langle u \rangle = 0$ and statistical homogeneity of the interface, i.e. σ does not depend on $\mathbf{x} = (x, y)$. The averaging $\langle \cdot \rangle$ in these definitions is performed over a statistical ensemble of all shapes of the interface. Usually we assume the validity of the ergodic hypothesis, i.e. the ensemble averaging can be replaced by averaging over a large interface area. We define the correlation function $\langle u(\mathbf{x})u(\mathbf{x}') \rangle$, the shape of which depends on the physical model of the interface.

In many cases the model of a random fractal is used, even if an interface is never exactly fractal-like. In this model, one assumes the scaling property

$$\langle (u(\mathbf{x}) - u(\mathbf{x}'))^2 \rangle \propto |\mathbf{x} - \mathbf{x}'|^{2H} \quad (66)$$

where $H \in (0, 1]$ is the fractal exponent, connected by the fractal (Hausdorff) dimension D as $D = 3 - H$. Within the fractal model, the roughness correlation function is assumed in the form

$$C(\mathbf{x} - \mathbf{x}') = \sigma^2 \exp \left[- \left(\frac{|\mathbf{x} - \mathbf{x}'|}{L} \right)^{2H} \right] \quad (67)$$

where L is the lateral correlation length. For distances much smaller than L the fractal scaling behavior is valid, for $|\mathbf{x} - \mathbf{x}'| \gg L$, the displacements in points \mathbf{x} and \mathbf{x}' are statistically independent.

In the case of a multilayer the description of an interface roughness is more complicated. We define the correlation matrix $C_{jk}(\mathbf{x} - \mathbf{x}') = \langle u_j(\mathbf{x})u_k(\mathbf{x}') \rangle$, $j, k = 1, \dots, N$, where the indexes run over the interfaces. The form of the correlation matrix depends on the physical model. In the frequently used model by D. G. Stearns [516] that the random displacement function of an interface j can be written as a superposition of two terms, one is the component of the roughness “inherited” from the interface $j-1$ below and the other is the “intrinsic” roughness $h_j(\mathbf{x})$ added to the system during the growth of the layer between the interfaces $j-1$ and j :

$$u_j(\mathbf{x}) = u_{j-1}(\mathbf{x}) \otimes a_j(\mathbf{x}) + h_j(\mathbf{x}) \quad (68)$$

here we denoted \otimes convolution and $a_j(\mathbf{x})$ is the inheritance function. From Eq. (64) explicit (albeit quite cumbersome) expression can be found for the matrix C_{jk} [515].

Several approaches can be found for the description of x-ray scattering from rough systems. Usually one assumes that the measured signal is averaged over the statistical ensemble mentioned above. Then, the averaged scattered intensity can be divided into the “coherent” and “diffuse” components

$$I(\mathbf{r}) \equiv \Gamma(\mathbf{r}, \mathbf{r}) = \langle |E(\mathbf{r})|^2 \rangle = \langle |E(\mathbf{r})|^2 \rangle + \langle |E(\mathbf{r}) - \langle E(\mathbf{r}) \rangle|^2 \rangle \quad (69)$$

For the coherent component, usually the approach by Névot and Croce is used [517]. Using this method, the coherent reflectivity of a single rough surface is

$$\mathcal{R}_{\text{coh}} = \mathcal{R}_{\text{flat}} |e^{-2\sigma^2 k_z^{(1)} k_z^{(2)}}|^2 \quad (70)$$

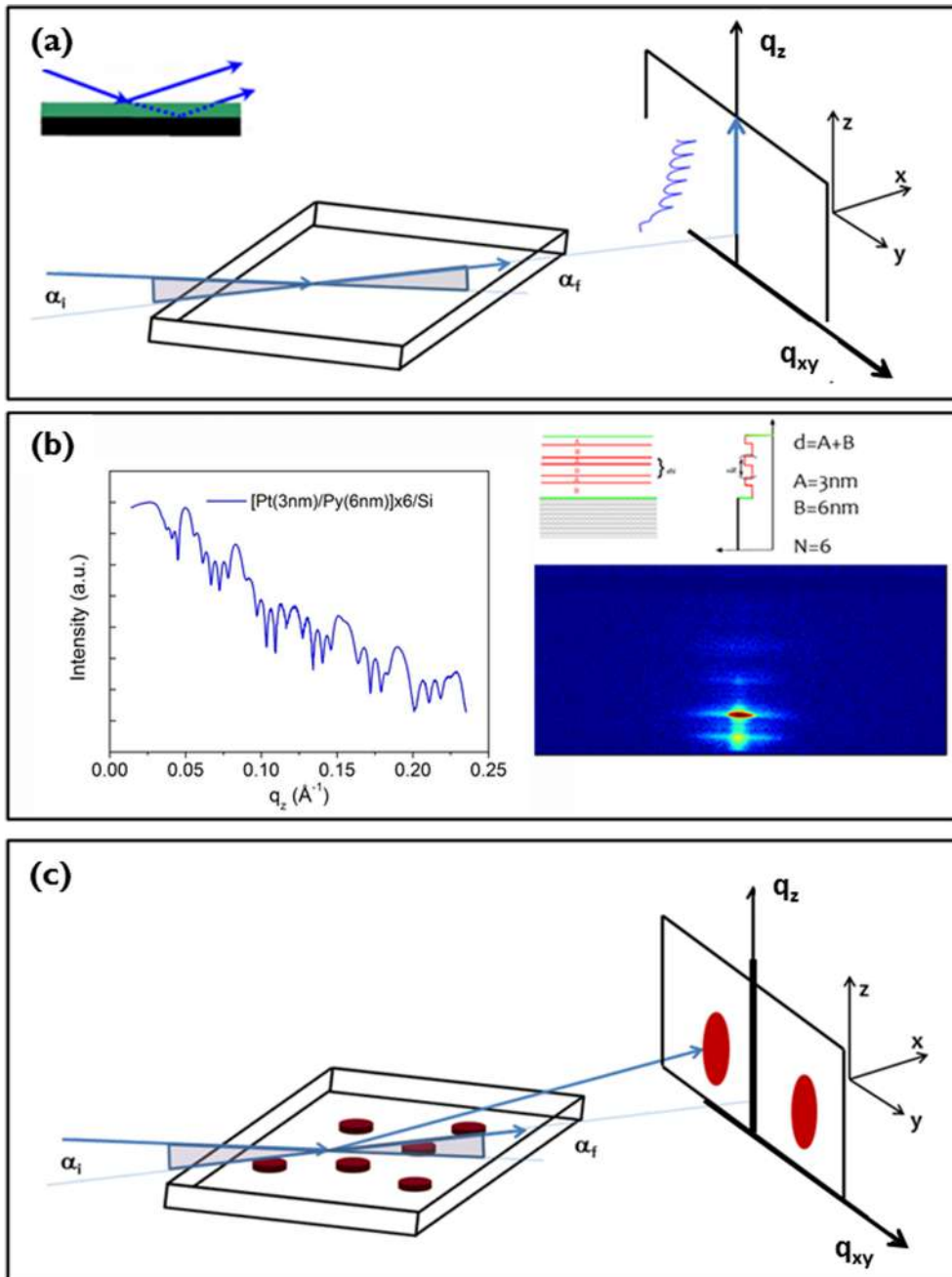


Fig. 35. (a) Main Part: schematic representation of the GISAXS experimental set-up. X-rays impinges with an incident angle α_i on a planar sample; the scattered beam exits at an angle α_f and is collected with a 2D detector perpendicular to the sample surface. Top left corner: unstructured GaAs substrate (black) with a 10 nm C thin film on top of it (green). Blue arrows represent the incoming and the scattered X-ray beams. The penetration depth of the beam is also reported; (b) Top right: scheme of a multilayer made 6 repeated periods of Pt(3 nm)/Py(6 nm) onto a silicon substrate; bottom right: diffracted signal collected on the 2D detector (q_y - q_z plane); left: corresponding signal obtained integrating the image over q_y (courtesy of Marcio Medeiros Soares –XRD2 beamline – LNLS, Campinas); (c) a surface with few nanostructures on top of it. The bold bare on the 2D detector represent the linear beam stopper used to obscure line at $q_y = 0$ in the scattering q_y - q_z plane. (For interpretation of the references to color in this figure legend, the reader is referred to the web version of this article.)

where $\mathcal{R}_{\text{flat}} = |r|^2$ is the reflectivity of a flat surface, $k_z^{(1,2)}$ are the perpendicular components of the wave vectors above and below the interface. From this formula, it follows that if the absorption in the material is negligible, below the critical angle α_c the component $k_z^{(2)}$ is purely imaginary and $\mathcal{R}_{\text{coh}} = \mathcal{R}_{\text{flat}}$. Therefore, within the approximation of Névot and Croce, the coherent reflectivity below the critical angle is not damped by roughness. The same approximation can be used for multilayers, the details can be found in the

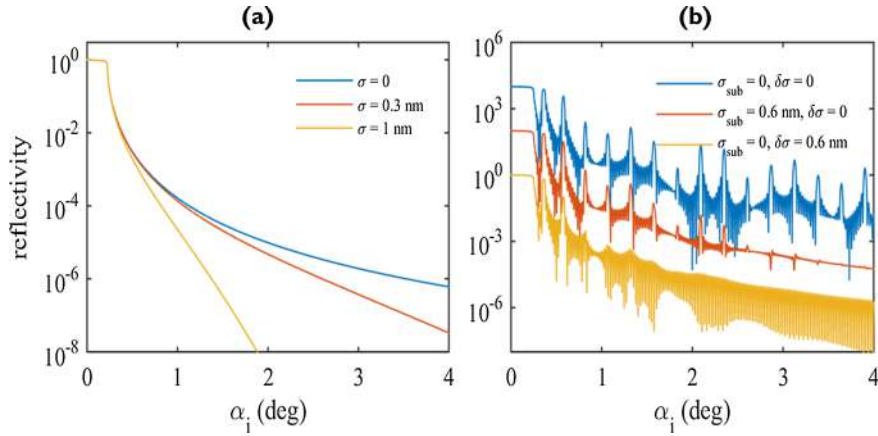


Fig. 36. Coherent reflectivity curves of a single Si surface (a) and SiGe periodic multilayer (b) calculated for various rms roughnesses. See the text for the details, the curves in the right panel are shifted vertically for clarity.

literature cited above.

As a simple illustration, we present in Fig. 36 reflectivity curves of a single Si rough surface and of a SiGe multilayer with rough interfaces.

In the case of a single surface, the tail of the reflectivity curve (left panel) is much suppressed, while the plateau below the critical angle is almost unaffected by the roughness. For a multilayer example we consider a [Si(12 nm)/Ge(5 nm)] \times 10 periodic multilayer on a Si substrate. The periodicity of the multilayer structure gives rise to satellite maxima, the position of which can be deduced from the Bragg's law of the one-dimensional "crystal" representing the multilayer:

$$2D\sqrt{n^2 - \cos^2(\alpha_i)} = p\lambda \quad (71)$$

where D is the multilayer period, n is the mean index of refraction of the multilayer structure and p is the order of the satellite maxima. The rms roughnesses of individual interfaces obey the formula $\sigma_j = \sqrt{(\sigma_{j-1})^2 + (\delta\sigma)^2}$, which follows from the Stearns model in Eq. (64) (j is the interface index), the rms roughness of the substrate is $\sigma_{\text{sub}} \equiv \sigma_0$. The incremental roughness $\delta\sigma$ affects the visibility of the satellite maxima much more than the substrate roughness.

The diffuse part of the scattered intensity is determined by the correlation properties of the interface roughness and is usually calculated by the distorted-wave Born approximation (DWBA), as described extensively elsewhere [515].

Here we present only one numerical example in Fig. 37 showing the reciprocal space maps of diffusely scattered intensity from the same [Si(12 nm)/Ge(5 nm)] \times 10 periodic multilayer. In the simulation we used the GISAXS scattering geometry keeping the incidence angle constant $\alpha_i = 0.3\text{deg}$. In panel (a) we assumed completely non-correlated roughness profiles, i.e. the inheritance

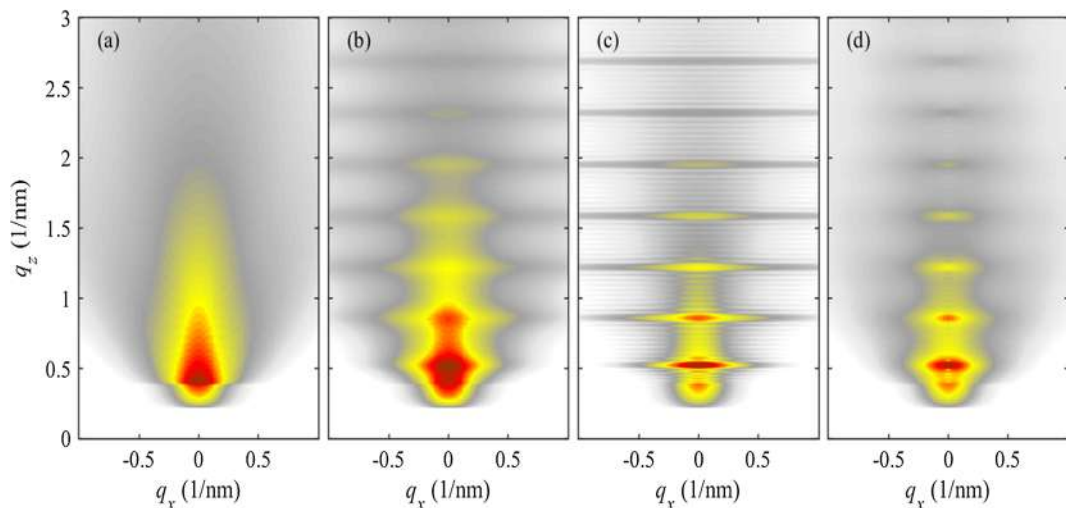


Fig. 37. Reciprocal-space distribution of the intensity diffusely scattered from a SiGe periodic multilayer, calculated for 4 various roughness models and assuming the GISAXS scattering geometry: (a) non-correlated roughness profiles with the inheritance functions placed equal to zero; (b) Gaussian shape of the inheritance function with width of 50 nm; (c) interfaces microscopically identical; (d) the degree of vertical roughness correlation depends on according to Eq. (72). See the text for details.

functions a_j defined in Eq. (25) were zero. In this case, the waves scattered from individual interfaces do not interfere and the reciprocal-space image is just similar to that from a single rough surface. In panel (c) we took $a_j(\mathbf{x}) = \delta^{(2)}(\mathbf{x})$, $h_j(\mathbf{x}) = 0$, i.e. the interfaces were microscopically identical. Then, the waves diffusely scattered from different interfaces have constant phase differences so that they interfere giving rise to a typical pattern of horizontal sheets. Panel (b) represents the intermediate case, in which we assumed a Gaussian shape of the inheritance function with the width of 50 nm.

The intensity sheets contain valuable information on the roughness correlation properties; the width of the sheet along q_x is inversely proportional to the lateral correlation length L , while its thickness along q_z is inversely proportional to the vertical correlation length L_v , i.e. the maximum vertical distance between the interfaces in the multilayer, where the roughness profiles are statistically correlated.

From the theory of multilayer growth [518] it follows that the degree of correlation of the roughness profiles at different interfaces in a multilayer depends on the space frequency of the roughness. In other words, the short-wave components of the roughness of an interface are less inherited at the interfaces close to the multilayer surface, than long-wave bumps. This fact can be taken into account assuming a special form of the Fourier transformation of the correlation matrix:

$$C_{jk}^{(FT)}(\mathbf{q}_{\parallel}) \sim \exp(-|\mathbf{q}_{\parallel}|^{\zeta} |z_j - z_k|) \quad (72)$$

Here we denoted $\mathbf{q}_{\parallel} = (q_x, q_y)$, z_j, z_k are the vertical coordinates of the interfaces j and k , and the exponent ζ depends on the growth mechanism [519]. The results of this model are demonstrated in Fig. 37d, where we put $\zeta = 1$. Since the roughness components with larger $|\mathbf{q}_{\parallel}|$ are less vertically correlated, the vertical width of the sheets increases with $|\mathbf{q}_{\parallel}|$. In experimental data, this increase can be used for investigating the mechanisms of the roughening and/or smoothing during the multilayer deposition.

5.3. Grazing incidence small angle X-Ray scattering

A GISAXS pattern may contain morphological and structural information of the objects laying on a planar surface or below it. In the case of diluted and randomly organized objects, the GISAXS pattern shows diffraction fringes due to the form factor of the objects, namely shape and size of the objects. If the objects are arranged into a periodic 2D or 3D assembly structural information is also encoded in the GISAXS pattern, i.e. the positions and symmetry of the objects can be determined. In case of correlated objects, the description of the GISAXS pattern needs also an interference function term accounting for the mutual position of the nano-objects into a 2D or 3D lattice [520,521].

The correct description of the scattering is realized by means of the Distorted Wave Born Approximation (DWBA) [522], as the sum of four terms accounting for: the direct scattering from the particle (as in the kinematic Born approximation), the reflection from the substrate surface followed by scattering by the particle (and *vice versa*), the reflection from the substrate surface followed by scattering by the particle and subsequent further reflection from the substrate. In the case of a perfectly diluted system (uncorrelated particles) the Decoupling Approximation (DA) holds, while for fully correlated objects the Local Monodisperse Approximation (LMA) is preferred. LMA is valid for a particle collection made of monodisperse domains whose size is larger than the coherence length of the X-ray beam.

As already said for SAXS, for systems of correlated particles, the intensity pattern is given by two contributions: the form factor and the interference factor. It is a good criterion, before fitting the entire pattern, to study the asymptotic behavior of the scattering (high scattering vectors) to determine the shape contribution only (especially for extremely mono-dispersed objects). Indeed, the intensity at high scattering vectors changes as the square of the form factor which depends on q^{-n} , with $n = 1$ for rod-like, $n = 2$ lamellar, $n = 4$ sphere [37,43,513].

Table 2 shows the GISAXS patterns computed for the case of: a diluted system of uncorrelated nanoparticles of different shapes (sphere, hollow sphere, cylinder and disk), where only the form factor is taken into account in the DWBA calculation; a 2D lattice of the same particles, with L_1 and L_2 as interparticle spacings, where the form and lattice contributions to the scattering are taken into account.

It is worth clarifying that the physical origin of the fringes in X-ray Specular Reflectivity and in SAXS or GISAXS scattering pattern, in case of form factor only, is the same. This is due to the electron density contrast between the scattering particles (or thin film) and the matrix embedding them (or substrate).

5.4. Periodically assembled nanocrystals

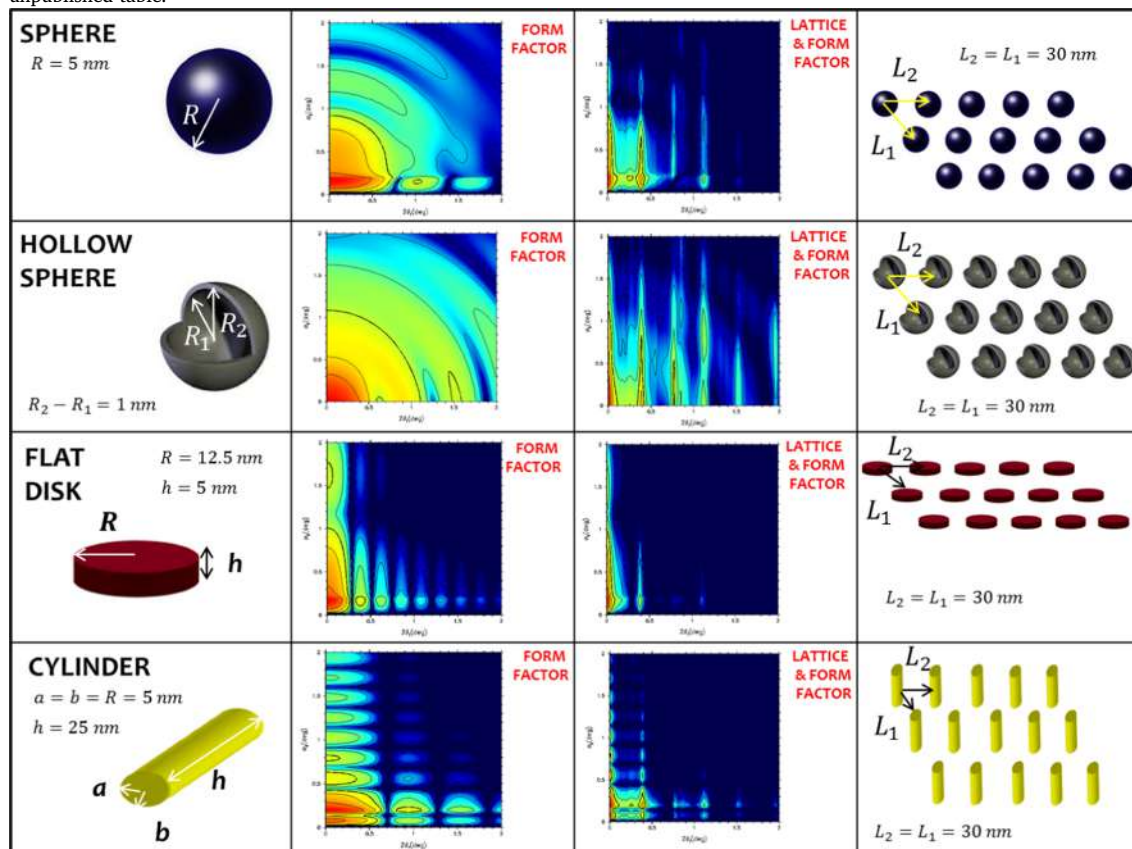
The following experiments on periodically 2D and 3D assembled nanocrystals were performed with the same laboratory (GI) SAXS/(GI)WAXS set-up of the XMI-L@b [287], benefiting of a high-brilliance synchrotron-class table top micro-source. GISAXS data were collected with a multi-wire detector. GIWAXS data were collected with an image plate detector. The distance sample-detector, and thus the covered q -region, was set depending on the specific sample to study.

5.4.1. 2D assemblies

Fig. 38A shows the Scanning Electron Microscopy (SEM) images of Au nanoparticles (NP) drop casted onto two different substrates: the silicon substrate with only the native SiO_2 oxide (Si/ SiO_2) and the teflon-modified silicon substrate (Si/TL+), with a thin teflon-like coating deposited via a cold plasma process. The GISAXS measurements and relative simulations prove that Au NP self-assembly in a 2D lattice with hexagonal symmetry. Fingerprint of the 2D assembly is the presence of vertical stripes in the diffraction

Table 2

List of GISAXS 2D simulated data: form factor only (2nd column) or form factor & lattice factor (3rd column) for relevant shapes (full sphere, hollow sphere, cylinder and flat disk); the lattice contribution is needed for nano-objects organized into 2D lattices (last column of the Table). Previously unpublished table.



pattern. Indeed, the Fourier Transform of a planar periodic array of objects is a pattern made by a periodic array of lines. Data also showed that the lateral extension of the lattice improves for the Si/TL+ substrate with respect to the Si/SiO₂, confirming scanning electron microscopy observations [523].

Fig. 38B shows the SEM image of a 2D lattice of octapod-shaped CdSe/CdS nanocrystals self-assembled on top of a silicon substrate. The inset is the TEM image of a single octapod, having a tip-to-tip mean pod length $2l = 87 \pm 2 \text{ nm}$ and a mean pod width $D = 12 \pm 2 \text{ nm}$. GISAXS data contain information on the nanocrystal shape and interference lattice. Indeed, the presence of a 2D array of nano-objects is clearly encoded in the vertical stripes measured in the data [524].

5.4.2. 3D assemblies

In the previous examples the arrangement of the nanocrystals in 2D arrays is encoded in the vertical sheets which can be clearly identified in the diffraction frame. Here, the organization of the nanocrystals according to a 3D lattice can be deduced by the 3D diffraction spots measured in the reciprocal space, localized according to specific symmetry rules.

Fig. 39A shows oxide spherical nanocrystals assembled in a 0.5 T magnetic field in several well-separated, distinct 3D islands with conic shape protruding outward the substrate surface. Collection and analysis of the GISAXS patterns allowed us to describe the actual face centered cubic (f.c.c.) symmetry of the 111-oriented nanocrystalline lattice, along with a lattice distortion with respect to a perfect f.c.c. crystal [525]. GISAXS analysis was the only technique able to determine the exact crystallographic symmetry of these 3D mesoscopic superlattices.

In Fig. 39B PbS quantum dots (QDs), synthesized with high control on size and size distribution, were used as building blocks for fabricating solid crystals by solvent evaporation. The spherical PbS QDs were found to self-assemble in several domains by electron microscopy. These domains form 111-oriented f.c.c. ordered 3D nanocrystalline lattices, as revealed by indexing of the GISAXS pattern. Cuts taken along the arrows, marked in the 2D GIWAXS map with relevant colors, are also displayed separately: in plane (black curve), out of plane (green curve) and at 45° (red curve). The cuts reveal that the PbS QDs are nano-sized crystals in the rock-salt phase. Furthermore, comparing the FWHM of the (111) and (220) peaks, the (220) planes appear slightly preferentially oriented parallel to the substrate which means that the QD superlattice is 111-oriented and its QD building blocks are 110-preferentially oriented [526]. Combination of GIWAXS and GISAXS allowed us to describe the 3D superlattice as an ensemble (GISAXS) but also to

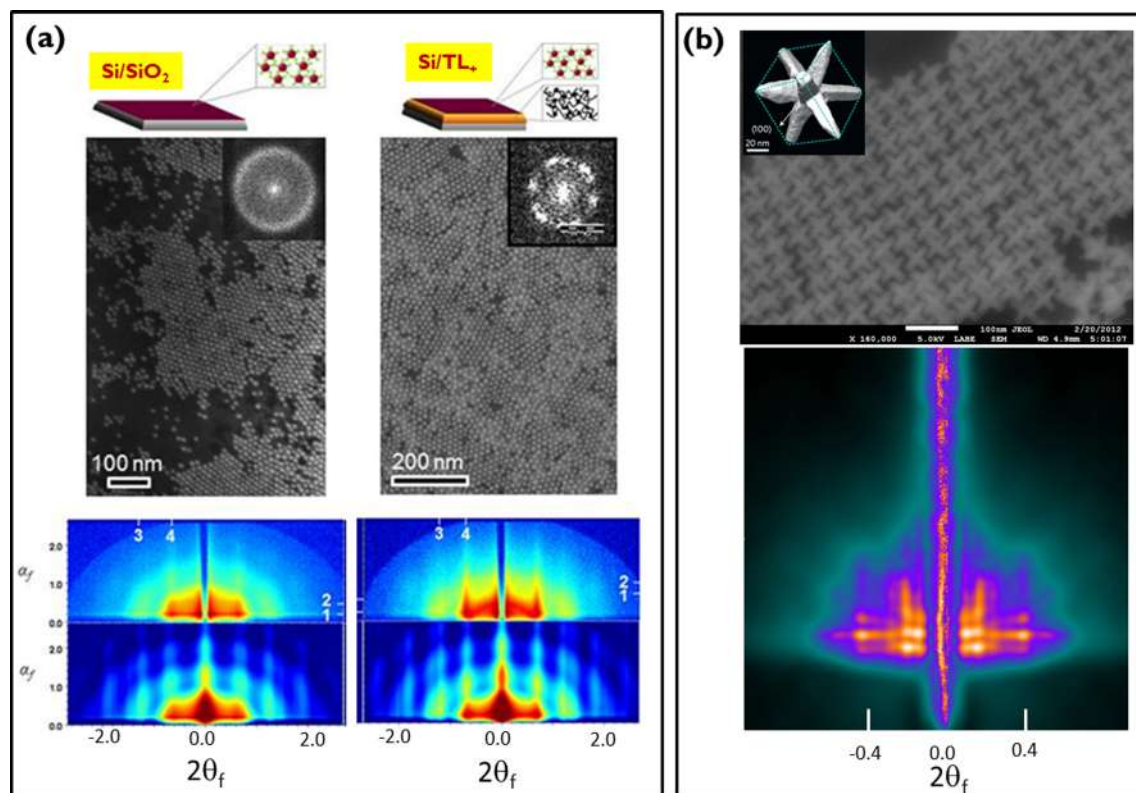


Fig. 38. (a) SEM images of Au self-assembled nanoparticles (NP) drop casted onto SiO₂ oxide/silicon substrate (Si/SiO₂) and on teflon-modified silicon substrate (Si/TL+), along with GISAXS measurements and relative simulations, reprinted with permission from Ref. [523]; (b) SEM image of octapod-shaped CdSe/CdS nanocrystals self-assembled on top of a silicon substrate. The inset is the TEM image of a single octapod. GISAXS data contain information on the nanocrystal shape and interference lattice (vertical stripes), reprinted with permission from Ref. [524], copyright International Union of Crystallography, 2012.

inspect the order of its QD build blocks (GIWAXS).

In the following we show an example of the application of the GISAXS method for the investigation of weakly ordered nanoparticles in multilayers. We consider Co/SiO₂ multilayers deposited on SiO₂ substrates by magnetron sputtering [527]. During a post-growth annealing originally amorphous Co layers crystallize creating weakly ordered crystalline Co nanoparticles. The multilayers have been investigated by x-ray diffraction, GISAXS, x-ray standing-wave method, high-resolution transmission electron microscopy (HRTEM) as well as by time-of-flight elastic recoil detection analysis (ToF ERDA); here we show only the GISAXS and TEM results. Fig. 40 presents HRTEM images of a Co/SiO₂ multilayer before (a) and after (b) annealing.

In Fig. 41a we display a GISAXS reciprocal space map of an annealed sample. The correlation of the positions of the Co nanoparticles both in one layer and in different layers in the multilayer gives rise to two columns of satellite maxima at $Q_y \approx \pm 0.6 \text{ nm}^{-1}$ (denoted by the white arrow). In addition, horizontal intensity sheets are visible (marked by horizontal white dashed lines). For the explanation of these sheets we assume that the Co crystalline nanoparticles are embedded in Co-containing SiO₂(Co) amorphous layers, the Co atoms in these layers are dissolved and they did not coalesce in the Co particles. The SiO₂(Co) layers contain crystalline Co particles and they are divided by layers of pure amorphous SiO₂. The horizontal intensity sheets are caused by vertically correlated roughness profiles of the SiO₂(Co)/SiO₂ interfaces. In addition, in the measured map we can resolve very thin horizontal lines (denoted by white dotted line). These lines can be explained by a dynamical effect caused by the periodicity of the Co/SiO₂ multilayer. If the incidence and/or exit angles of x-rays fulfill the one-dimensional Bragg condition in Eq. (28), the interference of the transmitted and specularly reflected wave-fields gives rise to a standing wave pattern, the period of which equals the multilayer period D . This standing wave is then diffusely scattered by the interface roughness. The dynamical effect can be described within the DWBA approximation [528] and it can be used for exact determination of the incidence angle. Fig. 41b explains the geometry of this effect.

In Fig. 42 we compare the GISAXS map as well as the line scans extracted from the map with simulations. From the comparison we determined the mean size of the Co particles, their mean distances as well as the degree of correlation of the particle positions.

5.5. Surface sensitive XAS experiments

As discussed in Section 4, due to the relatively large penetration depth of hard X-rays [22,73], EXAFS and XANES spectroscopies

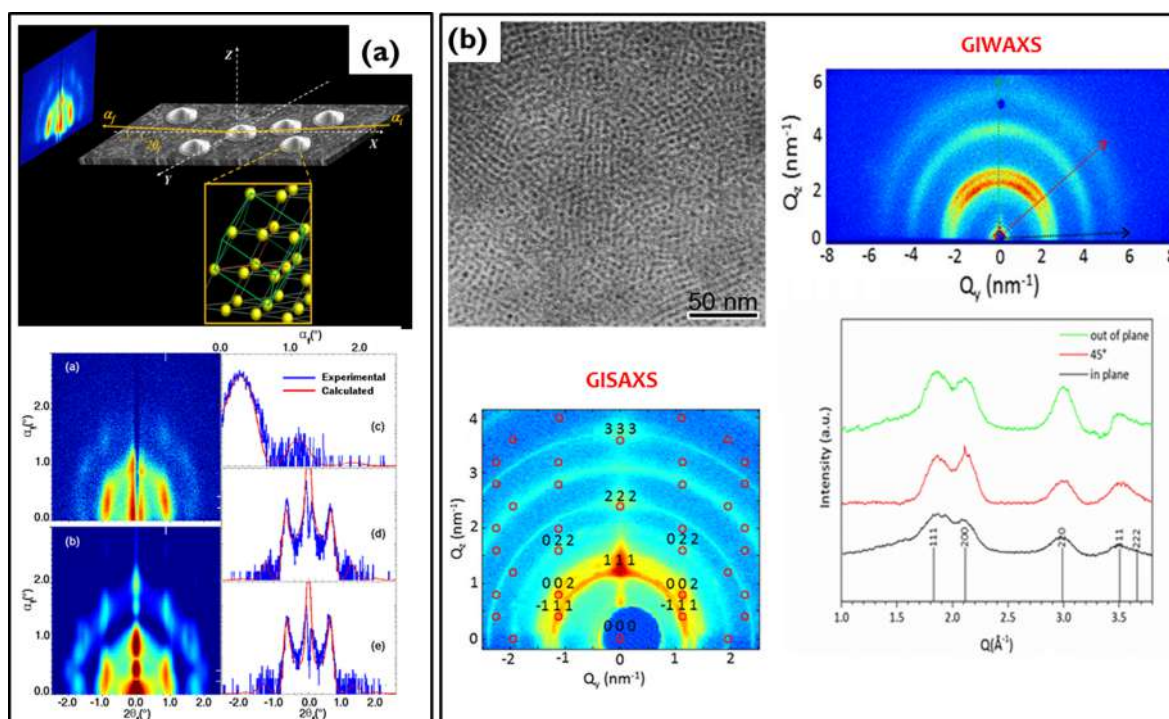


Fig. 39. (a) Iron oxide spherical nanocrystals assembled in magnetic field into 3D islands with conic shape and corresponding GISAXS patterns and simulations, reprinted with permission from Ref. [526]; (b) SEM image of the QD superlattice, GISAXS data of the spherical PbS QDs self-assembled in 111-oriented f.c.c. ordered 3D; GIWAXS 2D pattern and cuts taken along the arrow: in plane (black curve), out of plane (green curve) and at 45° (red curve) and printed separately to compare the profiles, reprinted with permission from Ref. [526], Copyright Royal Society of Chemistry, 2014 213 (<http://pubs.rsc.org/en/Content/ArticleLanding/2014/CE/c4ce01291g>). (For interpretation of the references to color in this figure legend, the reader is referred to the web version of this article.)

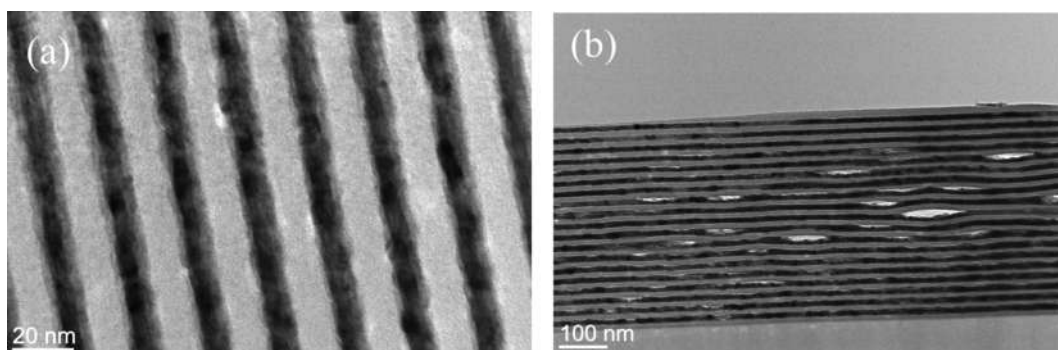


Fig. 40. Cross section transmission electron micrographs of a Co/SiO₂ multilayer (a) before and (b) after annealing. In (a) the Co-containing layers (dark) are inhomogeneous across their thickness and (b) reveals the presence of large empty voids in the annealed sample. Reproduced with permission from Ref. [527] copyright International Union of Crystallography, 2013.

are a bulk-sensitive techniques, that are intrinsically inadequate to determine the arrangement of atoms in the first 1–3 monolayers at the surface region of condensed matter, that is the key point in the understanding of surface phenomena such as surface science, interface physics/chemistry/electrochemistry, molecular adsorption and reactivity, catalysis, crystal growth, corrosion, erosion ... etc.

To avoid the contribution of the bulk atoms to the overall XAS spectrum, the experiment cannot be performed in transmission mode and should be conceived to collect only the signal coming from the surface. This request can be achieved either by working in electron yield mode or by working with an incidence angle α_i close to the critical one (α_c), see Eq. (63). In the former case, a large fraction of atoms, both at the surface and in the bulk, are involved in the X-ray absorption process, but the Auger electrons emitted by subsurface atoms will not reach the surface and thus will not be detected. The technique requires ultra-high vacuum conditions and is named surface EXAFS (SEXAFS) and will be described in Section 5.5.1. SEXAFS is particularly suited to understand the structure of molecules and atoms adsorbed on surfaces [322]. In the latter case the X-ray beam will penetrate only few monolayers from the

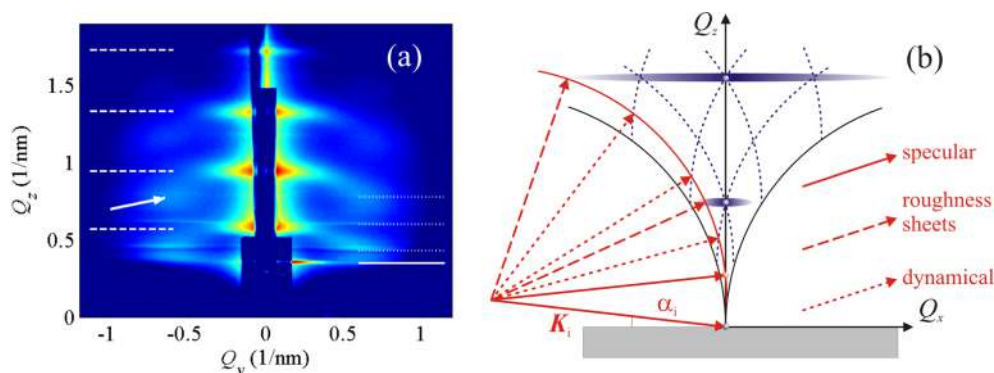


Fig. 41. Measured GISAXS map of an annealed Co/SiO₂ multilayer, with specular, roughness and dynamical sheets denoted by full, dashed and dotted lines, respectively. The arrow highlights the correlation. (b) Sketch of the GISAXS scattering geometry with specular maxima, roughness sheets and dynamical scattering maxima indicated. Reproduced with permission from Ref. [527], copyright International Union of Crystallography, 2013.

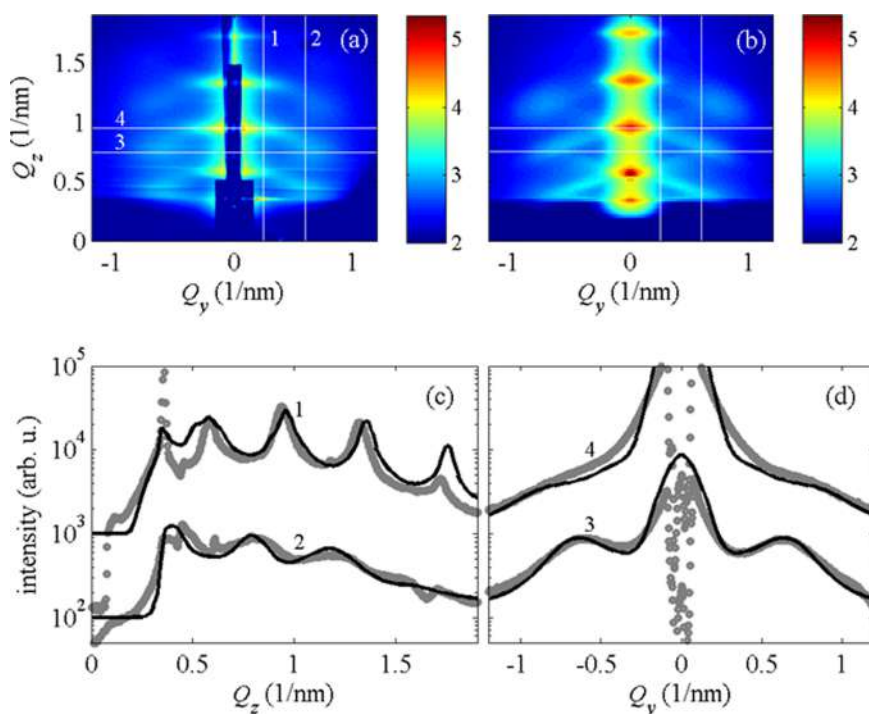


Fig. 42. Measured (a) and simulated (b) GISAXS map of the annealed Co/SiO₂ multilayer. In panels (c) and (d) the measured (points) and fitted (lines) vertical (c) and horizontal (d) scans are compared. The numbers 1–4 denote the trajectories in reciprocal space along which the measured data have been extracted; the trajectories are indicated in panels (a) and (b) by white lines. The color bars in panels (a) and (b) indicate the values of the logarithm (\log_{10}) of the intensity. Reproduced with permission from Ref. [527], copyright International Union of Crystallography, 2013.

surface (see Sections 5.1 and 5.2) guaranteeing that only surface atoms will be involved in the X-ray absorption process and thus in the measured XAS signal. This technique is referred as reflection EXAFS or Refl-EXAFS, requires quite long (some cm) samples and will be described in Section 5.5.2. Refl-EXAFS well adapts to the investigation of thin films, epitaxial layers, buried interfaces [119]. Obviously, the two set-ups may be used simultaneously, combining Auger-detection and reflection geometry [322,529]. In the literature some ReflEXAFS studies are also referred to SEXAFS.

A third way to get surface sensitivity is to take benefit of the elemental selectivity of the XAS technique. This approach is applicable in case the selected element is not present in the bulk. In case of thin films or of few ML adsorbed on a single crystal surface, a glancing angle geometry is still preferable to increase the surface illuminated by the X-ray beam (and so the signal) and to reduce the X-ray fluorescence emitted by the bulk atoms that increases the background and the deadtime of the solid-state fluorescence detectors. Glancing angle geometry will also allow to take benefit of the polarization of the X-ray emitted by synchrotrons and discriminate between in plane and out of plane bond-lengths [119]. In case of chemical species adsorbed or grafted on

polycrystalline materials, typically oxide or metal nanoparticles supported on high surface area oxides or carbons [72,131,530–535], then the sample can be prepared in form of a self-supported pellet containing a large number of polycrystals and the experiment can be performed in transmission mode as the surface sensitivity is assured by the fact that the selected element is present at the surface of the polycrystals only. Finally, standard transmission experiments can also be performed on microporous materials like zeolites [536–544] or metal-organic frameworks (MOFs) [545–547], where, due to the presence of internal surfaces, almost all atoms can be considered as surface atoms [548–551].

With respect to the surface-sensitive X-ray diffraction techniques here discussed above in Sections 5.1–5.4, surface sensitive XAS techniques has been particularly informative in cases where surface species do not exhibit long range order, as detailed in the next subsections. In this regard, low energy electron diffraction (LEED) technique, originally developed by Davisson and Germer [552], is intermediate between surface X-ray diffraction methods and surface XAS, being the LEED coherence length around about 10 nm [553] and has been widely used as surface structural determination tool [554,555].

5.5.1. Auger-detected surface EXAFS (SEXAFS)

Just five years after the publication of the milestone paper of Sayers, Stern and Lytle [237], a way to overcome the bulk sensitivity of XAS techniques was suggested independently by Lee [556] and by Landman and Adams [553] who proposed a variation of the EXAFS method consisting in the detection of the element specific Auger electrons along a scan of the incident photon flux across the K-, or L-, edge of the same element. The measured electron yield is proportional to the primary X-ray absorption process [21,75,160,314], so the signal is consistent with a standard EXAFS (or XANES) spectrum, see Eq. (50), but the surface sensitivity of the total process is guaranteed by the short escape length (typically below 2 nm [343,557,558]) of selected Auger electrons. Two years after this suggestion [553,556], Citrin, Eisenberger and Hewitt [559] investigated with SEXAFS the structure of I atoms on the surface of Ag(1 1 1) crystal at different iodine coverage θ (1/3 and 1–2 monolayers). They collected the intensity of the I ($L_{3, M_{4,5}, M_{4,5}}$) Auger line as a function of the photon energy scanned around the I(L_{3}) edge (Fig. 43). They found that the I-Ag distance of the surface I/Ag(1 1 1) system is stretched by $+ 0.07 \pm 0.03 \text{ \AA}$ with respect to that in the bulk AgI model compound (2.87 vs. 2.80 \AA) [559].

One year later, Bianconi and Bachrach reported the first SEXAFS study of the Al(1 1 1) surface showing that the interplanar distance of the first two layers is contracted by $-0.19 \pm 0.06 \text{ \AA}$ with respect to the bulk interplanar distance [560]; Citrin et al. extended the study of iodine adsorbed on metal surfaces investigating the I/Cu(1 1 0) [561] and I/Cu(1 1 1) and I/Cu(1 0 0) [562] interfaces. Since then, several experiments were successfully performed and SEXAFS became a complementary technique for the structural determination of surfaces and of adsorbates on surfaces [314,322,563–579].

5.5.2. Reflection EXAFS (ReflEXAFS)

An alternative way to induce surface sensitivity to the XAS technique is to limit the penetration depth of the incoming X-ray beam by working in glancing angle geometry. As discussed in Sections 5.1 and 5.2, once the energy of the photon has been fixed, the penetration depth of the X-ray beam $\Lambda(\lambda, \alpha_i)$ depends on the incidence angle α_i see Eq. (65). Changing α_i in proximity of the critical angle, is a tool to tune the penetration of the X-ray beam and consequently the sensitivity of the corresponding XAS study. In this acquisition configuration, the data collection can eventually also be also performed in fluorescence mode because the origin of the decay process is no longer responsible of the depth-sensitivity of the process.

The phenomenon was first reported by Parrat in the '50s [247], who observed that the analysis of the intensity of the reflected X-ray as a function of incidence angle α_i , across the critical angle α_c , provides insights on the structural properties of the material in the one to several tens of nm from the surface. He used the dispersion theory (see Eq. (9)) to interpret the observed reflectivity curves of Cu evaporated on a glass founding that the material was oxidized down to about 15 nm from the surface. After the understanding of the EXAFS phenomenon [237] the technique is named Refl-EXAFS and has been widely used to characterize the structure of surface species, thin films, epitaxial layers, buried interfaces, Langmuir Blodgett films etc... [505,529,580–603].

6. Microscopes

Atoms in matter are located at distances of the order of a few \AA . Since human eyes can distinguish objects that are separated by at least 0.1 mm, i.e. 10^6 \AA , a row of one million atoms will be perceived as a single point by naked eyes. As a consequence, a microscope is needed to observe the atomic structure of matter. The resolving power of a microscope, which describes its ability to image matter at different length scales, mainly depends on the contrast mechanism. In a typical microscope the sample is mounted on a stage with motorized movements for its precise positioning and rotation, as well as to adjust the magnification of the imaging system. The detector registers the intensity distribution scattered by the sample and returns a direct or indirect (diffraction) image of the sample.

Fig. 44A shows the pictorial view of a cell nucleus under a microscope. When increasing the magnification, it is possible to appreciate smaller details of the nucleus, such as the chromosome in Fig. 44B. By further increasing the magnification, and depending on the resolving power of the microscope, the enlarged image could lose the finer details (Fig. 44C) or disclose the internal chromosome structure (Fig. 44D), alias the DNA filament. Every microscope has a range of possible magnifications. It can reach an ultimate resolution which corresponds to the shortest distance between two points of the object distinguishable as separate entities.

The contrast and resolution of the different microscopies, shown in Fig. 5, allow them to image matter from human organs down to single atoms. Severe constraints on the experimental conditions have to be fulfilled. For example: fully hydrated 10 μm thick cells can be imaged with label-free hard X-ray tomography at resolutions better than 50 nm (frozen if using soft X-rays [604]); they have to be chemically fixed to be studied with light tomography at 200 nm resolution [605], often requiring dyes and labelling procedures;

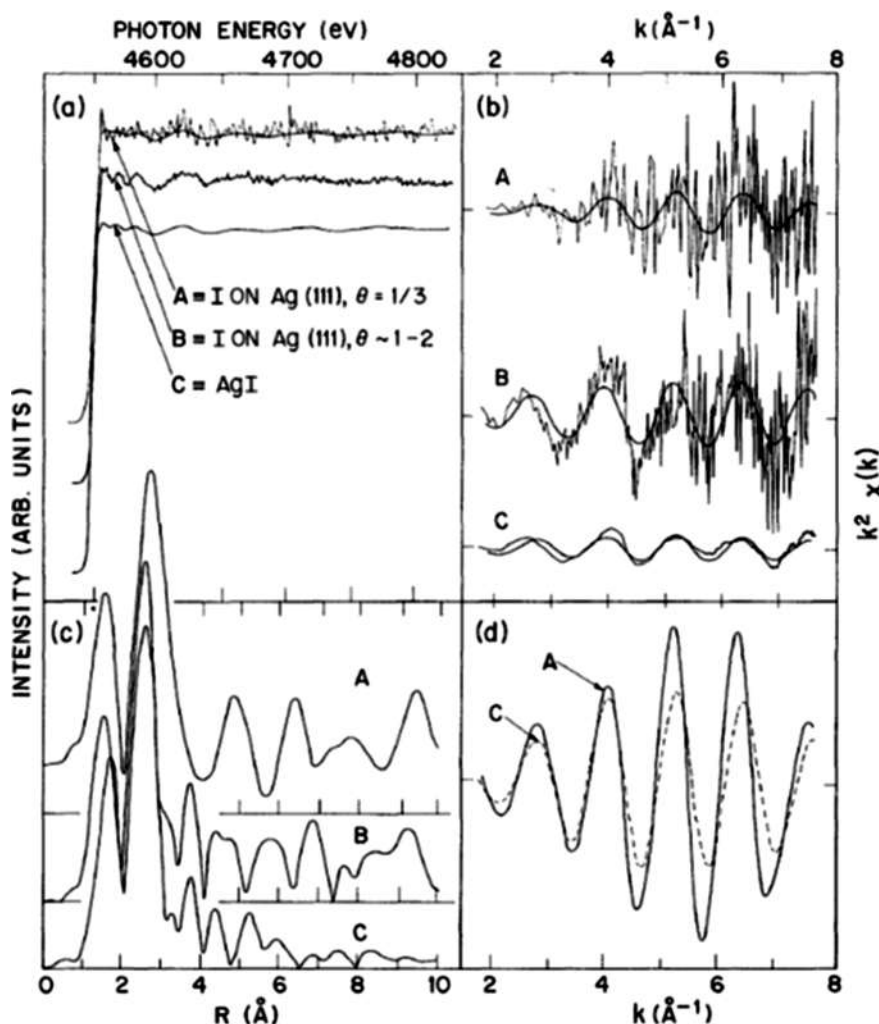


Fig. 43. (a) Auger-detected SEXAFS $\mu\chi(E)$ of I on Ag(1 1 1) surface at $\theta = 1/3$ and 1–2 coverages (curves A and B, respectively) and standard transmission-EXAFS $\mu\chi(E)$ for bulk γ -AgI powder. (b) as (a) for the corresponding extracted $k^2 \chi(k)$ functions. The smoothed curves are retransformed and filtered data, see part (d). (c) FT of the $k^2 \chi(k)$ reported in (b). (d) Back transformed data reported in (c) after filtering in the 1.6–3.8 \AA interval. Reproduced with permission from Ref. [559], copyright American Physical Society, 1978.

they have to be frozen and reduced to 50–100 nm thick sections to be investigated with electron cryo-tomography at 3–5 nm resolution [606].

6.1. Scanning X-ray microscopy

There are two possible types of microscopes: full-field and scanning microscopes. In full field microscopes the object is imaged as a whole. In scanning microscopes the sample is illuminated by means of a focusing optics (see more in §6.1) moving the nano or micro beam across different area of interest [158]. The image of the sample is obtained when the entire data collection is completed (composite map).

The brilliance of the source, the focusing primary optics and the detector characteristics determine the acquisition time to achieve a good signal to noise ratio, which affect the final data resolution.

Scanning X-ray Microscopy (SXM) with SAXS or WAXS contrast is an imaging technique widely used to inspect tissues or composites materials made of soft and hard matter components [607–613]. Let's consider a quite didactic example: type I collagen-hydroxyapatite bi-phasic tissue. Type I collagen is a fibrous protein, present in several tissues (tendon, ligament, skin, cornea, cartilage, bone, blood vessels, gut, and intervertebral disc), made of a hierarchic structure: molecular chains are grouped in fibrils (10–300 nm in diameter) and the fibrils in micrometric fibers (5 μm in diameter), as shown in Fig. 45. When mineralized – like in bones – the molecular chains are intercalated with hydroxyapatite (HA) nanocrystals in a self-assembled template. The hydroxyapatite ($\text{Ca}_5(\text{PO}_4)_3(\text{OH})$) nanocrystals have an hexagonal symmetry (space group P63/m, $a = b = 9.432 \text{\AA}$, $c = 6.881 \text{\AA}$) and form nano-sized domains (50 \times 25 \times 2 nm). The fiber is well described as an unidimensional crystal with a characteristic periodicity along

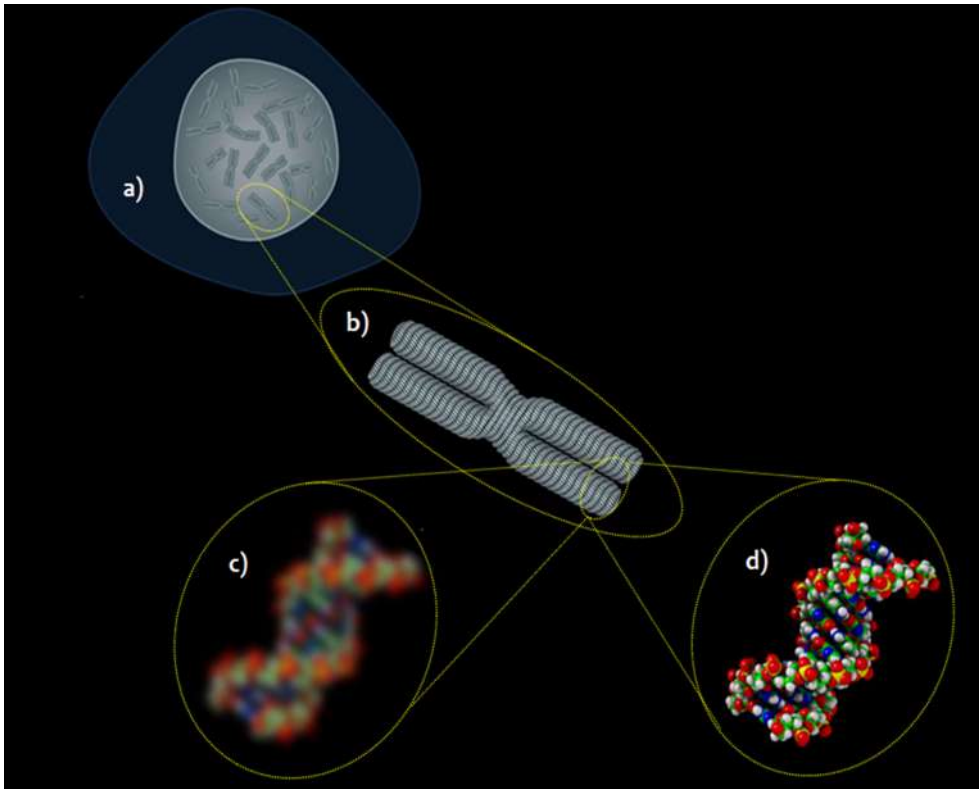


Fig. 44. (a) Pictorial view of a cell nucleus under a microscope; (b) magnified image which allows to zoom onto a chromosome; (c) and (d) further magnified images which allow to see a DNA filament with bad (c) or good contrast and resolution (d).

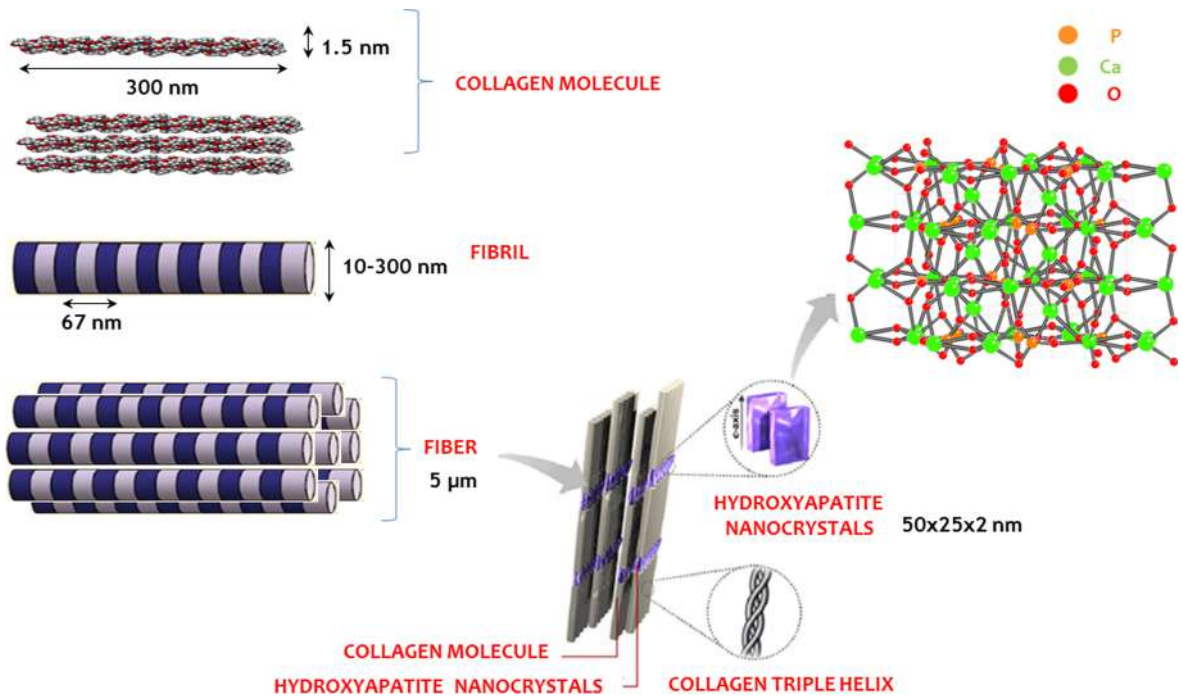


Fig. 45. Hierarchical structure of collagen: the molecular chains are grouped in fibrils (10–300 nm in diameter) and the fibrils in micrometric fibers (5 μm in diameter). If mineralized – like in bones - the molecular chains are intercalated with hydroxyapatite (HA) nanocrystals (50 × 25 × 2 nm) in a self-assembled template. The fiber is a unidimensional crystal with a characteristic periodicity along the fiber axis of about 67 nm. Partially reprinted with permission from Ref. [153], copyright Elsevier, 2013.

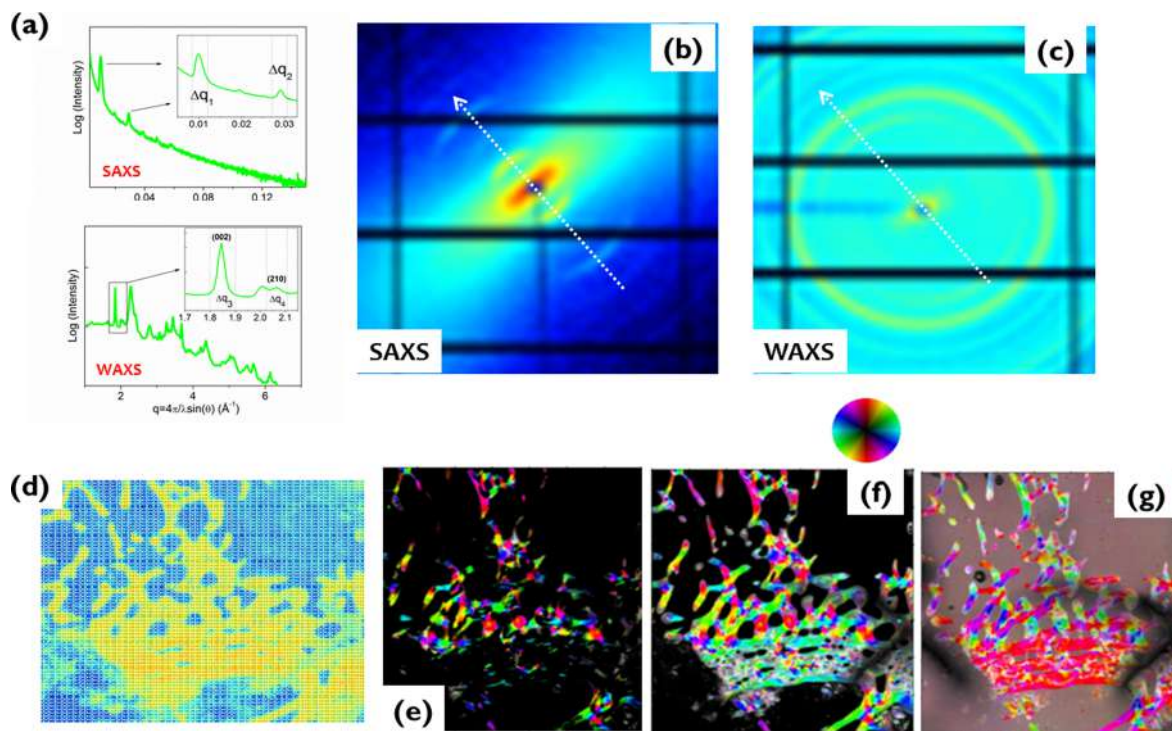


Fig. 46. (a) SAXS meridional reflections due to the 67 nm periodicity along the collagen fiber axis (first Δq_1 and Δq_2 third replica in the inset) and WAXS data indexed as the diffraction pattern of the HA crystalline phase ((002) and (210) reflections in the inset); (b) SAXS 2D pattern of the collagen fiber (dotted white line is fiber axis); (c) WAXS 2D pattern of the nanocrystalline HA (dotted white line is the [002] elongation axis); (d) raw SAXS data collected in the whole area of $7 \times 7 \text{ mm}^2$; microscopies displaying point by point the orientation of the collagen fiber (e) and of HA nanocrystals (f,g). Reprinted with permission from Ref. [614], copyright International Union of Crystallography, 2014.

the fiber axis of about 67 nm. The HA nanocrystals have the [0 0 2] as elongation direction (c-axis). In typical mineralization processes the nanocrystals are expected to form with collagen a unique template structure. Here, the nanocrystals are oriented with the c-axis parallel to the collagen fiber axis (see Fig. 45). This hierarchical order could be altered in presence of demineralization processes, diseases or structural defects. Therefore, it is worth to have a tool to inspect the actual tissue structure, also for diagnosis purposes. A scanning microscopy experiment can be conceived by collecting diffraction signals with a micrometric X-ray probe across a mm^2/cm^2 large area. The inspected area is laterally heterogeneous and statistically significant. In this precise system, two diffraction signals have to be collected: the collagen diffraction due to the nanoscale 67 nm periodicity, occurring at very small scattering angle (SAXS), and the diffraction from the HA nanocrystals whose atomic structure requires WAXS data. The SAXS and WAXS data have to be collected from the same area, either contemporarily with two detectors or in sequence, to have point by point a spatial correlation of the measurements. In the data, different information is encoded and the analysis of the SAXS and WAXS profiles can quantitatively describe the explored area, probing morphological or structural changes across it.

For example, bone tissues were studied at the cSAXS beamline of the SLS synchrotron in Villigen, with a $30 \times 30 \mu\text{m}^2$ beam spot and a Pilatus detector placed sequentially at a sample distance of 7000 and 100 mm for SAXS and WAXS data collection, respectively [614]. Before transforming the raw data into quantitative microscopies relevant structural features were identified (length scales): in the SAXS data (Fig. 46A and B) the 67 nm periodicity along the collagen fiber axis was selected corresponding to the diffraction peak at Δq_1 , or its third replica at Δq_2 ; in the WAXS data (Fig. 46A,C) among the many peaks, indexed as the diffraction pattern of the HA crystalline phase [152], the (002) and (210) reflections were chosen as relevant crystallographic planes of the HA nanocrystals (the [002] direction being along the nanocrystal c-axis and the [210] perpendicular to it). Aim of this specific choice was to check the relative alignment of the collagen fiber axis (Fig. 46B, dotted white line) with respect to the nanocrystal elongation axis (corresponding to the [002] direction, Fig. 46C, dotted white line). The additional [210] direction was considered as internal check. Specifically, raw data were collected in a whole area of $7 \times 7 \text{ mm}^2$ (Fig. 46D). Then, they were transformed into the microscopies in Fig. 46E, F, G displaying point by point: the orientation of the collagen fiber (Fig. 46E) and of HA nanocrystals (Fig. 46F,G along the [002] and [210] directions, respectively). Information encoded in these images are: (i) orientation of the collagen fibers/HA nanocrystals designated by the direction of the relevant sector within the colored wheel, with white assigned to un-oriented material; (ii) the local presence (color) or absence (black) of collagen/HA tissue components per pixel; (iii) degree of orientation of the collagen fibers/HA nanocrystals, determined as the brightness of the colors. The HA orientation is displayed both along the nanocrystal elongation direction, i.e. the [002] crystallographic direction (Fig. 46F), and perpendicular to it, along the [210] direction (Fig. 46G). A comparison of Fig. 46E and Fig. 46F immediately confirms that the c axis of the HA nanocrystals is parallel to the collagen fiber

axis, as expected from the literature [615,616]. The orthogonality of the [002] and [210] HA crystal axis orientations in Fig. 46F and G confirms the reliability of the automated orientation extraction, performed on the as-collected 80.000 SAXS and WAXS frames.

This example is here provided to clarify the central role of this technique whenever tissue engineered nanostructured biomaterials [616] have to be studied across statistically relevant areas to inspect the ultrastructure of an artificial smart hierarchical material in comparison with the corresponding natural tissue. Modern nanotechnology is rich of examples of bio-inspired hierarchical template tissues, based on the combination of an inorganic nanomaterial with proteins or polymers where this kind of characterization tool can be crucial [617–620].

6.2. Lens-less and lens-based imaging microscopes

Full-field or scanning microscopes can be lens-based and lens-less, no aberration affected, imaging systems [606]. For lens-based, the resolution is strongly affected by the objective lenses. The objective lens has to refocus the scattered waves with their associated phases to build the image. Every lens is unfortunately affected by aberrations. Let's consider an electron microscope of acceleration voltage $E = 200$ keV (electron wavelength $\lambda = 2.5$ pm) and low spherical aberration coefficient objective lens ($C_s = 0.47 \pm 0.01$ mm). The lenses aberrations may worsen the resolution of about two orders of magnitude with respect to the diffraction limit (\sim wavelength), becoming at optimum defocus 190 pm = 1.9 Å [621]. For lens-less imaging technique, as X-ray crystallography, the diffracted wavefield freely propagates from sample to detector where it is registered. The diffracted intensity contains only the modulus of the electron density distribution Fourier Transform. This pattern must be inverted to recover an image of the electron density distribution in real space. To perform this task one needs to recover the phase information (see more in §5.3 and §5.4).

6.3. Coherent diffractive imaging and ptychography

An alternative to crystallography, for those cases when a crystal cannot be used, is Coherent Diffractive Imaging (CDI) [154,205–211]. Let's summarize first basic concepts about coherence. In general, the spatial coherence of a wave field describes the correlation between wave phases at different points in space. Similarly, the temporal coherence describes the correlation or predictable relationship between wave phases observed at different moments in time.

Coherence is a measure of predictability. For scattered waves, it refers to the phase predictability of the phasor during wave propagation. Precisely, high coherence means that the phase of a wave can be predicted exactly, incoherence that the phase cannot be predicted at all, partial coherence that the phase can be predicted only approximately. Partial coherence is characterized by a coherence length l_c : the knowledge of the phase at a point x , allows the prediction of its evolution for points within a distance l_c from x . Typical X-ray sources, including also synchrotron sources, are intrinsically incoherent or partially coherent. For example, in the anode of a Roentgen tube, electrons radiate from different places with slightly different wavelengths (within the emission band of the anode) and at different times. Each electron, radiating from a source point, creates a coherent wave. Overall, the chaotically emitted X-ray photons add incoherently. For a source with a transverse size d , coherence will exist over a small angular range $\theta \sim d/R$ where R is the distance from the source and the spatial coherence length will be $l_c = R\lambda/d$ [622]. An ideal point-like source ($d = 0$) is fully spatially coherent ($l_c = \infty$). If the photons are emitted with the same frequency or wavelength (monochromatic source) the source will be also temporally coherent. The longitudinal coherence length of the source will depend on the emitted wavelength band ($\Delta\lambda$) as $l_o = \frac{1}{2} \lambda^2 / \Delta\lambda$ [622]. Spatial or frequency filters, used to produce spatially or longitudinally coherent beams, cause massive loss of intensity. The X-ray coherent beams, needed to perform experiments on non-periodic weakly scattering samples, are available only at 3rd generation synchrotron sources or Free Electron Lasers, thanks to the extremely high brilliance of these sources.

The first idea of X-ray CDI was due to David Sayre in 1952 [623]. About 50 years were needed to reach the proper technologic level for the realization of the first experiment, dated 1999 by Miao and coworkers [624].

Differently from crystallography, lacking the crystal, coherent X-ray beams are needed. In analogy to crystallography, the diffracted pattern must be phase-retrieved to reconstruct the electronic density information. The short X-ray wavelength of the hard X-rays employed for CDI experiments allows, at least in principle, to reach atomic resolutions. However, the real final resolution depends on several practical conditions (brilliance of the source, efficiency of the primary optics, thermal and mechanical stability of the setup, sample radiation damage, sample scattering factor, numerical aperture and dynamics of the detector, photon noise etc). When imaging non crystalline matter, the amplification effect due to the crystal periodicity is lost. Therefore, the diffracted wavefield is expected to be extremely faint, broad and buried into the background. This is why intense coherent X-rays beams are required. However, especially with soft-matter systems, the high photon flux typically imposes serious problems of radiation damage. This can affect the dynamics and, in more severe cases, the sample static properties (the morphology) as well. A tradeoff between photon flux and illumination time must be achieved.

Several CDI methods are available today: Plane-wave CDI [625–627] Bragg CDI; [628,629]; Ptychographic CDI [630–632]; Fresnel/Keyhole CDI [633–635]; Reflection CDI [636,637]; Electron CDI [638–644].

Plane-wave CDI (PCDI) was adopted for cell tomography, [645,646] Bragg CDI (BCDI) [647–649] and electron CDI [638–640] were used for size and strain analysis of single nanocrystals [649] or to study dislocations or even to image lysosome protein crystal [650].

Ptychography [651,652] is the method which combines CDI and SXM (see § 3.2). It is used to probe extended samples, crystalline or not, with coherent X-ray beams. When dealing with crystalline matter, Ptychography can be used also in Bragg diffraction to inspect local strain fields or lattice defects and plastic deformation with nano-scaled probes [653,654]. Operando and in-situ studies

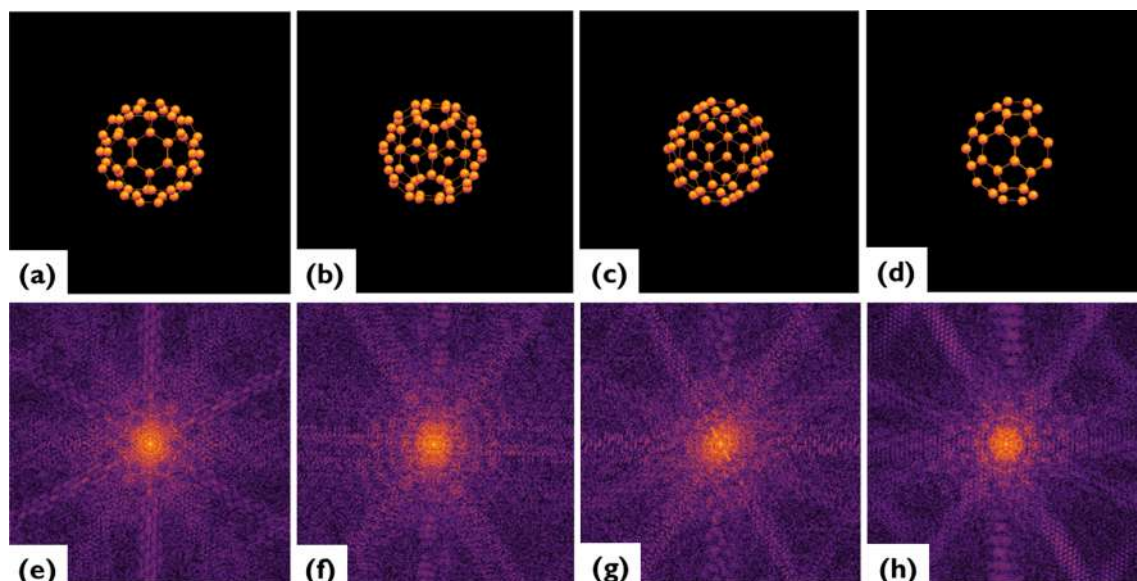


Fig. 47. (a),(b),(c) show three structures under different rotation angles, (d) same structure but with a missing section; (e),(f),(g) and (h) speckled diffraction patterns corresponding to the (a),(b),(c) and (d) structures, respectively.

on planar devices have been realized [653,655,656] and the technique has been also used for 3D tomographic reconstructions [632,657–659].

Liquid samples loaded into cells or capillaries, as well as natural and engineered tissues or nanomaterials embedded in some transparent matrices are typical examples of specimens worth to be explored with CDI [660–666]. In these cases, a typical forward transmission geometry is adopted, as for SAXS data collection, realizing a coherent SAXS experiment. Future fourth generation X-ray sources will allow to push further the limits of this imaging technique in terms of: better resolution (single cell imaging at 16 nm resolution was recently achieved [667]), larger volumes (a chip of $150 \times 150 \mu\text{m}^2$ was imaged at 5 nm resolution [659]) and dynamics for faster scanning [668].

6.4. Speckles

There are precise advantages in illuminating matter with a coherent beam.

Fig. 47A–C show the same object under different rotation angles. The Fourier transform modulus of the object density is displayed for each of them in Fig. 47E–G respectively. We mimic in this calculation the effect of illuminating this structure with a plane wave, i.e. with a coherent wavefield. The diffraction patterns are continuous, because of the finite size of the object, and ‘speckled’ i.e. they are spotty. Speckles depend on the actual structure and orientation of the illuminated object. Indeed, by a simple 3D rotation, the speckles’ structure changes accordingly. Fig. 47D shows the same object as in Fig. 47A but with a missing portion (defect), and the related Fourier transform modulus which presents a different speckled pattern (Fig. 47H). Clearly this is an ideal experiment, as in reality the diffraction pattern of a single object is so faint and broad that an extremely intense beam is stringently needed to collect it, out of the background. Indeed, when the crystal amplification effect is absent a continuous diffraction intensity pattern is awaited. However, the calculation indicates that collecting and inverting such a diffraction pattern would allow us to appreciate structural changes in the original structure, decoding defects or even the exact orientation of the illuminated object. Speckled diffraction patterns are registered whenever matter is illuminated with coherent X-ray beams. The position and relative intensity of the speckles correspond to the scattering objects non-periodic position in real space.

Therefore, whatever material could be studied independently of its crystallinity by using a coherent X-ray photon beam. The real limitation of such a choice is given by the actual spatial resolution achievable which depends on the scattering power and radiation damage of the material and the specific experimental conditions (X-ray wavelength, detector, optics, sample environment).

6.5. The Nyquist-Shannon sampling theorem and the phase problem

We learned in §3 that the structure factor of a crystal, namely the FT of the crystal electron density, is the product of the unit cell structure factor multiplied by the lattice sum, Eq. (22). The unit cell electron density is the function to reconstruct, which is non-zero in the cell of size a . The Shannon sampling theorem [669,670] states that a function which is non-zero within an interval a can be fully reconstructed by sampling its FT at a spacing $1/a$, corresponding to the inverse size of the scattering object (Nyquist frequency) [367]. Unfortunately, the measured diffracted intensity is not directly the structure factor, which is a complex function. The diffracted intensity is proportional only to the squared structure-factor modulus and there is no way to measure the phase of the

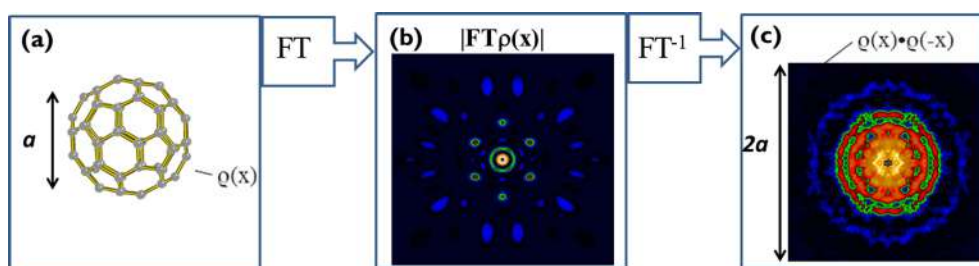


Fig. 48. (a) Electron density $\rho(x)$ of an object of size a (C60 molecule); (b) modulus of the Fourier Transform of $\rho(x)$, $FT(\rho(x))$, i.e. modulus of the form factor of the C60 molecule; (c) inverse FT of $|F(q)|^2$ which coincides with the autocorrelation function $A(x) = \rho(x) \cdot \rho(-x)$ of the scattering function.

structure factor which is lost in the experimental data collection (phase problem). The inverse FT of the measured diffracted intensity, without any phase information, is a modulus-only Fourier synthesis. The inverse FT of $|F(q)|^2$ coincides with the autocorrelation function $A(x) = \rho(x) \cdot \rho(-x)$ of the unit cell electron density, which has a size $2a$. The Shannon sampling theorem, applied to this function, would require its sampling in Fourier space (reciprocal space) with a step $1/2a$ to fully reconstruct it everywhere, but in between the Bragg peaks there is only a background signal, due to a destructive interference of secondary waves scattered by the ordered unit cells. Solving the phase problem is the task of crystallography. In order to reach this objective further additional structural information has to be added to constrain the phase retrieval problem, such as the positivity and the atomicity of the unknown crystal unit-cell electron density. Indeed, inverting an under-sampled (Bragg) diffraction pattern is an ill-posed mathematical problem. However, many theoretical approaches and algorithms have been realized to solve this issue with success in the last 100 years of crystallography [671].

When we are not dealing with periodic structures an alternative way to constrain phase retrieval problems, to reach the correct scattering function, is by oversampling the diffraction pattern [653,654]. Oversampling means to collect the diffraction pattern at a frequency higher than the Nyquist one corresponding to the size a of the scattering object.

Fig. 48A and B shows a single C60 molecule of size a , $\rho(x)$, and the modulus of the simulated molecular form factor, $|FT[\rho(x)]|$, respectively (see § 2.4). The inverse FT of $FT[\rho(x)]^2$ is related to the autocorrelation function of $\rho(x)$, shown in Fig. 48C. The autocorrelation function of $\rho(x)$, $A(x) = \rho(x) \cdot \rho(-x)$, has a size $2a$ [669,670].

The autocorrelation function $A(x)$ of isolated scattering objects becomes, for crystals, the Patterson function $P(x)$. Both can be deconvolved to solve the phase problem in the direct (object) space [672]. The auto-correlation deconvolution method consists in the translation of $A(x)$ in discrete positions x_{Mi} , with x_{Mi} selected among the most intense secondary maxima of $A(x)$, and in the computation of the product between $A(x)$ and its translated replicas $A(x-x_{M1}) \times A(x-x_{M2}) \times \dots$. Fig. 49A–D shows the original and the deconvoluted autocorrelation functions after three, six and nine intersections, respectively. At nine intersections, in the simple example under study, the original scattering function, $\rho(x)$, is fully recovered. Fig. 49E shows the overlapping of $\rho(x)$ and $A(x)$, and that $\rho(x)$ was contained in $A(x)$. Fig. 49F is the drawing of the C60 atomic model, displayed in the same orientation chosen to simulate the molecule form factor used in the calculations. For periodic structures, the Patterson function $P(x)$ is an aliased version of the autocorrelation function $A(x)$ that can be associated to one unit cell. For this reason, $P(x)$ deconvolution can be only partially achieved. Nevertheless even the structure of big proteins can be correctly retrieved by using the partial $P(x)$ deconvolution to obtain a starting phase set that has to be refined via suitable iterative phasing algorithms [673].

6.6. Iterative image-recovery algorithms

Another method to solve the phase problem is based on the use of iterative recovery algorithms which suitable constraints adopted in the direct (object) space and in the Fourier space. CDI experiments are realized with lens-less set-up, i.e. without introducing any optics between sample and detector. As a consequence, algorithms are needed, in order to transform diffraction data in the object image in real space [674–676]. Phase retrieval algorithms start from raw data $|F(q)|^2$ and guessed phases (steps 1 and 2 in Fig. 50) and give an initial approximate value of the electron density $\rho(x)$ which is then refined in successive iterative cycles. Several algorithms are available today; the hybrid input-output (HIO) and the error reduction (ER) are among the first developed ones [677–679]. Any algorithm makes use of two, or more, different constraints. For example, for the error reduction algorithm one has

- a support constraint in the object space, which automatically means to fix within a defined support region S the overall object position and physical extent, thus defining also the complementary no-scattering region, i.e., $\rho(x) \rightarrow Ps[\rho(x)]$, with $Ps(x) = 1$ for $x \in S$, $Ps(x) = 0$ otherwise.
- a modulus projection in its dual space (Fourier space), which means placing $|F(q)|^2$ equals to the measured intensity pattern (Fourier constraint), keeping unchanged the phases obtained by means of the FT of $Ps[\rho(x)]$.

Suitable Figure of Merits, which measure the reconstruction error both in real and Fourier space, help to monitor the convergence of the phasing algorithm towards a reliable solution.

Standard phasing approaches, such as the HIO, are deterministic iterative algorithms, which, going back and forth from the real to

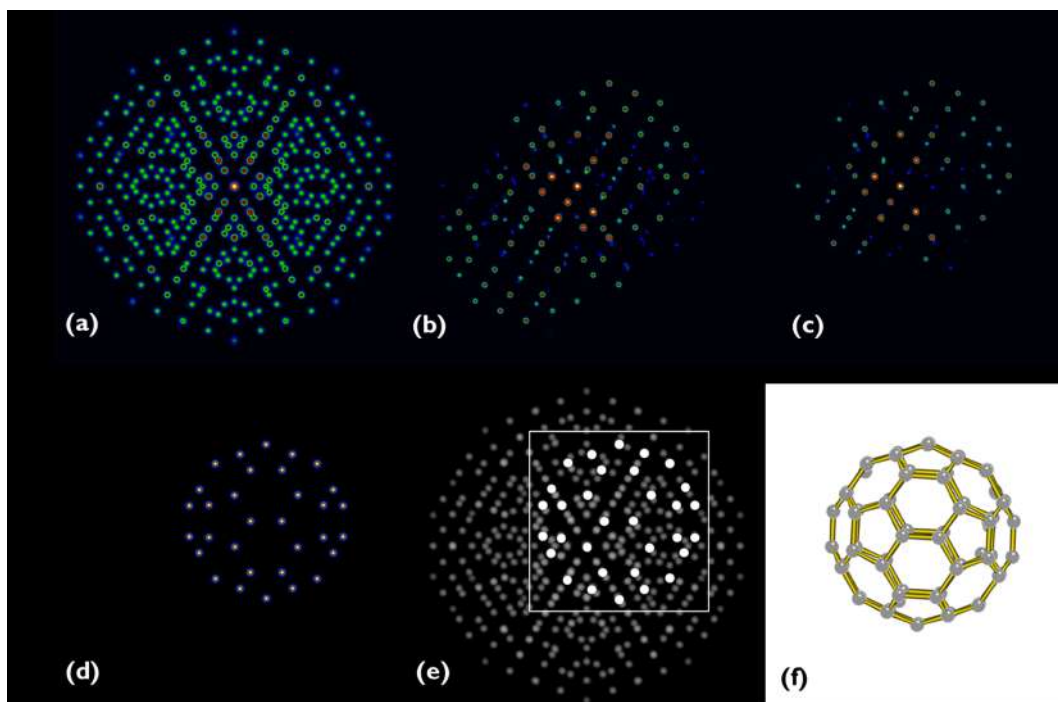


Fig. 49. (a) Auto-correlation $A(x)$ obtained by the C60 molecule in a high-symmetry orientation; (b) partial deconvolution of $A(x)$ after three intersections; (c) partial deconvolution of $A(x)$ after six intersections; (d) full deconvolution of $A(x)$ after nine intersections; (e) overlapping of scattering function $\rho(x)$ and autocorrelation function $A(x)$; (f) drawing of the C60 atomic model, to show the particular orientation chosen for the C60 molecule to simulate its $A(x)$.

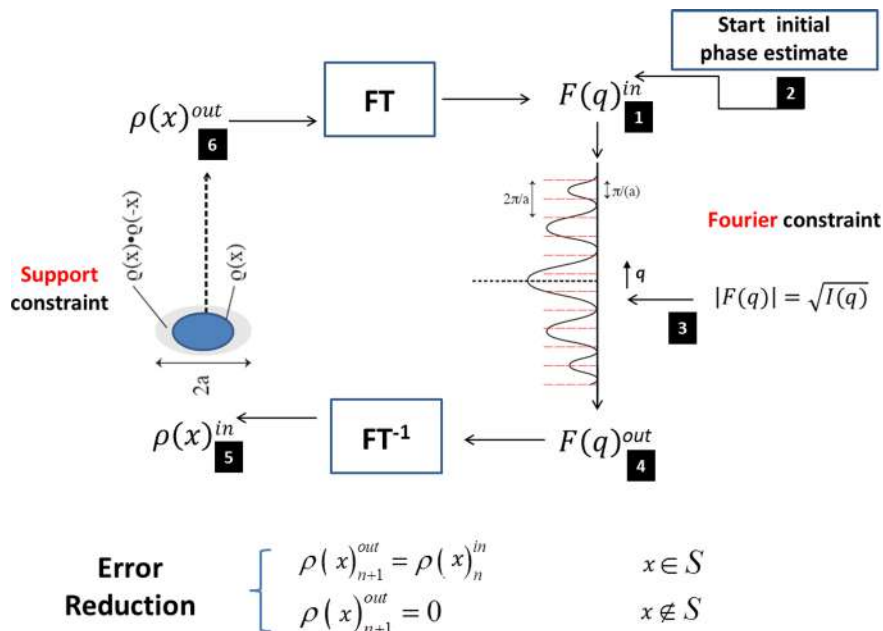


Fig. 50. Phase retrieval algorithms: here the error reduction is shown, which starting from the raw data $|F(q)|^2$ and initial guessed phases allow to find the electron density $\rho(x)$. Previously unpublished figure.

the Fourier space, try to optimize a specific error function. For this reason they suffer from stagnation mainly due to the incomplete knowledge of the support S and the scattering moduli. A recent and very promising approach is based on a more efficient exploration of the space of solutions through a stochastic search based on a smart use of Genetic Algorithms (GA). A new solution to the phase problem has been individuated in memetic algorithms which are hybrid GAs which exploit the synergy of deterministic – e.g. HIO –

and stochastic optimization methods [680]. To overcome stagnation into local minima, it is useful to introduce local iterative deterministic phase retrieval procedures as self-improvement operations. For this reason, the new proposed phasing approach is called Memetic Phase Retrieval (MPR). The standard deterministic phasing approach can be seen as a MPR without the genetic operators *Selection*, *Crossover* and *Mutation*. Any deterministic phase retrieval algorithm can be implemented in MPR. For example the use of ER and HIO algorithms as self-improvement operations has been recently exploited in a MPR framework in [680]. The Selection process is a delicate step in the Evolution process. A selection strongly favoring only the better elements – i.e., elements with the better *fitness* value – will improve the convergence speed, but the algorithm will suffer with stagnation in local minima. On the other side, a selection process that weakly favors better elements will have, instead, an unstable convergence and will require an excessive length of time to find the solution. In the Natural Evolution process, the Crossover operation is the mixing of the parents' genetic pool. Crossover can be tuned by means of a suitable parameter G , which can be called *genetic fraction*. It has values between 0 and $1G = 1$ means that all of the parent population is replaced by the sons, while $G = 0$ means that no sons are created, the genetic operators are switched off and we get a situation equivalent to the standard deterministic approach. Mutation means that very element in the population may be subjected to a stochastic modification. It can be also switched off, by using only Selection and Crossover genetic operations. The implementation in three dimension of fast phasing GAs is a challenge for the next future but, also it will constitute a very promising tool for reaching global minima in complex phase retrieval problems which usually occurs in X-ray and electron lensless microscopies.

6.7. Non periodically assembled nanocrystals

Composite materials based on polymers mixed with nanocrystals are in the focus of many recent research studies, including catalysis [681–684]. When polymers are extremely thin, few tenths of nanometers, scanning electron microscopy is the widely and more efficient imaging method to explore the architectures of the nanocrystals in the polymers. In the case of CdSe/CdS octapod-shaped nanocrystals self-assembly in polystyrene (PS) films the NCs tend to aggregate into linear arrays of particles, as revealed by transmission electron microscopy (TEM). However, when the octapods are embedded in free-standing PS films, several μm thick, they cannot be imaged through standard imaging techniques (such as TEM). Therefore, it is not possible to draw any conclusion on whether chain-like assemblies were still formed in polymers in such circumstances.

An imaging technique with nanometric resolution, able to explore several micron thick polymers, is needed. X-ray Ptychography (see Section 3.4.) is therefore the technique of choice in this case, being able to penetrate such thick specimens and to investigate non periodic extended assembly of objects with nanometric resolution. The experiments here reported [685] were performed at the cSAXS beamline of the Swiss Light Source in Villigen, on selected different samples: without polymer (OCT sample), thin octapod/PS films, with molecular weights (Mw) of 190 and 350 kg/mol, named PS190_thin and PS350_thin, and 24 μm free-standing octapod/PS films, named PS190 and PS350.

Fig. 51A shows a schematic description of the set-up where a Fresnel Zone Plate (see Section 5.2.4) was used to focus a 450 nm beam onto the sample and a total scanned area of $4 \times 4 \mu\text{m}^2$ was explored. Images of the phase retardation obtained by phase retrieval of the data are displayed in Fig. 51B. A quantitative comparison of the maximum phase retardation ($\Delta\phi$) is reported in the Table with the polymer thickness (t_{ps}). The $\Delta\phi$ values represent the phase shift contribution due to the NCs with respect to the phase retardation caused by the polymer matrix. It is interesting to note that ptychography allowed to visualize the self-assembly of octapods into linear and interconnected structures at the resolution of about 25 nm. Ptychographic data were used to explore the effect on the octapod aggregation of: (i) different polymer film thickness for the same polymer molecular weight in the PS350_thin and PS350 samples; and (ii) different molecular weights, for the same thickness of the polymer film in the PS350 and PS190 samples. The results from the analysis suggested that the octapods are connected through a network and their distribution in the polymer films is influenced by the molecular weight of the polymer and by the thickness of the resulting composite film.

This example evidences the potential use of the ptychography for the analysis of nanostructures in polymer matrices.

The next and last example concerns the possibility to use coherent X-rays in a CDI experiment on non-periodic self-assembly of Fe_2P nanocrystals [686]. With respect to the previous case, the nanocrystals are grouped into an isolated object, as the result of a free evaporation of the nanocrystals dropped from solution. A sketch of the optical scheme of the experiment, performed at the ID10 ESRF beamline, is reported in Fig. 52A (distance in meters). 2D diffraction patterns were taken for the sample tilts between -72° and $+72^\circ$ with a step of 2° . Top and side views of the reconstructed 3D image of the cluster is shown in Fig. 52B and compared with the SEM image in Fig. 52C. The 3D image resolution (59 nm) is not sufficient to resolve the individual nanorods forming the aggregate but we can easily identify the dense aggregates and voids in Fig. 52B. The formation of voids and high density areas on the top and in the middle of the cluster is driven by complex fluid hydrodynamics in the evaporating sessile drop.

7. Summary

In this review we provide the theoretical basis of well-known X-ray scattering and spectroscopy methods, available today for the nanoscience community to characterize materials across different length scales from atomic to mesoscale. A fairly large number of dedicated examples performed on nanomaterials are also reported to elucidate the benefit and complementarity of the different techniques. Some of the examples are related to soft matter, such as peptide-base nanostructures or hybrid inorganic-organic materials, but most of them refer to inorganic materials. Nanomaterials, or more in general nanostructures, can be dispersed in solutions (such as nanocrystals, liposomes, hydrogels for biomedical applications), embedded in different matrixes (such as meso-/nano-porous materials, polymers or in tissues) or deposited on top of surfaces or underneath them (nanostructured surfaces, planar devices).

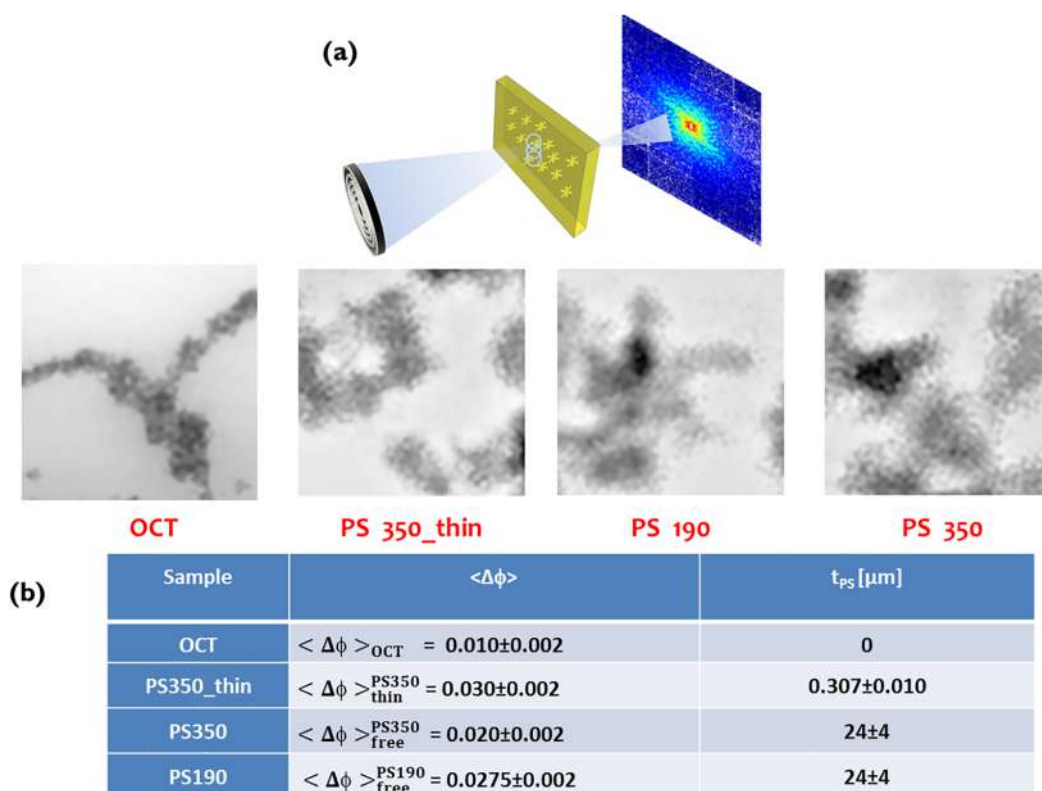


Fig. 51. (a) Schematic description of the experimental set-up; (b) phase retardation obtained by phase retrieval of the data; the table contains the maximum phase retardation ($\Delta\phi$) and the polymer thickness (t_{ps}). Reprinted with permission from ref. [685], copyright Nature Publishing Group, 2016.

Depending on their specific status they can be measured in: (i) transmission geometry, e.g. XAS (see 4.1), SAXS or WAXS data collection as well as with SXM with SAXS or WAXS contrast (see 6.1) or X-ray ptychography or CDI (see 6.3); (ii) in reflection geometry, e.g. GISAXS and GIWAXS, GI standing for Grazing Incidence [687], Bragg CDI [647,648] or reflection EXAFS (see 5.5.2).

Whenever structural or morphological properties change locally (spatial inhomogeneity), a focused X-ray beam becomes highly beneficial [160]. The eventual lack of any crystal coherence in the material to investigate requires a mandatory use of coherent X-ray beams. Nowadays, at 3rd and 4th generation synchrotrons or Free Electron lasers across the world, the first beamlines offer on-site combined scattering and spectroscopic techniques. As a very recent example, the Spectroscopy and Coherent Scattering (SCS) beamline at the XFEL in Hamburg will enable time-resolved experiments to unravel the electronic and structural properties of soft matter magnetic materials and complex structures. The most advanced and powerful X-ray sources allow today to realize in situ experiments with spatial resolution of few nanometers and time resolution of few femtoseconds. This means that we can foresee experiments to study processes such as electron-transfer dynamics or phonon propagations (time scale ~ 1 – 10 ps), energy transfer from electron to lattice, electronic transitions, atomic motions (time scale ~ 1 – 50 fs), and to follow chemical transformations in heterogeneous catalysis in real time [688] even illuminating a single nanocrystal [689]. Goals to be still reached concern, for example, how to benefit of the actual spatial and temporal resolution for in situ/operando fancy experiments but keeping under control the unavoidable radiation damage [160] or how to scan across larger and larger areas at the highest speed without compromising sample stability. A price to pay is definitively the amount of data collected in a single experimental run which can even reach petabytes (10^{15} bytes). This enormous amount of data will require *a posteriori* data approaches typical of the Artificial Intelligence research network [690], which means that increasingly large demand of interdisciplinary requirements will come into play for the new coming research decades.

Acknowledgments

All the authors dedicate this work to Carlo Lamberti, for his immense talent in life and science and for his friendship. C.G. wants to dedicate this work also to her father, Dante Giannini, who gave her the gift of a love for knowledge.

We gratefully acknowledge for the critical reading of the paper: Raffaella Buonsanti of the Institut des Sciences et Ingénierie Chimiques, Ecole Polytechnique Fédérale de Lausanne (EPFL)-Valais, Switzerland; Maurizio Dabbicco of the Physics Department, University of Bari, Italy; Fabia Gozzo of the Excelsus Structural Solutions, Bruxelles, Belgium. One of us (V.H.) acknowledges the support of the Czech Science Foundation, Czech Republic (ID project 19-10799J).

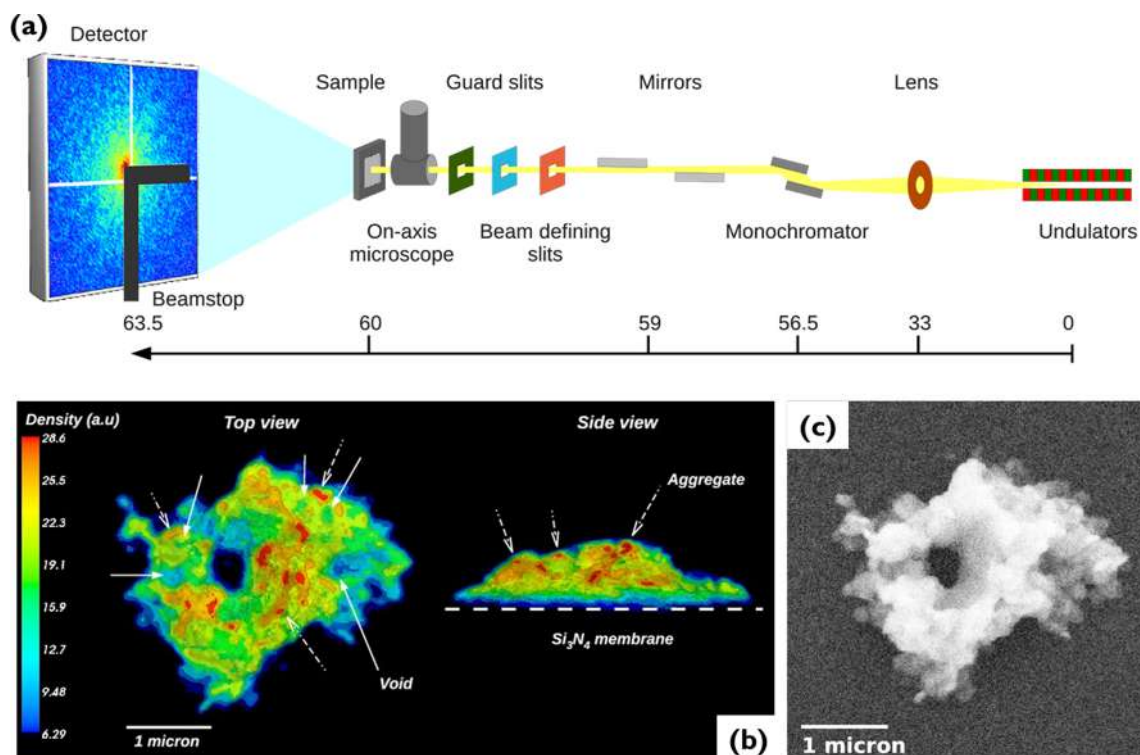


Fig. 52. (a) Sketch of the optical scheme available at the ID10 beamline of the ESRF and used in this experiment; (b) top and side views of the reconstructed 3D image of the Fe_2P cluster, (c) SEM image of the sample. Reprinted with permission from Ref. [686], copyright International Union of Crystallography, 2014.

References

- [1] Stangl J, Holy V, Bauer G. Structural properties of self-organized semiconductor nanostructures. *Rev. Mod. Phys.* 2004;76:725–83.
- [2] Klabunde KJ, Richards RM, editors. *Nanoscale materials in chemistry*. 2nd ed. New York: John Wiley & Sons; 2009.
- [3] Kovalenko MV, Manna L, Cabot A, Hens Z, Talapin DV, Kagan CR, et al. Prospects of nanoscience with nanocrystals. *ACS Nano* 2015;9:1012–57.
- [4] Klabunde KJ, Stark J, Koper O, Mohs C, Park DG, Decker S, et al. Nanocrystals as stoichiometric reagents with unique surface chemistry. *J Phys Chem* 1996;100:12142–53.
- [5] A. Khaleel, W.F. Li, K.J. Klabunde, Nanocrystals as stoichiometric reagents with unique surface chemistry. *New adsorbents for air purification*. *Nanostruct Mater* 1999;12:463–466.
- [6] Alivisatos AP. Nanocrystals: building blocks for modern materials design. *Endeavour* 1997;21:56–60.
- [7] Rao CNR, Kulkarni GU, Thomas PJ, Edwards PP. Size-dependent chemistry: properties of nanocrystals. *Chem-Eur J* 2002;8:28–35.
- [8] Burda C, Chen XB, Narayanan R, El-Sayed MA. Chemistry and properties of nanocrystals of different shapes. *Chem Rev* 2005;105:1025–102.
- [9] Roduner E. Size matters: why nanomaterials are different. *Chem Soc Rev* 2006;35:583–92.
- [10] Kaneko K, Inoke K, Freitag B, Hungria AB, Midgley PA, Hansen TW, et al. Structural and morphological characterization of cerium oxide nanocrystals prepared by hydrothermal synthesis. *Nano Lett* 2007;7:421–5.
- [11] Peng XG. An essay on synthetic chemistry of colloidal nanocrystals. *Nano Res* 2009;2:425–47.
- [12] Cozzoli PD, Pellegrino T, Manna L. Synthesis, properties and perspectives of hybrid nanocrystal structures. *Chem Soc Rev* 2006;35:1195–208.
- [13] Casavola M, Buonsanti R, Caputo G, Cozzoli PD. Colloidal strategies for preparing oxide-based hybrid nanocrystals. *Eur J Inorg Chem* 2008;837–854.
- [14] Ozin GA, Hou K, Lotsch BV, Cademartiri L, Puzzo DP, Scotognella F, et al. Nanofabrication by self-assembly. *Mater Today* 2009;12:12–23.
- [15] Keys AS, Iacovella CR, Glotzer SC. In: Langer JS, editor. *Annual Review of Condensed Matter Physics, Vol 2, Annual Reviews, Palo Alto, 2011*, pp. 263–285.
- [16] Thiruvengadathan R, Korampally V, Ghosh A, Chanda N, Gangopadhyay K, Gangopadhyay S. Nanomaterial processing using self-assembly-bottom-up chemical and biological approaches. *Rep Prog Phys* 2013;76:54.
- [17] Milliron DJ, Hughes SM, Cui Y, Manna L, Li JB, Wang LW, et al. Colloidal nanocrystal heterostructures with linear and branched topology. *Nature* 2004;430:190–5.
- [18] Rao CNR, Biswas K. Annual review of analytical chemistry. *Annual Reviews: Palo Alto*; 2009. p. 435–62.
- [19] Holt M, Harder R, Winarski R, Rose V. In: Clarke, DR, editor. *Annual Review of Materials Research, Vol 43, Annual Reviews, Palo Alto, 2013*, pp. 183–211.
- [20] Agostini G, Lamberti C, editors. *Characterization of semiconductor heterostructures and nanostructures*. 2nd edition. Elsevier Amsterdam; 2013.
- [21] Mino L, Agostini G, Borfecchia E, Gianolio D, Piovano A, Gallo E, Lamberti C. Low-dimensional systems investigated by x-ray absorption spectroscopy: a selection of 2D, 1D and 0D cases. *J Phys D: Appl Phys* 2013;46(42):423001.
- [22] Garino C, Borfecchia E, Gobetto R, van Bokhoven JA, Lamberti C. Determination of the electronic and structural configuration of coordination compounds by synchrotron-radiation techniques. *Coord Chem Rev* 2014;277:130–86.
- [23] Hexemer A, Muller-Buschbaum P. Advanced grazing-incidence techniques for modern soft-matter materials analysis. *IUCrJ* 2015;2:106–25.
- [24] Pennycook SJ, Chisholm MF, Lupini AR, Varela M, Borisevich AY, Oxley MP, et al. Aberration-corrected scanning transmission electron microscopy: from atomic imaging and analysis to solving energy problems. *Philos Trans R Soc A-Math Phys Eng Sci* 2009;367:3709–33.
- [25] Muller DA. Structure and bonding at the atomic scale by scanning transmission electron microscopy. *Nat Mater* 2009;8:263–70.
- [26] Ringe E. Nanocrystalline materials: recent advances in crystallographic characterization techniques. *IUCrJ* 2014;1:530–9.
- [27] Rivacoba A, Zabala N, Aizpurua J. Image potential in scanning transmission electron microscopy. *Prog Surf Sci* 2000;65:1–64.

- [28] Spence JCH. Absorption spectroscopy with sub-angstrom beams: ELS in STEM. *Rep Prog Phys* 2006;69:725–58.
- [29] Amelinckx S, Lucas A, Lambin P. Electron diffraction and microscopy of nanotubes. *Rep Prog Phys* 1999;62:1471–524.
- [30] Qin LC. Electron diffraction from carbon nanotubes. *Rep Prog Phys* 2006;69:2761–821.
- [31] Zewail AH. Annual review of physical chemistry. *Annual Reviews: Palo Alto*; 2006. p. 65–103.
- [32] Midgley PA, Eggeman AS. Precession electron diffraction – a topical review. *IUCrJ* 2015;2:126–36.
- [33] Miao J, Ercius P, Billinge SJL. Atomic electron tomography: 3D structures without crystals. *Science* 2016;353:9.
- [34] Levshov DI, Tran HN, Paillet M, Arenal R, Than XT, Zahab AA, et al. Accurate determination of the chiral indices of individual carbon nanotubes by combining electron diffraction and Resonant Raman spectroscopy. *Carbon* 2017;114:141–59.
- [35] Mino L, Gianolio D, Agostini G, Piovano A, Truccato M, Agostino A, et al. Structural characterization of multi-quantum wells in electroabsorption-modulated lasers by using synchrotron radiation micrometer-beams. *Adv Mater* 2010;22:2050–4.
- [36] Ferrari C, Buffagni E, Rossi F. In: Lamberti C, Agostini G, editors. *Characterization of semiconductor heterostructures and nanostructures*. 2nd edition. Elsevier, Amsterdam; 2013. p. 75–111.
- [37] Schüllli T, Favre-Nicolin V, Richard M-I, Renaud G. In: Lamberti C, Agostini G, editors. *Characterization of semiconductor heterostructures and nanostructures*. 2nd edition. Elsevier, Amsterdam; 2013. p. 113–173.
- [38] Chu B, Hsiao BS. Small-angle X-ray scattering of polymers. *Chem Rev* 2001;101:1727–61.
- [39] Doniach S. Changes in biomolecular conformation seen by small angle X-ray scattering. *Chem Rev* 2001;101:1763–78.
- [40] Svergun DI, Koch MHJ. Small-angle scattering studies of biological macromolecules in solution. *Rep Prog Phys* 2003;66:1735–82.
- [41] Lipfert J, Doniach S. Annual Review of biophysics and biomolecular structure, annual reviews, Palo Alto; 2007. p. 307–327.
- [42] Putnam CD, Hammel M, Hura GL, Tainer JA. X-ray solution scattering (SAXS) combined with crystallography and computation: defining accurate macromolecular structures, conformations and assemblies in solution. *Q Rev Biophys* 2007;40:191–285.
- [43] Renaud G, Lazzari R, Leroy F. Probing surface and interface morphology with grazing incidence small angle X-ray scattering surf. *Sci Rep* 2009;64:255–380.
- [44] Svergun DI, Shtykova EV, Volkov VV, Feigin LA. Small-angle X-ray scattering, synchrotron radiation, and the structure of bio- and nanosystems. *Crystallogr Rep* 2011;56:725–50.
- [45] Blanchet CE, Svergun DI. In: Johnson MA, Martinez TJ, editors. *Annual review of physical chemistry, Vol 64, Annual Reviews, Palo Alto*; 2013. p. 37–54.
- [46] Portale G, Longo A. In: Lamberti C, Agostini G, editors. *Characterization of semiconductor heterostructures and nanostructures*. 2nd edition. Elsevier, Amsterdam; 2013. p. 175–228.
- [47] Bras W, Koizumi S, Terrill NJ. Beyond simple small-angle X-ray scattering: developments in online complementary techniques and sample environments. *IUCrJ* 2014;1:478–91.
- [48] Petukhov AV, Meijer JM, Vroege GJ. Particle shape effects in colloidal crystals and colloidal liquid crystals: small-angle X-ray scattering studies with micro-radian resolution. *Curr Opin Colloid Interface Sci* 2015;20:272–81.
- [49] Li T, Senesi AJ, Lee B. Small angle X-ray scattering for nanoparticle research. *Chem Rev* 2016;116:11128–80.
- [50] Billinge SJL, Levin I. The problem with determining atomic structure at the nanoscale. *Science* 2007;316:561–5.
- [51] Bozin ES, Juhás P, Billinge SJL. In: Lamberti C, Agostini G, editors. *Characterization of semiconductor heterostructures and nanostructures*. 2nd edition. Elsevier, Amsterdam; 2013. p. 229–257.
- [52] Evans PG, Isaacs ED. Magnetic x-ray microdiffraction. *J Phys D-Appl Phys* 2006;39:R245–63.
- [53] Campion A, Kambhampati P. Surface-enhanced Raman scattering. *Chem Soc Rev* 1998;27:241–50.
- [54] Dresselhaus MS, Dresselhaus G, Saito R, Jorio A. Raman spectroscopy of carbon nanotubes. *Phys Rep-Rev Sec Phys Lett* 2005;409:47–99.
- [55] Ferrari AC. Raman spectroscopy of graphene and graphite: disorder, electron-phonon coupling, doping and nonadiabatic effects. *Solid State Commun*. 2007;143:47–57.
- [56] Malard LM, Pimenta MA, Dresselhaus G, Dresselhaus MS. Raman spectroscopy in graphene. *Phys Rep-Rev Sec Phys Lett* 2009;473:51–87.
- [57] Ferrari AC, Basko DM. Raman spectroscopy as a versatile tool for studying the properties of graphene. *Nat Nanotechnol* 2013;8:235–46.
- [58] Wolverson D. In: Lamberti C, Agostini G, editors. *Characterization of semiconductor heterostructures and nanostructures*. 2nd edition. Elsevier, Amsterdam; 2013. p. 753–802.
- [59] Alessandri I, Lombardi JR. Enhanced Raman scattering with dielectrics. *Chem Rev*. 2016;116:14921–81.
- [60] Lu X, Luo X, Zhang J, Quek SY, Xiong QH. Lattice vibrations and Raman scattering in two-dimensional layered materials beyond graphene. *Nano Res* 2016;9:3559–97.
- [61] Nam JM, Oh JW, Lee H, Suh YD. Plasmonic nanogap-enhanced Raman scattering with nanoparticles accounts. *Chem Res* 2016;49:2746–55.
- [62] Zaleski S, Wilson AJ, Mattei M, Chen X, Goubert G, Cardinal MF, et al. Investigating nanoscale electrochemistry with surface- and tip-enhanced Raman spectroscopy accounts. *Chem Res* 2016;49:2023–30.
- [63] Zhang N, Tong LM, Zhang J. Graphene-based enhanced Raman scattering toward analytical applications. *Chem Mat* 2016;28:6426–35.
- [64] Wood S, Hollis JR, Kim JS. Raman spectroscopy as an advanced structural nanoprobe for conjugated molecular semiconductors. *J Phys D-Appl Phys* 2017;50:Art. n. 073001.
- [65] Shinjo T, Keune W. Mossbauer-effect studies of multilayers and interfaces. *J Magn Magn Mater* 1999;200:598–615.
- [66] Filatov M. First principles calculation of Mossbauer isomer shift. *Coord Chem Rev* 2009;253:594–605.
- [67] Gutlich P. Fifty Years of Mossbauer spectroscopy in solid state research - remarkable achievements, future perspectives. *Z Anorg Allg Chem* 2012;638:15–43.
- [68] Rehr JJ, Albers RC. Theoretical approaches to x-ray absorption fine structure. *Rev Mod Phys* 2000;72:621–54.
- [69] Rehr JJ, Ankudinov AL. Progress in the theory and interpretation of XANES. *Coord Chem Rev* 2005;249:131–40.
- [70] Solomon EI, Hedman B, Hodgson KO, Dey A, Szilagyí RK. Ligand K-edge X-ray absorption spectroscopy: covalency of ligand-metal bonds. *Coord Chem Rev* 2005;249:97–129.
- [71] Bordiga S, Bonino F, Lillerud KP, Lamberti C. X-ray absorption spectroscopies: useful tools to understand metallorganic frameworks structure and reactivity. *Chem Soc Rev* 2010;39:4885–927.
- [72] Frenkel AI. Applications of extended X-ray absorption fine-structure spectroscopy to studies of bimetallic nanoparticle catalysts. *Chem Soc Rev* 2012;41:8163–78.
- [73] Bordiga S, Groppo E, Agostini G, van Bokhoven JA, Lamberti C. Reactivity of surface species in heterogeneous catalysts probed by in situ X-ray absorption techniques. *Chem Rev* 2013;113:1736–850.
- [74] Mino L, Gianolio D, Bardelli F, Prestipino C, Kumar ES, Bellarmine F, et al. EXAFS and XANES investigation of (Li, Ni) codoped ZnO thin films grown by pulsed laser deposition. *J Phys-Condens Mat* 2013;25:385402.
- [75] Boscherini F. In: Lamberti C, Agostini G, editors. *Characterization of semiconductor heterostructures and nanostructures*. 2nd edition. Elsevier, Amsterdam; 2013. p. 259–310.
- [76] Mino L, Borfecchia E, Groppo C, Castelli D, Martinez-Criado G, Spiess R, et al. Iron oxidation state variations in zoned micro-crystals measured using micro-XANES. *Catal Today* 2014;229:72–9.
- [77] de Groot F. High resolution X-ray emission and X-ray absorption spectroscopy. *Chem Rev* 2001;101:1779–808.
- [78] Nilsson A, Pettersson LGM. Chemical bonding on surfaces probed by X-ray emission spectroscopy and density functional theory. *Surf Sci Rep* 2004;55:49–167.
- [79] Glatzel P, Bergmann U. High resolution 1s core hole X-ray spectroscopy in 3d transition metal complexes - electronic and structural information. *Coord Chem Rev* 2005;249:65–95.
- [80] Bergmann U, Glatzel P. X-ray emission spectroscopy. *Photosynth Res* 2009;102:255–66.
- [81] Glatzel P, Sikora M, Fernandez-Garcia M. Resonant X-ray spectroscopy to study K absorption pre-edges in 3d transition metal compounds. *Eur Phys J-Spec Top* 2009;169:207–14.
- [82] Singh J, Lamberti C, van Bokhoven JA. Advanced X-ray absorption and emission spectroscopy: in situ catalytic studies. *Chem Soc Rev* 2010;39:4754–66.

- [83] Mino L, Colombo V, Vitillo JG, Lamberti C, Bordiga S, Gallo E, et al. Spectroscopic and adsorptive studies of a thermally robust pyrazolato-based PCP. *Dalton Trans* 2012;41:4012–9.
- [84] Rovezzi M, Glatzel P. Hard x-ray emission spectroscopy: a powerful tool for the characterization of magnetic semiconductors. *Semicond Sci Technol* 2014;29:Art. n. 023002.
- [85] Gallo E, Glatzel P. Valence to core X-ray emission spectroscopy. *Adv Mater* 2014;26:7730–46.
- [86] Pollock CJ, DeBeer S. Insights into the geometric and electronic structure of transition metal centers from valence-to-core X-ray emission spectroscopy accounts. *Chem Res* 2015;48:2967–75.
- [87] Mino L, Signorile M, Crocella V, Lamberti C. Ti-based catalysts and photocatalysts: characterization and modeling. *Chem Rec* 2019;19:1319–36.
- [88] Cagliero S, Piovano A, Lamberti C, Khan MMR, Agostino A, Agostini G, et al. Synchrotron study of oxygen depletion in a Bi-2212 whisker annealed at 363 K. *J Synchrotron Radiat* 2009;16:813–7.
- [89] Mino L, Agostino A, Codato S, Lamberti C. Study of epitaxial selective area growth In_{1-x}Ga_xAs films by synchrotron mu-XRF mapping. *J Anal At Spectrom* 2010;25:831–6.
- [90] Mino L, Gianolio D, Agostini G, Piovano A, Truccato M, Agostino A, et al. mu-EXAFS, mu-XRF, and mu-PL characterization of a multi-quantum-well electroabsorption modulated laser realized via selective area growth. *Small* 2011;7:930–8.
- [91] Majumdar S, Peralta-Videa JR, Castillo-Michel H, Hong J, Rico CM, Gardea-Torresdey JL. Applications of synchrotron mu-XRF to study the distribution of biologically important elements in different environmental matrices: a review. *Anal Chim Acta* 2012;755:1–16.
- [92] Roco MG, Mirkkin CA, Hersam MC. Nanotechnology research directions for societal needs in 2020: summary of international study 2011;13:897–919.
- [93] Liu JW, Lu Y. Smart nanomaterials responsive to multiple chemical stimuli with controllable cooperativity. *Adv Mater* 2006;18:1667–71.
- [94] Lu Y, Liu JW. Smart nanomaterials inspired by biology: dynamic assembly of error-free nanomaterials in response to multiple chemical and biological stimuli. *Accounts Chem Res* 2007;40:315–23.
- [95] Yoshida M, Lahann J. Smart nanomaterials. *ACS Nano* 2008;2:1101–7.
- [96] Habibi N, Kamaly N, Memic A, Shafiee H. Self-assembled peptide-based nanostructures: smart nanomaterials toward targeted drug delivery. *Nano Today* 2016;11:41–60.
- [97] Tapasztó L, Dumitrica T, Kim SJ, Nemes-Incze P, Hwang C, Biro LP. Breakdown of continuum mechanics for nanometre-wavelength rippling of graphene. *Nat Phys* 2012;8:739–42.
- [98] Riehemann K, Schneider SW, Luger TA, Godin B, Ferrari M, Fuchs H. Nanomedicine-challenge and perspectives. *Angew Chem-Int Edit* 2009;48:872–97.
- [99] Lim EK, Kim T, Paik S, Haam S, Huh YM, Lee K. Nanomaterials for theranostics: recent advances and future challenges. *Chem Rev* 2015;115:327–94.
- [100] Ren Z, Guo YB, Liu CH, Gao PX. Hierarchically nanostructured materials for sustainable environmental applications. *Front Chem* 2013;1:22.
- [101] Sanderson P, Delgado-Saborit JM, Harrison RM. A review of chemical and physical characterisation of atmospheric metallic nanoparticles. *Atmos Environ* 2014;94:353–65.
- [102] Mino L, Ferrari AM, Lacivita V, Spoto G, Bordiga S, Zecchina A. CO adsorption on anatase nanocrystals: a combined experimental and periodic DFT study. *J Phys Chem C* 2011;115:7694–700.
- [103] Mino L, Negri C, Zecchina A, Spoto G. Photodegradation of organic pollutants on TiO₂ P25 surfaces investigated by transmission FTIR spectroscopy under in situ UV-Vis irradiation. *Z Phys Chem* 2016;230:1441–51.
- [104] Mino L, Pellegrino F, Rades S, Radnik J, Hodoroaba V-D, Spoto G, et al. Beyond shape engineering of TiO₂ nanoparticles: post-synthesis treatment dependence of surface hydration, hydroxylation, lewis acidity and photocatalytic activity of TiO₂ anatase nanoparticles with dominant 001 or 101 facets. *ACS Appl Nano Mater* 2018;1:5355–65.
- [105] Mino L, Spoto G, Bordiga S, Zecchina A. Particles morphology and surface properties as investigated by HRTEM, FTIR, and periodic DFT calculations: from pyrogenic TiO₂ (P25) to nanoanatase. *J Phys Chem C* 2012;116:17008–18.
- [106] Mino L, Spoto G, Bordiga S, Zecchina A. Rutile surface properties beyond the single crystal approach: new insights from the experimental investigation of different polycrystalline samples and periodic DFT calculations. *J Phys Chem C* 2013;117:11186–96.
- [107] Mino L, Spoto G, Ferrari AM. CO₂ capture by TiO₂ anatase surfaces: a combined DFT and FTIR study. *J Phys Chem C* 2014;118:25016–26.
- [108] Mino L, Zecchina A, Martra G, Rossi AM, Spoto G. A surface science approach to TiO₂ P25 photocatalysis: an in situ FTIR study of phenol photodegradation at controlled water coverages from sub-monolayer to multilayer. *Appl Catal B-Environ* 2016;196:135–41.
- [109] Langer R, Vacanti JP. *Tissue Eng Sci* 1993;260:920–6.
- [110] Griffith LG, Naughton G. Tissue engineering – current challenges and expanding opportunities. *Science* 2002;295:1009–14.
- [111] Ortiz C, Boyce MC. Materials science – Bioinspired structural materials *Science* 2008; 319:1053–1054.
- [112] Khademhosseini A, Vacanti JP, Langer R. Progress in tissue engineering. *Sci Am* 2009;300:64–71.
- [113] Shi JJ, Votruba AR, Farokhzad OC, Langer R. Nanotechnology in drug delivery and tissue engineering: from discovery to applications. *Nano Lett* 2010;10:3223–30.
- [114] Wegst UGK, Bai H, Saiz E, Tomsia AP, Ritchie RO. Bioinspired structural materials. *Nat. Mater.* 2015;14:23–36.
- [115] Jariwala D, Sangwan VK, Lauhon LJ, Marks TJ, Hersam MC. Carbon nanomaterials for electronics, optoelectronics, photovoltaics, and sensing. *Chem Soc Rev* 2013;42:2824–60.
- [116] McEuen PL, Fuhrer MS, Park HK. Single-walled carbon nanotube electronics. *IEEE Trans Nanotechnol* 2002;1:78–85.
- [117] Ahn JH, Kim HS, Lee KJ, Jeon S, Kang SJ, Sun YG, et al. Heterogeneous three-dimensional electronics by use of printed semiconductor nanomaterials. *Science* 2006;314:1754–7.
- [118] Zeng W, Shu L, Li Q, Chen S, Wang F, Tao XM. Fiber-based wearable electronics: a review of materials, fabrication, devices, and applications. *Adv Mater* 2014;26:5310–36.
- [119] Lamberti C. The use of synchrotron radiation techniques in the characterization of strained semiconductor heterostructures and thin films. *Surf Sci Rep* 2004;53:1–197.
- [120] Zhao YS, Fu HB, Peng AD, Ma Y, Xiao DB, Yao JN. Low-dimensional nanomaterials based on small organic molecules: preparation and optoelectronic properties. *Adv Mater* 2008;20:2859–76.
- [121] Djuricic AB, Ng AMC, Chen XY. ZnO nanostructures for optoelectronics: material properties and device applications. *Prog Quantum Electron* 2010;34:191–259.
- [122] Zhao YS, Fu HB, Peng AD, Ma Y, Liao Q, Yao JN. Construction and optoelectronic properties of organic one-dimensional nanostructures accounts. *Chem Res* 2010;43:409–18.
- [123] Tovar JD. Supramolecular construction of optoelectronic biomaterials accounts. *Chem Res* 2013;46:1527–37.
- [124] Du JH, Pei SF, Ma LP, Cheng HM. 25th anniversary article: carbon nanotube- and graphene- based transparent conductive films for optoelectronic devices. *Adv Mater* 2014;26:1958–91.
- [125] Hirohata A, Takanashi K. Future perspectives for spintronic devices. *J Phys D-Appl Phys* 2014;47:Art. n. 193001 (193040 pages).
- [126] Majumdar S, van Dijken S. Pulsed laser deposition of La_{1-x}Sr_xMnO₃: thin-film properties and spintronic applications. *J Phys D: Appl Phys* 2014;47(3). Art. n. 034010 (034015 pages).
- [127] Bagnall DM, Boreland M. Photovoltaic technologies. *Energy Pol* 2008;36:4390–6.
- [128] El Chaar L, Lamont LA, El Zein N. Review of photovoltaic technologies. *Renew Sust Eng Rev* 2011;15:2165–75.
- [129] Chen DQ, Wang YS, Hong MC. Lanthanide nanomaterials with photon management characteristics for photovoltaic application. *Nano Energy* 2012;1:73–90.
- [130] Bai Y, Mora-Sero I, De Angelis F, Bisquert J, Wang P. Titanium dioxide nanomaterials for photovoltaic applications. *Chem Rev* 2014;114:10095–130.
- [131] Frenkel AI, Hills CW, Nuzzo RG. A view from the inside: Complexity in the atomic scale ordering of supported metal nanoparticles. *J Phys Chem B* 2001;105:12689–703.
- [132] Daniel MC, Astruc D. Gold nanoparticles: assembly, supramolecular chemistry, quantum-size-related properties, and applications toward biology, catalysis, and nanotechnology. *Chem Rev* 2004;104:293–346.

- [133] Li YM, Somorjai GA. Nanoscale advances in catalysis and energy applications. *Nano Lett* 2010;10:2289–95.
- [134] Grunwaldt JD, Schroer CG. Hard and soft X-ray microscopy and tomography in catalysis: bridging the different time and length scales. *Chem Soc Rev* 2010;39:4741–53.
- [135] Pan XL, Bao XH. The effects of confinement inside carbon nanotubes on catalysis accounts. *Chem Res* 2011;44:553–62.
- [136] Pyun J. Graphene oxide as catalyst: application of carbon materials beyond nanotechnology. *Angew Chem-Int Edit* 2011;50:46–8.
- [137] Zhou ZY, Tian N, Li JT, Broadwell I, Sun SG. Nanomaterials of high surface energy with exceptional properties in catalysis and energy storage. *Chem Soc Rev* 2011;40:4167–85.
- [138] Machado BF, Serp P. Graphene-based materials for catalysis. *Catal Sci Technol* 2012;2:54–75.
- [139] Grunwaldt JD, Wagner JB, Dunin-Borkowski RE. Imaging catalysts at work: a hierarchical approach from the macro- to the meso- and nano-scale. *ChemCatChem* 2013;5:62–80.
- [140] Prieto G, Zecevic J, Friedrich H, de Jong KP, de Jongh PE. Towards stable catalysts by controlling collective properties of supported metal nanoparticles. *Nat Mater* 2013;12:34–9.
- [141] Zaera F. Nanostructured materials for applications in heterogeneous catalysis. *Chem Soc Rev* 2013;42:2746–62.
- [142] Zhang Q, Lee I, Joo JB, Zaera F, Yin YD. Core-shell nanostructured catalysts accounts. *Chem Res* 2013;46:1816–24.
- [143] Maul J, Spoto G, Mino L, Erba A. Elucidating the structure and dynamics of CO ad-layers on MgO surfaces. *Phys Chem Chem Phys* 2019;21:26279–83.
- [144] Mino L, Barzan C, Martino GA, Piovano A, Spoto G, Zecchina A, et al. Photoinduced ethylene polymerization on the Cr-VI/SiO₂ Phillips catalyst. *J Phys Chem C* 2019;123:8145–52.
- [145] Mino L, Cesano F, Scarano D, Spoto G, Martra G. Molecules and heterostructures at TiO₂ surface: the cases of H₂O, CO₂, and organic and inorganic sensitizers. *Res Chem Intermed* 2019;45:5801–29.
- [146] Medintz IL, Uyeda HT, Goldman ER, Mattoussi H. Quantum dot bioconjugates for imaging, labelling and sensing. *Nat Mater* 2005;4:435–46.
- [147] Jain PK, Huang XH, El-Sayed IH, El-Sayed MA. Noble metals on the nanoscale: optical and photothermal properties and some applications in imaging, sensing, biology, and medicine accounts. *Chem Res* 2008;41:1578–86.
- [148] Li H, Yin ZY, He QY, Li H, Huang X, Lu G, et al. Fabrication of single- and multilayer MoS₂ film-based field-effect transistors for sensing NO at room temperature. *Small* 2012;8:63–7.
- [149] Zhu SJ, Meng QN, Wang L, Zhang JH, Song YB, Jin H, et al. Highly photoluminescent carbon dots for multicolor patterning, sensors, and bioimaging. *Angew Chem-Int Edit* 2013;52:3953–7.
- [150] Moyano DF, Rotello VM. Nano meets biology: structure and function at the nanoparticle interface. *Langmuir* 2011;27:10376–85.
- [151] Dujardin E, Mann S. Bio-inspired materials chemistry. *Adv Mater* 2002;14:775–88.
- [152] Kay MI, Young RA, Posner AS. Crystal structure of hydroxyapatite 1964;204:1050–1052.
- [153] Sadat-Shojai M, Khorasani MT, Dinpanah-Khoshdargi E, Jamshidi A. Synthesis methods for nanosized hydroxyapatite with diverse structures. *Acta Biomater* 2013;9:7591–621.
- [154] Sakdinawat A, Attwood D. Nanoscale X-ray imaging. *Nat Photonics* 2010;4:840–8.
- [155] Mimura H, Handa S, Kimura T, Yumoto H, Yamakawa D, Yokoyama H, et al. Breaking the 10 nm barrier in hard-X-ray focusing. *Nat Phys* 2010;6:122–5.
- [156] Ice GE, Budai JD, Pang JW. The race to X-ray microbeam and nanobeam science. *Science* 2011;334:1234–9.
- [157] Cagliero S, Borfecchia E, Mino L, Calore L, Bertolotti F, Martinez-Criado G, et al. Insight into non-linearly shaped superconducting whiskers via a synchrotron nanoprobe. *Supercond Sci Technol* 2012;25.
- [158] Martinez-Criado G, Borfecchia E, Mino L, Lamberti C. In: Lamberti C, Agostini G, editors. *Characterization of semiconductor heterostructures and nanostructures*. 2nd edition. Elsevier, Amsterdam; 2013. p. 361–412.
- [159] Suzuki Y, Terada Y. X-Ray absorption and X-ray emission spectroscopy: theory and applications. Chichester (UK): John Wiley & Sons; 2016. p. 251–79.
- [160] Mino L, Borfecchia E, Segura-Ruiz J, Giannini C, Martinez-Criado G, Lamberti C. Materials characterization by synchrotron x-ray microprobes and nanoprobe. *Rev Mod Phys* 2018;90:025007.
- [161] Bleuuet P, Lemelle L, Tucoulou R, Gergaud P, Delette G, Cloetens P, et al. 3D chemical imaging based on a third-generation synchrotron source. *Trac-Trends Anal Chem* 2010;29:518–27.
- [162] Falcaro P, Malfatti L, Vaccari L, Amenitsch H, Marmiroli B, Grecni G, et al. Fabrication of advanced functional devices combining soft chemistry with X-ray lithography in one step. *Adv Mater* 2009;21:4932–6.
- [163] Pagliero A, Mino L, Borfecchia E, Truccato M, Agostino A, Pascale L, et al. Doping change in the Bi-2212 superconductor directly induced by a hard X-ray. *Nanobeam Nano Lett* 2014;14:1583–9.
- [164] Mino L, Bonino V, Agostino A, Prestipino C, Borfecchia E, Lamberti C, Operti L, Fretto M, De Leo N, Truccato M. Maskless X-ray writing of electrical devices on a superconducting oxide with online monitoring: towards nanometer resolution. *Sci Rep* 2017;7:Art. n. 9066.
- [165] Torsello D, Mino L, Bonino V, Agostino A, Operti L, Borfecchia E, et al. Monte Carlo analysis of the oxygen knock-on effects induced by synchrotron x-ray radiation in the Bi₂Sr₂CaCu₂O_{8+d} superconductor. *Phys Rev Mater* 2018;2:8.
- [166] Mino L, Borfecchia E, Agostino A, Lamberti C, Truccato M. Oxygen doping tuning in superconducting oxides by thermal annealing and hard X-ray irradiation. *J Electron Spectroscop Relat Phenom* 2017;220:69–75.
- [167] Bonino V, Agostino A, Prestipino C, Hernandez O, Fretto M, Mino L, et al. Structural and functional modifications induced by X-ray nanopatterning in Bi-2212 single crystals. *CrystEngComm* 2018;20:6667–76.
- [168] Mino L, Bonino V, Picollo F, Fretto M, Agostino A, Truccato M. Tailoring the local conductivity of TiO₂ by X-ray nanobeam irradiation. *Adv Electron Mater* 2019;5:1900129.
- [169] Pfeiffer F, Bunk O, David C, Bech M, Le Duc G, Bravin A, et al. High-resolution brain tumor visualization using three-dimensional x-ray phase contrast tomography. *Phys Med Biol* 2007;52:6923–30.
- [170] Zhu PP, Zhang K, Wang ZL, Liu YJ, Liu XS, Wu ZY, et al. Low-dose, simple, and fast grating-based X-ray phase-contrast imaging. *Proc Natl Acad Sci USA* 2010;107:13576–81.
- [171] Tang RB, Xi Y, Chai WM, Wang YT, Guan YJ, Yang GY, et al. Microbubble-based synchrotron radiation phase contrast imaging: basic study and angiography applications. *Phys Med Biol* 2011;56:3503–12.
- [172] Donner E, Punshon T, Guerinet ML, Lombi E. Functional characterisation of metal(loid) processes in planta through the integration of synchrotron techniques and plant molecular biology. *Anal Bioanal Chem* 2012;402:3287–98.
- [173] Schlichting I, Miao JW. Emerging opportunities in structural biology with X-ray free-electron lasers. *Curr Opin Struct Biol* 2012;22:613–26.
- [174] Wilkins SW, Nesterets YI, Gureyev TE, Mayo SC, Pogany A, Stevenson AW. On the evolution and relative merits of hard X-ray phase-contrast imaging methods. *Philos Trans R Soc A-Math Phys Eng Sci* 2014;372:19.
- [175] Lamberti C, Palomino GT, Bordiga S, Berlier G, D'Acapito F, Zecchina A. Structure of homoleptic Cu-I(CO)₃ cations in Cu-I-exchanged ZSM-5 zeolite: an X-ray absorption study. *Angew Chem-Int Edit* 2000;39:2138–41.
- [176] Nenu CN, Groppo E, Lamberti C, Beale AM, Visser T, Zecchina A, et al. Dichloromethane as a selective modifying agent to create a family of highly reactive chromium polymerization sites. *Angew Chem-Int Edit* 2007;46:1465–8.
- [177] Groppo E, Uddin MJ, Bordiga S, Zecchina A, Lamberti C. Structure and redox activity of copper sites isolated in a nanoporous P4VP polymeric matrix. *Angew Chem-Int Edit* 2008;47:9269–73.
- [178] Borfecchia E, Lomachenko KA, Giordano F, Falsig H, Beato P, Soldatov AV, et al. Revisiting the nature of Cu sites in the activated Cu-SSZ-13 catalyst for SCR reaction. *Chem Sci* 2015;6:548–63.
- [179] Janssens TVW, Falsig H, Lundegaard LF, Vennestrom PNR, Rasmussen SB, Moses PG, et al. A consistent reaction scheme for the selective catalytic reduction of nitrogen oxides with ammonia. *ACS Catal* 2015;5:2832–45.
- [180] Lamberti C, Prestipino C, Bonino V, Capello L, Bordiga S, Spoto G, et al. The chemistry of the oxychlorination catalyst: an in situ, time-resolved XANES study.

- Angew Chem-Int Edit 2002;41:2341–4.
- [181] Grunwaldt JD, Hanneemann S, Schroer CG, Baiker A. 2D-mapping of the catalyst structure inside a catalytic microreactor at work: partial oxidation of methane over Rh/Al₂O₃. *J. Phys Chem B* 2006;110:8674–80.
- [182] Gonzalez-Jimenez ID, Cats K, Davidian T, Ruitenbeek M, Meirer F, Liu YJ, et al. Hard X-ray nanotomography of catalytic solids at work. *Angew Chem-Int Edit* 2012;51:11986–90.
- [183] Sowinska M, Bertaud T, Walczyk D, Thiess S, Calka P, Alff L, Walczyk C, Schroeder T. In-operando hard X-ray photoelectron spectroscopy study on the impact of current compliance and switching cycles on oxygen and carbon defects in resistive switching Ti/HfO₂/TiN cells. *J Appl Phys* 2014;115(20):204509.
- [184] Wang J, Chen-Wiegart Y-cK, Wang J. In operando tracking phase transformation evolution of lithium iron phosphate with hard X-ray microscopy. *Nat Commun* 2014;5(1).
- [185] Li L, Chen-Wiegart Y-cK, Wang J, Gao P, Ding Q, Yu Y-S, Wang F, Cabana J, Wang J, Jin S. Visualization of electrochemically driven solid-state phase transformations using operando hard X-ray spectro-imaging. *Nat Commun* 2015;6(1).
- [186] Oien S, Agostini G, Svelle S, Borfecchia E, Lomachenko KA, Mino L, et al. Probing reactive platinum sites in UiO-67 zirconium metal-organic frameworks. *Chem Mat* 2015;27:1042–56.
- [187] Lomachenko KA, Borfecchia E, Negri C, Berlier G, Lamberti C, Beato P, et al. The Cu-CHA deNO(x) catalyst in action: temperature-dependent NH₃-assisted selective catalytic reduction monitored by operando XAS and XES. *J Am Chem Soc* 2016;138:12025–8.
- [188] Kuppan S, Xu Y, Liu Y, Chen G. Phase transformation mechanism in lithium manganese nickel oxide revealed by single-crystal hard X-ray microscopy. *Nat Commun* 2017;8(1).
- [189] Bragg WL. The diffraction of short electromagnetic waves by a crystal. *Proc Cambridge Phil Soc* 1913;17:43–57.
- [190] Bragg WH. The reflection of X-rays by crystals (II.). *Proc R Soc Lond A* 1913;89:246–8.
- [191] Huygens C. *Traité de la Lumière*, Van der Aa, Leyden; 1690.
- [192] Nakazato T, Oyamada M, Niimura N, Urasawa S, Konno O, Kagaya A, et al. Observation of coherent synchrotron radiation. *Phys Rev Lett* 1989;63:1245–8.
- [193] Snigirev A, Snigireva I, Kohn V, Kuznetsov S, Schelokov I. On the possibilities of x-ray phase contrast microimaging by coherent high-energy synchrotron radiation. *Rev Sci Instrum* 1995;66:5486–92.
- [194] Hwu Y, Tsai WL, Grosio A, Margaritondo G, Je JH. Coherence-enhanced synchrotron radiology: simple theory and practical applications. *J Phys D-Appl Phys* 2002;35:R105–20.
- [195] Bilderback DH, Elleaume P, Weckert E. Review of third and next generation synchrotron light sources. *J Phys B-At Mol Opt Phys* 2005;38:S773–97.
- [196] Kneip S, McGuffey C, Martins JL, Martins SF, Bellei C, Chvykov V, et al. Bright spatially coherent synchrotron X-rays from a table-top source. *Nat Phys* 2010;6:980–3.
- [197] Margaritondo G. X-ray absorption and X-ray emission spectroscopy: theory and applications. Chichester (UK): John Wiley & Sons; 2016. p. 25–50.
- [198] Lambert G, Hara T, Garzella D, Tanikawa T, Labat M, Carre B, et al. Injection of harmonics generated in gas in a free-electron laser providing intense and coherent extreme-ultraviolet light. *Nat Phys* 2008;4:296–300.
- [199] Singer A, Vartanyants IA, Kuhlmann M, Duesterer S, Treusch R, Feldhaus J. Transverse-coherence properties of the free-electron-laser FLASH at DESY. *Phys Rev Lett* 2008;101(25). Art. n. 254801.
- [200] Vartanyants IA, Singer A. Coherence properties of hard x-ray synchrotron sources and x-ray free-electron lasers. *New J Phys* 2012;12(3):035004. <https://doi.org/10.1088/1367-2630/12/3/035004>.
- [201] Vartanyants IA, Singer A, Mancuso AP, Yefanov OM, Sakdinawat A, Liu Y, et al. Coherence properties of individual femtosecond pulses of an X-ray free-electron laser. *Phys Rev Lett* 2011;107(14).
- [202] Ribic PR, Margaritondo G. Status and prospects of x-ray free-electron lasers (X-FELs): a simple presentation. *J Phys D: Appl Phys* 2012;45(21):213001. Art. n. 213001.
- [203] Bostedt C, Bozek JD, Bucksbaum PH, Coffee RN, Hastings JB, Huang Z, Lee RW, Schorb S, Corlett JN, Denes P, Emma P, Falcone RW, Schoenlein RW, Doumy G, Kanter EP, Kraessig B, Southworth S, Young L, Fang L, Hoener M, Berrah N, Roedig C, DiMauro LF. Ultra-fast and ultra-intense x-ray sciences: first results from the Linac Coherent Light Source free-electron laser. *J. Phys. B: At. Mol. Opt. Phys.* 2013;46(16):164003. Art. n. 164003.
- [204] Authier A. *Early Days of X-ray Crystallography*. Oxford: Oxford University Press; 2013.
- [205] van der Veen F, Pfeiffer F. Coherent x-ray scattering. *J Phys-Condens Matter* 2004;16:5003–30.
- [206] Nugent KA. Coherent methods in the X-ray sciences. *Adv Phys* 2010;59:1–99.
- [207] Chapman HN, Fromme P, Barty A, White TA, Kirian RA, Aquila A, et al. Femtosecond X-ray protein nanocrystallography. *Nature* 2011;470:73–7.
- [208] Kern J, Alonso-Mori R, Tran R, Hatne J, Gildea RJ, Echols N, et al. Simultaneous femtosecond X-ray spectroscopy and diffraction of photosystem ii at room temperature. *Science* 2013;340:491–5.
- [209] Liu W, Wacker D, Gati C, Han GW, James D, Wang DJ, et al. Serial Femtosecond crystallography of G protein-coupled receptors. *Science* 2013;342:1521–4.
- [210] Tenboer J, Basu S, Zatsepin N, Pande K, Milathianaki D, Frank M, et al. Time-resolved serial crystallography captures high-resolution intermediates of photoactive yellow protein. *Science* 2014;346:1242–6.
- [211] Miao JW, Ishikawa T, Robinson IK, Murnane MM. Beyond crystallography: diffractive imaging using coherent x-ray light sources. *Science* 2015;348:530–5.
- [212] Tavares PF, Leemann SC, Sjöstrom M, Andersson A. The MAX IV storage ring project. *J Synchrotron Radiat* 2014;21:862–77.
- [213] Dester PS, Sa FH, Liu L. Energy acceptance and on momentum aperture optimization for the Sirius project. *J Phys: Conf Ser* 2017;874:012068.
- [214] Liu L, Westfahl Jr, H. Towards diffraction limited storage ring based light sources, IPAC2017. In: *Proc IPAC2017, Copenhagen, Denmark; 2017*.
- [215] Bostedt C, Boutet S, Fritz DM, Huang ZR, Lee HJ, Lemke HT, et al. Linac coherent light source: the first five years. *Rev Mod Phys* 2016;88:015007.
- [216] Schoenlein RW, Boutet S, Miniti MP, Dunne AM. The linac coherent light source: recent developments and future plans. *Appl Sci-Basel* 2017;7:850.
- [217] Howells MR, Beetz T, Chapman HN, Cui C, Holton JM, Jacobsen CJ, et al. An assessment of the resolution limitation due to radiation-damage in X-ray diffraction microscopy. *J Electron Spectroscop Relat Phenom* 2009;170:4–12.
- [218] Pedrini B, Tsai CJ, Capitani G, Padeste C, Hunter MS, Zatsepin NA et al. 7 angstrom resolution in protein two-dimensional-crystal X-ray diffraction at Linac Coherent Light Source *Philos Trans R Soc B-Biol Sci* 2014;369:Art. n. 20130500.
- [219] Ginn HM, Messerschmidt M, Ji XY, Zhang HW, Axford D, Gildea RJ et al. Structure of CPV17 polyhedrin determined by the improved analysis of serial femtosecond crystallographic data. *Nat Commun* 2015;6:Art. n. 6435.
- [220] Aquila A, Barty A, Bostedt C, Boutet S, Carini G, dePonte D. The linac coherent light source single particle imaging road map *Struct Dyn-US* 2015; 2:041701.
- [221] Falcone R, Jacobsen C, Kirz J, Marchesini S, Shapiro D, Spence J. New directions in X-ray microscopy. *Contemp Phys* 2011;52:293–318.
- [222] Giannini C, De Caro L. Cristallo o non cristallo, questo è il dilemma. *Sapere* 2014:16–21.
- [223] Hohenberg P, Kohn W. Inhomogeneous electron gas 1964;136:B864–B871.
- [224] Abrikosov AA, Gorkov LP, Dzialoshinski IE. *Methods of Quantum Field Theory in Statistical Physics*. Dover Publications; 1975.
- [225] Jackson JD. *Classical electrodynamics*. 3rd ed. New York: John Wiley & Sons Inc.; 1999.
- [226] Landau LD, Lifshitz EM. *The Classical Theory of Fields*. Vol. 2. 4th ed. Butterworth-Heinemann, London; 1975.
- [227] Feynman RP, Leighton RB, Sands M. *The Feynman Lectures on Physics*, Vol II (2nd Ed.), Addison-Wesley, Redwood City, CA, 2005. Now available online at <http://www.feynmanlectures.info/>.
- [228] Born M. *Quantenmechanik der Stoßvorgänge*. *Z. Phys* 1926;38:803–27.
- [229] Bearden JA, Burr AF. Reevaluation of X-ray atomic energy levels. *Rev Mod Phys* 1967;39:125–42.
- [230] Thompson AC, Kirz J, Attwood DT, Gullikson EM, Howells MR, Kortright JB, et al. X-ray data booklet. Berkeley: Lawrence Berkeley National Laboratory; 2009.
- [231] Waller I. Über eine verallgemeinerte Streuungsformel. *Z Phys* 1928;51:213–31.
- [232] Hönl H. Zur Dispersionstheorie der Röntgenstrahlen. *Z Phys* 1933;84:1–16.
- [233] Hönl H. Atomfaktor für Röntgenstrahlen als Problem der Dispersionstheorie (K-Schale). *Ann Phys* 1933;410:625–55.
- [234] Hodeau JL, Favre-Nicolin V, Bos S, Renevier H, Lorenzo E, Berar JF. Resonant diffraction. *Chem Rev* 2001;101:1843–67.

- [235] de L. Kronig R. On the theory of dispersion of X-rays. *J. Opt. Soc. Am.* 1926;12:547–57.
- [236] Kramers HA. La diffusion de la lumière par les atomes. *Atti Cong Intern. Fisici*, (Transactions of Volta Centenary Congress) Como 1927;2:545–57.
- [237] Sayers DE, Stern EA, Lytle FW. New technique for investigating noncrystalline structures: Fourier analysis of the extended X-Ray absorption fine structure. *Phys Rev Lett* 1971;27:1204–7.
- [238] Filippini A, Di Cicco A, Natoli CR. X-ray-absorption spectroscopy and n-body distribution functions in condensed matter.1. Theory. *Phys Rev B* 1995;52:15122–34.
- [239] Filippini A, Di Cicco A. X-ray-absorption spectroscopy and n-body distribution functions in condensed matter.2. Data analysis and applications. *Phys Rev B* 1995;52:15135–49.
- [240] Kas JJ, Jorissen K, Rehr JJ. X-Ray Absorption and X-Ray Emission Spectroscopy: Theory and Applications. Chichester (UK): John Wiley & Sons; 2016. p. 51–72.
- [241] Joly Y. X-ray absorption near-edge structure calculations beyond the muffin-tin approximation. *Phys Rev B* 2001;63:10.
- [242] Benfatto M, Della Longa S, Natoli CR. The MXAN procedure: a new method for analysing the XANES spectra of metalloproteins to obtain structural quantitative information. *J Synchrotron Radiat* 2003;10:51–7.
- [243] Guda SA, Guda AA, Soldatov MA, Lomachenko KA, Bugaev AL, Lamberti C, et al. Optimized finite difference method for the full-potential xanes simulations: application to molecular adsorption geometries in MOFs and metal-ligand intersystem crossing transients. *J Chem Theory Comput* 2015;11:4512–21.
- [244] Joly Y, Grenier S. X-Ray Absorption and X-Ray Emission Spectroscopy: Theory and Applications. Chichester (UK): John Wiley & Sons; 2016. p. 73–97.
- [245] Stragier H, Cross JO, Rehr JJ, Sorensen LB, Bouldin CE, Woicik JC. Diffraction anomalous fine-structure – a new X-Ray structural technique. *Phys Rev Lett* 1992;69:3064–7.
- [246] Pickering IJ, Sansone M, Marsch J, George GN. Diffraction anomalous fine-structure – a new technique for probing local atomic environment. *J Am Chem Soc* 1993;115:6302–11.
- [247] Parratt LG. Surface studies of solids by total reflection of X-rays. *Phys Rev* 1954;95:359–69.
- [248] James RW. The Optical Principles of the Diffraction of X-rays. Woodbridge: Ox Bow Press; 1962.
- [249] Born M, Wolf E. Principles of Optics: Electromagnetic Theory of Propagation, Interference and Diffraction of Light. VII ed. Cambridge: Cambridge University Press; 1999.
- [250] Hoppersky AN, Yavna VA. Scattering of photons by many-electron systems. Heidelberg: Springer; 2010.
- [251] Gianturco FA, Jain A. the theory of electron-scattering from polyatomic-molecules. *Phys Rep-Rev Sec Phys Lett* 1986;143:347–425.
- [252] Palmer RE, Rous PJ. resonances in electron-scattering by molecules on surfaces. *Rev Mod Phys* 1992;64:383–440.
- [253] Cockayne DJH. Annual review of materials research. *Annual Reviews*. Palo Alto; 2007. p. 159–87.
- [254] Bragg WH, Bragg WL. The reflection of X-rays by crystals. *Proc R Soc Lond A* 1913;88:428–38.
- [255] Compton AH. A quantum theory of the scattering of X-rays by light elements. *Phys Rev* 1923;21:483–502.
- [256] Einstein A. Über einen die Erzeugung und Verwandlung des Lichtes betreffenden heuristischen Gesichtspunkt. *Ann Phys* 1905;322:132–48.
- [257] Ewald P. Introduction to the dynamical theory of X-ray diffraction. *Acta Cryst A* 1969;25:103–8.
- [258] Miller WH. A treatise on crystallography. Cambridge: Deighton; 1839.
- [259] Egami T, Billinge SJL. Underneath the Bragg peaks – structural analysis of complex materials. 2nd ed. Oxford: Pergamon; 2012.
- [260] Friedrich W, Knipping P, von Laue M. Interferenz-Erscheinungen bei Röntgenstrahlen. Bayerische Akademie der Wissenschaften 1912:303–22.
- [261] Kittel C. Introduction to solid state physics. 8th ed New York: John Wiley & Sons; 2004.
- [262] Brillouin L. Les électrons dans les métaux et le classement des ondes de de Broglie correspondantes C. R. Acad. Sci. (Paris) 1930;191:292–4.
- [263] Bassani F, Grassano UM. Fisica dello Stato Solido. Turin: Bollati Boringhieri; 2000.
- [264] Borfecchia E, Gianolio D, Agostini G, Bordiga S, Lamberti C. In: Llabrés FX, Xamena i, Gascon J, editors. Metal Organic Frameworks as Heterogeneous Catalysts, Royal Soc Chemistry, Cambridge; 2013. p. 143–208.
- [265] Billinge SJL, Kanatzidis MG. Beyond crystallography: the study of disorder, nanocrystallinity and crystallographically challenged materials with pair distribution functions. *Chem Commun* 2004;749–60.
- [266] Debye P. Interferenz von Röntgenstrahlen und Wärmebewegung. *Ann Phys.* 1913;348:49–92.
- [267] Debye P. Dispersion of Roentgen rays. *Ann. Phys.* 1915;46:809–23.
- [268] Lamberti C, Borfecchia E, van Bokhoven JA, Fernández-García M. X-Ray Absorption and X-Ray Emission Spectroscopy: Theory and Applications. Chichester (UK): John Wiley & Sons; 2016. p. 303–50.
- [269] Svergun DI. Determination of the regularization parameter in indirect-transform methods using perceptual criteria. *J Appl Crystallogr* 1992;25:495–503.
- [270] Kornysushin Y. Application of Thomas-Fermi model to fullerene molecule and nanotube. *Facta Universitatis, Series: Phys Chem Technol* 2007;5:11–8.
- [271] Juhás P, Davis T, Farrow CL, Billinge SJL. PDFgetX3: A rapid and highly automatable program for processing powder diffraction data into total scattering pair distribution functions. *J Appl Crystallogr* 2013;46:560–6.
- [272] Farrow CL, Juhas P, Liu JW, Bryndin D, Boin ES, Bloch J, Proffen T, Billinge SJL, PDFfit2 and PDFgui: computer programs for studying nanostructure in crystals. *J Phys Condens Matter* 2007; 19:Art. n. 335219.
- [273] Jephcoat AP, Hriljac JA, Finger LW, Cox DE. Pressure-induced orientational order in C60 at 300 K. *Europhys Lett* 1994;25:429–34.
- [274] Sun Q, Dai ZF, Meng XJ, Xiao FS. Porous polymer catalysts with hierarchical structures. *Chem Soc Rev* 2015;44:6018–34.
- [275] Diaferia C, Mercurio FA, Giannini C, Sibillano T, Morelli G, Leone M, et al. Self-assembly of PEGylated tetra-phenylalanine derivatives: structural insights from solution and solid state studies *Sci Rep* 2016; 6:Art. n. 26638.
- [276] Diaferia C, Sibillano T, Balasco N, Giannini C, Roviello V, Vitagliano L, et al. Hierarchical analysis of self-assembled PEGylated hexaphenylalanine photoluminescent nanostructures. *Chem-Eur J* 2016;22:16586–97.
- [277] Fang B, Kim JH, Kim MS, Yu JS. Hierarchical nanostructured carbons with meso-macroporosity: design, characterization, and applications accounts. *Chem Res* 2013;46:1397–406.
- [278] Yu JG, Su YR, Cheng B. Template-free fabrication and enhanced photocatalytic activity of hierarchical macro-/mesoporous titania. *Adv Funct Mater* 2007;17:1984–90.
- [279] Fan W, Snyder MA, Kumar S, Lee PS, Yoo WC, McCormick AV, et al. Hierarchical nanofabrication of microporous crystals with ordered mesoporosity. *Nat Mater* 2008;7:984–91.
- [280] Serrano DP, Escola JM, Pizarro P. Synthesis strategies in the search for hierarchical zeolites. *Chem Soc Rev* 2013;42:4004–35.
- [281] de la Rica R, Matsui H. Applications of peptide and protein-based materials in bionanotechnology. *Chem Soc Rev* 2010;39:3499–509.
- [282] Fleming S, Ulijn RV. Design of nanostructures based on aromatic peptide amphiphiles. *Chem Soc Rev* 2014;43:8150–77.
- [283] Yan XH, Zhu PL, Li JB. Self-assembly and application of diphenylalanine-based nanostructures. *Chem Soc Rev* 2010;39:1877–90.
- [284] Gazit E. Self-assembled peptide nanostructures: the design of molecular building blocks and their technological utilization. *Chem Soc Rev* 2007;36:1263–9.
- [285] Huang RL, Su RX, Qi W, Zhao J, He ZM. Hierarchical interface-induced self-assembly of diphenylalanine: formation of peptide nanofibers and microvesicles. *Nanotechnology* 2011;22:7.
- [286] Rosenman G, Bekker P, Koren I, Yevnin M, Bank-Srouer B, Mishina E, et al. Bioinspired peptide nanotubes: deposition technology, basic physics and nanotechnology applications. *J Pept Sci* 2011;17:75–87.
- [287] Altamura D, Lassandro R, Vittoria FA, De Caro L, Siliqi D, Ladisa M, et al. X-ray microimaging laboratory (XMI-LAB). *J Appl Crystallogr* 2012;45:869–73.
- [288] Sibillano T, De Caro L, Altamura D, Siliqi D, Ramella M, Boccafocchi F, et al. An optimized table-top small-angle X-ray scattering set-up for the nanoscale structural analysis of soft. *Matter Sci Rep* 2014;4:7.
- [289] Serpell LC. Alzheimer's amyloid fibrils: structure and assembly. *Biochim Biophys Acta-Mol Basis Dis* 2000;1502:16–30.
- [290] Semenyuk AV, Svergun DI. Gnom – a program package for small-angle scattering data-processing. *J Appl Crystallogr* 1991;24:537–40.
- [291] Dorfs D, Krahne R, Falqui A, Manna L, Giannini C, Zanchet D. *Comprehensive Nanoscience and Technology, Vol 1: Nanomaterials*. Amsterdam: Elsevier Science Bv; 2011. p. 219–70.

- [292] Schaaff TG, Shafiqullin MN, Khoury JT, Vezmar I, Whetten RL, Cullen WG, et al. Isolation of smaller nanocrystal Au molecules: robust quantum effects in optical spectra. *J Phys Chem B* 1997;101:7885–91.
- [293] Gordon TR, Diroll BT, Paik T, Doan-Nguyen VVT, Gaubing EA, Murray CB. Characterization of shape and monodispersity of anisotropic nanocrystals through atomistic X-ray scattering simulation. *Chem Mat* 2015;27:2502–6.
- [294] Decuzzi P, Pasqualini R, Arap W, Ferrari M. Intravascular delivery of particulate systems: does geometry really matter? *Pharm Res* 2009;26:235–43.
- [295] Ananta JS, Godin B, Sethi R, Moriggi L, Liu XW, Serda RE, et al. Geometrical confinement of gadolinium-based contrast agents in nanoporous particles enhances T-1 contrast. *Nat Nanotechnol* 2010;5:815–21.
- [296] Fiore A, Mastria R, Lupu MG, Lanzani G, Giannini C, Carlino E, et al. Tetrapod-shaped colloidal nanocrystals of II-VI semiconductors prepared by seeded growth. *J Am Chem Soc* 2009;131:2274–82.
- [297] Frey F, Boysen H. Disorder in cobalt single crystals. *Acta Crystallogr Sect A Found Crystallogr* 1981;37:819–26.
- [298] Ornstein LS, Zernike F. *Phys Z* 1918;17:134.
- [299] Ornstein LS, Zernike F. *Phys Z* 1926;257:761.
- [300] Percus JK, Yevick GJ. Analysis of classical statistical mechanics by means of collective coordinates. *Phys Rev* 1958;110:1–13.
- [301] Lambert RJ. Percus-Yevick equation for hard spheres with surface adhesion. *J Chem Phys* 1968;49:2770–4.
- [302] Mandel F, Bearman RJ, Bearman MY. Numerical solutions of the Percus-Yevick equation for the Lennard-Jones (6–12) and hard-sphere potentials. *J Chem Phys* 1970;52:3315–23.
- [303] Hosemann R. Die parakristalline Feinstruktur natürlicher und synthetischer Eiweisse. Visuelles Näherungsverfahren zur Bestimmung der Schwingungstensoren von Gitterzellen. *Acta Cryst* 1951;4:520–30.
- [304] Matsuoka H, Tanaka H, Hashimoto T, Ise N. Elastic scattering from cubic lattice systems with paracrystalline distortion. *Phys Rev. B* 1987;36:1754–65.
- [305] Matsuoka H, Tanaka H, Iizuka N, Hashimoto T, Ise N. Elastic scattering from cubic lattice systems with paracrystalline distortion. II. *Phys Rev B* 1990;41:3854–6.
- [306] Eads JL, Millane RP. Diffraction by the ideal paracrystal. *Acta Crystallogr A* 2001;57:507–17.
- [307] Buljan M, Radic N, Bernstorff S, Drazic G, Bogdanovic-Radovic I, Holy V. Grazing-incidence small-angle X-ray scattering: application to the study of quantum dot lattices. *Acta Crystallogr Sect A* 2012;68:124–38.
- [308] Eisenberger P, Kincaid BM. EXAFS: New Horizons in Structure Determinations Science 1978;200:1441–1447.
- [309] Lee PA, Citrin PH, Eisenberger P, Kincaid BM. Extended x-ray absorption fine structure - its strengths and limitations as a structural tool. *Rev Mod Phys* 1981;53:769–806.
- [310] Calvin S. XAFS for Everyone. Boca Raton FL: Taylor & Francis; 2013.
- [311] van Bokhoven JA, Lamberti C. X-ray absorption and X-ray emission spectroscopy: theory and applications. Chichester (UK): John Wiley & Sons; 2016.
- [312] Kuzmin A, Chaboy J. EXAFS and XANES analysis of oxides at the nanoscale. *IUCrJ* 2014;1:571–89.
- [313] Soldatov AV, Lomachenko KA. X-Ray Absorption and X-Ray Emission Spectroscopy: Theory and Applications. Chichester (UK): John Wiley & Sons; 2016. p. 809–27.
- [314] Hayes TM, Boyce JB. Extended X-ray absorption fine structure spectroscopy. *Solid State Phys* 1983;37:173–351.
- [315] Boscherini F. X-Ray Absorption and X-Ray Emission Spectroscopy: Theory and Applications. Chichester (UK): John Wiley & Sons; 2016. p. 437–58.
- [316] Lamberti C, Bordiga S, Boscherini F, Pascarelli S, Schiavini GM. Extended x-ray-absorption fine-structure investigation on buried InAsP/InP interfaces. *Appl Phys Lett* 1994;64:1430–2.
- [317] Pascarelli S, Boscherini F, Lamberti C, Mobilio S. Tetragonal-strain-induced local structural modifications in InAs_xP_{1-x}/InP superlattices: a detailed x-ray-absorption investigation. *Phys Rev B* 1997;56:1936–47.
- [318] Boscherini F, Lamberti C, Pascarelli S, Rigo C, Mobilio S. Local atomic structure in strained interfaces of In_xGa_{1-x}As/InP heterostructures. *Phys Rev B* 1998;58:10745–53.
- [319] Lamberti C, Bordiga S, Boscherini F, Mobilio S, Pascarelli S, Gastaldi L, et al. Structural and optical investigation of InAs_xP_{1-x}/InP strained superlattices. *J. Appl. Phys.* 1998;83:1058–77.
- [320] Romanato F, De Salvador D, Berti M, Drigo A, Natali M, Tormen M, et al. Bond-length variation in In_xGa_{1-x}As/InP strained epitaxial layers. *Phys Rev B* 1998;57:14619–22.
- [321] Bianconi A. Surface X-ray absorption spectroscopy: surface EXAFS and surface XANES. *Appl Surf Sci* 1980;6:392–418.
- [322] Stöhr J. NEXAFS Spectroscopy. Heidelberg: Springer; 1992.
- [323] Chen JG. NEXAFS investigations of transition metal oxides, nitrides, carbides, sulfides and other interstitial compounds. *Surf Sci Rep* 1997;30:1–152.
- [324] Ade H, Hitchcock AP. NEXAFS microscopy and resonant scattering: composition and orientation probed in real and reciprocal space. *Polymer* 2008;49:643–75.
- [325] Watts B, Ade H. NEXAFS imaging of synthetic organic materials. *Mater Today* 2012;15:148–57.
- [326] Dirac PAM. The quantum theory of emission and absorption of radiation. *Proc Roy Soc (London) A* 1927;114:243–65.
- [327] Fermi E. Nuclear Physics. Chicago, IL: University of Chicago Press; 1950.
- [328] Brillson LJ. Surfaces and Interfaces of Electronic Materials. Weinheim: Wiley-VCH Verlag GmbH & Co. KGaA; 2010. p. 552–4.
- [329] Lambert JH. Photometria sive de mensura et gradibus luminis, colorum et umbrae (Latin: Photometry, or, on the measure and gradations of light, colors, and shade). Eberhardt. Klett, Augsburg; 1760.
- [330] Beer A. Bestimmung der Absorption des rothen Lichts in farbigen Flüssigkeiten (Determination of the absorption of red light in colored liquids). *Ann Phys Chem* 1852;86:78–88.
- [331] Jaklevic J, Kirby JA, Klein MP, Robertson AS, Brown GS, Eisenberger P. Fluorescence detection of EXAFS: sensitivity enhancement for dilute species and thin films. *Solid State Commun* 1977;23:679–82.
- [332] Bambynek W, Crasemann B, Fink RW, Freund HU, Mark H, Swift CD, et al. X-Ray fluorescence yields, Auger, and Coster-Kronig transition probabilities. *Rev Mod Phys* 1972;44:716–813.
- [333] Krause MO. Atomic radiative and radiationless yields for K and L shells. *J Phys Chem Ref Data* 1979;8:307–27.
- [334] Ruizlopez MF, Loos M, Goulon J, Benfatto M, Natoli CR. Reinvestigation of the EXAFS and XANES spectra of ferrocene and nickelocene in the framework of the multiple-scattering theory. *Chem Phys* 1988;121:419–37.
- [335] Brouder C, Lopez MFR, Benfatto M, Natoli CR, Pettifer RF. Systematic-approach to the calculation of the polarization-dependent (and polarization-averaged) general term of the curved-wave multiple-scattering series in the x-ray-absorption cross-section. *Phys Rev B* 1989;39:1488–500.
- [336] Krause MO, Oliver JH. Natural widths of atomic K and L levels, K α X-ray lines and several KLL Auger lines. *J Phys Chem Ref Data* 1979;8:329–38.
- [337] Filipponi A, Diccico A, Tyson TA, Natoli CR. Ab initio modeling of X-ray absorption spectra. *Solid State Commun* 1991;78:265–8.
- [338] Westre TE, Diccico A, Filipponi A, Natoli CR, Hedman B, Solomon EI, et al. GNXAS, a multiple-scattering approach to EXAFS analysis – methodology and applications to iron complexes. *J Am Chem Soc* 1995;117:1566–83.
- [339] Stern EA, Sayers DE, Lytle FW. Extended X-ray-absorption fine-structure technique 3. Determination of physical parameters. *Phys Rev B* 1975;11:4836–46.
- [340] Lytle FW, Sayers DE, Stern EA. Extended X-ray-absorption fine-structure technique. 2. Experimental practice and selected results. *Phys Rev B* 1975;11:4825–35.
- [341] Kas JJ, Sorini AP, Prange MP, Cambell LW, Sojinin JA, Rehr JJ. Many-pole model of inelastic losses in x-ray absorption spectra. *Phys Rev B* 2007;76:195116.
- [342] Kas JJ, Rehr JJ, Curtis JB. Particle-hole cumulant approach for inelastic losses in x-ray spectra. *Phys Rev B* 2016;94:035156.
- [343] Seah MP, Dench WA. Quantitative electron spectroscopy of surfaces: a standard data base for electron inelastic mean free paths in solids. *Surf Interface Anal* 1979;1:2–11.
- [344] Beni G, Platzman PM. Temperature and polarization dependence of extended x-ray absorption fine-structure spectra. *Phys Rev B* 1976;14:1514–8.
- [345] Kuzmin A, Purans J. The influence of the focusing effect on the X-ray-absorption fine-structure above all the tungsten-L edges in nonstoichiometric tungsten-oxides. *J Phys-Condens Matter* 1993;5:9423–30.
- [346] Yokoyama T, Kobayashi K, Ohta T, Ugawa A. Anharmonic interatomic potentials of diatomic and linear triatomic molecules studied by extended x-ray-

- absorption fine structure. *Phys Rev B* 1996;53:6111–22.
- [347] Westre TE, Diccico A, Filipponi A, Natoli CR, Hedman B, Solomon EI, et al. Determination of the Fe-N-O angle in $(\text{FeNO})_7$ complexes using multiple-scattering EXAFS analysis by GNXAS. *J Am Chem Soc* 1994;116:6757–68.
- [348] Crusemann R, Bokman F, Fritzsche V, Bertagnolli H. A multiple-scattering EXAFS study of organometallic compounds - $\text{W}(\text{CO})_6$ and (1,3,5-trimethylbenzene) $\text{W}(\text{CO})(3)(1,3,5\text{-trimethylbenzene})\text{W}(\text{CO})_3$. *Chem Phys* 1995;194:81–90.
- [349] Lamberti C, Palomino GT, Bordiga S, Berlier G, D'Acapito F, Zecchina A. Structure of homoleptic $\text{Cu}^I(\text{CO})_3$ cations in Cu^I -exchanged ZSM-5 zeolite: an X-ray absorption study. *Angew Chem-Int Edit* 2000;39:2138–41.
- [350] Prestipino C, Capello L, D'Acapito F, Lamberti C. Local structure of $\text{Cu}(\text{CO})_2^+$ adducts hosted inside ZSM-5 zeolite probed by EXAFS, XANES and IR spectroscopies. *Phys Chem Chem Phys* 2005;7:1743–6.
- [351] Gianolio D, Groppo E, Vitillo JG, Damin A, Bordiga S, Zecchina A, et al. Direct evidence of adsorption induced Cr^{II} mobility on the SiO_2 surface upon complexation by CO. *Chem Commun* 2010;46:976–8.
- [352] Chen LX, Bowman MK, Thurnauer MC, Lytle FW, Norris JR. Molecular-structure of nickelcyclopentadienylnitrosyl in condensed phases studied by EXAFS. *Chem Phys Lett* 1992;200:290–6.
- [353] El Nahhas A, van der Veen RM, Penfold TJ, Pham VT, Lima FA, Abela R, et al. X-ray absorption spectroscopy of ground and excited rhenium-carbonyl diimine-complexes: evidence for a two-center electron transfer. *J Phys Chem A* 2013;117:361–9.
- [354] Tyrstedt C, Borfecchia E, Berlier G, Lomachenko KA, Lamberti C, Bordiga S, et al. Nitrate-nitrite equilibrium in the reaction of NO with a Cu-CHA catalyst for $\text{NH}_3\text{-SCR}$. *Catal Sci Technol* 2016;6:8314–24.
- [355] Kuzmin A, Purans J, Benfatto M, Natoli CR. X-ray-absorption study of rhenium L_3 and L_1 edges in ReO_3 – multiple-scattering approach. *Phys Rev B* 1993;47:2480–6.
- [356] Groppo E, Prestipino C, Lamberti C, Luches P, Giovanardi C, Boscherini F. Growth of NiO on Ag(001): atomic environment, strain, and interface relaxations studied by polarization dependent extended X-ray absorption fine structure. *J Phys Chem B* 2003;107:4597–606.
- [357] Lamberti C, Groppo E, Prestipino C, Casassa S, Ferrari AM, Pisani C, et al. Oxide/metal interface distance and epitaxial strain in the NiO/Ag(001) system. *Phys Rev Lett* 2003;91:046101.
- [358] Luches P, D'Addato S, Valeri S, Groppo E, Prestipino C, Lamberti C, et al. X-ray absorption study at the Mg and OK edges of ultrathin MgO epilayers on Ag(001). *Phys Rev B* 2004;69:045412.
- [359] Lee PA, Pendry JB. Theory of the extended x-ray absorption fine structure 1975;11:2795–2811.
- [360] Zabinsky SI, Rehr JJ, Ankudinov A, Albers RC, Eller MJ. Multiple-scattering calculations of X-ray-absorption spectra. *Phys Rev B* 1995;52:2995–3009.
- [361] Frenkel A. Solving the 3D structure of metal nanoparticles. *Z Kristall* 2007;222:605–11.
- [362] Witkowska A, Di Cicco A, Principi E. Local ordering of nanostructured Pt probed by multiple-scattering XAFS. *Phys Rev B* 2007;76:12.
- [363] Beale AM, Weckhuysen BM. EXAFS as a tool to interrogate the size and shape of mono and bimetallic catalyst nanoparticles. *Phys Chem Chem Phys* 2010;12:5562–74.
- [364] Greco G, Witkowska A, Principi E, Minicucci M, Di Cicco A. Local structural and chemical ordering of nanosized $\text{Pt}_{3\pm d}\text{Co}$ probed by multiple-scattering x-ray absorption spectroscopy. *Phys Rev B* 2011;83:134103.
- [365] Agostini G, Piovano A, Bertinetti L, Pellegrini R, Leofanti G, Groppo E, et al. Effect of different face centered cubic nanoparticle distributions on particle size and surface area determination: a theoretical study. *J Phys Chem C* 2014;118:4085–94.
- [366] Bugaev AL, Guda AA, Lomachenko KA, Shapovalov VV, Lazzarini A, Vitillo JG, et al. Core-shell structure of palladium hydride nanoparticles revealed by combined X-ray absorption spectroscopy and X-ray diffraction. *J Phys Chem C* 2017;121:18202–13.
- [367] Nyquist H. Certain topics in telegraph transmission theory. *Trans Am Instit Elec Eng* 1928;47:617–44.
- [368] Shannon CE. A mathematical theory of communication. *Bell Syst Tech J* 1948;27:623–56.
- [369] Shannon CE. Communication in the presence of noise. *Proc IRE* 1949;37:10–21.
- [370] Bonino F, Chavan S, Vitillo JG, Groppo E, Agostini G, Lamberti C, et al. Local structure of CPO-27-Ni metallorganic framework upon dehydration and coordination of NO. *Chem Mat* 2008;20:4957–68.
- [371] Chavan S, Vitillo JG, Groppo E, Bonino F, Lamberti C, Dietzel PDC, et al. CO adsorption on CPO-27-Ni coordination polymer: spectroscopic features and interaction energy. *J Phys Chem C* 2009;113:3292–9.
- [372] Valenzano L, Civalleri B, Chavan S, Bordiga S, Nilsen MH, Jakobsen S, et al. Disclosing the complex structure of UiO-66 metal organic framework: a synergic combination of experiment and theory. *Chem Mat* 2011;23:1700–18.
- [373] Chavan S, Vitillo JG, Gianolio D, Zavorotynska O, Civalleri B, Jakobsen S, et al. H_2 storage in isostructural UiO-67 and UiO-66 MOFs. *Phys Chem Chem Phys* 2012;14:1614–26.
- [374] Valenzano L, Vitillo JG, Chavan S, Civalleri B, Bonino F, Bordiga S, et al. Structure-activity relationships of simple molecules adsorbed on CPO-27-Ni metal-organic framework: in situ experiments vs. theory. *Catal Today* 2012;182:67–79.
- [375] Chavan S, Bonino F, Valenzano L, Civalleri B, Lamberti C, Acerbi N, et al. Fundamental aspects of H_2S adsorption on CPO-27-Ni. *J Phys Chem C* 2013;117:15615–22.
- [376] Jakobsen S, Gianolio D, Wragg DS, Nilsen MH, Emerich H, Bordiga S, et al. Structural determination of a highly stable metal-organic framework with possible application to interim radioactive waste scavenging: Hf-UiO-66. *Phys Rev B* 2012;86:11.
- [377] Tulchinsky Y, Hendon CH, Lomachenko KA, Borfecchia E, Melot BC, Hudson MR, et al. Reversible capture and release of Cl_2 and Br_2 with a redox-active metal-organic framework. *J Am Chem Soc* 2017;139:5992–7.
- [378] Stubbs AW, Braglia L, Borfecchia E, Meyer RJ, Roman-Leshkov Y, Lamberti C, et al. Selective catalytic olefin epoxidation with Mn-II-exchanged MOF-5. *ACS Catal* 2018;8:596–601.
- [379] Salassa L, Garino C, Salassa G, Nervi C, Gobetto R, Lamberti C, et al. Ligand-selective photodissociation from $[\text{Ru}(\text{bpy})(4\text{AP})_4]^{2+}$: a spectroscopic and computational study. *Inorg Chem* 2009;48:1469–81.
- [380] Estephane J, Groppo E, Vitillo JG, Damin A, Gianolio D, Lamberti C, et al. A multitechnique approach to spin-flips for $\text{Cp}_2\text{Cr}(\text{II})$ chemistry in confined state. *J Phys Chem C* 2010;114:4451–8.
- [381] Salassa L, Ruiu T, Garino C, Pizarro AM, Bardelli F, Gianolio D, et al. Light-induced nucleobase binding, and cytotoxicity of the photoactive complex $\text{cis-}[\text{Ru}(\text{bpy})_2(\text{CO})\text{Cl}]^+$. *Organometallics* 2010;29:6703–10.
- [382] Borfecchia E, Garino C, Salassa L, Ruiu T, Gianolio D, Zhang XY, et al. X-ray transient absorption structural characterization of the $^3\text{MLCT}$ triplet excited state of $\text{cis-}[\text{Ru}(\text{bpy})_2(\text{py})_2]^{2+}$. *Dalton Trans* 2013;42:6564–71.
- [383] Korzynski MD, Braglia L, Borfecchia E, Lamberti C, Dinca M. Molecular niobium precursors in various oxidation states: An XAS case study. *Inorg Chem* 2018;57:13998–4004.
- [384] Estephane J, Groppo E, Damin A, Vitillo JG, Gianolio D, Lamberti C, et al. Structure and enhanced reactivity of chromocene carbonyl confined inside cavities of NaY zeolite. *J Phys Chem C* 2009;113:7305–15.
- [385] Agostini G, Grisenti R, Lamberti C, Piovano A, Fornasini P. Thermal effects on Rhodium nanoparticles supported on carbon. *J Phys: Conf Ser* 2013;430:012031.
- [386] Teo BK. EXAFS: Basic Principles and Data Analysis. Berlin: Springer; 1986.
- [387] D'Angelo P, Dinola A, Filipponi A, Pavel NV, Roccatano D. An extended X-ray-absorption fine-structure study of aqueous-solutions by employing molecular-dynamics simulations. *J Chem Phys* 1994;100:985–94.
- [388] Dangelo P, Dinola A, Filipponi A, Pavel NV, Roccatano D. An extended X-ray-absorption fine-structure study of aqueous-solutions by employing molecular-dynamics simulations. *J Chem Phys* 1994;100:985–94.
- [389] D'Angelo P, Pavel NV, Roccatano D, Nolting HF. Multielectron excitations at the L edges of barium in aqueous solution. *Phys Rev B* 1996;54:12129–38.
- [390] D'Angelo P, DiNola A, Mangoni M, Pavel NV. An extended x-ray absorption fine structure study by employing molecular dynamics simulations: bromide ion in methanolic solution. *J Chem Phys* 1996;104:1779–90.

- [391] McCarthy MI, Schenter GK, ChaconTaylor MR, Rehr JJ, Brown GE. Prediction of extended x-ray-absorption fine-structure spectra from molecular interaction models: $\text{Na}^+(\text{H}_2\text{O})_n\text{-MgO}$ (100) interface. *Phys Rev B* 1997;56:9925–36.
- [392] Chillemi G, D'Angelo P, Pavel NV, Sanna N, Barone V. Development and validation of an integrated computational approach for the study of ionic species in solution by means of effective two-body potentials. The case of Zn^{2+} , Ni^{2+} , and Co^{2+} in aqueous solutions. *J Am Chem Soc* 2002;124:1968–76.
- [393] D'Angelo P, Barone V, Chillemi G, Sanna N, Meyer-Klaucke W, Pavel NV. Hydrogen and higher shell contributions in Zn^{2+} , Ni^{2+} , and Co^{2+} aqueous solutions: an X-ray absorption fine structure and molecular dynamics study. *J Am Chem Soc* 2002;124:1958–67.
- [394] Merkling PJ, Munoz-Paez A, Marcos ES. Exploring the capabilities of X-ray absorption spectroscopy for determining the structure of electrolyte solutions: computed spectra for Cr^{3+} or Rh^{3+} in water based on molecular dynamics. *J Am Chem Soc* 2002;124:10911–20.
- [395] Okamoto Y. XAFS simulation of highly disordered materials. *Nucl Instrum Methods Phys Res Sect A-Accel Spectrom Dect Assoc Equip* 2004;526:572–83.
- [396] Ferlat G, Soetens JC, San Miguel A, Bopp PA. Combining extended x-ray absorption fine structure with numerical simulations for disordered systems. *J Phys-Condens Matter* 2005;17:S145–57.
- [397] Kuzmin A, Evarestov RA. Quantum mechanics-classical molecular dynamics approach to EXAFS. *J Phys Conf Ser* 2009;190:012024.
- [398] D'Angelo P, Migliorati V, Guidoni L. Hydration properties of the bromide aqua ion: the interplay of first principle and classical molecular dynamics, and x-ray absorption spectroscopy. *Inorg Chem* 2010;49:4224–31.
- [399] D'Angelo P, Zitolo A, Migliorati V, Chillemi G, Duvail M, Vitorge P, et al. Revised ionic radii of lanthanoid(III) ions in aqueous solution. *Inorg Chem* 2011;50:4572–9.
- [400] Roscioni OM, Zonias N, Price SWT, Russell AE, Comaschi T, Skylaris CK. Computational prediction of L_3 EXAFS spectra of gold nanoparticles from classical molecular dynamics simulations. *Phys Rev B* 2011;83:8.
- [401] Price SWT, Zonias N, Skylaris CK, Hyde TI, Ravel B, Russell AE. Fitting EXAFS data using molecular dynamics outputs and a histogram approach. *Phys Rev B* 2012;85:14.
- [402] D'Angelo P, Martelli F, Spezia R, Filippini A, Denecke MA. Hydration properties and ionic radii of actinide(III) ions in aqueous solution. *Inorg Chem* 2013;52:10318–24.
- [403] Timoshenko J, Anspoks A, Kalinko A, Kuzmin A. Temperature dependence of the local structure and lattice dynamics of wurtzite-type ZnO. *Acta Mater* 2014;79:194–202.
- [404] Migliorati V, D'Angelo P. Unraveling the Sc^{3+} hydration geometry: the strange case of the far-coordinated water molecule. *Inorg Chem* 2016;55:6703–11.
- [405] Migliorati V, Serva A, Terenzio FM, D'Angelo P. Development of Lennard-Jones and Buckingham potentials for lanthanoid ions in water. *Inorg Chem* 2017;56:6214–24.
- [406] Serva A, Migliorati V, Spezia R, D'Angelo P. How does Ce^{III} nitrate dissolve in a protic ionic liquid? A combined molecular dynamics and EXAFS study. *Chem-Eur J* 2017;23:8424–33.
- [407] Migliorati V, Serva A, Sessa F, Lapi A, D'Angelo P. Influence of counterions on the hydration structure of lanthanide ions in dilute aqueous solutions. *J Phys Chem B* 2018;122:2779–91.
- [408] Sessa F, Migliorati V, Serva A, Lapi A, Aquilanti G, Mancini G, et al. On the coordination of Zn^{2+} ion in Tf_2N^- based ionic liquids: structural and dynamic properties depending on the nature of the organic cation. *Phys Chem Chem Phys* 2018;20:2662–75.
- [409] Atta-Fynn R, Bylaska EJ, Schenter GK, de Jong WA. Hydration shell structure and dynamics of curium(III) in aqueous solution: first principles and empirical studies. *J Phys Chem A* 2011;115:4665–77.
- [410] Atta-Fynn R, Johnson DF, Bylaska EJ, Ilton ES, Schenter GK, de Jong WA. Structure and hydrolysis of the U(IV), U(V), and U(VI) aqua ions from ab initio molecular simulations. *Inorg Chem* 2012;51:3016–24.
- [411] Kirchner B, di Dio PJ, Hutter J. *Multiscale Molecular Methods in Applied Chemistry*. Berlin, Berlin: Springer-Verlag; 2012. p. 109–53.
- [412] Yancey DF, Chill ST, Zhang L, Frenkel AI, Henkelman G, Crooks RM. A theoretical and experimental examination of systematic ligand-induced disorder in Au dendrimer-encapsulated nanoparticles. *Chem Sci* 2013;4:2912–21.
- [413] Buchholz DB, Ma Q, Alducin D, Ponce A, Jose-Yacamán M, Khanal R, et al. The structure and properties of amorphous indium oxide. *Chem Mat* 2014;26:5401–11.
- [414] Aupiais J, Bonin L, Den Auwer C, Moisy P, Siberchicot B, Topin S. On the use of speciation techniques and ab initio modelling to understand tetravalent actinide behavior in a biological medium: an(IV)DTPA case. *Dalton Trans* 2016;45:3759–70.
- [415] Kerisit S, Bylaska EJ, Massey MS, McBriarty ME, Ilton ES. Ab initio molecular dynamics of uranium incorporated in goethite ($\alpha\text{-FeOOH}$): interpretation of X-ray absorption spectroscopy of trace polyvalent metals. *Inorg Chem* 2016;55:11736–46.
- [416] Ayala R, Martinez JM, Pappalardo RR, Refson K, Marcos ES. Effect of basicity on the hydrolysis of the Bi(III) aqua ion in solution: an ab initio molecular dynamics study. *J Phys Chem A* 2018;122:1905–15.
- [417] Etschmann BE, Mei Y, Liu W, Sherman D, Testemale D, Muller H, et al. The role of Pb(II) complexes in hydrothermal mass transfer: an X-ray absorption spectroscopic study. *Chem Geol* 2018;502:88–106.
- [418] Sarker D, Bhattacharya S, Kumar H, Srivastava P, Ghosh S. Evidence of local structural influence on the shape driven magnetic anisotropy in electronically excited Ni nanoparticles embedded in SiO_2 matrix. *Sci Rep* 2018;8:1040.
- [419] Ellis PJ, Freeman HC. XFIT – an interactive EXAFS analysis program. *J Synchrotron Radiat* 1995;2:190–5.
- [420] Filippini A. Statistical errors in X-ray-absorption fine-structure data-analysis. *J Phys-Condens Matter* 1995;7:9343–56.
- [421] Wicks JD, Borjesson L, Bushnellwye G, Howells WS, McGreevy RL. Structure and ionic-conduction in $(\text{AgI})_x(\text{AgPO}_3)_{1-x}$ glasses. *Phys Rev Lett* 1995;74:726–9.
- [422] Bichara C, Raty JY, Gaspard JP. Structure and bonding in liquid tellurium. *Phys Rev B* 1996;53:206–11.
- [423] DiCiccio A, Filippini A, Itie JP, Polian A. High-pressure EXAFS measurements of solid and liquid Kr. *Phys Rev B* 1996;54:9086–98.
- [424] Bengaard HS, Norskov JK, Sehested J, Clausen BS, Nielsen LP, Molenbroek AM, et al. Steam reforming and graphite formation on Ni catalysts. *J Catal* 2002;209:365–84.
- [425] Di Ciccio A, Trapananti A, Faggioni S, Filippini A. Is there icosahedral ordering in liquid and undercooled metals? *Phys Rev Lett* 2003;91:135505.
- [426] Merkling PJ, Ayala R, Martinez JM, Pappalardo RR, Marcos ES. Interplay of computer simulations and x-ray absorption spectra in the study of the bromide hydration structure. *J Chem Phys* 2003;119:6647–54.
- [427] Oudenhuijzen MK, van Bokhoven JA, Koningsberger DC. Support-induced compensation effects in H/D exchange of cyclopentane. *J Catal* 2003;219:134–45.
- [428] Deng L, Hu WY, Deng HQ, Xiao SF, Tang JF. Au-Ag bimetallic nanoparticles: surface segregation and atomic-scale structure. *J Phys Chem C* 2011;115:11355–63.
- [429] Bugaev AL, Guda AA, Lazzarini A, Lomachenko KA, Groppo E, Pellegrini R, et al. In situ formation of hydrides and carbides in palladium catalyst: when XANES is better than EXAFS and XRD. *Catal Today* 2017;283:119–26.
- [430] Gurman SJ, McGreevy RL. Reverse Monte-Carlo simulation for the analysis of EXAFS data. *J Phys-Condens Matter* 1990;2:9463–73.
- [431] Wang YR, Lu KQ, Li CX. Structures of liquid GaSb and InSb studied with the extended X-ray-absorption fine-structure method. *Phys Rev Lett* 1997;79:3664–7.
- [432] Winterer M. Reverse Monte Carlo analysis of extended x-ray absorption fine structure spectra of monoclinic and amorphous zirconia. *J Appl Phys* 2000;88:5635–44.
- [433] McGreevy RL. Reverse Monte Carlo modelling. *J Phys-Condens Matter* 2001;13:R877–913.
- [434] Winterer M, Delaplane R, McGreevy R. X-ray diffraction, neutron scattering and EXAFS spectroscopy of monoclinic zirconia: analysis by Rietveld refinement and reverse Monte Carlo simulations. *J Appl Crystallogr* 2002;35:434–42.
- [435] Luo WK, Sheng HW, Alamgir FM, Bai JM, He JH, Ma E. Icosahedral short-range order in amorphous alloys. *Phys Rev Lett* 2004;92:145502.
- [436] Di Ciccio A, Trapananti A. Reverse Monte Carlo refinement of molecular and condensed systems by x-ray absorption spectroscopy. *J Phys-Condens Matter* 2005;17:S135–44.
- [437] Gereben O, Jovari P, Temleitner L, Pusztai L. A new version of the RMC++ Reverse Monte Carlo programme, aimed at investigating the structure of covalent glasses. *J Optoelectron Adv Mater* 2007;9:3021–7.

- [438] Krayzman V, Levin I, Tucker MG. Simultaneous reverse Monte Carlo refinements of local structures in perovskite solid solutions using EXAFS and the total scattering pair-distribution function. *J Appl Crystallogr* 2008;41:705–14.
- [439] Krayzman V, Levin I, Woicik JC, Proffen T, Vanderah TA, Tucker MG. A combined fit of total scattering and extended X-ray absorption fine structure data for local-structure determination in crystalline materials. *J Appl Crystallogr* 2009;42:867–77.
- [440] Krayzman V, Levin I. Reverse Monte Carlo refinements of local displacive order in perovskites: AgNbO₃ case study. *J Phys-Condens Matter* 2010;22:8.
- [441] Timoshenko J, Kuzmin A, Purans J. Reverse Monte Carlo modeling of thermal disorder in crystalline materials from EXAFS spectra. *Comput Phys Commun* 2012;183:1237–45.
- [442] Tupy SA, Karim AM, Bagia C, Deng WH, Huang YL, Vlachos DG, et al. Correlating ethylene glycol reforming activity with in situ EXAFS detection of Ni segregation in supported NiPt bimetallic catalysts. *ACS Catal* 2012;2:2290–6.
- [443] Akola J, Kohara S, Ohara K, Fujiwara A, Watanabe Y, Masuno A, et al. Network topology for the formation of solvated electrons in binary CaO-Al₂O₃ composition glasses. *Proc Natl Acad Sci USA* 2013;110:10129–34.
- [444] Levin I, Krayzman V, Woicik JC. Local structure in perovskite (Ba, Sr)Ti_{0.3}: Reverse Monte Carlo refinements from multiple measurement techniques *Phys. Rev. B* 2014;89:024106.
- [445] Timoshenko J, Anspoks A, Kalinko A, Kuzmin A. Analysis of extended x-ray absorption fine structure data from copper tungstate by the reverse Monte Carlo method. *Phys Scr* 2014;89:044006.
- [446] Jovari P, Cui S, Nazabal V, Kaban I, Beuneu B, Dussauze M, et al. Network rearrangement in Ag^I-doped GeTe₄ glasses. *J Am Ceram Soc* 2015;98:1034–9.
- [447] Levin I, Krayzman V, Cibin G, Tucker MG, Eremenko M, Chapman K, et al. Coupling of emergent octahedral rotations to polarization in (K, Na) NbO₃ ferroelectrics. *Sci Rep* 2017;7:15620.
- [448] Timoshenko J, Anspoks A, Kalinko A, Kuzmin A. *Physica Status Solidi C: Current Topics in Solid State Physics*, Vol 11, No 9–10. Weinheim: Wiley-VCH Verlag GmbH; 2014. p. 1472–5.
- [449] Timoshenko J, Kuzmin A, Purans J. EXAFS study of hydrogen intercalation into ReO₃ using the evolutionary algorithm. *J Phys-Condens Matter* 2014;26:15.
- [450] Timoshenko J, Anspoks A, Kalinko A, Kuzmin A. Local structure of nanosized tungstates revealed by evolutionary algorithm. *Phys Status Solidi A-Appl Mat* 2015;212:265–73.
- [451] Jonane I, Lazdins K, Timoshenko J, Kuzmin A, Purans J, Vladimirov P, et al. Temperature-dependent EXAFS study of the local structure and lattice dynamics in cubic Y₂O₃. *J Synchrotr Radiat* 2016;23:510–8.
- [452] Jonane I, Timoshenko J, Kuzmin A. Atomistic simulations of the Fe K-edge EXAFS in FeF₃ using molecular dynamics and reverse Monte Carlo methods. *Phys Scr* 2016;91:104001.
- [453] Timoshenko J, Anspoks A, Kalinko A, Kuzmin A. Local structure of copper nitride revealed by EXAFS spectroscopy and a reverse Monte Carlo/evolutionary algorithm approach. *Phys Scr* 2016;91:054003.
- [454] Timoshenko J, Anspoks A, Kalinko A, Kuzmin A. Local structure of cobalt tungstate revealed by EXAFS spectroscopy and reverse Monte Carlo/evolutionary algorithm simulations. *Z Phys Chemie-Int J Res Phys Chem Chem Phys* 2016;230:551–68.
- [455] Timoshenko, J., Kuzmin, A., Purans, J., Iop, 16th International Conference on X-Ray Absorption Fine Structure, Iop Publishing Ltd, Bristol; 2016.
- [456] Timoshenko J, Anspoks A, Kalinko A, Kuzmin A. Thermal disorder and correlation effects in anti-perovskite-type copper nitride. *Acta Mater* 2017;129:61–71.
- [457] Timoshenko J, Frenkel AI. Probing structural relaxation in nanosized catalysts by combining EXAFS and reverse Monte Carlo methods. *Catal Today* 2017;280:274–82.
- [458] Abraham FF. Computational statistical mechanics methodology, applications and supercomputing. *Adv Phys* 1986;35:1–111.
- [459] McGreevy RL, Pusztai L. Reverse Monte Carlo simulation: a new technique for the determination of disordered structures. *Mol Simul* 1988;1:359–67.
- [460] Anspoks A, Kalinko A, Kalendarev R, Kuzmin A. Atomic structure relaxation in nanocrystalline NiO studied by EXAFS spectroscopy: role of nickel vacancies. *Phys Rev B* 2012;86:174114.
- [461] Turney JE, McGaughey AJH, Amon CH. Assessing the applicability of quantum corrections to classical thermal conductivity predictions. *Phys Rev B* 2009;79:224305.
- [462] Anspoks A, Kuzmin A, Kalinko A, Timoshenko J. Probing NiO nanocrystals by EXAFS spectroscopy. *Solid State Commun* 2010;150:2270–4.
- [463] Van Nordsthand RA. The use of X-ray K-absorption edges in the study of catalytically active solids. *Adv Catal* 1960;12:149–87.
- [464] Borfecchia E, Mino L, Gianolio D, Groppo C, Malaspina N, Martinez-Criado G, et al. Iron oxidation state in garnet from a subduction setting: a micro-XANES and electron microprobe (“flank method”) comparative study. *J Anal Atom Spectrom* 2012;27:1725–33.
- [465] Rosenberg RA, Love PJ, Rehn V. Polarization-dependent C(K) near-edge X-ray-absorption FINE-structure of graphite. *Phys Rev B* 1986;33:4034–7.
- [466] Pacile D, Papagno M, Rodriguez AF, Grioni M, Papagno L. Near-edge x-ray absorption fine-structure investigation of graphene. *Phys Rev Lett* 2008;101:066806.
- [467] Zhou SY, Girit CO, Scholl A, Jozwiak CJ, Siegel DA, Yu P, et al. Instability of two-dimensional graphene: Breaking sp² bonds with soft x rays. *Phys Rev B* 2009;80:121409.
- [468] Papagno M, Rodriguez AF, Girit CO, Meyer JC, Zettl A, Pacile D. Polarization-dependent C K near-edge X-ray absorption fine-structure of graphene. *Chem Phys Lett* 2009;475:269–71.
- [469] Hua WJ, Gao B, Li SH, Agren H, Luo Y. X-ray absorption spectra of graphene from first-principles simulations. *Phys Rev B* 2010;82:155433.
- [470] Coffman FL, Cao R, Pianetta PA, Kapoor S, Kelly M, Terminello LJ. Near-edge x-ray absorption of carbon materials for determining bond hybridization in mixed sp²/sp³ bonded materials. *Appl Phys Lett* 1996;69:568–70.
- [471] Hemraj-Benny T, Banerjee S, Sambasivan S, Balasubramanian M, Fischer DA, Eres G, et al. Near-edge X-ray absorption fine structure spectroscopy as a tool for investigating nanomaterials. *Small* 2006;2:26–35.
- [472] Hemraj-Benny T, Banerjee S, Sambasivan S, Fischer DA, Eres G, Puzos AA, et al. Imperfect surface order and functionalization in vertical carbon nanotube arrays probed by near edge X-ray absorption fine structure spectroscopy (NEXAFS). *Phys Chem Chem Phys* 2006;8:5038–44.
- [473] Girard-Lauriault PL, Ilgen R, Ruiz JC, Wertheimer MR, Unger WES. Surface functionalization of graphite and carbon nanotubes by vacuum-ultraviolet photochemical reactions. *Appl Surf Sci* 2012;258:8448–54.
- [474] Bianconi A, Garcia J, Benfatto M, Marcelli A, Natoli CR, Ruiz-Lopez MF. Multielectron excitations in the K-edge x-ray-absorption near-edge spectra of V, Cr, and Mn 3d⁰ compounds with tetrahedral coordination. *Phys Rev B* 1991;43:6885–92.
- [475] Fossard F, Hug G, Gilmore K, Kas JJ, Rehr JJ, Vila FD, et al. Quantitative first-principles calculations of valence and core excitation spectra of solid C-60. *Phys Rev B* 2017;95:115112.
- [476] Yagi H, Nakajima K, Koswattage KR, Nakagawa K, Huang C, Proddhan MSI, et al. Photoabsorption cross section of C-60 thin films from the visible to vacuum ultraviolet. *Carbon* 2009;47:1152–7.
- [477] Xing L, Yang F, Rasouli S, Qiu Y, Li ZF, Uzunoglu A, et al. Understanding Pt nanoparticle anchoring on graphene supports through surface functionalization. *ACS Catal* 2016;6:2642–53.
- [478] Jiang FL, Li C, Fu HY, Guo XJ, Wu GZ, Chen SM. Probing the spontaneous reduction mechanism of platinum ions confined in the nanospace by X-ray absorption fine structure spectroscopy. *Phys Chem Chem Phys* 2016;18:19259–66.
- [479] Mandic L, Fazinic S, Jaksic M. Chemical effects on the K beta(1) and K beta(2,5) x-ray lines of titanium and its compounds. *Phys Rev A* 2009;80:Art. n. 042519.
- [480] Hasegawa J, Tada T, Oguri Y, Hayashi M, Toriyama T, Kawabata T, Masai K. Development of a high-efficiency high-resolution particle-induced x-ray emission system for chemical state analysis of environmental samples. *Rev Sci Instrum* 2007;78:Art. n. 073105.
- [481] Alonso-Mori R, Kern J, Sokaras D, Weng TC, Nordlund D, Tran R et al. A multi-crystal wavelength dispersive x-ray spectrometer. *Rev Sci Instrum* 2012;83:Art. n. 073114.
- [482] Mattern BA, Seidler GT, Haave M, Pacold JJ, Gordon RA, et al. A plastic miniature x-ray emission spectrometer based on the cylindrical von Hamos geometry *Rev Sci Instrum* 2012;83:Art. n. 023901.
- [483] Sakurai K, Eba H. X-ray fluorescence analysis with a Johansson-type spectrometer *Jpn. J Appl Phys Part 1 – Regul Pap Short Notes Rev Pap* 1999;38:650–653.
- [484] Sakurai K, Eba H, Inoue K, Yagi N. Downsizing of Johansson spectrometer for X-ray fluorescence trace analysis with brilliant undulator source. *Nucl Instrum*

- Methods Phys Res Sect A-Accel Spectrom Dect Assoc Equip 2001;467:1549–52.
- [485] Kleimenov E, Bergamaschi A, van Bokhoven JA, Janousch M, Schmitt B, Nachtegaal M. High-resolution hard-X-ray fluorescence spectrometer. *J Phys: Conf Ser* 2009;190:012035.
- [486] de Groot F. Multiplet effects in X-ray spectroscopy. *Coord Chem Rev* 2005;249:31–63.
- [487] de Groot F, Kotani A. Core level spectroscopy of solids. London: CRC Press; 2008.
- [488] de Groot FMF, Glatzel P, Bergmann U, van Aken PA, Barrea RA, Klemme S, et al. 1s_{2p} resonant inelastic X-ray scattering of iron oxides. *J Phys Chem B* 2005;109:20751–62.
- [489] de Groot FMF, Krisch MH, Vogel J. Spectral sharpening of the Pt L edges by high-resolution x-ray emission. *Phys Rev B* 2002;66:Art. n. 195112.
- [490] Kotani A. Resonant inelastic X-ray scattering in d and f electron systems. *Eur Phys J B* 2005;47:3–27.
- [491] Kotani A, Shin S. Resonant inelastic x-ray scattering spectra for electrons in solids. *Rev Mod Phys* 2001;73:203–46.
- [492] Vanko G, Neisius T, Molnar G, Renz F, Karpati S, Shukla A, et al. Probing the 3d spin momentum with X-ray emission spectroscopy: the case of molecular-spin transitions. *J Phys Chem B* 2006;110:11647–53.
- [493] Bauer M. HERFD-XAS and valence-to-core-XES: new tools to push the limits in research with hard X-rays? *Phys Chem Chem Phys* 2014;16:13827–37.
- [494] Eliseev AA, Yashina LV, Verbitskiy NI, Brzhezinskaya MM, Kharlamova MV, Chernysheva MV, et al. Interaction between single walled carbon nanotube and 1D crystal in CuX@SWCNT (X = Cl, Br, I) nanostructures. *Carbon* 2012;50:4021–39.
- [495] Frenkel AI, Wang Q, Marinkovic N, Chen JG, Barrio L, Si R, et al. Combining X-ray absorption and X-ray diffraction techniques for in situ studies of chemical transformations in heterogeneous catalysis: advantages and limitations. *J Phys Chem C* 2011;115:17884–90.
- [496] van Beek W, Safonova OV, Wiker G, Emerich H. SNBL, a dedicated beamline for combined in situ X-ray diffraction, X-ray absorption and Raman scattering experiments. *Phase Transit* 2011;84:726–32.
- [497] Abdala PM, Safonova OV, Wiker G, van Beek W, Emerich H, van Bokhoven JA, et al. Scientific opportunities for heterogeneous catalysis research at the SuperXAS and SNBL beam lines. *Chimia* 2012;66:699–705.
- [498] Bugaev AL, Guda AA, Lomachenko KA, Kamysheva EG, Soldatov MA, Kaur G, et al. Operando study of palladium nanoparticles inside UiO-67 MOF for catalytic hydrogenation of hydrocarbons. *Faraday Discuss*. 2018;208:287–306.
- [499] Bugaev AL, Usoltsev OA, Lazzarini A, Lomachenko KA, Guda AA, Pellegrini R, et al. Time-resolved operando studies of carbon supported Pd nanoparticles under hydrogenation reactions by X-ray diffraction and absorption. *Faraday Discuss* 2018;208:187–205.
- [500] Martini A, Borfecchia E, Lomachenko KA, Pankin IA, Negri C, Berlier G, et al. Composition-driven Cu-speciation and reducibility in Cu-CHA zeolite catalysts: a multivariate XAS/FTIR approach to complexity. *Chem Sci* 2017;8:6836–51.
- [501] Andersen CW, Borfecchia E, Bremholm M, Jorgensen MRV, Vennestrom PNR, Lamberti C, et al. Redox-driven migration of copper ions in the Cu-CHA zeolite as shown by the in situ PXRD/XANES technique. *Angew Chem-Int Edit* 2017;56:10367–72.
- [502] Ronning M, Tsakoumis NE, Voronov A, Johnsen RE, Norby P, van Beek W, et al. Combined XRD and XANES studies of a Re-promoted Co/γ-Al₂O₃ catalyst at Fischer-Tropsch synthesis conditions. *Catal Today* 2010;155:289–95.
- [503] Favre-Nicolin V, Proietti MG, Leclere C, Katcho NA, Richard MI, Renevier H. Multiwavelength anomalous diffraction and diffraction anomalous fine structure to study composition and strain of semiconductor nanostructures. *Eur Phys J-Spec Top* 2012;208:189–216.
- [504] Tobbens DM, Schorr S. The use of anomalous x-ray diffraction as a tool for the analysis of compound semiconductors. *Semicond Sci Technol* 2017;32:13.
- [505] Abruna HD. Probing electrochemical interfaces with X-rays. *Adv Chem Phys* 1990;77:255–335.
- [506] Abruna HD, Bommarito GM, Yee HS. X-ray standing waves and surface exafs studies of electrochemical interfaces. *Acc Chem Res* 1995;28:273–9.
- [507] Kazimirov AY, Zegenhagen J. X-Ray standing wave technique: principles and applications. Singapore: World Scientific Publ Co Pte Ltd; 2013.
- [508] Wrodruff DP. Surface structure determination using x-ray standing waves. *Rep Prog Phys* 2005;68:743–98.
- [509] Feng ZX, Kim CY, Elam JW, Ma Q, Zhang Z, Bedzyk MJ. Direct atomic-scale observation of redox-induced cation dynamics in an oxide-supported monolayer catalyst: Wox/α-Fe₂O₃(0001). *J Am Chem Soc* 2009;131:18200–+.
- [510] Wolf KB, Kröttsch G. Geometry and dynamics in refracting systems. *Euro J Phys* 1995;16:14–20.
- [511] Marra WC, Eisenberger P, Cho AY. X-ray total-external-reflection-Bragg diffraction: a structural study of the GaAs-Al interface. *J Appl Phys* 1979;50:6927–33.
- [512] Weng S-L, Cho AY, Marra WC, Eisenberger P. A structural study of the Al-Ge(001) interface using total-reflected x-ray diffraction. *Solid State Commun* 1980;34:843–6.
- [513] Cloetens P, Barrett R, Baruchel J, Guigay JP, Schlenker M. Phase objects in synchrotron radiation hard x-ray imaging. *J Phys D* 1996;29:133–46.
- [514] Daillant J, Gibaud A, editors. X-ray and Neutron Reflectivity. Springer, Berlin: Principles and Applications; 2009.
- [515] Pietsch U, Holy V, Baumbach T. High-Resolution X-Ray Scattering From Thin Films to Lateral Nanostructures. New York: Springer; 2004.
- [516] Stearns DG. X-ray scattering from interfacial roughness in multilayer structures. *J Appl Phys* 1992;71:4286–98.
- [517] Névot L, Croce P. Caractérisation des surfaces par réflexion rasante de rayons X. Application à l'étude du polissage de quelques verres silicates. *Rev Phys Appl (Paris)* 1980;15:761–79.
- [518] Barabási A-L, Stanley HE. Fractal concepts in surface growth. Cambridge: Cambridge University Press; 1995.
- [519] Villain J. Continuum models of crystal growth from atomic beams with and without desorption. *J Phys I France* 1991;1:19–42.
- [520] Veggo K, Siffalovic P, Benkovicova M, Jergel M, Luby S, Majkova E, et al. GISAXS analysis of 3D nanoparticle assemblies effect of vertical nanoparticle ordering. *Nanotechnology* 2012;23.
- [521] Altamura D, Sibillano T, Siliqi D, De Caro L, Giannini C. Assembled nanostructured architectures studied by grazing incidence X-ray scattering invited. *Rev Article Nanomater Nanotechnol* 2012:2.
- [522] Sinha SK, Sirota EB, Garoff S, Stanley HB. X-ray and neutron scattering from rough surfaces. *Phys Rev B* 1988;38:2297–311.
- [523] Corricelli M, Depalo N, Fanizza E, Altamura D, Giannini C, Siliqi D, et al. Two-dimensional plasmonic superlattice based on Au nanoparticles self-assembling onto a functionalized substrate. *J Phys Chem C* 2014;118:7579–90.
- [524] De Caro L, Altamura D, Vittoria FA, Carbone G, Qiao F, Manna L, et al. A superbright X-ray laboratory microsource empowered by a novel restoration algorithm. *J Appl Crystallog* 2012;45:1228–35.
- [525] Altamura D, Holy V, Siliqi D, Lekshmi IC, Nobile C, Maruccio G, et al. Exploiting GISAXS for the study of a 3D ordered superlattice of self-assembled colloidal iron oxide nanocrystals. *Cryst Growth Des* 2012;12:5505–12.
- [526] Corricelli M, Altamura D, Curri ML, Sibillano T, Siliqi D, Mazzone A, et al. GISAXS and GIWAXS study on self-assembling processes of nanoparticle based superlattices. *Crystengcomm* 2014;16:9482–92.
- [527] Bernstorff S, Holy V, Endres J, Valeš V, Sobota J, Siketić Z, et al. Co nanocrystals in amorphous multilayers – a structure study. *J Appl Crystallog* 2013;46:1711–21.
- [528] Holy V, Baumbach T. Non specular x-ray reflection from rough multilayers. *Phys Rev B* 1994;49:10668–76.
- [529] Jiang DT, Crozier ED, Heinrich B. Structure determination of metastable epitaxial Cu layers on Ag(001) by glancing-incidence X-ray-absorption fine-structure. *Phys Rev B* 1991;44:6401–9.
- [530] Nashner MS, Frenkel AI, Adler DL, Shapley JR, Nuzzo RG. Structural characterization of carbon-supported platinum-ruthenium nanoparticles from the molecular cluster precursor PtRu₅C(CO)₁₆. *J Am Chem Soc* 1997;119:7760–71.
- [531] Kim JY, Rodriguez JA, Hanson JC, Frenkel AI, Lee PL. Reduction of CuO and Cu₂O with H₂: H embedding and kinetic effects in the formation of suboxides. *J Am Chem Soc* 2003;125:10684–92.
- [532] Agostini G, Pellegrini R, Leofanti G, Bertinetti L, Bertarione S, Groppo E, et al. Determination of the particle size, available surface area, and nature of exposed sites for silica-alumina-supported pd nanoparticles: a multitechnical approach. *J Phys Chem C* 2009;113:10485–92.
- [533] Mostafa S, Behafarid F, Croy JR, Ono LK, Li L, Yang JC, et al. Shape-dependent catalytic properties of Pt nanoparticles. *J Am Chem Soc* 2010;132:15714–9.
- [534] Bugaev AL, Guda AA, Lomachenko KA, Srabonyan VV, Bugaev LA, Soldatov AV, et al. Temperature- and pressure-dependent hydrogen concentration in supported PdH_x nanoparticles by Pd K-edge X-ray absorption spectroscopy. *J Phys Chem C* 2014;118:10416–23.

- [535] Bugaev AL, Usoltsev OA, Guda AA, Lomachenko KA, Pankin IA, Rusalev YV, et al. Palladium carbide and hydride formation in the bulk and at the surface of palladium nanoparticles. *J Phys Chem C* 2018;122:12029–37.
- [536] Bordiga S, Boscherini F, Coluccia S, Genoni F, Lamberti C, Leofanti G, et al. XAFS study of ti-silicalite – structure of framework Ti(IV) in presence and in absence of reactive molecules (H₂O, NH₃). *Catal Lett* 1994;26:195–208.
- [537] Bordiga S, Buzzoni R, Geobaldo F, Lamberti C, Giamello E, Zecchina A, et al. Structure and reactivity of framework and extraframework iron in Fe-silicalite as investigated by spectroscopic and physicochemical methods. *J Catal* 1996;158:486–501.
- [538] Lamberti C, Bordiga S, Salvalaggio M, Spoto G, Zecchina A, Geobaldo F, et al. XAFS, IR, and UV-vis study of the Cu^I environment in Cu^I-ZSM-5. *J Phys Chem B* 1997;101:344–60.
- [539] Lamberti C, Bordiga S, Zecchina A, Salvalaggio M, Geobaldo F, Areato CO, et al. EXAFS and FTIR characterization of copper-exchanged mordenite. *J Chem Soc-Faraday Trans* 1998;94:1519–25.
- [540] Zecchina A, Bordiga S, Palomino GT, Scarano D, Lamberti C, Salvalaggio M. Mono-, di-, and tricarbonylic species in copper(I)-exchanged zeolite ZSM-5: comparison with homogeneous copper(I) carbonylic structures. *J Phys Chem B* 1999;103:3833–44.
- [541] Lamberti C, Palomino GT, Bordiga S, Berlier G, D'Acapito F, Zecchina A. Structure of homoleptic Cu^I(CO)₃ cations in Cu-I-exchanged ZSM-5 zeolite: an X-ray absorption study. *Angew Chem-Int Edit* 2000;39:2138–41.
- [542] Palomino GT, Bordiga S, Zecchina A, Marra GL, Lamberti C. XRD, XAS, and IR characterization of copper-exchanged Y zeolite. *J Phys Chem B* 2000;104:8641–51.
- [543] Bordiga S, Bonino F, Damin A, Lamberti C. Reactivity of Ti(IV) species hosted in TS-1 towards H₂O₂-H₂O solutions investigated by ab initio cluster and periodic approaches combined with experimental XANES and EXAFS data: a review and new highlights. *Phys Chem Chem Phys* 2007;9:4854–78.
- [544] Giordanino F, Borfecchia E, Lomachenko KA, Lazzarini A, Agostini G, Gallo E, et al. Interaction of NH₃ with Cu-SSZ-13 catalyst: a complementary FTIR, XANES, and XES study. *J Phys Chem Lett* 2014;5:1552–9.
- [545] Prestipino C, Regli L, Vitillo JG, Bonino F, Damin A, Lamberti C, et al. Local structure of framework Cu(II) in HKUST-1 metal-organic framework: spectroscopic characterization upon activation and interaction with adsorbates. *Chem Mat* 2006;18:1337–46.
- [546] Chavan S, Vitillo JG, Uddin MJ, Bonino F, Lamberti C, Groppo E et al. Functionalization of UiO-66 metal-organic framework and highly cross-linked polystyrene with Cr(CO)₃: in situ formation, stability, and photoreactivity. *Chem Mat* 2010;22:4602–4611.
- [547] Borfecchia E, Maurelli S, Gianolio D, Groppo E, Chiesa M, Bonino F, et al. Insights into adsorption of NH₃ on HKUST-1 metal-organic framework: a multi-technique approach. *J Phys Chem C* 2012;116:19839–50.
- [548] Davis ME. Ordered porous materials for emerging applications. *Nature* 2002;417:813–21.
- [549] Rowsell JLC, Yaghi OM. Metal-organic frameworks: a new class of porous materials. *Microporous Mesoporous Mat* 2004;73:3–14.
- [550] Horike S, Shimomura S, Kitagawa S. Soft porous crystals. *Nat Chem* 2009;1:695–704.
- [551] Butova VV, Soldatov MA, Guda AA, Lomachenko KA, Lamberti C. Metal-organic frameworks: structure, properties, methods of synthesis and characterization. *Russ Chem Rev* 2016;85:280–307.
- [552] Davisson C, Germer LH. Diffraction of electrons by a crystal of nickel. *Phys Rev* 1927;30:705–40.
- [553] Landman U, Adams DL. Extended x-ray-absorption fine structure—Auger process for surface structure analysis: theoretical considerations of a proposed experiment. *Proc Nat Acad Sci US* 1976;73:2550–3.
- [554] Jona F. LEED crystallography. *J Phys C: Solid State Phys* 1978;11:4271–306.
- [555] Pendry JB, Roberts MW, Wong J, Grimley TB. Theoretical aspects of the nature of the surface chemical bond [and Discussion]. *Phil Trans Roy Soc (London.) A, Math Phys Sci* 1986;318:121–5.
- [556] Lee PA. Possibility of adsorbate position determination using final-state interference effects. *Phys Rev B* 1976;13:5261–71.
- [557] Schroeder SLM, Moggridge GD, Ormerod RM, Rayment T, Lambert RM. What determines the probing depth of electron yield XAS. *Surf Sci* 1995;324:L371–7.
- [558] Schroeder SLM. Towards a 'universal curve' for total electron-yield XAS. *Solid State Commun* 1996;98:405–9.
- [559] Citrin PH, Eisenberger P, Hewitt RC. Extended X-ray-absorption fine structure of surface atoms on single-crystal substrates: iodine adsorbed on Ag(111). *Phys Rev Lett* 1978;41:309–12.
- [560] Bianconi A, Bachrach RZ. Al surface relaxation using surface extended X-ray-absorption fine structure. *Phys Rev Lett* 1979;42:104–8.
- [561] Citrin PH, Eisenberger P, Hewitt RC. SEXAFS studies of iodine adsorbed on single crystal substrates. *Surf Sci* 1979;89:28–40.
- [562] Citrin PH, Eisenberger P, Hewitt RC. Adsorption sites and bond lengths of iodine on Cu{111} and Cu{100} from surface extended X-ray-absorption fine structure. *Phys Rev Lett* 1980;45:1948–51.
- [563] Johansson LI, Stöhr J. Bonding of oxygen on Al(111): a surface extended X-ray absorption fine-structure study. *Phys Rev Lett* 1979;43:1882–5.
- [564] Stöhr J, Johansson L, Lindau I, Pianetta P. Extended-x-ray-absorption-fine-structure studies of low-Z atoms in solids and on surfaces: Studies of Si₃N₄, SiO₂, and oxygen on Si(111). *Phys Rev B* 1979;20:664–80.
- [565] Stöhr J, Johansson LI, Brennan S, Hecht M, Miller JN. Surface extended-x-ray-absorption-fine-structure study of oxygen interaction with Al(111) surfaces. *Phys Rev B* 1980;22:4052–65.
- [566] Bachrach RZ, Hansson GV, Bauer RS. Pressure dependent oxidation of Al(111): sa photoemission and surface exafs study. *Surf Sci* 1981;109:L560–6.
- [567] Stöhr J, Jaeger R. Absorption-edge resonances, core-hole screening, and orientation of chemisorbed molecules: CO, NO, and N₂ on Ni(100). *Phys Rev B* 1982;26:4111–31.
- [568] Stöhr J, Outka DA, Madix RJ, Dobler U. Evidence for a novel chemisorption bond - formate (HCO₂) on Cu (100). *Phys Rev Lett* 1985;54:1256–9.
- [569] Sette F, Stöhr J, Kollin EB, Dwyer DJ, Gland JL, Robbins JL, et al. Na-induced bonding and bond-length changes for Co on Pt(111) – a near-edge X-ray-absorption fine-structure study. *Phys Rev Lett* 1985;54:935–8.
- [570] Stöhr J. X-Ray Absorption: Principles. Techniques of EXAFS, SEXAFS and XANES, Wiley, New-York: Applications; 1988. p. 443–572.
- [571] Outka DA, Madix RJ. Structural studies of formate and methoxy groups on the Cu(100) surface using NEXAFS and SEXAFS. *Surf Sci* 1985;164:235–59.
- [572] Richter M, Woicik JC, Nogami J, Pianetta P, Miyano KE, Baski AA, et al. Surface extended-x-ray-absorption fine-structure and scanning tunneling microscopy of Si(001)2x1-Sb. *Phys Rev Lett* 1990;65:3417–20.
- [573] Schmalz A, Aminpirooz S, Becker L, Haase J, Neugebauer J, Scheffler M, et al. Unusual chemisorption geometry of Na on Al(111) *Phys. Rev. Lett.* 1991;67:2163–6.
- [574] Purdie D, Muryn CA, Prakash NS, Wincott PL, Thornton G, Law DSL. Origin of the photon induced Cl⁺ yield from Si(111)7 x 7-Cl at the Cl and Si K-edges. *Surf Sci* 1991;251:546–50.
- [575] Prabhakaran K, Purdie D, Casanova R, Muryn CA, Hardman PJ, Wincott PL, et al. Alkali-metal-to-substrate charge-transfer in TiO₂(100)c(2X2)K. *Phys Rev B* 1992;45:6969–72.
- [576] Kendelewicz T, Liu P, Labiosa WB, Brown GE. Surface EXAFS and x-ray standing-wave study of the cleaved CaO(100) surface. *Phys B* 1995;208:441–2.
- [577] Hutt DA, Cooper E, Leggett GJ. A SEXAFS investigation of self-assembled monolayers on silver. *Surf Sci* 1998;397:154–63.
- [578] Liedieu J, Dhanak VR, Diehl RD, Lograsso TA, Delaney DW, McGrath R. Sulphur adsorption on the fivefold surface of the i-Al-Pd-Mn quasicrystal *Surf. Sci.* 2002;512:77–83.
- [579] Isomura N, Murai T, Nomoto T, Kimoto Y. Surface EXAFS via differential electron yield. *J Synchrotron Radiat* 2017;24:445–8.
- [580] Heald SM, Chen H, Tranquada JM. Glancing-angle extended X-ray-absorption fine-structure and reflectivity studies of interfacial regions. *Phys Rev B* 1988;38:1016–26.
- [581] Macdowell AA, Hashizume T, Citrin PH. A soft/hard X-ray beamline for surface EXAFS studies in the energy-range 0.8-15 keV. *Rev Sci Instrum* 1989;60:1901–4.
- [582] Blum L, Abruna HD, White J, Gordon JG, Borges GL, Samant MG, et al. Study of underpotentially deposited copper on gold by fluorescence detected surface EXAFS. *J Chem Phys* 1986;85:6732–8.
- [583] Cortes R, Delichere P, Froment M, Joiret S. RefEXAFS studies in interfacial electrochemistry. *J. Electrochem. Soc.* 1988;135:C144.

- [584] Jiang DT, Alberding N, Seary AJ, Crozier ED. Angular scanning stage for glancing-incidence surface EXAFS. *Rev Sci Instrum* 1988;59:60–3.
- [585] Melroy OR, Samant MG, Borges GL, Gordon JG, Blum L, White JH, et al. In-plane structure of underpotentially deposited copper on gold(111) determined by surface EXAFS. *Langmuir* 1988;4:728–32.
- [586] Guo T, Denboer ML. Surface EXAFS study of the crystallization of a metallic-glass. *J Non-Cryst Solids* 1989;110:111–7.
- [587] Bandyopadhyay P, Bunker BA. Reflection EXAFS studies of metal-semiconductor interfaces. *Phys B* 1989;158:653–4.
- [588] Barrett NT, Gibson PN, Greaves GN, Mackle P, Roberts KJ, Sacchi M. RefEXAFS investigation of the local atomic-structure around Fe during the oxidation of stainless-steel. *J Phys D-Appl Phys* 1989;22:542–6.
- [589] Cortes R, Froment M, Hugotleoff A, Joiret S. Characterization of passive films on Ni and Ni-alloys by RefEXAFS and Raman-spectroscopy. *Corrosion Sci* 1990;31:121–7.
- [590] Heald SM. EXAFS at grazing-incidence – data-collection and analysis. *Rev Sci Instrum* 1992;63:873–8.
- [591] Tuillier MH, Wetzel P, Pirri C, Bolmont D, Gewinner G. Interfacial structure of 2-dimensional epitaxial Er silicide on Si(111). *Phys Rev B* 1994;50:2333–8.
- [592] Shirai M, Nomura M, Asakura K, Iwasawa Y. Development of a chamber for in situ polarized total-reflection fluorescence x-ray absorption fine structure spectroscopy. *Rev Sci Instrum* 1995;66:5493–8.
- [593] Farquhar ML, Charnock JM, England KER, Vaughan DJ. Adsorption of Cu(II) on the (0001) plane of mica: a REFLEXAFS and XPS study. *J Colloid Interface Sci* 1996;177:561–7.
- [594] d'Acapito F, Mobilio S, Cikmacs P, Merlo V, Davoli I. Temperature modification of the Nb oxidation at the Nb/Al interface studied by refEXAFS. *Surf Sci* 2000;468:77–84.
- [595] d'Acapito F, Emelianov I, Relini A, Cavatorta P, Gliozzi A, Minicozzi V, et al. Total external reflection X-ray absorption spectroscopy reveals a zinc coordination shell in phospholipid Langmuir-Blodgett films. *Langmuir* 2002;18:5277–82.
- [596] Gordon RA, Crozier ED, Shoults J, Jiang DT. Ultrahigh vacuum-compatible fluorescence x-ray absorption fine structure detector. *Rev Sci Instrum* 2002;73:2849–51.
- [597] D'Acapito F, Davoli I, Ghigna P, Mobilio S. The RefEXAFS station at the GILDA beamline (BM08) of ESRF. *J Synchrotron Radiat* 2003;10:260–4.
- [598] Ghigna P, Spinolo G, Alessandri I, Davoli I, D'Acapito F. Do we have a probe for the initial stages of solid state reactions? *Phys Chem Chem Phys* 2003;5:2244–7.
- [599] Lopez-Flores V, Ansell S, Bowron DT, Diaz-Moreno S, Ramos S, Munoz-Paez A. Optimized end station and operating protocols for reflection extended x-ray absorption fine structure (RefEXAFS) investigations of surface structure at the European Synchrotron Radiation Facility beamline BM29. *Rev Sci Instrum* 2007;78:12.
- [600] Benzi F, Davoli I, Rovezzi M, d'Acapito F. A new procedure for the quantitative analysis of extended x-ray absorption fine structure data in total reflection geometry. *Rev Sci Instrum* 2008;79:6.
- [601] Battachio C, Fratoddi I, Venditti I, Yarzhenyky VG, Norov YV, Russo MV, et al. EXAFS in total reflection (refEXAFS) for the study of organometallic Pd(II) thiol complexes based self-assembled monolayers on gold. *Chem Phys* 2011;379:92–8.
- [602] Costanzo T, Benzi F, Ghigna P, Pin S, Spinolo G, d'Acapito F. Studying the surface reaction between NiO and Al₂O₃ via total reflection EXAFS (RefEXAFS). *J Synchrotron Radiat* 2014;21:395–400.
- [603] d'Acapito F, Souchier E, Noe P, Blaise P, Bernard M, Jousseume V. Chemical state of Ag in conducting bridge random access memory cells: a depth resolved X-ray absorption spectroscopy investigation. *J Phys: Conf Ser* 2016;712:012046.
- [604] Le Gros MA, Knoechel CG, Uchida M, Parkinson DY, McDermott G, Larabell CA. *Comprehensive Biophysics*. Amsterdam: Elsevier; 2012. p. 90–110.
- [605] Egner A, Jakobs S, Hell SW. Fast 100-nm resolution three-dimensional microscope reveals structural plasticity of mitochondria in live yeast. *Proc Natl Acad Sci USA* 2002;99:3370–5.
- [606] de Jonge N, Peckys DB, Kremers GJ, Piston DW. Electron microscopy of whole cells in liquid with nanometer resolution. *Proc Natl Acad Sci USA* 2009;106:2159–64.
- [607] Fratzl P, Jakob HF, Rinnerthaler S, Roschger P, Klaushofer K. Position-resolved small-angle X-ray scattering of complex biological materials. *J Appl Crystallogr* 1997;30:765–9.
- [608] Paris O, Zizak I, Lichtenegger H, Roschger P, Klaushofer K, Fratzl P. Analysis of the hierarchical structure of biological tissues by scanning X-ray scattering using a micro-beam. *Cell Mol Biol* 2000;46:993–1004.
- [609] Riekel C, Burghammer M, Muller M. Microbeam small-angle scattering experiments and their combination with microdiffraction. *J Appl Crystallogr* 2000;33:421–3.
- [610] Liebi M, Georgiadis M, Menzel A, Schneider P, Kohlbrecher J, Bunk O, et al. Nanostructure surveys of macroscopic specimens by small-angle scattering tensor tomography. *Nature* 2015;527:349–52.
- [611] Schaff F, Bech M, Zaslansky P, Jud C, Liebi M, Guizar-Sicairos M, et al. Six-dimensional real and reciprocal space small-angle X-ray scattering tomography. *Nature* 2015;527:353–6.
- [612] Liebi M, Georgiadis M, Kohlbrecher J, Holler M, Raabe J, Usov I, et al. Small-angle X-ray scattering tensor tomography: model of the three-dimensional reciprocal-space map, reconstruction algorithm and angular sampling requirements. *Acta Crystallogr Sect A* 2018;74:12–24.
- [613] Holler M, Raabe J, Diaz AMGS, Tsai EHR, Odstrcil M, Menzel A, Bunk O. High-resolution 3D scanning X-ray microscopes at the Swiss light source. *Microsc Microanal* 2018;24:168–71.
- [614] Giannini C, Siliqi D, Ladisa M, Altamura D, Diaz A, Beraudi A, et al. Scanning SAXS-WAXS microscopy on osteoarthritis-affected bone – an age-related study. *J Appl Crystallogr* 2014;47:110–7.
- [615] Paris O. From diffraction to imaging: New avenues in studying hierarchical biological tissues with x-ray microbeams (Review) *Biointerphases* 2008; 3:FB16-FB26.
- [616] *Annual Review of Materials Research* 2010;40:1–24.
- [617] Shastri VP, Altankov G, Lendlein A. *Advances in Regenerative Medicine: Role of Nanotechnology, and Engineering Principles*. Dordrecht: Springer Science & Business Media; 2010.
- [618] Guarino V, Gloria A, Raucchi MG, De Santis R, Ambrosio L. Bio-inspired composite and cell instructive platforms for bone regeneration *Int. Mater Rev* 2012;57:256–75.
- [619] Acton QA, editor. *Advances in Bioartificial Materials and Tissue Engineering Research and Application*. Atlanta: Scholarly Editions; 2013.
- [620] Netti P. *Biomedical foams for tissue engineering applications*. Amsterdam: Elsevier; 2014.
- [621] De Caro L, Carlino E, Siliqi D, Giannini C. *Handbook of Coherent-Domain Optical Methods*. New York: Springer; 2012. p. 291–314.
- [622] Born M, Wolf E. *Principles of optics: electromagnetic theory of propagation, interference and diffraction of light (VII expanded Ed.)*. Cambridge University Press. Cambridge; 2002.
- [623] Sayre D. Some implications of a theorem due to Shannon. *Acta Cryst* 1952;5:843.
- [624] Miao JW, Charalambous P, Kirz J, Sayre D. Extending the methodology of X-ray crystallography to allow imaging of micrometre-sized non-crystalline specimens. *Nature* 1999;400:342–4.
- [625] Miao JW, Ishikawa T, Johnson B, Anderson EH, Lai B, Hodgson KO. High resolution 3D x-ray diffraction microscopy. *Phys Rev Lett* 2002;89:Art. n. 088303.
- [626] Chapman HN, Barty A, Bogan MJ, Boutet S, Frank M, Hau-Riege SP, et al. Femtosecond diffractive imaging with a soft-X-ray free-electron laser. *Nat Phys* 2006;2:839–43.
- [627] Seibert MM, Ekeberg T, Maia F, Svenda M, Andreasson J, Jonsson O, et al. Single mimivirus particles intercepted and imaged with an X-ray laser. *Nature* 2011;470:78–86.
- [628] Pfeifer MA, Williams GJ, Vartanyants IA, Harder R, Robinson IK. Three-dimensional mapping of a deformation field inside a nanocrystal. *Nature* 2006;442:63–6.
- [629] Clark JN, Beitra L, Xiong G, Higginbotham A, Fritz DM, Lemke HT, et al. Ultrafast three-dimensional imaging of lattice dynamics in individual gold nanocrystals. *Science* 2013;341:56–9.

- [630] Rodenburg JM, Hurst AC, Cullis AG, Dobson BR, Pfeiffer F, Bunk O et al. Hard-x-ray lensless imaging of extended objects. *Phys Rev Lett* 2007;98:Art. n. 034801.
- [631] Thibault P, Dierolf M, Menzel A, Bunk O, David C, Pfeiffer F. High-resolution scanning x-ray diffraction microscopy. *Science* 2008;321:379–82.
- [632] Dierolf M, Menzel A, Thibault P, Schneider P, Kewish CM, Wepf R, et al. Ptychographic X-ray computed tomography at the nanoscale. *Nature* 2010;467:436–82.
- [633] Williams GJ, Quiney HM, Dhal BB, Tran CQ, Nugent KA, Peele AG et al. Fresnel coherent diffractive imaging. *Phys Rev Lett* 2006;97:Art. n. 025506.
- [634] Abbey B, Nugent KA, Williams GJ, Clark JN, Peele AG, Pfeifer MA, et al. Keyhole coherent diffractive imaging. *Nat Phys* 2008;4:394–8.
- [635] Williams GJ, Quiney HM, Peele AG, Nugent KA. Fresnel coherent diffractive imaging: treatment and analysis of data *New J Phys* 2010;12:Art. n. 035020.
- [636] Seaberg MD, Adams DE, Townsend EL, Raymondson DA, Schlotter WF, Liu YW, et al. Ultrahigh 22 nm resolution coherent diffractive imaging using a desktop 13 nm high harmonic source. *Opt Express* 2011;19:22470–9.
- [637] Roy S, Parks D, Seu KA, Su R, Turner JJ, Chao W, et al. Lensless X-ray imaging in reflection geometry. *Nat Photonics* 2011;5:243–5.
- [638] Miao J, Ohsuna T, Terasaki O, Hodgson KO, O'Keefe MA. Atomic resolution three-dimensional electron diffraction microscopy *Phys Rev Lett* 2002;89:Art. n. 155502.
- [639] Zuo JM, Vartanyants I, Gao M, Zhang R, Nagahara LA. Atomic resolution imaging of a carbon nanotube from diffraction intensities. *Science* 2003;300:1419–21.
- [640] De Caro L, Carlino E, Caputo G, Cozzoli PD, Giannini C. Electron diffractive imaging of oxygen atoms in nanocrystals at sub-angstrom resolution. *Nat Nanotechnol* 2010;5:360–5.
- [641] Singer A, Ulvestad A, Cho HM, Kim JW, Maser J, Harder R, et al. Nonequilibrium structural dynamics of nanoparticles in LiNi1/2Mn3/2O4 cathode under operando conditions. *Nano Lett* 2014;14:5295–300.
- [642] Ulvestad A, Cho HM, Harder R, Kim JW, Dietze SH, Fohtung E, et al. Nanoscale strain mapping in battery nanostructures. *Appl Phys Lett* 2014;104:5.
- [643] Ulvestad A, Singer A, Clark JN, Cho HM, Kim JW, Harder R, et al. Topological defect dynamics in operando battery nanoparticles. *Science* 2015;348:1344–7.
- [644] Quiney HM, Williams GJ, Fohtung E. Editorial for special issue on coherent diffractive imaging. *J Opt* 2018;20:010201.
- [645] Jiang HD, Song CY, Chen CC, Xu R, Raines KS, Fahimian BP, et al. Quantitative 3D imaging of whole, unstained cells by using X-ray diffraction microscopy. *Proc Natl Acad Sci USA* 2010;107:11234–9.
- [646] Nam D, Park J, Gallagher-Jones M, Kim S, Kim S, Kohmura Y. Imaging fully hydrated whole cells by coherent X-ray diffraction microscopy. *Phys Rev Lett* 2013;110:Art. n. 098103.
- [647] Robinson IK, Vartanyants IA, Williams GJ, Pfeifer MA, Pitney JA. Reconstruction of the shapes of gold nanocrystals using coherent x-ray diffraction. *Phys Rev Lett* 2001;87:Art. n. 195505.
- [648] Robinson I, Harder R. Coherent X-ray diffraction imaging of strain at the nanoscale. *Nat Mater* 2009;8:291–8.
- [649] Clark JN, Beitra L, Xiong G, Fritz DM, Lemke HT, Zhu DL, et al. Imaging transient melting of a nanocrystal using an X-ray laser. *Proc Natl Acad Sci USA* 2015;112:7444–8.
- [650] Coughlan HD, Darmanin C, Kirkwood HJ, Phillips NW, Hoxley D, Clark JN, et al. Three-dimensional reconstruction of the size and shape of protein microcrystals using Bragg coherent diffractive imaging. *J Opt* 2016;18:9.
- [651] Pfeiffer F. X-ray ptychography. *Nat Photonics* 2018;12:9–17.
- [652] Sala S, Kuppili VSC, Chalkidis S, Batey DJ, Shi XW, Rau C, et al. Multiscale X-ray imaging using ptychography. *J Synchrotron Radiat* 2018;25:1214–21.
- [653] Godard P, Carbone G, Allain M, Mastropietro F, Chen G, Capello L et al. Three-dimensional high-resolution quantitative microscopy of extended crystals. *Nat Commun* 2011;2:Art. n. 568.
- [654] Takahashi Y, Suzuki A, Furutaku S, Yamauchi K, Kohmura Y, Ishikawa T. Bragg x-ray ptychography of a silicon crystal: visualization of the dislocation strain field and the production of a vortex beam. *Phys Rev B* 2013; 87:Art. n. 121201.
- [655] Hruszkewycz SO, Highland MJ, Holt MV, Kim D, Folkman CM, Thompson C, et al. Imaging local polarization in ferroelectric thin films by coherent X-ray bragg projection ptychography. *Phys Rev Lett* 2013; 110:Art. n. 177601.
- [656] Mastropietro F, Godard P, Burghammer M, Chevallard C, Daillant J, Duboisset J et al. Revealing crystalline domains in a mollusc shell single-crystalline prism. *Nat Mater* 2017;16:946–+.
- [657] da Silva JC, Trtik P, Diaz A, Holler M, Guizar-Sicairos M, Raabe J, et al. Mass density and water content of saturated never-dried calcium silicate hydrates. *Langmuir* 2015;31:3779–83.
- [658] Cuesta A, De la Torre AG, Santacruz I, Trtik P, da Silva JC, Diaz A, et al. Chemistry and mass density of aluminum hydroxide gel in eco-cements by ptychographic X-ray computed tomography. *J Phys Chem C* 2017;121:3044–54.
- [659] Holler M, Guizar-Sicairos M, Tsai EHR, Dinapoli R, Muller E, Bunk O, et al. High-resolution non-destructive three-dimensional imaging of integrated circuits. *Nature* 2017;543:402–6.
- [660] Giewekemeyer K, Thibault P, Kalbfleisch S, Beerlink A, Kewish CM, Dierolf M, et al. Quantitative biological imaging by ptychographic x-ray diffraction microscopy. *Proc Natl Acad Sci USA* 2010;107:529–34.
- [661] Vine DJ, Pelliccia D, Holzner C, Baines SB, Berry A, McNulty I, et al. Simultaneous X-ray fluorescence and ptychographic microscopy of *Cyclotella meneghiniana*. *Opt Express* 2012;20:18287–96.
- [662] Marrison J, Raty L, Marriott P, O'Toole P. Ptychography – a label free, high-contrast imaging technique for live cells using quantitative phase information. *Sci Rep* 2013;3:Art. n. 2369.
- [663] Berenguer F, Bean RJ, Bozec L, Vila-Comamala J, Zhang FC, Kewish CM, et al. Coherent X-ray imaging of collagen fibril distributions within intact tendons. *Biophys J* 2014;106:459–66.
- [664] Deng JJ, Vine DJ, Chen S, Nashed YSG, Jin QL, Phillips NW, et al. Simultaneous cryo X-ray ptychographic and fluorescence microscopy of green algae. *Proc Natl Acad Sci USA* 2015;112:2314–9.
- [665] Diaz A, Malkova B, Holler M, Guizar-Sicairos M, Lima E, Panneels V, et al. Three-dimensional mass density mapping of cellular ultrastructure by ptychographic X-ray nanotomography. *J Struct Biol* 2015;192:461–9.
- [666] Shahmoradian SH, Tsai EHR, Diaz A, Guizar-Sicairos M, Raabe J, Spycher L, et al. Three-dimensional imaging of biological tissue by cryo X-ray ptychography. *Sci Rep* 2017;7:12.
- [667] Holler M, Raabe J, Diaz A, Guizar-Sicairos M, Wepf R, Odstrcil M, et al. OMNY-A tomography Nano cryo stage. *Rev Sci Instrum* 2018;89:13.
- [668] De Angelis S, Jorgensen PS, Esposito V, Tsai EHR, Holler M, Kreka K, et al. Ex-situ tracking solid oxide cell electrode microstructural evolution in a redox cycle by high resolution ptychographic nanotomography. *J. Power Sources* 2017;360:520–7.
- [669] Shannon CE, Proc IRE. Communications in the presence of noise. *Proc Inst Radio Eng* 1949;37:10–21.
- [670] Jerrri AJ. The Shannon sampling theorem – its various extensions and applications: a tutorial review. *Proc IEEE* 1977;64:1565–96.
- [671] Giacovazzo C, Monaco HL, Artigli G, Viterbo D, Milanesio M, Gilli G, et al. Fundamentals of Crystallography. Oxford: Oxford University Press; 2011.
- [672] Burla MC, Caliendo R, Carrozzini B, Cascarano GL, De Caro L, Giacovazzo C, et al. Ab initio protein phasing: the Patterson deconvolution method in SIR2002. *J Appl Crystallogr* 2004;37:258–64.
- [673] Caliendo R, Carrozzini B, Cascarano GL, De Caro L, Giacovazzo C, Siliqi D. Advances in ab initio protein phasing by Patterson deconvolution techniques. *J Appl Crystallogr* 2007;40:883–90.
- [674] Miao J, Sayre D, Chapman HN. Phase retrieval from the magnitude of the Fourier transforms of nonperiodic objects. *J Opt Soc Am A-Opt Image Sci Vis* 1998;15:1662–9.
- [675] Chen CC, Miao J, Wang CW, Lee TK. Application of optimization technique to noncrystalline x-ray diffraction microscopy: guided hybrid input-output method. *Phys Rev B* 2007;76:Art. n. 064113.
- [676] Rodenburg JM, Hurst AC, Cullis AG. Transmission microscopy without lenses for objects of unlimited size. *Ultramicroscopy* 2007;107:227–31.
- [677] Gerchberg RW, Saxton WO. A practical algorithm for the determination of phase from image and diffraction plane pictures. *Optik* 1972;35:237–46.
- [678] Fienup JR. Phase retrieval algorithms: a comparison. *Appl Opt* 1982;21:2758–69.
- [679] Fienup JR. Phase retrieval algorithms: a personal tour. *Appl Optics* 2013;52:45–56.
- [680] Colombo A, Galli DE, De Caro L, Scattarella F, Carlino E. Facing the phase problem in coherent diffractive imaging via memetic algorithms. *Sci Rep*

- 2017;7:42236.
- [681] Groppo E, Liu W, Zavorotynska O, Agostini G, Spoto G, Bordiga S, et al. Subnanometric Pd particles stabilized inside highly cross-linked polymeric supports. *Chem Mat* 2010;22:2297–308.
- [682] Groppo E, Agostini G, Borfecchia E, Wei L, Giannici F, Portale G, et al. Formation and growth of Pd nanoparticles inside a highly cross-linked polystyrene support: role of the reducing agent. *J Phys Chem C* 2014;118:8406–15.
- [683] Groppo E, Agostini G, Borfecchia E, Lazzarini A, Liu W, Lamberti C, et al. The pyridyl functional groups guide the formation of Pd nanoparticles inside a porous poly(4-vinyl-pyridine). *ChemCatChem* 2015;7:2188–95.
- [684] Lazzarini A, Groppo E, Agostini G, Borfecchia E, Giannici F, Portale G, et al. Formation and growth of palladium nanoparticles inside porous poly(4-vinyl-pyridine) monitored by operando techniques: the role of different reducing agents. *Catal Today* 2017;283:144–50.
- [685] De Caro L, Altamura D, Arciniegas M, Siliqi D, Kim MR, Sibillano T et al. Ptychographic imaging of branched colloidal nanocrystals embedded in free-standing thick polystyrene films. *Sci Rep* 2016; 6:Art. n. 19397.
- [686] Chushkin Y, Zontone F, Lima E, De Caro L, Guardia P, Manna L, et al. Three-dimensional coherent diffractive imaging on non-periodic specimens at the ESRF beamline ID10. *J Synchrotr Radiat* 2014;21:594–9.
- [687] Ruderer MA, Muller-Buschbaum P. Morphology of polymer-based bulk heterojunction films for organic photovoltaics. *Soft Matter* 2011;7:5482–93.
- [688] Nilsson A, LaRue J, Öberg H, Ogasawara H, Dell'Angela M, Beye M, et al. Catalysis in real time using X-ray lasers. *Chem Phys Lett* 2017;675:145–73.
- [689] Meirer F, Weckhuysen BM. Spatial and temporal exploration of heterogeneous catalysts with synchrotron radiation. *Nat Rev Mater* 2018;3:324–40.
- [690] Bordallo HN, Liom C, Taylor J, Argyriou DN. Is artificial intelligence magic dust for big-science facilities? *IUCrJ* 2020;7:1–2.